



Università degli Studi di Padova

Department of Physics and Astronomy “Galileo Galilei”

Ph.D. course in Physics

Cycle XXXVII

FINAL DISSERTATION

Hamiltonian Lattice Gauge Theories: emergent properties from tensor network methods

Supervisor:

Prof. Simone Montangero

Coordinator:

Prof. Giulio Monaco

Candidate:

Giovanni Cataldi

Year of the final exam: 2025

Abstract

This thesis develops advanced Tensor Network (TN) methods to address Hamiltonian Lattice Gauge Theories (LGTs), overcoming limitations in real-time dynamics and finite-density regimes. A novel dressed-site formalism is introduced, enabling efficient truncation of gauge fields while preserving gauge invariance for both Abelian and non-Abelian theories. This formalism is successfully applied to SU(2) Yang-Mills LGTs in two dimensions, providing the first TN simulations of this system and revealing critical aspects of its phase diagram and non-equilibrium behavior, such as a Quantum Many-Body (QMB) scarring dynamics. A generalization of the dressed-site formalism is proposed through a new fermion-to-qubit mapping for general lattice fermion theories, revealing powerful for classical and quantum simulations. Numerical innovations, including the use of optimal space-filling curves such as the Hilbert curve to preserve locality in high-dimensional simulations, further enhance the efficiency of these methods. Together with high-performance computing techniques, these advances open current and future development pathways toward optimized, efficient, and faster simulations on scales comparable to Monte Carlo state-of-the-art.

This thesis¹ is based on the following preprints, publications, and codes to which the author significantly contributed²:

- [1] Giovanni Cataldi, Ashkan Abedi, Giuseppe Magnifico, Simone Notarnicola, Nicola Dalla Pozza, Vittorio Giovannetti, and Simone Montangelo. “Hilbert Curve vs Hilbert Space: Exploiting Fractal 2D Covering to Increase Tensor Network Efficiency”. *Quantum*, Sept. 2021. DOI: [10.22331/q-2021-09-29-556](https://doi.org/10.22331/q-2021-09-29-556).
- [2] Giovanni Cataldi, Giuseppe Magnifico, Pietro Silvi, and Simone Montangelo. “Simulating (2+1)D SU(2) Yang-Mills Lattice Gauge Theory at Finite Density with Tensor Networks”. *Physical Review Research*, July 2024. DOI: [10.1103/PhysRevResearch.6.033057](https://doi.org/10.1103/PhysRevResearch.6.033057).
- [3] Giovanni Cataldi*, Marco Ballarin*, Giuseppe Magnifico, Daniel Jaschke, Marco Di Liberto, Ilaria Siloi, Simone Montangelo, and Pietro Silvi. “Digital Quantum Simulation of Lattice Fermion Theories with Local Encoding”. *Quantum*, Sept. 2024. DOI: [10.22331/q-2024-09-04-1460](https://doi.org/10.22331/q-2024-09-04-1460).
- [4] Giovanni Cataldi*, Giuseppe Calajò*, Marco Rigobello, Darvin Wanisch, Giuseppe Magnifico, Pietro Silvi, Simone Montangelo, and Jad C. Halimeh. *Quantum Many-Body Scarring in a Non-Abelian Lattice Gauge Theory*. May 2024. DOI: [10.48550/arXiv.2405.13112](https://doi.org/10.48550/arXiv.2405.13112).
- [5] Giuseppe Magnifico, Giovanni Cataldi, Marco Rigobello, Peter Majcen, Daniel Jaschke, Pietro Silvi, and Simone Montangelo. *Tensor Networks for Lattice Gauge Theories beyond One Dimension: A Roadmap*. July 2024. DOI: [10.48550/arXiv.2407.03058](https://doi.org/10.48550/arXiv.2407.03058).
- [6] Giovanni Cataldi. *Ed-Lgt*. Exact Diagonalization Code for Lattice Gauge Theories and Quantum Many Body Hamiltonians. May 2024. DOI: [10.5281/ZENODO.11145318](https://doi.org/10.5281/ZENODO.11145318).

¹**Acknowledgements** Written with the financial support of MIUR through the PRIN2017 and PRIN2022 projects TANQU; of the European Union via the QuantERA projects QuantHEP and T-NISQ, the Quantum Flagship project PASQuanS2, and the NextGenerationEU (PNRR) project CN00000013 - Italian Research Center on HPC, Big Data and Quantum Computing; of the WCRI-Quantum Computing and Simulation Center of the University of Padova, Fondazione CARIPARO, and Progetti Dipartimenti di Eccellenza through the project Frontiere Quantistiche (FQ), and the INFN project QUANTUM. We acknowledge the computational resources provided by Cloud Veneto, CINECA, the BwUniCluster, and the University of Padova Strategic Research Infrastructure Grant 2017: CAPRI (Calcolo ad Alte Prestazioni per la Ricerca e l’Innovazione).

²The authors with * equally contributed to the work.

Contents

Introduction	vii
1 Hamiltonian Lattice Gauge Theories	1
1.1 Lattice discretization	2
1.1.1 Preliminaries	2
1.1.2 Continuum limit and Lorentz invariance	3
1.1.3 Discretization of fermions fields	3
1.1.4 Discretization of gauge fields	7
1.2 Dressed-site model for Hamiltonian Lattice Gauge Theories	12
1.2.1 Gauge field truncation	13
1.2.2 Gauss law and the dressed site	14
1.2.3 Projecting dressed site operators onto the gauge-invariant basis	15
1.2.4 Defermionization	15
1.3 SU(2) Yang-Mills Lattice Gauge Theory	16
1.3.1 The model	16
1.3.2 Truncating the SU(2) gauge group	17
1.3.3 Rishon decomposition of SU(2) gauge fields	19
1.3.4 Constructing dressed site operators	22
1.3.5 Hardcore-gluon model: minimally truncated gauge-fields	24
1.4 U(1) Lattice Gauge Theory	28
1.4.1 The model	28
1.4.2 Truncating the U(1) gauge group	29
1.4.3 Rishon decomposition of U(1) gauge fields	29
1.4.4 Constructing the dressed-site operators	31
1.4.5 Scaling of the local basis dimension	34
1.5 Summary	35
2 Tensor Networks methods for LGTs	37
2.1 Exact Representation of Quantum Many-Body Systems	38
2.1.1 Block Diagonalization	39
2.1.2 Basic Tensor Operations	41
2.1.3 Entanglement area law	45
2.2 Tensor Networks Methods	45
2.2.1 Tensor Network state	45
2.2.2 Loopless Tensor Networks ansätze	47
2.2.3 Matrix product states	49
2.2.4 Tree Tensor Networks	51
2.2.5 Tensor Network ansätze with loops	52

2.3	Efficient Tensor Network geometries beyond one dimension	52
2.3.1	Preserving the locality of interactions	53
2.3.2	Hilbert curve	54
2.3.3	Numerical evidences	55
2.3.4	Distance distributions	56
2.3.5	Conclusions	58
2.4	Variational ground state search algorithm	59
2.4.1	High level operations	59
2.4.2	Ground state reach algorithm in details	61
2.5	Time Evolution Algorithms for Tensor Network	62
2.5.1	Time Evolved Block Decimation	64
2.5.2	Time-Dependent Variational Principle	64
2.6	Roadmap for advanced LGT simulations via tensor networks	64
2.6.1	Local basis truncation	65
2.6.2	Tailored initial states	68
2.6.3	Leverage HPC techniques for local optimization	69
2.6.4	Sweeps and HPC parallelization	70
2.6.5	Finite temperature regime	73
2.7	Summary	73
3	Equilibrium properties of SU(2) LGT	75
3.1	The model	75
3.1.1	Local Observables	76
3.2	Magneto-electric transition in the pure theory	77
3.3	Baryonic spectrum	78
3.4	Baryon-liquid phase	79
3.5	Non-local/Topological properties	81
3.5.1	Topological Invariants	85
3.5.2	Topological properties the pure theory	85
3.5.3	Dynamical matter removes the topological symmetry	87
3.6	Large-coupling phase via perturbation theory	87
3.7	Phase Diagram	91
3.8	Summary	91
4	Non-Ergodic dynamics of LGTs	95
4.1	Thermalization in Classical Systems	96
4.2	Thermalization in Quantum Systems	97
4.2.1	The Eigenstate Thermalization Hypothesis (ETH)	98
4.3	Quantum Many-Body Scars and Lattice Gauge Theories	99
4.3.1	Experimental observations of scars in Rydberg atoms	100
4.3.2	Scars in Abelian Lattice Gauge Theories	101
4.3.3	Gauge theory interpretation of slow dynamics	102
4.4	Scars in Non-Abelian Lattice Gauge Theories	103
4.4.1	The model	103
4.4.2	Observing scarred dynamics	105
4.4.3	Tower of scar states	106
4.4.4	Ergodic dynamics for other initial states	107
4.4.5	Ergodic dynamics for other parameter regimes	107
4.4.6	Scars at higher gauge link truncation	108
4.4.7	Scaling with the system size	109

4.4.8	Long-time dynamics	109
4.5	Summary	110
5	Simulating Lattice Fermion Theories	113
5.1	Gauge Defermionization of Lattice Fermion Theories	115
5.1.1	Mapping into a \mathbb{Z}_2 gauge theory	115
5.1.2	Restoring equivalence with Plaquette Operators	117
5.1.3	Fermionic Rishons	118
5.1.4	The price of deferfionization	119
5.2	Hubbard Model, Deferfionized for tensor networks	119
5.2.1	Dressed-site Hamiltonian	121
5.2.2	Numerical Results	121
5.3	Digital quantum simulation	124
5.3.1	Fermion to qubits mapping of the deferfionized Hubbard Hamiltonian . .	125
5.3.2	Vertex and plaquette constraints	127
5.3.3	Link constraint	128
5.3.4	Preparation of spin and charge excitations	128
5.3.5	Propagation of spin and charge excitations	131
5.4	Summary	133
6	Conclusions and Outlook	135
	Bibliography	139

Introduction

Quantum field theory (QFT) is a foundational framework in particle physics, offering a comprehensive description of how particles interact. It integrates the principles of quantum mechanics with special relativity to provide insights into the behavior of particles under different forces. Gauge invariance is a fundamental principle in QFT, representing a special symmetry where the equations describing a physical system remain unchanged under local transformations of the fields. Then, a gauge theory is a framework that imposes these local symmetries as constraints, ensuring that certain transformations can occur independently at each point in space and time without altering the observable outcomes. The Standard Model (SM) of particle physics [7] represents the current state-of-the-art in our understanding of gauge theories, as it successfully unifies the electromagnetic, weak, and strong interactions under a common theoretical framework, incorporating both Abelian and non-Abelian gauge symmetries. It has proven remarkably successful in explaining a wide range of experimental results and predicting new phenomena.

However, non-Abelian gauge theories, particularly QCD, pose significant challenges, especially in the low-energy, non-perturbative regime. At high energies, where the gauge coupling constant is small, perturbation theory is an effective tool for making predictions, such as those concerning high-energy collisions in particle accelerators. However, at lower energies, typical of the hadronic scale (below 1 GeV), the gauge coupling constant becomes large, making perturbative methods inadequate. To overcome these limitations, lattice gauge theories (LGTs) provide a non-perturbative framework for studying QCD and other gauge theories [8–10], allowing numerical simulations to be performed. LGTs discretize spacetime into a lattice grid where matter and gauge fields occupy lattice sites and links respectively. One of the most successful applications of LGTs is lattice QCD [11–13], which has been instrumental in computing the hadronic spectrum, such as the masses of protons and neutrons, and understanding phenomena like confinement [14–19], chiral symmetry breaking [20–23], and the role of topology in QCD at finite temperatures [15, 24–26]. In these terms, Monte Carlo (MC) simulations of LGTs play a critical role by providing statistically meaningful results for observables that are otherwise inaccessible through analytical methods [24, 27–37]. Despite these successes, MC simulations face challenges, particularly the sign problem, which hampers the simulation of a wide class of physical settings described by complex or negative actions (finite charge-density phases, fermions, real-time dynamics), whose numerical investigations remain – to date – an open problem [38, 39].

According to Feynman, all these challenges could have been solved by attacking quantum systems with a quantum computer, where traditional classical numerical methods could be circumvented, particularly in handling quantum correlations (i.e. entanglement). After his seminal proposal and the recent fast development of quantum hardware, there is growing interest in experimental platforms for simulating LGTs, such as ultra-cold atoms, optical lattices, and superconducting circuits. Recently, quantum-inspired strategies have been applied to LGTs, attempting to reproduce their quantum dynamics [40–45].

While awaiting noiseless and scalable quantum hardware, in the current *Noisy Intermediate-Scale Quantum* (NISQ) era, MC problems have inspired the development of novel classical numerical algorithms based on Tensor Networks (TN) [46–49]. These techniques exploit the area-law entanglement bounds satisfied by a large class of quantum many-body (QMB) systems [50] and allow for an efficient representation of the low-energy sector by retaining in memory only the relevant states that contribute to equilibrium and non-equilibrium properties. This is achieved by compressing the exponentially large wavefunctions into a network of tensors interconnected through auxiliary indices with bond dimension χ . The main TN ansätze for representing QMB states are Matrix Product States (MPS) for 1D systems [51–55], Projected Entangled Pair States (PEPS) [46, 56–68], Tree Tensor Networks (TTN) [49, 69–72] and Multiscale Entanglement Renormalization Ansatz (MERA) [72–74], which can be defined in any dimension.

Recent advances in TN methods offered promising alternatives for studying LGTs without MC limitations like the sign problem. Indeed, TNs are particularly valuable for attacking non-perturbative LGT phenomena in the Hamiltonian formulation, accessing real-time dynamics and finite-density phases. Exploiting TN algorithms, noteworthy results have been produced for Abelian LGTs in one [75–88] and higher spatial dimensions [89–91]. As for non-Abelian LGTs, TN-based simulations were so far limited to one spatial dimension [92–94], but recently, they have been successfully applied to two dimensional systems [2].

Despite all these achievements, one main challenge for numerical and quantum simulations of LGTs remains the finite-dimensional encoding of the continuous gauge fields, especially beyond one spatial dimension, where decoupling the gauge field’s longitudinal component is required [95]. Among known truncation recipes are Quantum Link Models (QLM) [96–100], an approach already considered for practical quantum simulation of LGTs [101–111], finite subgroups [82, 86, 112], digitization of gauge fields [113], and fusion-algebra deformation [114]. Whatever the adopted solution, further effort is required to satisfy gauge symmetry at each local site, which involves the concurrent evaluation of all the gauge links and the attached matter site [93, 115, 116]. As it represents the highest energy-scale of the model, any violation of this constraint would prevent the correctness of simulations.

Another important issue to be faced in simulating LGTs is to account for the Fermi statistics of matter fields. In several TN methods as well on well-established conventional digital quantum simulation platforms (e.g. superconducting qubits, trapped-ions, Rydberg arrays, quantum dots) [117–121], which are built on distinguishable, spatially localized qubits (or qudits), fermionic algebra (mutually-anticommuting operations) must be encoded into a genuinely local algebra (mutually-commuting operations) of qudits. Standard fermion-to-qubit encodings, such as the Jordan-Wigner (JW) transformation [122], and other modern approaches [123–125] make any fermionic Hamiltonian interaction inherently long-range and expensive from a computational perspective. Together with the truncation of the gauge fields and the Gauss’s law constraint, these challenges necessitate further advancements in numerical and quantum simulation strategies to accurately capture the ground-state and dynamical properties of LGTs.

In this thesis, we address these challenges: we discuss a theoretical and numerical formalism that provides a controllable gauge field truncation (in Casimir spectrum) and directly accesses the Hilbert subspace of gauge invariant states where gauge and matter fields are combined in a *dressed-site* encoded with a bosonic statistics. Such a formalism is detailed and quantitatively discussed in [2, 5] for both Abelian and non-Abelian LGT, yet successfully generalizes to lattice fermion theories without gauge invariance occurring in condensed matter [3]. We exploit this approach to perform numerical simulations of the SU(2) Yang-Mills LGT in and out of equilibrium, exploring compelling regimes in the phase diagram [2] and exotic behaviors like

QMB scarring dynamics [4]. In parallel, we review the state-of-the-art TN methods for Hamiltonian LGTs, providing and testing optimal encodings for high-dimensional Hamiltonians [1] and figuring strategies for parallelized high-performance large-scale simulations of LGTs [5].

All the achievements conveyed in this work [1–5] not only advance the theoretical and numerical understanding of LGT by means of TN methods, but also provide valuable benchmarks for experimental quantum simulations [126–139], contributing to systematically identify the quantum advantage threshold [140, 141] towards a deeper understanding of the fundamental interactions governing particle and condensed matter physics.

The thesis is structured as follows: in Chap. 1, we provide a detailed overview of all the fundamental ingredients of an LGT. Starting from the basics of QFT, we discuss the main effects arising from the lattice discretization of the theory, with a special focus on fermion fields and energy cutoffs. The whole discussion is based on the Hamiltonian formalism, as it will be lately exploited for all the presented numerical results. The innovative part of this chapter starts from the dressed-site formalism discussed in Sec. 1.2, a theoretical scheme that reveals extremely useful for simulating LGTs via TN and quantum hardware. Such an approach is detailed and quantitatively applied first to the challenging non-Abelian SU(2) Yang-Mills theory (Sec. 1.3) and secondly to the Abelian U(1) case (Sec. 1.4). In both scenarios, we derive a pedagogical strategy to simulate the LGT in any spatial dimensions, with a controllable and scalable truncation of the gauge fields, where Gauss law is automatically satisfied. The resulting theories are made out of bosonic degrees of freedom, preventing simulations from the challenging sign problem that characterizes MC methods.

In Chap. 2, we discuss the state-of-the-art numerical methods for attacking QMB Hamiltonians and, more in detail, the previously discussed LGTs. We start reviewing Exact Diagonalization (ED) methods and the numerical strategies to exploit the global symmetries such as particle-number or momentum conservation via block diagonalization. These features are currently implemented in the ED-LGT Python library [6], developed throughout these three years for simulating and benchmarking QMB systems and dressed-site formulated LGTs such as the ones presented in Chap. 1. We then switch to reviewing TN methods, from the fundamental tensor operations to advanced algorithms for ground-state search and time evolution of QMB systems tailored for MPS and TTN ansätze.

A noteworthy section compares different ways of mapping high-dimensional Hamiltonians onto TN structures, demonstrating the Hilbert curve [1] as the optimal ordering for preserving distances and quantum correlations when simulating large scale high-dimensional QMB systems. We conclude the chapter by discussing the status of TN methods dedicated to LGTs, providing current and future lines of development towards optimized, efficient, and faster simulations on scales comparable to MC state-of-the-art. All these strategies are conveyed in a recent roadmap [5] and stimulate benchmarking tests for quantum simulations of LGTs.

After discussing all theoretical and numerical tools that are necessary for simulating LGTs, we devote the second part of the thesis to the presentation of the most compelling results achieved and conveyed in the following recent scientific works: [2–4]. In Chap. 3, we present the first TN simulations of a SU(2) Yang-Mills LGT with flavorless fermionic dynamical matter in two spatial dimensions [2]. The simulations rely on the *hardcore-gluon* approximation, the smallest nontrivial electric-truncation of the SU(2) gauge fields discussed in Sec. 1.3.5. However, they provide a clear phase diagram of the model both at zero and finite baryon density, exploring challenging regimes of the couplings and addressing the continuum limit location.

In Chap. 4, we discuss the non-equilibrium properties of LGTs, with compelling regard to the

non-ergodic behaviors observed in non-Abelian LGTs. After a pedagogical introduction to classical and quantum ergodicity, we expose the Eigenstate Thermalization Hypothesis (ETH) for isolated QMB systems concerning their spectral and dynamical properties. We review the first experimental and numerical observations of QMB systems with *scarring* dynamics, an exotic behavior that weakly violates ETH. We highlight the strong connection between the main features of QMB scars and the fundamental mechanism appearing in Abelian LGTs. Remarkably, we extend such a relation to non-Abelian LGTs by simulating a one-dimensional truncated SU(2) Yang-Mills LGT and observing all the spectral and dynamical properties of a scarring dynamics [4]. These phenomena are further explained through meson-baryon creation processes that are intrinsically due to the non-Abelian nature of the model.

Finally, Chap. 5 focuses on the recent work [3], where we discuss an extension of the dressed-site formalism for generic lattice fermion theories without gauge invariance. In detail, we propose an efficient fermion-to-qubit mapping that is suitable for classical and (digital) quantum simulations. We test its applicability on the spin-(1/2) Fermi-Hubbard model in two spatial dimensions investigating both equilibrium and non-equilibrium properties via TN methods. We demonstrate the perfect equivalence with the original model and recover interesting features of the expected physics. The presented encoding is then compared in detail with other theoretical strategies to remove Fermi statistics, revealing efficient, scalable, and competitive.

Chapter 1

Hamiltonian Lattice Gauge Theories

As anticipated, gauge theories form the backbone of our understanding of fundamental interactions in particle physics. Central to gauge theories is the principle of gauge invariance, where physical laws remain unchanged under local transformations of certain fields. Different realizations of gauge theories correspond to different symmetry groups and interaction structures. In Quantum Electrodynamics (QED), the $U(1)$ symmetry group governing electromagnetic interactions, with the photon as the associated gauge boson. Non-Abelian gauge theories, such as those based on $SU(2)$ and $SU(3)$ symmetry groups, describe the weak and strong interactions, respectively. These groups allow for more complex transformations, where the gauge bosons themselves interact with one another. For instance, in Quantum Chromodynamics (QCD), the $SU(3)$ gauge theory of the strong force, gluons are the gauge bosons that mediate interactions between quarks and also interact among themselves due to the non-Abelian nature of the theory.

Lattice Gauge Theories (LGTs) [8–10] offer a non-perturbative framework for studying these models, particularly in regimes where perturbative methods fail, such as in low-energy QCD [11–13]. By discretizing spacetime into a lattice, LGTs enable numerical simulations of gauge theories, allowing us to explore compelling phenomena such as confinement [14–19], chiral symmetry breaking [20–23], the hadronic spectrum, and the dynamics of quarks and gluons [142].

In traditional Monte Carlo (MC) approach to LGTs [24, 27–37], the action of a continuum gauge theory is regularized by working on a finite and discrete Euclidean spacetime, where both space and (imaginary) time are discretized [29]. Instead, Tensor Networks (TN) and quantum simulations typically rely on the Hamiltonian formalism, where time remains a real continuous variable, while space is discretized on a D -dimensional lattice. The Hamiltonian discretization of gauge theories explicitly breaks Lorentz invariance, which is however restored in the continuum limit. Simultaneously, Hamiltonian LGTs present features that distinguish them from other QMB systems commonly simulated via TN or quantum hardware [8]. Next, we discuss these properties in more detail and outline the main steps that have to be taken to exploit TN algorithms. Without any loss of generality, we focus on matter-coupled LGTs of the Yang-Mills type, routinely employed in high-energy physics to describe nature’s fundamental interactions.

We start from a pedagogical review of lattice discretization in Sec. 1.1, with special regard for fermion fields within the staggered fermion solution in Sec. 1.1.3 and gauge fields in Sec. 1.1.4. The original contribution of this chapter starts from Sec. 1.2, where we present the *dressed-site* formalism, a theoretical scheme that is suitable for attacking LGTs via TNs and quantum hardware directly within the gauge-invariant sector, where all the logical degrees of freedom undergo a bosonic statistics. In Secs. 1.3 and 1.4, we respectively detail two specific realizations

of this formalism, $SU(2)$ for the non-Abelian and $U(1)$ for the Abelian scenario. Such an approach has been successfully applied to obtain all the numerical results detailed in Chaps. 3 and 4 (see also [2, 4, 5, 143]) and is generalized to pure fermion theories (without gauge fields, i.e. no LGTs) in [3] and Chap. 5.

1.1 Lattice discretization

Let us consider continuous $(D+1)$ spacetime domain $(\mathbb{R}^D \times \mathbb{R})$ identified by the $(D+1)$ -dimensional point $r = (t, \mathbf{r})$, where $\mathbf{r} = (r_1, \dots, r_D)$. When performing spatial discretization, the time variable t remains continuous, while the spatial domain \mathbb{R}^D is replaced by a hyper-cubic D -dimensional lattice Λ , whose sites are equally spaced by lattice constant a_0 (see Fig. 1.1). Lattice sites are then labelled by coordinates $\mathbf{n} = (n_1, \dots, n_D)$, where $r_k = a_0 n_k$ and $n_k \in \{1 \dots N_k\}$, with N_k denoting the number of lattice sites along the k^{th} direction $\forall k = 1, \dots, D$. Then, if $N = \prod_{k=1}^D N_k$ is the total number of lattice sites, with the corresponding lattice volume given by $V = a_0^D N$. Additionally, we define the unit lattice vectors $\pm \boldsymbol{\mu}_k$ pointing along the $\pm k^{\text{th}}$ direction, assuming $\pm \boldsymbol{\mu}_k = \boldsymbol{\mu}_{\pm k}$. We use the convention where summations over lattice vectors include only positive directions. Then, the lattice link connecting two neighboring sites \mathbf{n} and $\mathbf{n} + \boldsymbol{\mu}_k$ along the direction $+\boldsymbol{\mu}_k$, is denoted by the couple $(\mathbf{n}, \boldsymbol{\mu}_k)$ or equivalently with $(\mathbf{n} + \boldsymbol{\mu}_k, -\boldsymbol{\mu}_k)$. For future purposes, we refer to an *even* (*odd*) site, if $(-1)^{\mathbf{n}} = (-1)^{\sum_k n_k}$ is even (odd).

1.1.1 Preliminaries

Lattice discretization of spatial dimensions affects all the mathematical objects: for a general scalar field $f(\mathbf{r})$ whose absolute value is *square-integrable*

$$\int_{\mathbb{R}^D} dr^D |f(\mathbf{r})|^2 = L < \infty, \quad (1.1.1)$$

we have to consider the following replacements:

$$\int_{\mathbb{R}^D} dr^D \longrightarrow a_0^D \sum_{\mathbf{n}}, \quad f(\mathbf{r}) \longrightarrow \hat{f}_{\mathbf{n}}, \quad \partial_k f(\mathbf{r}) \longrightarrow \frac{\hat{f}_{\mathbf{n}+\boldsymbol{\mu}_k} - \hat{f}_{\mathbf{n}-\boldsymbol{\mu}_k}}{2a_0}. \quad (1.1.2)$$

Such a discretization prescription introduces an *ultraviolet cut-off*, in energy and momentum, which depends on the inverse of the lattice spacing a_0 . Namely, for each spatial direction k , momentum is anisotropic and assumes N_k discrete values $p_k(i) \in \left[-\frac{\pi}{a_0}, \frac{\pi}{a_0}\right]$, where $i \in \{1 \dots N_k\}$. The maximal momentum along each direction is then $p_{\max} = \pi/a_0$, and corresponds to the maximal energy $E_{\max} = \sqrt{\mathbf{p}_{\max}^2 + m_0^2}$, where $\mathbf{p}_{\max} = (\pi/a_0, \pi/a_0, \pi/a_0)$. Correspondingly, assuming the lattice Λ with periodic boundary conditions, the continuous Fourier transform is adapted as follows:

$$f(\mathbf{r}) = \int_{\mathbb{R}^D} \frac{d\mathbf{p}}{(2\pi)^D} \tilde{f}(\mathbf{p}) e^{i\mathbf{r}\cdot\mathbf{p}} \quad \longrightarrow \quad f(\mathbf{n}) = \left(\frac{a_0}{2\pi}\right)^D \sum_{\mathbf{p}}^{\text{BZ}} \tilde{f}_{a_0}(\mathbf{p}) e^{ia_0\mathbf{n}\cdot\mathbf{p}}, \quad (1.1.3)$$

where BZ stands for the 1st Brillouin zone $\left[-\frac{\pi}{a_0}, \frac{\pi}{a_0}\right]^D$ and $\tilde{f}_{a_0}(\mathbf{p}_{\max}) = \tilde{f}_{a_0}(-\mathbf{p}_{\max})$. We can then express $\tilde{f}_{a_0}(\mathbf{p})$ in (finite) Fourier-series

$$\tilde{f}_{a_0}(\mathbf{p}) = a_0^D \sum_{\mathbf{n}} \hat{f}_{\mathbf{n}} e^{-ia_0\mathbf{n}\cdot\mathbf{p}}. \quad (1.1.4)$$

If we set $\hat{f}_{\mathbf{n}} = (2\pi)^{-D}$, then (1.1.4) reduces to the Fourier series representation of the δ function in the 1st BZ, namely

$$\delta_p(\mathbf{p}) = \left(\frac{a_0}{2\pi}\right)^D \sum_{\mathbf{p}}^{BZ} e^{-ia_0\mathbf{n}\cdot\mathbf{p}}, \quad (1.1.5)$$

where p stands for *periodic*. Note that, unlike the continuum limit, where $a_0 \rightarrow 0$, here $\delta_p(\mathbf{p})$ has "non-vanishing" support in $\mathbf{p} = 0$ (modulo $2m\pi$ for $m \in \mathbb{N}$). Similarly, the Dirac $\delta(\mathbf{r} - \mathbf{r}')$ becomes a Kronecker $\delta_{\mathbf{nn}'}$ (multiplied by a factor a_0^{-D})

$$\delta_{\mathbf{nn}'} = \left(\frac{a_0}{2\pi}\right)^D \sum_{\mathbf{p}}^{BZ} e^{ia_0\mathbf{n}\cdot\mathbf{p}}. \quad (1.1.6)$$

1.1.2 Continuum limit and Lorentz invariance

The main physical consequence of the ultraviolet cutoff is the following: the discretized theory does not describe physics at scales (momenta) smaller (larger) than the lattice spacing a_0 (π/a_0), i.e., all the short-distance (high-energy) phenomena [8].

Another effect of lattice discretization is the loss of the Lorentz invariance (the symmetry of special relativity), as the lattice spacing a_0 introduces a preferred reference frame. In the Lagrangian formalism, where both space and time are discretized, the spacetime lattice does not support continuous Lorentz transformations, but the theory retains a discrete version of spacetime symmetry, such as discrete rotations or translations. On the contrary, the spatial discretization performed in Hamiltonian LGTs breaks the symmetry between space and time, which is a crucial part of Lorentz invariance. In these terms, the Hamiltonian formalism is said to explicitly break Lorentz invariance.

Restoring the continuum theory and the Lorentz invariance requires to take the continuum limit, where $a_0 \rightarrow 0$, $N \rightarrow \infty$, while keeping $a_0 \cdot N$ fixed [144]. In this regime, maximum momentum \mathbf{p}_{\max} and energy E_{\max} become infinite and the lattice approximates the continuous space. The continuum limit is typically associated with the process of *renormalization*, where the theory is adjusted to correctly reproduce physical observables (which should be insensitive to the discretization) as the lattice spacing goes to zero. Unfortunately, the continuum limit location is non trivial and requires a lot of attention in understanding the relation between the lattice spacing and the Hamiltonian parameters. A comprehensive dissertation about the continuum limit would require a dedicated effort out of the purposes of the thesis. Nonetheless, we will partially discuss it in Secs. 1.1.3 and 1.1.4 by using simple dimensional analysis. For a deeper discussion, see [9, 14, 24, 144–147].

1.1.3 Discretization of fermions fields

Discretization of more complex objects such as fermion fields, i.e. spinors, requires more attention and encounters a set of problems whose solutions are not univocal nor perfect. Throughout this section, we will cover these challenges by focusing on one of the possible solutions: *staggered fermions*. For a more general and complete discussion about fermion discretization, see [14, 144, 148].

Let us start from the continuum Dirac equation for a massive free fermion. Assuming the spacetime coordinate $r = (t, \mathbf{r})$ and the metric $\eta^{\mu\nu} = \text{diag}(+1, -1, -1, -1)$, we have:

$$(i\hbar\gamma^\mu\partial_\mu - m_0c)\psi(r) = \left(i\frac{\hbar}{c}\gamma^0\partial_t - i\hbar\gamma^k\partial_k - m_0c\right)\psi(r) = 0, \quad (1.1.7)$$

where c is the speed of light, \hbar is the Planck constant, m_0 is the mass parameter, and γ^μ are the 4×4 Dirac matrices satisfying Clifford's algebra

$$\{\gamma^\mu, \gamma^\nu\} = 2\eta^{\mu\nu}. \quad (1.1.8)$$

The field $\psi(r)$ is a 4-dimensional spinor, whose Hermitian conjugate is $\bar{\psi}(r) = \psi^\dagger(r)\gamma^0$. The corresponding quantized version satisfies the canonical equal-time commutation relations

$$\{\hat{\psi}_\alpha(t, \mathbf{r}), \hat{\psi}_\beta^\dagger(t, \mathbf{r}')\} = i\hbar\delta_{\alpha\beta}\delta^3(\mathbf{r} - \mathbf{r}'), \quad (1.1.9)$$

where the α and β indices label spinor components. In the Hamiltonian form, Eq. (1.1.7) reads:

$$-i\hbar\partial_t\hat{\psi}(t, \mathbf{r}) = \left(ic\hbar\gamma^0\gamma^k\partial_k + m_0c^2\gamma^0 \right)\hat{\psi}(t, \mathbf{r}). \quad (1.1.10)$$

Omitting the time dependence, the Dirac Hamiltonian in this form becomes

$$\hat{H}_{\text{Dirac}} = \int d\mathbf{r}\hat{H}(\mathbf{r}) = \int d\mathbf{r}\left[\hat{\psi}^\dagger(\mathbf{r})(ic\hbar\gamma^0\gamma^k\partial_k + m_0c^2\gamma^0)\hat{\psi}(\mathbf{r})\right], \quad (1.1.11)$$

When discretizing the space on a D -dimensional spatial lattice Λ , we replace $\hat{\psi}(t, \mathbf{r}) \rightarrow \hat{\psi}_{\mathbf{n}}(t)$, where $\mathbf{r} = a_0\mathbf{n}$. Correspondingly, the canonical equal-time commutation relations become:

$$\{\hat{\psi}_{\mathbf{n},\alpha}(t), \hat{\psi}_{\mathbf{n}',\beta}^\dagger(t)\} = i\hbar\delta_{\alpha\beta}\delta_{\mathbf{n},\mathbf{n}'}. \quad (1.1.12)$$

Unless required, from now on, we will omit the temporal dependence, by simply focusing on $\hat{\psi}_{\mathbf{n}}$. Similarly, spatial derivatives $\partial_k\hat{\psi}(\mathbf{r})$ are replaced by (symmetric) finite differences:

$$\partial_k\hat{\psi}(\mathbf{r}) \longrightarrow \frac{1}{2a_0}\left[\hat{\psi}_{\mathbf{n}+\boldsymbol{\mu}_k} - \hat{\psi}_{\mathbf{n}-\boldsymbol{\mu}_k}\right]. \quad (1.1.13)$$

By recalling Eq. (1.1.2), the lattice Dirac Hamiltonian reads

$$\hat{H}_{\text{Dirac}}^{\text{latt}} = a_0^D \sum_{\mathbf{n},k} \hat{\psi}_{\mathbf{n}}^\dagger \left[ic\hbar \frac{\gamma^0\gamma^k}{2a_0} (\hat{\psi}_{\mathbf{n}+\boldsymbol{\mu}_k} - \hat{\psi}_{\mathbf{n}-\boldsymbol{\mu}_k}) \right] + a_0^D m_0 c^2 \sum_{\mathbf{n}} \hat{\psi}_{\mathbf{n}}^\dagger \gamma^0 \hat{\psi}_{\mathbf{n}}. \quad (1.1.14)$$

We then redefine $\hat{\psi}_{\mathbf{n}} \rightarrow a_0^{-D/2}\hat{\psi}_{\mathbf{n}}$ and obtain

$$\hat{H}_{\text{Dirac}}^{\text{latt}} = \sum_{\mathbf{n},k} \hat{\psi}_{\mathbf{n}}^\dagger \left[ic\hbar \frac{\gamma^0\gamma^k}{2a_0} (\hat{\psi}_{\mathbf{n}+\boldsymbol{\mu}_k} - \hat{\psi}_{\mathbf{n}-\boldsymbol{\mu}_k}) \right] + m_0 c^2 \sum_{\mathbf{n}} \hat{\psi}_{\mathbf{n}}^\dagger \gamma^0 \hat{\psi}_{\mathbf{n}}. \quad (1.1.15)$$

This choice makes the lattice fermion fields adimensional, even if their hidden dependence on the lattice spacing becomes important when considering the continuum limit location.

Fermion Doubling Problem

An artifact of the lattice discretization of fermions is the appearance of extra solutions of the Dirac equation, known as *doublers* [9]. In a D -dimensional space, these doublers lead to the appearance of $2^D - 1$ extra fermion species with respect to the continuum theory: namely, each spatial direction k contributes a factor of 2 to the number of solutions (one at $p_k = 0$ and one at $p_k = \pi/a_0$).

In order to formally visualize these extra solutions, let us transform the lattice spinor field to the momentum space using the previously defined Fourier transform:

$$\hat{\psi}_{\mathbf{n}} = \frac{1}{V} \sum_{\mathbf{p}} e^{i\mathbf{p}\cdot\mathbf{n}a_0} \hat{\psi}(\mathbf{p}), \quad (1.1.16)$$

where \mathbf{p} is the lattice momentum, while V is the lattice volume. Substituting Eq. (1.1.16) into the discretized derivative, we have:

$$\frac{\hat{\psi}_{\mathbf{n}+\boldsymbol{\mu}_k} - \hat{\psi}_{\mathbf{n}-\boldsymbol{\mu}_k}}{2a_0} = \frac{1}{V} \sum_{\mathbf{p}} e^{i\mathbf{p}\cdot\mathbf{n}a_0} \frac{e^{ip_k a_0} - e^{-ip_k a_0}}{2a_0} \hat{\psi}(\mathbf{p}) = \frac{1}{V} \sum_{\mathbf{p}} e^{i\mathbf{p}\cdot\mathbf{n}a_0} \frac{i \sin(p_k a_0)}{a} \hat{\psi}(\mathbf{p}). \quad (1.1.17)$$

Then, the lattice Dirac Hamiltonian in the momentum space becomes

$$\hat{H}(\mathbf{p}) = \hat{\psi}(\mathbf{p})^\dagger \left[- \sum_{k=1}^3 \gamma^0 \gamma^k \frac{c\hbar}{a_0} \sin(p_k a_0) + m_0 c^2 \gamma^0 \right] \hat{\psi}(\mathbf{p}). \quad (1.1.18)$$

From the eigenvalue equation $H(\mathbf{p})\hat{\psi}(\mathbf{p}) = E(\mathbf{p})\hat{\psi}(\mathbf{p})$, we have

$$\left[- \sum_{k=1}^3 \gamma^0 \gamma^k \frac{c\hbar}{a_0} \sin(p_k a_0) + m_0 c^2 \gamma^0 \right] \hat{\psi}(\mathbf{p}) = E(\mathbf{p})\hat{\psi}(\mathbf{p}) \quad (1.1.19)$$

Squaring both sides of the eigenvalue equation, we have:

$$\begin{aligned} \gamma^0 \left[- \sum_{k=1}^3 \frac{c\hbar \gamma^k}{a_0} \sin(p_k a_0) + m_0 c^2 \right] \gamma^0 \left[- \sum_{k'=1}^3 \frac{c\hbar \gamma^{k'}}{a_0} \sin(p_{k'} a_0) + m_0 c^2 \right] \hat{\psi}(\mathbf{p}) &= E^2(\mathbf{p}) \hat{\psi}(\mathbf{p}) \\ \left[\sum_{k=1}^3 \left(\frac{c\hbar}{a_0} \sin(p_k a_0) \right)^2 + m_0^2 c^4 \right] \hat{\psi}(\mathbf{p}) &= \end{aligned} \quad (1.1.20)$$

where, in the second passage, we canceled all the mixed terms by exploiting the following properties from the Clifford's algebra in Eq. (1.1.8):

$$\gamma^0 \gamma^0 = \mathbb{1} \quad \gamma^0 \gamma^k + \gamma^k \gamma^0 = 0 \quad \gamma^j \gamma^k + \gamma^k \gamma^j = 2\delta^{jk} \mathbb{1}. \quad (1.1.21)$$

Clearly, when $p_k a_0 \ll 1$, then $\sin(p_k a_0) \sim p_k a_0$ and the energy reduces to the familiar dispersion relation of relativistic particles: $E(\mathbf{p}) = \pm \sqrt{c^2 \hbar^2 \mathbf{p}^2 + m_0^2 c^4}$. However, the sine function $\sin(p_k a_0)$ has an additional zero at $p_k = \pi/a_0$, which yields another low-energy solution at the border of the BZ. Therefore, in D spatial dimensions, we obtain 2^D fermion species. The extra degrees of freedom affect the extrapolation to the continuum limit such that the correct continuum results can not be recovered.

Nielsen & Ninomiya Theorem

Handling and removing fermion doublers is neither easy nor without cost. Indeed, according to the Nielsen and Ninomiya no-go theorem [149, 150], any *local, hermitian*, lattice fermion theory, with *translational invariance* and *chiral symmetry*, necessarily displays fermion doublers. Hence, any attempt to remove doublers requires violating at least one of the four hypotheses of the theorem. Choosing which of these characteristics to compromise allows for different strategies, with the Wilson fermion [14] and staggered fermion [148] methods being some of the most well-known approaches. While the former one being already studied for quantum simulations [151–154], throughout the whole thesis, we will rely on the second solution, staggered fermions, introduced by Kogut and Susskind in [144], which has been widely exploited in numerical and quantum simulations [2, 4, 87, 89, 90, 93, 143, 155].

Staggered Fermions

Staggered fermions do not completely resolve the Fermion doubling problem, yet they represent a compromise that reduces the number of doublers by distributing the components of the Dirac spinor across multiple lattice sites. This doubles the periodicity of the lattice, from a_0 to $2a_0$, and halves the Brillouin zone to $[-\frac{\pi}{2a_0}, \frac{\pi}{2a_0}]^D$. Such a solution loses locality, but maintains a modified translational invariance with a checkerboard pattern and a remnant of chiral symmetry, which is important for maintaining some of the physical characteristics of massless lattice fermions [154].

The practical realization of staggered fermions strongly depends on the spatial dimension of the lattice, as it affects the representation of spinors and gamma matrices [156]. In detail, we need to adjust the matrices γ^0 and $\gamma^0\gamma^k$ for $k = 1 \dots D$ while maintaining all the Clifford's algebra properties.

(1+1)D Case In one spatial dimension, $\mathbf{n} = n_1$, and the four-component spinor reduces to a two-spinor with the 0^{th} (time) component and the 3^{rd} (space) component: $\begin{pmatrix} \hat{\psi}_0 \\ \hat{\psi}_3 \end{pmatrix}$. Correspondingly, γ^0 and $\gamma^0\gamma^1$ can be any two Pauli matrices, for example σ^z and σ^x . We have then:

$$\hat{H}_{\mathbf{n}}^{1D} = \begin{pmatrix} \hat{\psi}_{0,\mathbf{n}}^\dagger & \hat{\psi}_{3,\mathbf{n}}^\dagger \end{pmatrix} \begin{pmatrix} m_0c^2 & i\hbar\partial_1 \\ i\hbar\partial_1 & -m_0c^2 \end{pmatrix} \begin{pmatrix} \hat{\psi}_{0,\mathbf{n}} \\ \hat{\psi}_{3,\mathbf{n}} \end{pmatrix}. \quad (1.1.22)$$

Then, in the staggered fermion solution, we decompose the spinor components by placing $\hat{\psi}_0$ on *even* sites (where $(-1)^{n_1} = +1$) and $\hat{\psi}_3$ on *odd* sites (where $(-1)^{n_1} = -1$). Then, for *even* sites, we have:

$$\hat{H}_{\text{even}}^{1D} = m_0c^2 \sum_{\mathbf{n}} \hat{\psi}_{\mathbf{n}}^\dagger \hat{\psi}_{\mathbf{n}} + \frac{i\hbar}{2a_0} \sum_{\mathbf{n}} \hat{\psi}_{\mathbf{n}}^\dagger (\hat{\psi}_{\mathbf{n}+\mu_1} - \hat{\psi}_{\mathbf{n}-\mu_1}), \quad (1.1.23)$$

whereas, for *odd* sites, we have

$$\hat{H}_{\text{odd}}^{1D} = +\frac{i\hbar}{2a_0} \sum_{\mathbf{n}} \hat{\psi}_{\mathbf{n}}^\dagger (\hat{\psi}_{\mathbf{n}+\mu_1} - \hat{\psi}_{\mathbf{n}-\mu_1}) - m_0c^2 \sum_{\mathbf{n}} \hat{\psi}_{\mathbf{n}}^\dagger \hat{\psi}_{\mathbf{n}}. \quad (1.1.24)$$

Notice that each of these two contributions contains the hermitian conjugate of the hopping term of the other one. Therefore, combining even and odd sites, the (1+1)D Dirac Hamiltonian via staggered fermions reads:

$$\hat{H}_{\text{Dirac}}^{1D} = \sum_{\mathbf{n}} \left[\frac{i\hbar}{2a_0} \hat{\psi}_{\mathbf{n}}^\dagger \hat{\psi}_{\mathbf{n}+\mu_1} + \text{h.c.} \right] + m_0c^2 \sum_{\mathbf{n}} (-1)^{\mathbf{n}} \hat{\psi}_{\mathbf{n}}^\dagger \hat{\psi}_{\mathbf{n}}, \quad (1.1.25)$$

(2+1)D Case The case of two-spatial dimensions is less trivial, as there are multiple ways of defining the matrices $(\gamma^0, \gamma^0\gamma^1, \gamma^0\gamma^2)$. For instance, using two-spinors, there are two solutions: $(\gamma^0, \gamma^0\gamma^1, \gamma^0\gamma^2) \rightarrow (\sigma^z, \sigma^x, \pm\sigma^y)$. Choosing the case with $+\sigma^y$, we obtain:

$$\hat{H}_{\mathbf{n}}^{2D} = \begin{pmatrix} \hat{\psi}_{0,\mathbf{n}}^\dagger & \hat{\psi}_{3,\mathbf{n}}^\dagger \end{pmatrix} \begin{pmatrix} m_0c^2 & i\hbar(\partial_1 - i\partial_2) \\ i\hbar(\partial_1 + i\partial_2) & -m_0c^2 \end{pmatrix} \begin{pmatrix} \hat{\psi}_{0,\mathbf{n}} \\ \hat{\psi}_{3,\mathbf{n}} \end{pmatrix}. \quad (1.1.26)$$

The decomposition of the spinor components along the lattice is similar to the (1+1)D case: we place $\hat{\psi}_0$ in *even* sites (where $(-1)^{n_1+n_2} = +1$) and $\hat{\psi}_3$ in *odd* ones (where $(-1)^{n_1+n_2} = -1$). Then, for *even* sites, we have:

$$\hat{H}_{\text{even}}^{2D} = m_0c^2 \sum_{\mathbf{n}} \hat{\psi}_{\mathbf{n}}^\dagger \hat{\psi}_{\mathbf{n}} + \frac{i\hbar}{2a_0} \sum_{\mathbf{n}} \hat{\psi}_{\mathbf{n}}^\dagger (\hat{\psi}_{\mathbf{n}+\mu_1} - \hat{\psi}_{\mathbf{n}-\mu_1}) + \frac{c\hbar}{2a_0} \sum_{\mathbf{n}} \hat{\psi}_{\mathbf{n}}^\dagger (\hat{\psi}_{\mathbf{n}+\mu_2} - \hat{\psi}_{\mathbf{n}-\mu_2}) \quad (1.1.27)$$

As for the *odd* sites, we have

$$\hat{H}_{\text{odd}}^{2\text{D}} = -m_0c^2 \sum_{\mathbf{n}} \hat{\psi}_{\mathbf{n}}^\dagger \hat{\psi}_{\mathbf{n}} + \frac{ic\hbar}{2a_0} \sum_{\mathbf{n}} \hat{\psi}_{\mathbf{n}}^\dagger (\hat{\psi}_{\mathbf{n}+\mu_1} - \hat{\psi}_{\mathbf{n}-\mu_1}) - \frac{c\hbar}{2a_0} \sum_{\mathbf{n}} \hat{\psi}_{\mathbf{n}}^\dagger (\hat{\psi}_{\mathbf{n}+\mu_2} - \hat{\psi}_{\mathbf{n}-\mu_2}) \quad (1.1.28)$$

Combining the two cases and noting the hermitian conjugate of the hopping terms, we find

$$\hat{H}^{2\text{D}} = \frac{c\hbar}{2a_0} \sum_{\mathbf{n}} \left[\left[i\hat{\psi}_{\mathbf{n}}^\dagger \hat{\psi}_{\mathbf{n}+\mu_1} + (-1)^{n_1+n_2} \hat{\psi}_{\mathbf{n}}^\dagger \hat{\psi}_{\mathbf{n}+\mu_2} \right] + \text{h.c.} \right] + m_0c^2 \sum_{\mathbf{n}} (-1)^{\mathbf{n}} \hat{\psi}_{\mathbf{n}}^\dagger \hat{\psi}_{\mathbf{n}}. \quad (1.1.29)$$

(3+1)D Case In the three-dimensional case, we have to use the full 4-component spinor and the original definition of the gamma matrices:

$$\gamma^0 = \begin{pmatrix} \mathbb{1}_2 & \\ & -\mathbb{1}_2 \end{pmatrix} \quad \text{and} \quad \gamma^k = \begin{pmatrix} & \sigma^k \\ \sigma^k & \end{pmatrix}. \quad (1.1.30)$$

Correspondingly, we have:

$$\hat{H}_{\mathbf{n}}^{3\text{D}} = \begin{pmatrix} \hat{\psi}_{0,\mathbf{n}}^\dagger & \hat{\psi}_{1,\mathbf{n}}^\dagger & \hat{\psi}_{2,\mathbf{n}}^\dagger & \hat{\psi}_{3,\mathbf{n}}^\dagger \end{pmatrix} \begin{pmatrix} m_0c^2 & & ic\hbar\partial_3 & ic\hbar(\partial_1 - i\partial_2) \\ & m_0c^2 & ic\hbar(\partial_1 + i\partial_2) & -ic\hbar\partial_3 \\ ic\hbar\partial_3 & ic\hbar(\partial_1 - i\partial_2) & -m_0c^2 & \\ ic\hbar(\partial_1 + i\partial_2) & -ic\hbar\partial_3 & & -m_0c^2 \end{pmatrix} \begin{pmatrix} \hat{\psi}_{0,\mathbf{n}} \\ \hat{\psi}_{1,\mathbf{n}} \\ \hat{\psi}_{2,\mathbf{n}} \\ \hat{\psi}_{3,\mathbf{n}} \end{pmatrix}. \quad (1.1.31)$$

In this case, decomposing the spinor components along the lattice is less intuitive, but affordable. Namely, we place the component $\hat{\psi}_0$ at site $\mathbf{n} = (0, 0, 0)$: it couples with $\hat{\psi}_3$ at sites where $n_1 + n_2$ is odd and n_3 is even, with $\hat{\psi}_2$ at sites where $n_1 + n_2$ is even and n_3 is odd, with $\hat{\psi}_1$ at sites where $n_1 + n_2$ is odd and n_3 is odd, and finally with $\hat{\psi}_0$ at sites where $n_1 + n_2$ is even and n_3 is even. Correspondingly, $\hat{H}^{3\text{D}}$ decomposes into four separate sub-theories, with each theory touching a single fermion specie per site. In particular, $\hat{\psi}_0$ and $\hat{\psi}_1$ occupy even sites, while $\hat{\psi}_2$ and $\hat{\psi}_3$ occupy odd sites. As for the mass term, it acts positively on $\hat{\psi}_0$ and $\hat{\psi}_1$ (even sites), and negatively on $\hat{\psi}_2$ and $\hat{\psi}_3$ (odd sites). As for the x -derivative, it acts positively everywhere, while the y - and z -derivatives act positively on $\hat{\psi}_0$ and $\hat{\psi}_2$ (where $n_1 + n_2$ is even) and negatively on $\hat{\psi}_1$ and $\hat{\psi}_3$ (where $n_1 + n_2$ is odd). Summarizing, we obtain:

$$\begin{aligned} \hat{H}_{\text{Dirac}}^{3\text{D}} = & + \frac{c\hbar}{2a_0} \sum_{\mathbf{n}} \left[\left[i\hat{\psi}_{\mathbf{n}}^\dagger \hat{\psi}_{\mathbf{n}+\mu_1} + (-1)^{n_1+n_2} \hat{\psi}_{\mathbf{n}}^\dagger \hat{\psi}_{\mathbf{n}+\mu_2} + i(-1)^{n_1+n_2} \hat{\psi}_{\mathbf{n}}^\dagger \hat{\psi}_{\mathbf{n}+\mu_3} \right] + \text{h.c.} \right] \\ & + m_0c^2 \sum_{\mathbf{n}} (-1)^{\mathbf{n}} \hat{\psi}_{\mathbf{n}}^\dagger \hat{\psi}_{\mathbf{n}}, \end{aligned} \quad (1.1.32)$$

which perfectly matches [148]. We stress that the staggered phases in the hopping and the mass term are fundamental for recovering correct results.

1.1.4 Discretization of gauge fields

In QFT, the principle of gauge invariance underlies the interactions between matter fields (such as fermions) and gauge fields (such as bosons, e.g. photons or gluons). Such an interaction is ruled by local (gauge) transformations from a corresponding gauge group.

Basics of group theory

Let us consider a generic compact Lie group \mathcal{G} (e.g., $\text{SU}(N)$ or $\text{U}(1)$), whose algebra has generators T^a , where $a \in \{1 \dots \dim \mathcal{G}\}$. In the fundamental representation of non-Abelian groups \mathcal{G} like

SU(N), these generators could be the Gell-Mann matrices for SU(3), or Pauli matrices for SU(2). In general, the generators T^a satisfy the following commutations rules

$$[T^a, T^b] = if^{abc}T^c, \quad (1.1.33)$$

where f^{abc} are the *structure constants* of the gauge group \mathcal{G} . For a non-Abelian group, these constants are fully antisymmetric in the indices a, b, c , encoding the non-commuting relation between the generators (and correspondingly between the resulting transformations). For instance, in the SU(2) case, f^{abc} is the Levi-Civita symbol ϵ^{abc} . Conversely, in the Abelian scenario, like U(1), the generator is unique and scalar $T = 1$ and $f^{abc} = 0$.

Then, any group element $\Omega(r)$ can vary from point to point in spacetime and is defined as

$$\Omega(r) = \exp(i\theta^a(r)T^a) \quad \text{with} \quad \Omega(r)\Omega^\dagger(r) = \Omega^\dagger(r)\Omega(r) = \mathbb{1}, \quad (1.1.34)$$

where $\theta^a(r)$ are the local parameters of the gauge transformation. For example, in the case of SU(2), $\Omega(r)$ could be a 2×2 unitary matrix with determinant 1. For U(1) (electromagnetism), $\Omega(r)$ would simply be a phase factor $\exp(i\theta(r))$.

Matter fields

Assuming a single matter flavor in the fundamental representation of the gauge group \mathcal{G} , gauge transformations of spinors are generated by the charge operator $\hat{Q}^a(r)$, defined as:

$$\hat{Q}^a(r) = \sum_{\alpha, \beta} \hat{\psi}_\alpha^\dagger(r) T_{\alpha\beta}^a \hat{\psi}_\beta(r). \quad (1.1.35)$$

This operator represents how the matter fields interact with the gauge fields and underlies the dynamics of the gauge theory when multiple flavors are present. Correspondingly, under a local gauge transformation $\Omega(r)$, matter fields transform as follows:

$$\hat{\psi}(r) \rightarrow \hat{\psi}'(r) = \Omega(r)\hat{\psi}(r). \quad (1.1.36)$$

The covariant derivative

The original Dirac equation of Eq. (1.1.7) is clearly not invariant under local gauge transformations such as the ones in Eq. (1.1.36); indeed when transforming the derivative, we find:

$$\partial_\mu \hat{\psi}(r) \rightarrow \partial_\mu \hat{\psi}'(r) = \partial_\mu (\Omega(r)\hat{\psi}(r)) = (\partial_\mu \Omega(r))\hat{\psi}(r) + \Omega(r)\partial_\mu \hat{\psi}(r), \quad (1.1.37)$$

so that the transformed Dirac equation reads

$$\begin{aligned} 0 &= i\hbar\gamma^\mu \left[(\partial_\mu \Omega(r))\hat{\psi}(r) + \Omega(r)\partial_\mu \hat{\psi}(r) \right] - m_0 c \Omega(r)\hat{\psi}(r) \\ &= \Omega(r) \left(i\hbar\gamma^\mu \partial_\mu \hat{\psi}(r) - m_0 c \hat{\psi}(r) \right) + i\hbar\gamma^\mu (\partial_\mu \Omega(r))\hat{\psi}(r). \end{aligned} \quad (1.1.38)$$

To impose invariance under this transformation, the extra term $i\hbar\gamma^\mu (\partial_\mu \Omega(r))\hat{\psi}(r)$ must vanish. This would spontaneously happen just in case $\Omega(r)$ is constant (which corresponds to a *global*, rather than local, gauge transformation). In general, to achieve gauge invariance, the ordinary derivative ∂_μ must be replaced by the covariant derivative \hat{D}_μ , which transforms covariantly under gauge transformations thereby canceling the extra terms introduced by the local gauge transformation. Namely, we have:

$$\hat{D}_\mu \hat{\psi}(r) = \left(\partial_\mu - i\frac{q}{\hbar} \hat{A}_\mu(r) \right) \hat{\psi}(r) = \left(\partial_\mu - ig_0 \hat{A}_\mu(r) \right) \hat{\psi}(r), \quad (1.1.39)$$

where q is the charge, $g_0 = q/\hbar$ is the gauge coupling, while $\hat{A}_\mu(r) = \hat{A}_\mu^a(r)T^a$ is the full gauge field operator obtained by contracting the gauge field components $\hat{A}_\mu^a(r)$ to the generators T^a via the gauge group index a . The gauge field operator transforms as follows:

$$\hat{A}_\mu(r) \rightarrow \hat{A}'_\mu(r) = \Omega(r)\hat{A}_\mu(r)\Omega^\dagger(r) + \frac{i}{g_0}\Omega(r)\partial_\mu\Omega^\dagger(r). \quad (1.1.40)$$

Correspondingly, the continuum Dirac Hamiltonian in Eq. (1.1.11) is made covariant as follows:

$$\hat{H}_{\text{Dirac}} = \int d\mathbf{r} \left[\hat{\psi}^\dagger(\mathbf{r})(ic\hbar\gamma^0\gamma^k(\partial_k - ig_0\hat{A}_k) + m_0c^2\gamma^0)\hat{\psi}(\mathbf{r}) \right]. \quad (1.1.41)$$

The pure gauge Hamiltonian

To make the Dirac equation gauge invariant, we needed to introduce an extra d.o.f., a gauge field, whose dynamics needs to be properly accounted and added to the Dirac Hamiltonian. In the continuum, the dynamics of gauge fields is captured by the field strength tensor $\hat{F}_{\mu\nu}(r)$, which for a generic non-Abelian gauge field $\hat{A}_\mu(r)$ is given by:

$$\begin{aligned} \hat{F}_{\mu\nu}(r) &= \partial_\mu\hat{A}_\nu(r) - \partial_\nu\hat{A}_\mu(r) - ig_0[\hat{A}_\mu(r), \hat{A}_\nu(r)] \\ \hat{F}_{\mu\nu}^a(r)T^a &= \left[\partial_\mu\hat{A}_\nu^a(r) - \partial_\nu\hat{A}_\mu^a(r) + g_0f^{abc}\hat{A}_\mu^b(r)\hat{A}_\nu^c(r) \right] T^a. \end{aligned} \quad (1.1.42)$$

To move towards the Hamiltonian formalism, we separate its electric and magnetic components:

$$\hat{E}_k^a(r) = \hat{F}_{0k}^a(r) = \frac{1}{c}\partial_t\hat{A}_k^a(r) - \partial_k\hat{A}_0^a(r) - g_0f^{abc}\hat{A}_0^b(r)\hat{A}_k^c(r) \quad (1.1.43a)$$

$$\hat{B}_i^a(r) = -\frac{1}{2}\epsilon_{ijk}\hat{F}_{jk}^a(r) = \epsilon_{ijk}\left(\partial_j\hat{A}_k^a(r) - \frac{g_0}{2}f^{abc}\hat{A}_j^b(r)\hat{A}_k^c(r)\right), \quad (1.1.43b)$$

where i, j, k are spatial indices. In the Coulomb gauge, where $\hat{A}^0(r) = 0$, the electric field reduces to $\hat{E}_k^a(r) = \hat{F}_{0k}^a(r) = \partial_t\hat{A}_k^a(r)/c$. This choice does not change the physics, as it simply exploits an extra freedom in defining the gauge fields.

The corresponding Hamiltonian of the pure gauge fields is

$$\hat{H}_{\text{gauge}} = \int d\mathbf{r} \left[\frac{\epsilon_0}{2}\hat{E}_k^a(r)\hat{E}_k^a(r) + \frac{1}{2\mu_0}\hat{B}_k^a(r)\hat{B}_k^a(r) \right]. \quad (1.1.44)$$

where ϵ_0 and $\mu_0 = (c^2\epsilon_0)^{-1}$ correspond to the vacuum permittivity and permeability respectively. In dimensioned units (such as SI), the physical dimensions of the constants read

$$\begin{aligned} [\epsilon_0] &= (\text{charge})^2(\text{length})^{2-D}(\text{energy})^{-1} \\ [\mu_0] &= (\text{charge})^{-2}(\text{length})^{D-2}(\text{energy}) \cdot (\text{length})^{-2}(\text{time})^2 \\ &= (\text{charge})^{-2}(\text{length})^{D-4}(\text{energy})(\text{time})^2. \end{aligned} \quad (1.1.45)$$

Correspondingly, the electric and magnetic fields have the following dimensions:

$$\begin{aligned} [\hat{E}] &= (\text{charge})^{-1}(\text{length})^{-1}(\text{energy}) \\ [\hat{B}] &= (\text{charge})^{-1}(\text{length})^{-2}(\text{energy})(\text{time}). \end{aligned} \quad (1.1.46)$$

As for the coupling constant g_0 , its dimensional analysis reads

$$[g_0] = (\text{charge})(\text{energy})^{-1}(\text{time})^{-1}, \quad (1.1.47)$$

while for the vector potential we have:

$$[\hat{A}] = (\text{charge})^{-1}(\text{length})^{-1}(\text{energy})(\text{time}). \quad (1.1.48)$$

Discretized gauge fields

When moving from the continuum to the lattice, each spatial component k of the covariant derivative in Eq. (1.1.39) is replaced by the *parallel transport*¹ $\hat{U}_{\mathbf{n},\boldsymbol{\mu}_k}(t)$, a dimensionless link variable reflecting the gauge field's influence along the link connecting neighboring lattice sites \mathbf{n} and $\mathbf{n} + \boldsymbol{\mu}_k$. Omitting again the time dependence, we define the parallel transport as:

$$\hat{D}_k = (\partial_k - ig_0 \hat{A}^k) \quad \longrightarrow \quad \hat{U}_{\mathbf{n},\boldsymbol{\mu}_k} = \exp\left(ig_0 \int_{\mathbf{n}}^{\mathbf{n}+\boldsymbol{\mu}_k} \hat{A}^k(\mathbf{r}) d\ell\right) \sim \exp\left(ig_0 a_0 \hat{A}^k\right), \quad (1.1.49)$$

where in the second step we assumed $\hat{A}^k(r) \sim \hat{A}_{\mathbf{n}}^k$ to be almost constant along the lattice link $(\mathbf{n}, \boldsymbol{\mu}_k)$ of length a_0 . Assuming a_0 to be sufficiently small, we can further expand the parallel transporter up to the first order and notice that:

$$\begin{aligned} \left[\frac{i\hat{\psi}_{\mathbf{n}}^\dagger \hat{U}_{\mathbf{n},\boldsymbol{\mu}_k} \hat{\psi}_{\mathbf{n}+\boldsymbol{\mu}_k} + \text{h.c.}}{2a_0} \right] &= i \left[\frac{\hat{\psi}_{\mathbf{n}}^\dagger \hat{U}_{\mathbf{n},\boldsymbol{\mu}_k} \hat{\psi}_{\mathbf{n}+\boldsymbol{\mu}_k} - \hat{\psi}_{\mathbf{n}+\boldsymbol{\mu}_k}^\dagger \hat{U}_{\mathbf{n},\boldsymbol{\mu}_k}^\dagger \hat{\psi}_{\mathbf{n}}}{2a_0} \right] \\ &= i \left[\frac{\hat{\psi}_{\mathbf{n}}^\dagger \hat{U}_{\mathbf{n},\boldsymbol{\mu}_k} \hat{\psi}_{\mathbf{n}+\boldsymbol{\mu}_k} - \hat{\psi}_{\mathbf{n}}^\dagger \hat{U}_{\mathbf{n}-\boldsymbol{\mu}_k,\boldsymbol{\mu}_k}^\dagger \hat{\psi}_{\mathbf{n}-\boldsymbol{\mu}_k}}{2a_0} \right] \\ &= i\hat{\psi}_{\mathbf{n}}^\dagger \left[\frac{\hat{U}_{\mathbf{n},\boldsymbol{\mu}_k} \hat{\psi}_{\mathbf{n}+\boldsymbol{\mu}_k} - \hat{U}_{\mathbf{n}-\boldsymbol{\mu}_k,\boldsymbol{\mu}_k}^\dagger \hat{\psi}_{\mathbf{n}-\boldsymbol{\mu}_k}}{2a_0} \right] \\ &\sim \frac{i\hat{\psi}_{\mathbf{n}}^\dagger}{2a_0} \left[(1 - ig_0 \hat{A}_{\mathbf{n}}^k a_0) \hat{\psi}_{\mathbf{n}+\boldsymbol{\mu}_k} - (1 + ig_0 \hat{A}_{\mathbf{n}-\boldsymbol{\mu}_k}^k a_0) \hat{\psi}_{\mathbf{n}-\boldsymbol{\mu}_k} \right] \\ &= i\hat{\psi}_{\mathbf{n}}^\dagger \left[\frac{\hat{\psi}_{\mathbf{n}+\boldsymbol{\mu}_k} - \hat{\psi}_{\mathbf{n}-\boldsymbol{\mu}_k}}{2a_0} - ig_0 \hat{A}_{\mathbf{n}}^k \hat{\psi}_{\mathbf{n}+\boldsymbol{\mu}_k} \right] \xrightarrow{a_0 \rightarrow 0} i\hat{\psi}_{\mathbf{n}}^\dagger(\mathbf{r})(\partial_k - ig_0 \hat{A}^k(\mathbf{r}))\hat{\psi}(\mathbf{r}). \end{aligned} \quad (1.1.50)$$

Then, the lattice version of the covariant Dirac Hamiltonian with staggered fermions is

$$\hat{H}_{\text{Dirac}} = \frac{c\hbar}{2a_0} \sum_{\mathbf{n},\boldsymbol{\mu}} \left[s_{\mathbf{n},\boldsymbol{\mu}} \hat{\psi}_{\mathbf{n}} \hat{U}_{\mathbf{n},\boldsymbol{\mu}} \hat{\psi}_{\mathbf{n}+\boldsymbol{\mu}} + \text{h.c.} \right] + m_0 c^2 \sum_{\mathbf{n}} s_{\mathbf{n}} \hat{\psi}_{\mathbf{n}}^\dagger \hat{\psi}_{\mathbf{n},\boldsymbol{\mu}}, \quad (1.1.51)$$

where $s_{\mathbf{n},\boldsymbol{\mu}}$ and $s_{\mathbf{n}}$ are phases that arise when using staggered fermions.

Similarly to the vector potential, gauge transformations of the parallel transporter read:

$$\hat{U}_{\mathbf{n},\boldsymbol{\mu}_k} \rightarrow \Omega_{\mathbf{n}} \hat{U}_{\mathbf{n},\boldsymbol{\mu}_k} \Omega_{\mathbf{n}+\boldsymbol{\mu}_k}^\dagger, \quad (1.1.52)$$

where $\Omega_{\mathbf{n}}$ is the gauge transformation matrix at site \mathbf{n} . In general, due to the non-commuting algebra in Eq. (1.3.32), the left $\Omega_{\mathbf{n}}$ and the right $\Omega_{\mathbf{n}+\boldsymbol{\mu}_k}^\dagger$ gauge transformations are different and generated by the dimensionless conjugate fields $\hat{L}_{\mathbf{n},\boldsymbol{\mu}}^a$ and $\hat{R}_{\mathbf{n},\boldsymbol{\mu}}^a$ respectively, which satisfy the following relations:

$$[\hat{L}_{\mathbf{n},\boldsymbol{\mu}}^a, \hat{U}_{\mathbf{n}',\boldsymbol{\mu}'}^{\alpha\beta}] = -\delta_{\mathbf{n}\mathbf{n}'} \delta_{\boldsymbol{\mu}\boldsymbol{\mu}'} \sum_{\gamma} T_{\alpha\gamma}^a \hat{U}_{\mathbf{x},\boldsymbol{\mu}}^{\gamma\beta}, \quad (1.1.53a)$$

$$[\hat{R}_{\mathbf{n},\boldsymbol{\mu}}^a, \hat{U}_{\mathbf{n}',\boldsymbol{\mu}'}^{\alpha\beta}] = +\delta_{\mathbf{n}\mathbf{n}'} \delta_{\boldsymbol{\mu}\boldsymbol{\mu}'} \sum_{\gamma} \hat{U}_{\mathbf{x},\boldsymbol{\mu}}^{\alpha\gamma} T_{\gamma\beta}^a, \quad (1.1.53b)$$

¹Parallel transports have several names in literature. Sometimes they are also called *connections* referring to a differential geometry framework. Sometimes, they are called *comparators*.

where $\alpha, \beta, \gamma, \delta$ span the matrix indices of the group generators T^a . In the Abelian U(1) case, where there is only one generator, there is only one electric field and the parallel transporter acts as a raising operator. Namely, we have:

$$\hat{E}_{\mathbf{n},\mu} = \hat{L}_{\mathbf{n},\mu} = \hat{R}_{\mathbf{n},\mu} \quad [\hat{E}_{\mathbf{n},\mu}, \hat{U}_{\mathbf{n},\mu}] = \hat{U}_{\mathbf{n},\mu}. \quad (1.1.54)$$

The pure gauge lattice Hamiltonian

Once we have discretized all the gauge fields, we can build the corresponding lattice version of the pure gauge Hamiltonian in Eq. (1.1.44). The electric energy density is given by the Casimir operator:

$$\hat{E}_{\mathbf{n},\mu}^2 = \hat{L}_{\mathbf{n},\mu}^a \hat{L}_{\mathbf{n},\mu}^a = \hat{R}_{\mathbf{n},\mu}^a \hat{R}_{\mathbf{n},\mu}^a. \quad (1.1.55)$$

To make the Casimir operator adimensional, the electric Hamiltonian is redefined as follows:

$$\hat{H}_{\text{elec}} = \frac{\epsilon_0}{2} \int d^D \mathbf{r} \hat{E}_k(r) \hat{E}_k(r) \quad \rightarrow \quad \hat{H}_{\text{elec}}^{\text{latt}} = a_0^D \frac{\epsilon_0}{2} \sum_{\mathbf{n},k} \frac{q^2 a_0^{2-2D}}{\epsilon_0^2} \hat{E}_{\mathbf{n},\mu_k}^2 = \sum_{\mathbf{n},k} \frac{q^2 a_0^{2-D}}{2\epsilon_0} \hat{E}_{\mathbf{n},\mu_k}^2. \quad (1.1.56)$$

We can recast the latter in dimensionless units, by redefining the gauge coupling constant as

$$g = g_0 \sqrt{\frac{\hbar}{c\epsilon_0}} a_0^{\frac{3-D}{2}} = q \frac{a_0^{\frac{3-D}{2}}}{\sqrt{c\hbar\epsilon_0}} = q a_0^{\frac{3-D}{2}} \sqrt{\frac{c\mu_0}{\hbar}}. \quad (1.1.57)$$

By doing so, we obtain

$$\hat{H}_{\text{elec}}^{\text{latt}} = \sum_{\mathbf{n},k} \frac{g^2 c \hbar}{2a_0} \hat{E}_{\mathbf{n},\mu_k}^2. \quad (1.1.58)$$

Notice that the new gauge coupling constant g is dimensionless yet depends on the lattice spacing. As discussed for the matter fields, such a hidden relation becomes important when discussing the continuum limit.

Correspondingly, the simplest way to describe the magnetic energy density on the lattice is by using Wilson loops [14, 144], i.e. gauge-invariant loops made out of parallel transporters \hat{U} . On a hypercubic lattice, the smallest non-trivial loop is represented by a plaquette operator

$$\hat{U}_{\square} = \sum_{\alpha,\beta,\gamma,\delta} \hat{U}_{\mathbf{n},\mu}^{\alpha\beta} \hat{U}_{\mathbf{n}+\mu,\mu'}^{\beta\gamma} \hat{U}_{\mathbf{n}+\mu',\mu}^{\gamma\delta\dagger} \hat{U}_{\mathbf{n},\mu'}^{\delta\gamma\dagger}, \quad (1.1.59)$$

where μ and μ' span the plaquette's plane. Since the parallel transporters in Eq. (1.1.49) commutes when acting on different links (and so the vector potentials do), one can notice that:

$$\hat{U}_{\square} = \exp\left(ig_0 \oint_{\partial\square} \hat{A}_k dl_k\right) \underset{*}{=} \exp\left(ig_0 \oint_{\square} \nabla \times \hat{\mathbf{A}} \cdot d\mathbf{s}\right) = \exp\left(ig_0 \oint_{\square} \hat{\mathbf{B}} \cdot d\mathbf{s}\right) \sim \exp\left(ig_0 a_0^2 \hat{B}\right). \quad (1.1.60)$$

where in the $*$ we used the Stokes theorem, while in the last step we assumed the magnetic field to be almost constant in the plaquette of area a_0^2 . Given these assumptions, we have:

$$\text{Tr}\left(\hat{U}_{\square} + \hat{U}_{\square}^{\dagger}\right) = 2 \cos\left(g_0 a_0^2 \hat{B}\right) \sim 2 \left[1 - \frac{1}{2} g_0^2 a_0^4 \hat{B}^2\right], \quad (1.1.61)$$

from which we obtain that

$$\hat{B}^2 \sim -\frac{1}{g_0^2 a_0^4} \text{Tr}\left(\hat{U}_{\square} + \hat{U}_{\square}^{\dagger}\right). \quad (1.1.62)$$

Then, the magnetic Hamiltonian can be discretized as follows:

$$\hat{H}_{\text{magn}} = \frac{1}{2\mu_0} \int d^D \mathbf{r} B_k(r) B_k(r) \quad \rightarrow \quad \hat{H}_{\text{magn}}^{\text{latt}} = -\frac{1}{2\mu_0 g_0^2 a_0^{4-D}} \sum_{\square} \text{Tr}(\hat{U}_{\square} + \hat{U}_{\square}^{\dagger}). \quad (1.1.63)$$

Finally, by using the dimensionless gauge coupling in Eq. (1.1.57), we obtain:

$$\hat{H}_{\text{magn}}^{\text{latt}} = -\frac{c\hbar}{2g^2 a_0} \sum_{\square} \text{Tr}(\hat{U}_{\square} + \hat{U}_{\square}^{\dagger}). \quad (1.1.64)$$

Notice that plaquette terms only exist in $D > 1$, contributing to the increased complexity of quantum and TN simulations of LGTs in higher dimensions [106].

The lattice gauge Hamiltonian with staggered fermions

Summarizing and combining all the ingredients (matter and gauge fields), the general *Kogut-Susskind Hamiltonian* via staggered fermions [8] reads:

$$\begin{aligned} H_{\text{LGT}} = & \frac{c\hbar}{2a_0} \sum_{\mathbf{n}, \boldsymbol{\mu}} \sum_{\alpha, \beta} \left[s_{\mathbf{n}, \boldsymbol{\mu}} \hat{\psi}_{\mathbf{n}, \alpha} \hat{U}_{\mathbf{n}, \boldsymbol{\mu}}^{\alpha\beta} \hat{\psi}_{\mathbf{n}+\boldsymbol{\mu}, \beta} + \text{h.c.} \right] + m_0 c^2 \sum_{\mathbf{n}, \alpha} s_{\mathbf{n}} \hat{\psi}_{\mathbf{n}, \alpha}^{\dagger} \hat{\psi}_{\mathbf{n}, \mu} \\ & + \frac{c\hbar g^2}{2a_0} \sum_{\mathbf{n}, \boldsymbol{\mu}} \hat{E}_{\mathbf{n}, \boldsymbol{\mu}}^2 - \frac{c\hbar}{2g^2 a_0} \sum_{\square} \text{Tr}(\hat{U}_{\square} + \hat{U}_{\square}^{\dagger}), \end{aligned} \quad (1.1.65)$$

where we expressed the dependence on the matrix indices α, β of the gauge algebra generators.

1.2 Dressed-site model for Hamiltonian Lattice Gauge Theories

We have seen all the ingredients for discretizing an LGT with dynamical matter. However, there remain fundamental challenges to be faced for attacking Hamiltonians like Eq. (1.1.65) with numerical methods.

First of all, we need to achieve a finite-dimensional encoding of the continuous gauge fields such as U(1) or SU(N), especially beyond one spatial dimension, where decoupling the gauge field's longitudinal component is required [95]. Among known truncation recipes are Quantum Link Models (QLM) [96–100], finite subgroups [82, 86, 112], digitization of gauge fields [113], and fusion-algebra deformation [114]. Whatever the adopted solution, further effort is required to satisfy gauge symmetry at each local site, which involves the concurrent evaluation of all the gauge links and the attached matter site. In practice, an extensive number of local constraints (energy penalties), which corresponds to QMB operators concurrently acting on 2D+1 sites (2D gauge links and 1 matter site), where D is the number of spatial dimensions. Moreover, since the Gauss law represents the fundamental conservation law underpinning the theory (the highest energy scale of the model), enforcing it is essential for the simulation to remain meaningful. Any small violation of these local constraints would incur a significant energy cost, reflecting the critical role of gauge invariance in reproducing the correct physical behavior.

Another important issue to be faced in simulating LGTs is to account for the Fermi statistics of matter fields. In several TN methods as well on well-established conventional digital quantum simulation platforms (e.g. superconducting qubits, trapped-ions, Rydberg arrays, quantum dots) [117–121], fermionic algebra (mutually-anticommuting operations) must be encoded into a genuinely local algebra (mutually-commuting operations) of qubits. Standard fermion-to-qubit encodings, such as the Jordan-Wigner (JW) transformation [122], and other modern approaches

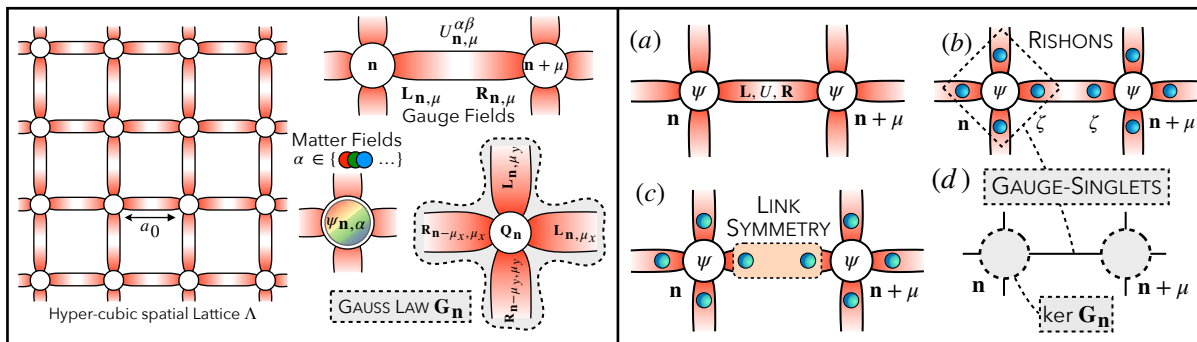


Figure 1.1: [Left] Graphical representation of the degrees of freedom of a 2D LGT: fermionic matter fields, defined on lattice sites, and gauge fields (the parallel transporter, and the chromo-electric fields, $\hat{L}_{\mathbf{n},\mu}$ and $\hat{R}_{\mathbf{n},\mu}$), living on lattice links. A local gauge transformation at n acts on a matter site and all its attached links. [Right] Pictorial representation of the dressed site formalism adopted for TN simulations of LGTs: (a) we truncate the gauge link fields with an energy cutoff in the irreducible representation basis; (b) the truncated gauge link is split into two representations, one per half-link; each is equipped with a proper fermionic rishon mode $\hat{\zeta}$. (c) All the half-links are absorbed into the attached matter site, forming a gauge-invariant dressed site (d) whose Hilbert space spans all the possible gauge singlets.

[62, 63, 123–125, 157] make any fermionic Hamiltonian interaction inherently long-range and expensive from a computational perspective.

In numerical methods such as TNs, as well as in quantum computations, all these requirements significantly impact the computational resources needed for the simulations, as well as their efficiency. In this section, we present a theoretical scheme which is able to order achieve a finite and controllable gauge field truncation, avoid the Fermi statistics of matter fields and directly access the gauge invariant subspace, revealing suitable for TN methods as well as for quantum simulations of LGTs. Building on the work of [129, 158], we *dress* every physical matter site with the information related to its adjacent gauge links. A pictorial scheme of this approach is outlined in Fig. 1.1[Right]: (a) starting from the original description matter fields on sites and gauge fields on links in Eq. (1.1.65), we truncate the gauge group imposing an energy cut-off on the Casimir operator. Then, (b) we express each truncated gauge link as a pair of fermionic rishon modes $\hat{\zeta}$ and (c) constrain their link dynamics according to the original gauge group algebra. Ultimately, (d) we merge each of these modes to its adjacent matter site, ending up in a compact *dressed-site* formalism [115, 129, 158]. The resulting effective Hamiltonian is made out of only bosonic operators and directly acts on the gauge invariant Hilbert sub-space. Correspondingly, as done in Loop String Hadrons methods [159], the original (Abelian/non-Abelian) gauge invariance is exactly rewritten into an Abelian, nearest-neighbor, diagonal selection rule, and the explicit dependence on the fermionic matter is eliminated [89, 115, 116]. Such an approach is especially suitable when dealing with LGTs in high-dimensional lattices.

We will practically apply the dressed-site formalism on two paradigmatic examples that have been exploited for numerical simulations [2, 4, 5]: SU(2) in Sec. 1.3 and U(1) in Sec. 1.4.

1.2.1 Gauge field truncation

The link Hilbert space is the space of square-integrable functions on the gauge group \mathcal{G} , $L^2(\mathcal{G})$, which is infinite-dimensional for continuous groups such as U(1) or SU(N) [160].

In one space dimension, gauge degrees of freedom are unphysical (absence of transverse polarizations) and can thus be integrated out, albeit at the price of introducing non-local interactions [161]. Beyond one dimension, the removal is much more delicate, because it requires first decoupling the gauge field's longitudinal component [95]. When impossible or inconvenient to remove, gauge degrees of freedom might have to be truncated to perform TN or quantum simulation. Among known truncation recipes are Quantum Link Models (QLM) [96–100], an approach already considered for practical quantum simulation of LGTs [101–111], finite subgroups [82, 86, 112], digitization of gauge fields [113], and fusion-algebra deformation [114].

Another approach is to truncate the spectrum of the electric energy density operator $\|\hat{E}^2\| \leq \Theta$ on each link [2, 155]. The cutoff is conveniently imposed in the irreducible representation (irrep) basis $\{|jm_L m_R\rangle\}$ [160] of $L^2(\mathcal{G})$, where \hat{E}^2 is diagonal:

$$\hat{E}^2 |jm_L m_R\rangle = C_2(j) |jm_L m_R\rangle . \quad (1.2.1)$$

Here, m_L and m_R are indices in the j -irrep of \mathcal{G} and $C_2(j)$ is the quadratic Casimir of j [160]. In the strong coupling limit, where the electric energy term dominates H_{LGT} , this truncation is equivalent to an energy cutoff [155].

1.2.2 Gauss law and the dressed site

The most distinctive feature of gauge theories is arguably the presence of local constraints, analogous to the Gauss law of classical electrodynamics, relating the configuration of the gauge field to the spatial distribution of charges [162]. At the quantum level, Gauss law is the statement that only gauge invariant states are physical, namely, $\hat{G}_{\mathbf{n}}^a |\Psi_{\text{phys}}\rangle = 0 \ \forall \mathbf{n}, a$, where $\hat{G}_{\mathbf{n}}^a$ are the generators of local gauge transformations at \mathbf{n} :

$$\hat{G}_{\mathbf{n}}^a = \hat{Q}_{\mathbf{n}}^a + q_{\mathbf{n}}^a + \sum_{\mu} [\hat{L}_{\mathbf{n},\mu}^a + \hat{R}_{\mathbf{n}-\mu,\mu}^a] , \quad (1.2.2)$$

with $q_{\mathbf{n}}^a$ representing eventual static background charges (typically vanishing). Lattice Gauss law provides a set of *vertex constraints*, each involving a lattice site and its 2D neighboring links.

Due to Gauss law, the physical Hilbert space of LGTs is much smaller than the tensor product of all local sites and link Hilbert spaces. Properly exploiting gauge symmetries can thus significantly speed up numerical simulations [158]. Strategies that solve Gauss law by eliminating (partially or entirely) either the gauge fields or the matter fields have been developed. Nonetheless, such approaches come with specific limitations: the range of interaction has to be extended, moreover, integrating-out gauge fields become problematic in $D > 1$ [95], while the recipe for removing matter is a model (matter content) dependent [116].

Another possibility is to enforce Gauss law using a dressed site construction [115, 116, 129, 158], sketched in Fig. 1.1 and outlined below. Dressed sites have local dimensions typically larger than those resulting from the aforementioned approaches, but they are obtained from a model-independent prescription which has the advantage of preserving the locality of the interactions [155, 158].

As a first step, we factorize each gauge link in a pair of modes, living at its edges. Namely, every link is decomposed into a pair of left (L) and right (R) *rishon* d.o.f., each associated with a Hilbert space spanned by the basis states $|jm\rangle$, identifying $|jm_L m_R\rangle \leftrightarrow |jm_L\rangle \otimes |jm_R\rangle$, and writing parallel transporters as rishon bilinears [2]:

$$\hat{U}_{\mathbf{n},\mu}^{\alpha\beta} \rightarrow \sum_i \hat{\zeta}_{\mathbf{n},+\mu}^{L(i)\alpha} \hat{\zeta}_{\mathbf{n}+\mu,-\mu}^{R(i)\beta\dagger} . \quad (1.2.3)$$

Physical gauge link configurations, i.e. those with the left and right rishons in the same irrep, are selected introducing a local link symmetry at the TN simulation level [6, 155, 158]. Notice that such a constraint is always Abelian, regardless of the Abelian or non-Abelian nature of the gauge group.

1.2.3 Projecting dressed site operators onto the gauge-invariant basis

Crucially, the gauge generators $\hat{G}_{\mathbf{n}}^a$ now involve only the matter site at \mathbf{n} and its $2D$ neighboring rishons. Fusing these degrees of freedom in a composite site, Gauss law becomes an internal constraint that singles out the dressed site Hilbert space as its gauge invariant subspace:

$$\mathcal{H}_{\text{dress}} = \ker G \subset \mathcal{H}_{\text{matt}} \otimes (\mathcal{H}_{\text{rish}})^{\otimes 2D}. \quad (1.2.4)$$

Therefore, the effective operators of the resulting dressed-site Hamiltonian should be obtained by projecting the obtained ones on the subspace generated by a gauge-invariant basis M . Namely, for any dressed-site operator O among the previously defined, the corresponding effective operator O^{eff} acting on gauge-invariant states reads:

$$O^{\text{eff}} = M^\dagger \cdot O \cdot M, \quad \text{where} \quad M^\dagger \cdot M = \mathbb{1} \quad \text{and} \quad (M \cdot M^\dagger)^2 = (M \cdot M^\dagger). \quad (1.2.5)$$

The practical computation of the gauge-invariant basis M can be determined as the kernel of the Gauss Law operator of the corresponding LGT (see Sec. 1.3 for SU(2) and Sec. 1.4 for U(1)). The expansion of the gauge singlet basis states of $\mathcal{H}_{\text{dress}}$ in terms of the matter and rishon bases is computed via Clebsch-Gordan decomposition [155].

The resulting operators O^{eff} , for any spatial dimension D and any value of the gauge truncation j_{max} , are available for U(1) and SU(2) in the GitHub repository [ed-lgt](#) [6], which also allows for simulations of these LGTs via Exact Diagonalization.

1.2.4 Defermionization

As aforementioned in the introduction, an important challenge to be faced in simulating LGTs is to account for the Fermi statistics of matter fields. In several TN methods and conventional digital quantum simulation platforms [117–121], fermionic (anticommuting) algebra must be encoded into a genuinely local (commuting) algebra of qub(d)its. Standard fermion-to-qubit encodings, such as the Jordan-Wigner (JW) transformation [122], and other modern approaches [123–125] make any fermionic Hamiltonian interaction inherently long-range and expensive from a computational perspective [46], especially for higher-dimensional LGTs.

Within the dressed-site formalism, it is additionally possible resolve this problem and effectively eliminate the Fermi statistics of matter fields. This is possible for any gauge theory where the gauge field has a well-defined parity. Specifically, a local parity operator $\hat{P}_{\mathbf{n},\mu} = \hat{P}_{\mathbf{n},\mu}^\dagger$ such that $\hat{P}_{\mathbf{n},\mu}^2 = 1$ must satisfy $\{\hat{U}_{\mathbf{n},\mu}, \hat{P}_{\mathbf{n},\mu}\} = 0$, as it happens for \mathbb{Z}_{2N} , U(N), and SU(2N) [2, 115, 116]. In these cases, it is possible to consider rishons with a Fermi statistics, and, as a result, all physical (gauge invariant) dressed site operators are genuinely local, i.e. they mutually commute at a nonzero distance (as spins or bosons) [3].

As the resulting Hamiltonian in the dressed site formalism is made out of different fermions (matter fields and gauge rishons), it is convenient to rule the tensor product of general fermion operators. For a fermionic QMB system with particles arbitrarily sorted along a certain path, any

tensor product of fermionic operators should take into consideration the proper anti-commutation rules. Namely, a generic fermionic operator $\hat{F}_{\mathbf{n}}$ acting on the \mathbf{n}^{th} position along the path reads:

$$\hat{F}_{\mathbf{n}} = \begin{pmatrix} \hat{f}_{11} & \cdots & \hat{f}_{1N} \\ \vdots & & \vdots \\ \hat{f}_{N1} & \cdots & \hat{f}_{NN} \end{pmatrix}_F = \cdots \otimes \hat{P}_{\mathbf{n}-\boldsymbol{\mu}} \otimes \hat{F}_{\mathbf{n}} \otimes \mathbb{1}_{\mathbf{n}+\boldsymbol{\mu}} \otimes \cdots, \quad (1.2.6)$$

where $\hat{P}_{\mathbf{n}} = \hat{P}_{\mathbf{n}}^\dagger = \hat{P}_{\mathbf{n}}^{-1}$ is a fermion parity operator that gets inverted after the action of a fermionic operator:

$$\left\{ \hat{P}_{\mathbf{n}}, \hat{F}_{\mathbf{n}} \right\} = 0 \quad \left[\hat{P}_{\mathbf{n}}, \hat{F}_{\mathbf{n}' \neq \mathbf{n}} \right] = 0 \quad \forall \mathbf{n}, \mathbf{n}' \in \Lambda. \quad (1.2.7)$$

Therefore, matter fields admit a notion of parity satisfying Eq. (1.2.7). For Dirac fermions

$$\hat{\psi}_{\text{Dirac}} = \begin{pmatrix} 0 & 1 \\ 0 & 0 \end{pmatrix}_F \quad \hat{P}_{\text{Dirac}} = \begin{pmatrix} +1 & 0 \\ 0 & -1 \end{pmatrix}, \quad (1.2.8)$$

where the subscript F is a reminder that the $\hat{\psi}$ matrix is meant 'as a fermion', with the global action in Eq. (1.2.6). Similarly, as for Majorana fermions, we have:

$$\hat{\gamma}_{\text{Majorana}} = \begin{pmatrix} 0 & 1 \\ 1 & 0 \end{pmatrix}_F \quad \hat{P}_{\text{Majorana}} = \begin{pmatrix} +1 & 0 \\ 0 & -1 \end{pmatrix}. \quad (1.2.9)$$

Similarly, as for the incoming (fermion) rishon-operators, we will provide an adequate notion of parity (see Eq. (1.3.30) for SU(2) and Eq. (1.4.13) for U(1)).

1.3 SU(2) Yang-Mills Lattice Gauge Theory

In this section, we apply the dressed-site formalism to a non-Abelian scenario, focusing on the SU(2) Yang-Mills (YM) LGT, including dynamical matter. For simplicity we will focus on a (2+1)D system, where both the electric and magnetic gauge contributions play a non-trivial role. Generalizations to the (3+1)D are trivial, provided to consider the correct phase factors in Eq. (1.1.32) due to staggered fermions. Restrictions to the (1+1)D case are considered in Sec. 1.3.5 and applied in [4, 93, 143].

1.3.1 The model

Before introducing the SU(2) YM Hamiltonian, let us recall the main properties of the SU(2) gauge theory. First, the SU(2) algebra generators are the Pauli matrices $\hat{T}^a = \hat{\sigma}^a/2$, while the structure constants are equal to the Levi-Civita tensor $f^{abc} = \varepsilon^{abc}$. Correspondingly, left/right generators of SU(2) gauge transformations $\hat{L}_{\mathbf{n},\boldsymbol{\mu}}/\hat{R}_{\mathbf{n},\boldsymbol{\mu}}$ are hermitian and related each other as follows: for $a, b, c \in \{x, y, z\}$

$$\left[\hat{L}_{\mathbf{n},\boldsymbol{\mu}}^a, \hat{R}_{\mathbf{n},\boldsymbol{\mu}}^b \right] = 0 \quad \left[\hat{L}_{\mathbf{n},\boldsymbol{\mu}}^a, \hat{L}_{\mathbf{n}',\mathbf{n}'+\boldsymbol{\mu}'}^b \right] = i\delta_{\mathbf{nn}'}\delta_{\boldsymbol{\mu}\boldsymbol{\mu}'}\epsilon_{abc}\hat{L}_{\mathbf{n},\boldsymbol{\mu}}^c \quad (\text{same with } \hat{R}). \quad (1.3.1)$$

Their trace yields the Casimir operator

$$\hat{E}_{\mathbf{n},\boldsymbol{\mu}}^2 = \sum_a \hat{L}_{\mathbf{n},\boldsymbol{\mu}}^a \hat{L}_{\mathbf{n},\boldsymbol{\mu}}^a = \sum_a \hat{R}_{\mathbf{n},\boldsymbol{\mu}}^a \hat{R}_{\mathbf{n},\boldsymbol{\mu}}^a, \quad (1.3.2)$$

and the commutations rules with the parallel transporter $\hat{U}^{\alpha\beta}$ read

$$\left[\hat{L}_{\mathbf{n},\boldsymbol{\mu}}^a, \hat{U}_{\mathbf{n}',\boldsymbol{\mu}'}^{\alpha\beta} \right] = -\delta_{\mathbf{nn}'} \delta_{\boldsymbol{\mu}\boldsymbol{\mu}'} \sum_{\gamma} \frac{\sigma_{\alpha\gamma}^a}{2} \hat{U}_{\mathbf{n},\boldsymbol{\mu}}^{\gamma\beta}, \quad \left[\hat{R}_{\mathbf{n},\boldsymbol{\mu}}^a, \hat{U}_{\mathbf{n}',\boldsymbol{\mu}'}^{\alpha\beta} \right] = +\delta_{\mathbf{nn}'} \delta_{\boldsymbol{\mu}\boldsymbol{\mu}'} \sum_{\gamma} \hat{U}_{\mathbf{n},\boldsymbol{\mu}}^{\alpha\gamma} \frac{\sigma_{\gamma\beta}^a}{2}. \quad (1.3.3)$$

Then, when introducing dynamical matter, we focus on single-flavor matter fields with SU(2)-color 1/2, expressed in terms of SU(2)-color staggered (Dirac) fermions $\hat{\psi}_{\mathbf{n},\alpha}$ [148] and satisfying

$$\left\{ \hat{\psi}_{\mathbf{n},\alpha}^{\dagger} \hat{\psi}_{\mathbf{n}',\beta} \right\} = i\hbar \delta_{\mathbf{nn}'} \delta_{\alpha,\beta}, \quad \text{where} \quad \alpha, \beta \in \{r, g\} \quad \text{are SU(2)-colors.} \quad (1.3.4)$$

From Eq. (1.2.2) and assuming no background charges, Gauss Law operators are defined as

$$\hat{G}_{\mathbf{n}}^a = \hat{Q}_{\mathbf{n}}^a + \sum_{\boldsymbol{\mu}} \left(\hat{R}_{\mathbf{n}-\boldsymbol{\mu},\mathbf{n}}^a + \hat{L}_{\mathbf{n},\boldsymbol{\mu}}^a \right), \quad \text{where} \quad \hat{Q}_{\mathbf{n}}^a = \sum_{\alpha\beta} \hat{\psi}_{\mathbf{n},\alpha}^{\dagger} \frac{\sigma_{\alpha\beta}^a}{2} \hat{\psi}_{\mathbf{n},\beta} \quad (1.3.5)$$

rotates the quark field at \mathbf{n} , and, if squared, it yields the *matter color density*, i.e. the quadratic Casimir operator of the matter field gauge group transformations:

$$\hat{S}_{\text{matt},\mathbf{n}}^2 = \sum_a \hat{Q}_{\mathbf{n}}^a \hat{Q}_{\mathbf{n}}^a. \quad (1.3.6)$$

Correspondingly, $\hat{L}_{\mathbf{n}-\boldsymbol{\mu},\mathbf{n}}^a$ and $\hat{R}_{\mathbf{n},\boldsymbol{\mu}}^a$ account for the transformation of the gauge links at its left and its right respectively [130].

Then, the corresponding (2+1)D Hamiltonian with staggered fermions (see Sec. 1.1.3) reads:

$$\begin{aligned} \hat{H}_{\text{SU}(2)}^{\text{YM}} = & + \frac{c\hbar}{2a_0} \sum_{\alpha,\beta} \sum_{\mathbf{n}} \left[-i \hat{\psi}_{\mathbf{n},\alpha}^{\dagger} \hat{U}_{\mathbf{n},\boldsymbol{\mu}_x}^{\alpha\beta} \hat{\psi}_{\mathbf{n}+\boldsymbol{\mu}_x,\beta} - (-1)^{n_x+n_y} \hat{\psi}_{\mathbf{n},\alpha}^{\dagger} \hat{U}_{\mathbf{n},\boldsymbol{\mu}_y}^{\alpha\beta} \hat{\psi}_{\mathbf{n}+\boldsymbol{\mu}_y,\beta} + \text{h.c.} \right] \\ & + m_0 c^2 \sum_{\mathbf{n}} (-1)^{n_x+n_y} \sum_{\alpha} \hat{\psi}_{\mathbf{n},\alpha}^{\dagger} \hat{\psi}_{\mathbf{n},\alpha} + \hat{H}_{\text{pure}}. \end{aligned} \quad (1.3.7)$$

As for the pure gauge Hamiltonian, we have

$$\hat{H}_{\text{pure}} = g^2 \frac{c\hbar}{2a_0} \sum_{\mathbf{n},\boldsymbol{\mu}} \hat{E}_{\mathbf{n},\boldsymbol{\mu}}^2 - \frac{c\hbar}{2a_0 g^2} \sum_{\square} \text{Tr} \left(\hat{U}_{\square} + \hat{U}_{\square}^{\dagger} \right), \quad (1.3.8)$$

where \hat{U}_{\square} is the plaquette operator defined in Eq. (1.1.59), while the gauge coupling $g(q, a_0) \propto q\sqrt{a_0}$ defined Eq. (1.1.57) is dimensionless, but scales nonetheless with the lattice spacing a_0 to ensure that the color charge q of a quark stays finite in the continuum limit.

1.3.2 Truncating the SU(2) gauge group

As discussed in Sec. 1.2.1, to make LGT Hamiltonians in Eqs. (1.3.7) and (1.3.8) suitable for TN methods and quantum hardware, a finite-dimensional gauge-link Hilbert space is typically required. Here, we propose an effective truncation for the SU(2) gauge fields that can be applied to lattices of any spatial dimension and scalable to arbitrarily large truncations. In the limit of an infinitely large spin irreducible representation of the SU(2) gauge group, it recovers all the properties of the original SU(2) Yang-Mills LGT. Remarkably, the use of this approach in the smallest non-trivial truncation of SU(2), labeled as *hardcore-gluon* approximation, has been used to achieve non-trivial results as the ones discussed in Chap. 3 [2] and Sec. 4.4 [4, 143]. Of course, to accurately represent the full theory, for weak- g , larger gauge representations are required:

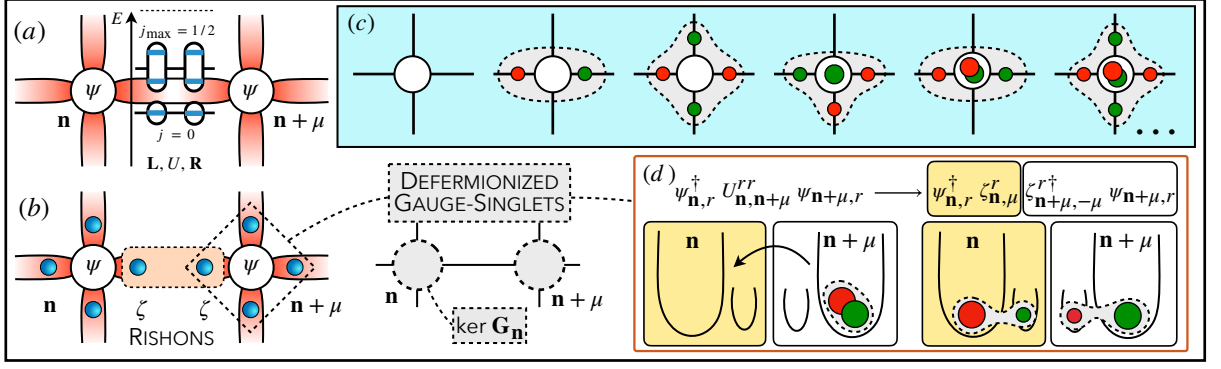


Figure 1.2: Sketched representation of the dressed-site model developed in Sec. 1.3 for SU(2): (a) starting from the formulation with matter sites and truncated SU(2) gauge links, (b) we split the latter in pairs of rishon modes $\hat{\zeta}$ defined in Eq. (1.3.27) and constrain their dynamics with the SU(2) link symmetry in Eq. (1.3.36). We then (c) merge them with matter fields into dressed SU(2) gauge-singlets with a bosonic statistics. As a consequence, within the dressed-site formalism, the hopping always involves an even number of fermions, i.e. the matter field plus a rishon mode (d). Figure inspired by [2, 5].

this increases the computational challenges but it is still potentially accessible via TNs. Anyway, such a description of the gauge group is the first building block for building logical dressed-sites discussed in Sec. 1.2, where Gauss Law is already satisfied (see Fig. 1.2).

To truncate the continuous SU(2) gauge group, we express it in terms of the irreducible representation (irrep) basis [160, 163]. As SU(2) admits a *quasi-real*-representation, where the fundamental and the anti-fundamental representations coincide, $\forall \mathbf{n}, \boldsymbol{\mu} \in \Lambda$, the gauge Hilbert space of the $(\mathbf{n}, \boldsymbol{\mu})$ link can be written as:

$$\mathcal{H}_{\text{gauge}} = \{|j, m_L, m_R\rangle\}, \quad \text{where} \quad -j \leq m_{L(R)} \leq j \quad (1.3.9)$$

is the corresponding third spin component associated with the left (right) side of the SU(2) link-irrep j . Then, the parallel transporter $\hat{U}^{\alpha\beta}$ is given in terms of Clebsh-Gordan coefficients:

$$\langle j' m'_L m'_R | \hat{U}^{\alpha\beta} | j m_L m_R \rangle = \sqrt{\frac{2j+1}{2j'+1}} C_{\frac{1}{2}, \alpha; j' m'_L}^{j m_L} C_{j m_R; \frac{1}{2}, \beta}^{j' m'_R}. \quad (1.3.10)$$

Correspondingly, left and right generators are defined as:

$$\langle j' m'_L m'_R | \hat{L}^a | j m_L m_R \rangle = \delta_{j, j'} S_{m'_L, m_L}^{(j)a} \delta_{m'_R, m_R}, \quad (1.3.11a)$$

$$\langle j' m'_L m'_R | \hat{R}^a | j m_L m_R \rangle = \delta_{j, j'} \delta_{m'_L, m_L} S_{m'_R, m_R}^{(j)a}. \quad (1.3.11b)$$

Then, the chromo-electric energy operator, i.e. the quadratic Casimir in Eq. (1.3.2) reads [130]:

$$\hat{E}^2 |j m_L m_R\rangle = j(j+1) |j m_L m_R\rangle. \quad (1.3.12)$$

Then, the truncation of the gauge fields is applied by imposing a local energy cutoff Θ on the \hat{E}^2 spectrum, keeping the irreps $j \leq j_{\text{max}}$ such that $C_2(j_{\text{max}}) \leq \Theta$. The truncation keeps the electric field operator \hat{E} hermitian and protects the SU(2) gauge algebra rules of Eqs. (1.3.1) and (1.3.3). Namely, truncated $\hat{U}^{\alpha\beta}$ fields satisfy the following left and right gauge transformations:

$$\left[\hat{L}_{j_{\text{max}}}^a, \hat{U}^{\alpha\beta} \right] = - \sum_{\gamma} \frac{\sigma_{\alpha\gamma}^a}{2} \hat{U}_{\gamma\beta} \quad \left[\hat{R}_{j_{\text{max}}}^a, \hat{U}_{\alpha\beta} \right] = + \sum_{\gamma} \hat{U}_{\alpha\gamma} \frac{\sigma_{\gamma\beta}^a}{2}, \quad (1.3.13)$$

where $\hat{L}_{j_{\max}}^a$ and $\hat{R}_{j_{\max}}^a$ are (truncated) generators of the left- and right-handed groups of SU(2) transformations. They can be expressed as the block-diagonal direct sum of spin matrices S_j^a in consecutive j -representations from the smallest ($j = 0$) to the largest one ($j = j_{\max}$):

$$\begin{aligned}\hat{L}_{j_{\max}}^a &= \bigoplus_{j=0}^{j_{\max}} (S_j^a \otimes \mathbb{1}_j) = \text{diag}(S_0^a \otimes \mathbb{1}_0, \dots, S_{j_{\max}}^a \otimes \mathbb{1}_{j_{\max}}) \\ \hat{R}_{j_{\max}}^a &= \bigoplus_{j=0}^{j_{\max}} (\mathbb{1}_j \otimes S_j^a) = \text{diag}(\mathbb{1}_0 \otimes S_0^a, \dots, \mathbb{1}_{j_{\max}} \otimes S_{j_{\max}}^a).\end{aligned}\tag{1.3.14}$$

Unfortunately, the truncation makes $\hat{U}^{\alpha\beta}$ unitary only as long as it acts on spin shells with $j < j_{\max}$ (it loses norm on the largest spin shell). Correspondingly, Wilson loops stay unitary as long as the outer spin shell $j = j_{\max}$ is nowhere populated. Namely, it implies that, $\forall j < j_{\max}$

$$\sum_{\beta\gamma} \hat{U}^{\alpha\beta} |0;0,0\rangle \otimes \hat{U}_{\beta\gamma} |j;m_L, m_R\rangle \otimes \hat{U}_{\gamma\delta} |0;0,0\rangle\tag{1.3.15}$$

displays the same norm of $\hat{U}_{\alpha\delta} |000\rangle \forall \alpha, \delta$, that is $1/\sqrt{2}$. Ultimately, we require the parallel transporter to display *spatial reflection symmetry*. Namely:

$$\hat{U}_{\alpha\beta}^\dagger = -\hat{\mathcal{F}} \hat{U}_{\beta\alpha} \hat{\mathcal{F}},\tag{1.3.16}$$

where $\hat{\mathcal{F}}$ is the *swap operator* on a gauge link:

$$\hat{\mathcal{F}} = \sum_{j, m_L, m_R} |j; m_L, m_R\rangle \langle j; m_R, m_L| = \hat{\mathcal{F}}^{-1} = \hat{\mathcal{F}}^\dagger.\tag{1.3.17}$$

Whatever the gauge field truncation, in hopping terms, the action of \hat{U} has to match the fundamental irrep of the matter field, whose Hilbert space in the Fock space, can be written as:

$$\mathcal{H}_{\text{site}} = \left\{ |0\rangle = |\Omega\rangle, |r\rangle = \psi_r^\dagger |\Omega\rangle, |g\rangle = \psi_g^\dagger |\Omega\rangle, |2\rangle = \psi_r^\dagger \psi_g^\dagger |\Omega\rangle \right\},\tag{1.3.18}$$

whose action in the irrep basis $|j, m\rangle$ corresponds to the following SU(2) charges:

$$\mathcal{H}_{\text{site}} = \left\{ |0, 0\rangle, \left| \frac{1}{2}, \frac{1}{2} \right\rangle, \left| \frac{1}{2}, -\frac{1}{2} \right\rangle, |0, 0\rangle \right\}.\tag{1.3.19}$$

1.3.3 Rishon decomposition of SU(2) gauge fields

With all these premises, the resulting truncated SU(2) Yang-Mills Hamiltonian of Eq. (1.3.7)-(1.3.8) will act on the Hilbert space resulting from the tensor product of all the single matter Hilbert spaces and the corresponding ones of each truncated gauge field:

$$\mathcal{H} = \bigotimes_{\mathbf{n}} \mathcal{H}_{\text{matt}} \bigotimes_{\mathbf{n}, \boldsymbol{\mu}} \mathcal{H}_{\text{tr.link}}.\tag{1.3.20}$$

Notice that matter and gauge fields display different statistics. In these terms, we expect $\hat{U}_{\mathbf{n}, \boldsymbol{\mu}}^{\alpha\beta}$ to be *mutually bosonic*, as it commutes with all the matter-fields operators:

$$\left[\hat{U}_{\mathbf{n}, \boldsymbol{\mu}}^{\alpha\beta}, \hat{\psi}_{\mathbf{n}, \alpha}^{(\dagger)} \right] = 0 \quad \forall \mathbf{n}, \forall \boldsymbol{\mu}, \forall \alpha, \beta\tag{1.3.21}$$

and *purely local*, as its link-algebra commutes with the one of any other link:

$$\left[\hat{U}_{\mathbf{n},\mu}^{\alpha\beta}, \hat{U}_{\mathbf{n}',\mathbf{n}'+\mu'}^{\gamma\delta} \right] = 0 \quad \forall \mathbf{n} \neq \mathbf{n}', \mu \neq \mu', \forall \alpha, \beta, \gamma, \delta. \quad (1.3.22)$$

As anticipated in Sec. 1.2, in the electric basis, the parallel transporter $\hat{U}^{\alpha\beta}$ admits a rishon-decomposition to arbitrary truncation of the maximum allowed spin shell j_{\max} . Starting from a given spin shell j , we have to separately account for the action when both rishons are increased to shell $j + \frac{1}{2}$, and both are decreased to shell $j - \frac{1}{2}$. We can then decompose $\hat{U}^{\alpha\beta}$ as follows:

$$\hat{U}_{\mathbf{n},\mathbf{n}+\mu}^{\alpha\beta} = \hat{\zeta}_{A,\mathbf{n},\mu}^{\alpha} \hat{\zeta}_{B,\mathbf{n}+\mu,-\mu}^{\beta\dagger} + \hat{\zeta}_{B,\mathbf{n},\mu}^{\alpha} \hat{\zeta}_{A,\mathbf{n}+\mu,-\mu}^{\beta\dagger}, \quad (1.3.23)$$

where the two $\hat{\zeta}$ -rishon species, A and B, act respectively as raising and lowering the spin shell of the SU(2) gauge irrep. Interestingly, they are related to each other as:

$$\hat{\zeta}_A^{\alpha} = i\sigma_{\alpha,\beta}^y \hat{\zeta}_B^{\beta\dagger} \quad \hat{\zeta}_A^{\alpha\dagger} = i\sigma_{\alpha,\beta}^y \hat{\zeta}_B^{\beta}. \quad (1.3.24)$$

We can then rewrite Eq. (1.3.23) in terms of one species, e.g. B. Renaming $\hat{\zeta}_B^{\alpha} = \hat{\zeta}^{\alpha}$, we obtain:

$$\hat{U}_{\mathbf{n},\mathbf{n}+\mu}^{\alpha\beta} = i\sigma_{\alpha\gamma}^y \hat{\zeta}_{\mathbf{n},\mu}^{\gamma\dagger} \hat{\zeta}_{\mathbf{n}+\mu,-\mu}^{\beta\dagger} + i\sigma_{\beta\gamma}^y \hat{\zeta}_{\mathbf{n},\mu}^{\alpha} \hat{\zeta}_{\mathbf{n}+\mu,-\mu}^{\gamma}, \quad (1.3.25)$$

or equivalently

$$\begin{aligned} \hat{U}_{\mathbf{n},\mathbf{n}+\mu}^{rr} &= \hat{\zeta}_{\mathbf{n},\mu}^{g\dagger} \hat{\zeta}_{\mathbf{n}+\mu,-\mu}^{r\dagger} + \hat{\zeta}_{\mathbf{n},\mu}^r \hat{\zeta}_{\mathbf{n}+\mu,-\mu}^g \\ \hat{U}_{\mathbf{n},\mathbf{n}+\mu}^{rg} &= \hat{\zeta}_{\mathbf{n},\mu}^{g\dagger} \hat{\zeta}_{\mathbf{n}+\mu,-\mu}^{g\dagger} - \hat{\zeta}_{\mathbf{n},\mu}^r \hat{\zeta}_{\mathbf{n}+\mu,-\mu}^r \\ \hat{U}_{\mathbf{n},\mathbf{n}+\mu}^{gr} &= -\hat{\zeta}_{\mathbf{n},\mu}^{r\dagger} \hat{\zeta}_{\mathbf{n}+\mu,-\mu}^{r\dagger} + \hat{\zeta}_{\mathbf{n},\mu}^g \hat{\zeta}_{\mathbf{n}+\mu,-\mu}^g \\ \hat{U}_{\mathbf{n},\mathbf{n}+\mu}^{gg} &= -\hat{\zeta}_{\mathbf{n},\mu}^{r\dagger} \hat{\zeta}_{\mathbf{n}+\mu,-\mu}^{g\dagger} - \hat{\zeta}_{\mathbf{n},\mu}^g \hat{\zeta}_{\mathbf{n}+\mu,-\mu}^r. \end{aligned} \quad (1.3.26)$$

For a chosen truncation j_{\max} of the SU(2) irreducible representation, $\hat{\zeta}$ -rishons are defined as:

$$\hat{\zeta}^{g(r)} = \left[\sum_{j=0}^{j_{\max}-\frac{1}{2}} \sum_{m=-j}^j \chi(j, m, g(r)) |j, m\rangle \langle j + \frac{1}{2}, m \mp \frac{1}{2}| \right]_F, \quad (1.3.27)$$

where the function $\chi(j, m, \alpha)$ reads

$$\chi(j, m, g(r)) = \sqrt{\frac{j \mp m + 1}{\sqrt{(2j+1)(2j+2)}}}. \quad (1.3.28)$$

It is possible to show that this construction is indeed compatible with the explicit form of the parallel transport reported in Eq. (1.3.10).

SU(2) Rishon Parity

Being fermions, $\hat{\zeta}$ -rishons anti-commute at different orbitals and with matter fields:

$$\left\{ \hat{\zeta}_{\mathbf{n},\mu}^{\alpha}, \hat{\zeta}_{\mathbf{n}+\mu,-\mu}^{\beta} \right\} = 0 \quad \left\{ \hat{\zeta}_{\mathbf{n},\mu}^{\alpha}, \hat{\psi}_{\mathbf{n},\beta} \right\} = 0 \quad \forall \alpha, \beta. \quad (1.3.29)$$

To satisfy Eq. (1.3.29), we need to characterize them as fermion operators properly. As discussed in Sec. 1.2.4, we can then introduce the notion of a parity for the SU(2) rishon modes. Similarly

to Eqs. (1.2.8) and (1.2.9), we define the SU(2) rishon parity operator \hat{P}_ζ with an even (+1) parity sector on *integer* irreps and odd (-1) sector on *semi-integer* ones:

$$\hat{P}_\zeta = \text{diag}(+1 | -1, -1 | +1, +1, +1 | \dots). \quad (1.3.30)$$

The action of the single rishon inverts the local parity: $\{\hat{P}, \hat{\zeta}^\alpha\} = 0$. Correspondingly, the parallel transporter $\hat{U}_{\mathbf{n}, \boldsymbol{\mu}}^{\alpha\beta}$ reads:

$$\begin{aligned} \hat{U}_{\mathbf{n}, \boldsymbol{\mu}}^{\alpha\beta} &= i\sigma_{\alpha\gamma}^y \hat{\zeta}_{\mathbf{n}, \boldsymbol{\mu}}^{\gamma\dagger} \hat{\zeta}_{\mathbf{n}+\boldsymbol{\mu}, -\boldsymbol{\mu}}^{\beta\dagger} + i\sigma_{\beta\gamma}^y \hat{\zeta}_{\mathbf{n}, \boldsymbol{\mu}}^\alpha \hat{\zeta}_{\mathbf{n}+\boldsymbol{\mu}, -\boldsymbol{\mu}}^\gamma \\ &= + i\sigma_{\alpha\gamma}^y \left(\hat{\zeta}_{\mathbf{n}, \boldsymbol{\mu}}^{\gamma\dagger} \cdot \hat{P}_{\zeta, \mathbf{n}, \boldsymbol{\mu}} \right) \otimes \hat{\zeta}_{\mathbf{n}+\boldsymbol{\mu}, -\boldsymbol{\mu}}^{\beta\dagger} + i\sigma_{\beta\gamma}^y \left(\hat{\zeta}_{\mathbf{n}, \boldsymbol{\mu}}^\alpha \cdot \hat{P}_{\zeta, \mathbf{n}, \boldsymbol{\mu}} \right) \otimes \hat{\zeta}_{\mathbf{n}+\boldsymbol{\mu}, -\boldsymbol{\mu}}^\gamma. \end{aligned} \quad (1.3.31)$$

Notice that the right-hand side of Eq. (1.3.31) preserves the SU(2) link parity, as desired.

SU(2) Rishon Algebra

Instead of relying on two separate set of SU(2) generators, \hat{L}^a and \hat{R}^a , $\hat{\zeta}$ -rishons have a unique gauge transformation algebra. The generators of SU(2) gauge rotations upon the $\hat{\zeta}$ -rishon space read:

$$\hat{\mathcal{T}}_{j_{\max}}^a = \bigoplus_{j=0}^{j_{\max}} S_j^a = \text{diag}(S_0^a, S_1^a, \dots, S_{j_{\max}}^a). \quad (1.3.32)$$

By construction, $\hat{\zeta}$ operators are SU(2) covariant, as they transform as follows:

$$\left[\hat{\zeta}^\alpha, \hat{\mathcal{T}}^a \right] = \frac{1}{2} \sum_{\beta} \hat{\sigma}_{\alpha\beta}^a \hat{\zeta}^\beta \quad \left[\hat{\mathcal{T}}^a, \hat{\zeta}_\alpha^\dagger \right] = \frac{1}{2} \sum_{\beta} \hat{\zeta}^{\beta\dagger} \hat{\sigma}_{\beta\alpha}^a. \quad (1.3.33)$$

Moreover, $\hat{\mathcal{T}}^a$ is genuinely *local*: for $\forall \mathbf{n} \neq \mathbf{n}'$, $\forall \boldsymbol{\mu} \neq \boldsymbol{\mu}'$, and $\forall \alpha \in \{r, g\}$:

$$\left[\hat{\mathcal{T}}_{\mathbf{n}, +\boldsymbol{\mu}}^a, \hat{\zeta}_{\mathbf{n}', +\boldsymbol{\mu}'}^\alpha \right] = \left[\hat{\mathcal{T}}_{\mathbf{n}, +\boldsymbol{\mu}}^a, \hat{\psi}_{\mathbf{n}', \alpha} \right] = 0. \quad (1.3.34)$$

We easily recover the left and right generators of the gauge field at link $(\mathbf{n}, \boldsymbol{\mu})$ as:

$$\hat{L}_{\mathbf{n}, +\boldsymbol{\mu}}^a = \hat{\mathcal{T}}_{\mathbf{n}, +\boldsymbol{\mu}}^a \otimes \mathbb{1}_{\mathbf{n}+\boldsymbol{\mu}, -\boldsymbol{\mu}} \quad \hat{R}_{\mathbf{n}, +\boldsymbol{\mu}}^a = \mathbb{1}_{\mathbf{n}, +\boldsymbol{\mu}} \otimes \hat{\mathcal{T}}_{\mathbf{n}+\boldsymbol{\mu}, -\boldsymbol{\mu}}^a. \quad (1.3.35)$$

Since in the SU(2) group the fundamental and the anti-fundamental representations coincide, the rishon formalism is meaningful as long as the quadratic Casimir operator of the two sides of the link coincide as in Eq. (1.1.55):

$$\left| \hat{L}_{\mathbf{n}, +\boldsymbol{\mu}}^a \right|^2 = \left| \hat{R}_{\mathbf{n}+\boldsymbol{\mu}, -\boldsymbol{\mu}}^a \right|^2. \quad (1.3.36)$$

Thanks to Eq. (1.3.36), the two rishons of the link are in the same SU(2) irrep, and the parallel transport in Eq. (1.3.23) coincides with the one in Eq. (1.3.10). Correspondingly, the Casimir operator of the $(\mathbf{n}, \boldsymbol{\mu})$ link in Eq. (1.1.55) can be expressed as:

$$\hat{E}_{\mathbf{n}, \boldsymbol{\mu}}^2 = \frac{1}{2} \left[\left| \hat{L}_{\mathbf{n}, +\boldsymbol{\mu}}^a \right|^2 + \left| \hat{R}_{\mathbf{n}+\boldsymbol{\mu}, -\boldsymbol{\mu}}^a \right|^2 \right] = \frac{1}{2} \left[\left| \hat{\mathcal{T}}_{\mathbf{n}, +\boldsymbol{\mu}}^a \right|^2 + \left| \hat{\mathcal{T}}_{\mathbf{n}+\boldsymbol{\mu}, -\boldsymbol{\mu}}^a \right|^2 \right], \quad (1.3.37)$$

which looks explicitly symmetric under link reversal.

1.3.4 Constructing dressed site operators

We have then all the ingredients to build a *dressed-site* compact representation. In the case of a 2D lattice, one possible pictorial description of *dressed-site* states reads:

$$\left| \begin{array}{c} \hat{\zeta}_{\mathbf{n},-\mu_x} \\ \hat{\zeta}_{\mathbf{n},+\mu_y} \\ \left(\hat{\psi}_{\mathbf{n},r} \hat{\psi}_{\mathbf{n},g} \right) \\ \hat{\zeta}_{\mathbf{n},+\mu_x} \\ \hat{\zeta}_{\mathbf{n},-\mu_y} \end{array} \right\rangle, \quad \text{where} \quad \left| \begin{array}{c} 5 \\ 2 \quad (0,1) \quad 4 \\ 3 \end{array} \right\rangle \quad (1.3.38)$$

is a possible internal ordering to be used as in Eq. (1.2.6) when constructing composite operators out of matter fields and rishons inside the dressed site.

We can then rewrite the SU(2) Yang-Mills Hamiltonian in Eq. (1.3.7)-(1.3.8) via rishon modes.

Arrival operators Let us start with the hopping Hamiltonian term. Discarding all the prefactors, we have²:

$$\begin{aligned} \hat{H}_{\mathbf{n},\mu}^{\text{hopping}} &= \sum_{\alpha,\beta} \hat{\psi}_{\mathbf{n},\alpha}^\dagger \hat{U}_{\mathbf{n},\mu}^{\alpha\beta} \hat{\psi}_{\mathbf{n}+\mu,\beta} \\ &= \sum_{\alpha,\beta} \hat{\psi}_{\mathbf{n},\alpha}^\dagger \left[\hat{\zeta}_{A,\mathbf{n},\mu}^\alpha \hat{\zeta}_{B,\mathbf{n}+\mu,-\mu}^{\beta\dagger} + \hat{\zeta}_{B,\mathbf{n},\mu}^\alpha \hat{\zeta}_{A,\mathbf{n}+\mu,-\mu}^{\beta\dagger} \right] \hat{\psi}_{\mathbf{n}+\mu,\beta} \\ &= \left[\hat{Q}_{A,\mathbf{n},\mu}^\dagger \hat{Q}_{B,\mathbf{n}+\mu,-\mu} + \hat{Q}_{B,\mathbf{n}}^\dagger \hat{Q}_{A,\mathbf{n}+\mu,-\mu} \right], \end{aligned}$$

where we defined two species of *arrival* operators:

$$\hat{Q}_{A,\mathbf{n},\mu}^\dagger = \sum_{\alpha} \hat{\psi}_{\mathbf{n},\alpha}^\dagger \hat{\zeta}_{A,\mathbf{n},\mu}^\alpha \quad \hat{Q}_{B,\mathbf{n},\mu}^\dagger = \sum_{\alpha} \hat{\psi}_{\mathbf{n},\alpha}^\dagger \hat{\zeta}_{B,\mathbf{n},\mu}^\alpha. \quad (1.3.39)$$

These operators' practical construction must be consistent with the internal order in Eq. (1.3.38).

Matter number density operators Similarly, number density operators are expressed as

$$\hat{N}_{\mathbf{n},r} = \psi_{\mathbf{n}}^\dagger \psi_{\mathbf{n},r} \otimes \mathbb{1}_{\mathbf{n},g} \bigotimes_{\mu} \mathbb{1}_{\mathbf{n},\mu} \quad \hat{N}_{\mathbf{n},g} = \mathbb{1}_{\mathbf{n},r} \otimes \psi_{\mathbf{n}}^\dagger \psi_{\mathbf{n},g} \bigotimes_{\mu} \mathbb{1}_{\mathbf{n},\mu} \quad (1.3.40)$$

and give access to other observables like:

$$\hat{N}_{\mathbf{n},\text{tot}} = \hat{N}_{\mathbf{n},r} + \hat{N}_{\mathbf{n},g} \quad \hat{N}_{\mathbf{n},\text{pair}} = \hat{N}_{\mathbf{n},r} \hat{N}_{\mathbf{n},g} \quad \hat{N}_{\mathbf{n},\text{single}} = \hat{N}_{\mathbf{n},\text{tot}} - \hat{N}_{\mathbf{n},\text{pair}}, \quad (1.3.41)$$

which respectively measure the total matter density and the corresponding occupancy of pairs or single particles.

Casimir operator As we assumed via Eq. (1.3.37) that each of the two $\hat{\zeta}$ -rishons equally contributes to the link-electric energy density, we can equivalently define a dressed-site operator summing the Casimir contributions from its attached rishons:

$$\hat{\Gamma}_{\mathbf{n}} = \frac{1}{2} \sum_{\mu} (\hat{\mathcal{T}}_{\mathbf{n},\mu}^a)^2. \quad (1.3.42)$$

²Just for practical implementation in numerical simulations, the definition of the arrival operators here recalls the parallel transporter definition in terms of the two rishon species. Of course, an equivalent definition in terms of only one of the two species is available.

Magnetic Operators Expressing \hat{U} as in Eq. (1.3.23), the plaquette term gives rise to 16 contributions:

$$\begin{aligned}
\hat{U}_{\square} &= \sum_{\alpha,\beta,\delta,\gamma} \left[\hat{U}_{\mathbf{n},\boldsymbol{\mu}_x}^{\alpha\beta} \hat{U}_{\mathbf{n}+\boldsymbol{\mu}_x,\mathbf{n}+\boldsymbol{\mu}_x+\boldsymbol{\mu}_y}^{\beta\gamma} \hat{U}_{\mathbf{n}+\boldsymbol{\mu}_x+\boldsymbol{\mu}_y,\mathbf{n}+\boldsymbol{\mu}_y}^{\gamma\delta} \hat{U}_{\mathbf{n}+\boldsymbol{\mu}_y,\mathbf{n}}^{\delta\alpha} \right] \\
&= \sum_{\alpha,\beta,\delta,\gamma} \left(\begin{array}{ccc} \ulcorner & \hat{\zeta}_{B,+\boldsymbol{\mu}_x}^{\delta\dagger} \hat{\zeta}_{A,-\boldsymbol{\mu}_x}^{\gamma} & \urcorner \\ \hat{\zeta}_{A,-\boldsymbol{\mu}_y}^{\delta} & & \hat{\zeta}_{B,-\boldsymbol{\mu}_y}^{\gamma\dagger} \\ \hat{\zeta}_{B,+\boldsymbol{\mu}_y}^{\alpha\dagger} & & \hat{\zeta}_{A,+\boldsymbol{\mu}_y}^{\beta} \end{array} \right) + \dots \\
&= - \left[\begin{array}{cc} C_{-\boldsymbol{\mu}_y,+\boldsymbol{\mu}_x}^{AA} & - C_{-\boldsymbol{\mu}_x,-\boldsymbol{\mu}_y}^{AA} \\ C_{+\boldsymbol{\mu}_x,+\boldsymbol{\mu}_y}^{AA} & - C_{+\boldsymbol{\mu}_y,-\boldsymbol{\mu}_x}^{AA} \end{array} \right] + \dots,
\end{aligned}$$

where, in *, we combined rishons in pairs to form *corner operators* like the following:

$$\begin{aligned}
\hat{C}_{\mathbf{n},\boldsymbol{\mu}_1,\boldsymbol{\mu}_2}^{AA} &= \sum_{\alpha} \hat{\zeta}_{A,\mathbf{n},\boldsymbol{\mu}_1}^{\alpha} \hat{\zeta}_{A,\mathbf{n},\boldsymbol{\mu}_2}^{\alpha\dagger} = \sum_{\alpha,\kappa,\kappa'} i\sigma_{\alpha,\kappa}^y \hat{\zeta}_{B,\mathbf{n},\boldsymbol{\mu}_1}^{\kappa\dagger} i\sigma_{\alpha,\kappa'}^y \hat{\zeta}_{B,\mathbf{n},\boldsymbol{\mu}_2}^{\kappa'} \\
\hat{C}_{\mathbf{n},\boldsymbol{\mu}_1,\boldsymbol{\mu}_2}^{BB} &= \sum_{\alpha} \hat{\zeta}_{B,\mathbf{n},\boldsymbol{\mu}_1}^{\alpha} \hat{\zeta}_{B,\mathbf{n},\boldsymbol{\mu}_2}^{\alpha\dagger} = \hat{C}_{\mathbf{n},\boldsymbol{\mu}_2,\boldsymbol{\mu}_1}^{AA} \\
\hat{C}_{\mathbf{n},\boldsymbol{\mu}_1,\boldsymbol{\mu}_2}^{AB} &= \sum_{\alpha} \hat{\zeta}_{A,\mathbf{n},\boldsymbol{\mu}_1}^{\alpha} \hat{\zeta}_{B,\mathbf{n},\boldsymbol{\mu}_2}^{\alpha\dagger} = \left(\hat{C}_{\mathbf{n},\boldsymbol{\mu}_2,\boldsymbol{\mu}_1}^{BA} \right)^{\dagger}.
\end{aligned} \tag{1.3.43}$$

As for the previous dressed-site operators, the practical construction of corner operators has to be consistent with the internal ordering in Eq. (1.3.38).

SU(2) Link Symmetry Within the dressed-site formalism, the condition in Eq. (1.3.36) requiring the two rishon of the links to display the same Casimir operator (i.e. to be in the same spin shell j) is simply an Abelian \mathbb{Z}_2 Link Symmetry. It can be then easily encoded in ED and TN libraries employing symmetries [6, 49].

Projecting the operators on the SU(2) gauge invariant subspace

All the dressed-site operators previously derived must be projected in the SU(2) gauge-invariant basis M . The latter is made by SU(2) singlets and can be determined as the kernel of the Gauss Law operators $\hat{\mathbf{G}}_{\mathbf{n}}^a$:

$$\hat{\mathbf{G}}_{\mathbf{n}} \cdot M = \left[\hat{S}_{\text{matt},\mathbf{n}}^2 + \sum_{\boldsymbol{\mu}} \sum_a \hat{\mathcal{T}}_{\mathbf{n},\boldsymbol{\mu}}^a \hat{\mathcal{T}}_{\mathbf{n},\boldsymbol{\mu}}^a \right] \cdot M = 0, \tag{1.3.44}$$

where $\hat{\mathcal{T}}_{\boldsymbol{\mu}}^a$ are the $\hat{\zeta}$ -rishon generators along the $\boldsymbol{\mu}^{\text{th}}$ direction and defined in Eq. (1.3.32), while $\hat{S}_{\text{matt},\mathbf{n}}^2$ is the matter color density introduced in Eq. (1.3.6). In the minimal $j_{\text{max}} = \frac{1}{2}$ truncation of SU(2), the gauge-invariant Hilbert space of every dressed site of the full Hamiltonian has 30 gauge invariant states, whereas, restricting to the pure theory, the local Hilbert space is 9-dimensional.

The operative deformed Hamiltonian

We are then ready to rewrite the SU(2) lattice Yang-Mills Hamiltonian in Eq. (1.3.7) making use of dressed-site operators in Eqs. (1.3.39) and (1.3.43). Namely, we have:

$$\begin{aligned} \hat{H} = & -\frac{c\hbar}{2a_0} \sum_{\mathbf{n}} \left[i \left[\hat{Q}_{A,\mathbf{n},+\mu_x}^\dagger \hat{Q}_{B,\mathbf{n}+\mu_x,-\mu_x} \right] + (-1)^{n_x+n_y} \left[\hat{Q}_{A,\mathbf{n},+\mu_y}^\dagger \hat{Q}_{B,\mathbf{n}+\mu_y,-\mu_y} \right] + (A \rightleftharpoons B) \right] + \text{h.c.} \\ & + m_0 c^2 \sum_{\mathbf{n}} (-1)^{n_x+n_y} \hat{N}_{\mathbf{n},\text{tot}} + \frac{c\hbar g^2}{4} \sum_{\mathbf{n}} \hat{\Gamma}_{\mathbf{n}} \\ & - \frac{c\hbar}{2a_0 g^2} \sum_{\square} \text{Tr} \left[\begin{bmatrix} -\hat{C}_{\square}^{AA} & \hat{C}_{\square}^{AA} & \hat{C}_{\square}^{BB} & \hat{C}_{\square}^{AB} \\ \hat{C}_{\square}^{AA} & \hat{C}_{\square}^{AA} + \hat{C}_{\square}^{AA} & \hat{C}_{\square}^{AB} & \hat{C}_{\square}^{AB} + \dots \end{bmatrix} + \text{h.c.} \right]. \end{aligned} \quad (1.3.45)$$

Not surprisingly, Eq. (1.3.45) is completely *bosonic*, as all the dressed-site operators are made out of pairs of fermions (matter field + rishon, pairs of matter fields, or rishon pairs). Then, fermionic degrees of freedom are completely hidden inside each dressed site and there is no more need to face anti-commutation rules (see Fig. 1.2(d)).

1.3.5 Hardcore-gluon model: minimally truncated gauge-fields

As an example, we consider the *hardcore-gluon* approximation, corresponding to the smallest non-trivial representations of the gauge fields, obtained truncating the Casimir up to $j_{\text{max}} = \frac{1}{2}$. In analogy to cold quantum gases, the label *hardcore-gluon* aims to stress that the only accessible local configurations are those states reachable from the bare vacuum with at most one application of $\hat{U}^{\alpha\beta}$. Namely, we consider $(0 \otimes 0) \oplus (\frac{1}{2} \otimes \frac{1}{2})$ as the gauge field space, where (j) is the irreducible representation of SU(2) [96, 97, 99, 164, 165]. Such a truncation is enough to guarantee the contribution of all the terms in the Hamiltonian Eqs. (1.3.7) and (1.3.8), and provides a good approximation of the untruncated low energy physics in the strong coupling limit $g \gg 1$, where the gauge field energy term dominates the Hamiltonian. Remarkably, it has been successfully adopted in [2, 4, 143] to extract interesting physics in and out of equilibrium (see Chap. 3 and Sec. 4.4 respectively).

Within the *hardcore-gluon* approximation, the gauge-link Hilbert space reduces to the states $|j, m\rangle$ with $j_{\text{max}} = \frac{1}{2}$. In analogy to the fundamental representation of SU(2), we can parametrize the $m = \pm \frac{1}{2}$ values with the colors *r, g* respectively:

$$\mathcal{H}_{\text{gauge}} = \{|0, 0\rangle, |r, r\rangle, |r, g\rangle, |g, r\rangle, |g, g\rangle\}. \quad (1.3.46)$$

We can then define the corresponding versions of the truncated gauge fields. As for the quadratic Casimir operator in Eq. (1.1.55), we have:

$$\hat{E}^2 = \frac{3}{4} \text{diag}(0 | +1, +1, +1, +1). \quad (1.3.47)$$

Correspondingly, the truncated parallel transport reduces to [160]:

$$\hat{U}^{\alpha\beta} = \frac{1}{\sqrt{2}} \left(\begin{array}{c|cccc} 0 & +\delta_{\alpha r} \delta_{\beta g} & -\delta_{\alpha r} \delta_{\beta r} & +\delta_{\alpha g} \delta_{\beta g} & -\delta_{\alpha g} \delta_{\beta r} \\ \hline -\delta_{\alpha g} \delta_{\beta r} & 0 & 0 & 0 & 0 \\ -\delta_{\alpha g} \delta_{\beta g} & 0 & 0 & 0 & 0 \\ +\delta_{\alpha r} \delta_{\beta r} & 0 & 0 & 0 & 0 \\ +\delta_{\alpha r} \delta_{\beta g} & 0 & 0 & 0 & 0 \end{array} \right), \quad (1.3.48)$$

where the $1/\sqrt{2}$ factor ensures that the hopping term preserves the state norm on its support. Similarly, also the rishon-decomposition in Eq. (1.3.23) can be simplified as follows:

$$\hat{U}_{\mathbf{n},\boldsymbol{\mu}}^{\alpha\beta} = \hat{\zeta}_{\mathbf{n},\boldsymbol{\mu}}^{\alpha} \hat{\zeta}_{\mathbf{n}+\boldsymbol{\mu},-\boldsymbol{\mu}}^{\beta\dagger}, \quad (1.3.49)$$

where $\hat{\zeta}$ -rishons in Eq. (1.3.27) reduce to:

$$\hat{\zeta}_r = \frac{|0\rangle\langle r| + |g\rangle\langle 0|}{\sqrt[4]{2}} = \frac{1}{\sqrt[4]{2}} \left(\begin{array}{c|cc} 0 & 1 & 0 \\ \hline 0 & 0 & 0 \\ 1 & 0 & 0 \end{array} \right)_F, \quad \hat{\zeta}_g = \frac{|0\rangle\langle g| - |r\rangle\langle 0|}{\sqrt[4]{2}} = \frac{1}{\sqrt[4]{2}} \left(\begin{array}{c|cc} 0 & 0 & 1 \\ \hline -1 & 0 & 0 \\ 0 & 0 & 0 \end{array} \right)_F, \quad (1.3.50)$$

with the corresponding parity operator

$$\hat{P}_{\zeta} = +|0\rangle\langle 0| - (|r\rangle\langle r| + |g\rangle\langle g|) = \text{diag}(+1 | -1, -1) \quad (1.3.51)$$

and SU(2) rishon-generators

$$\hat{T}_{1/2}^x = \frac{1}{2} \left(\begin{array}{c|cc} 0 & & \\ \hline & 0 & 1 \\ & 1 & 0 \end{array} \right) \quad \hat{T}_{1/2}^y = \frac{1}{2} \left(\begin{array}{c|cc} 0 & & \\ \hline & 0 & -i \\ & i & 0 \end{array} \right) \quad \hat{T}_{1/2}^z = \frac{1}{2} \left(\begin{array}{c|cc} 0 & & \\ \hline & 1 & 0 \\ & 0 & -1 \end{array} \right). \quad (1.3.52)$$

By definition, the spin-Hilbert space of every side of the link $(\mathbf{n}, \boldsymbol{\mu})$ is 3-dimensional:

$$\mathcal{H}_{\mathbf{n},+\boldsymbol{\mu}} = \{|0\rangle, |r\rangle, |g\rangle\} = \mathcal{H}_{\mathbf{n}+\boldsymbol{\mu},-\boldsymbol{\mu}}. \quad (1.3.53)$$

Correspondingly, the Hilbert space of the whole link $\mathcal{H}_{\text{link}} = \mathcal{H}_{\mathbf{n},+\boldsymbol{\mu}} \otimes \mathcal{H}_{\mathbf{n}+\boldsymbol{\mu},-\boldsymbol{\mu}}$ has 9 states. To recover the original 5-dimensional space in Eq. (1.3.46), we must constrain the left and right rishons on each link to be in the same spin shell j by selecting the even parity sector of a local \mathbb{Z}_2 symmetry defined in Eq. (1.3.36).

(1+1)D hardcore-gluon SU(2) LGT: a qudit model

In one spatial dimension, the Hamiltonian in Eq. (1.3.7) reduces to

$$\hat{H}_{\text{SU}(2)}^{1\text{D}} = \frac{c\hbar}{2a_0} \sum_{\alpha,\beta} \sum_{\mathbf{n}} \left[-i\hat{\psi}_{\mathbf{n},\alpha}^{\dagger} \hat{U}_{\mathbf{n},\boldsymbol{\mu}}^{\alpha\beta} \hat{\psi}_{\mathbf{n}+\boldsymbol{\mu},\beta} + \text{h.c.} \right] + m_0 c^2 \sum_{\mathbf{n},\alpha} (-1)^{\mathbf{n}} \hat{\psi}_{\mathbf{n},\alpha}^{\dagger} \hat{\psi}_{\mathbf{n},\alpha} + \frac{g^2 c\hbar}{2a_0} \sum_{\mathbf{n},\boldsymbol{\mu}} \hat{E}_{\mathbf{n},\boldsymbol{\mu}}^2. \quad (1.3.54)$$

Correspondingly, the dressed-site formalism obtained in the *hardcore-gluon* approximation results in a 6-dimensional local basis [143]:

$$\{|\alpha\rangle = |m_{\text{R}}^{\alpha}(\mathbf{n} - \boldsymbol{\mu}, \mathbf{n}), q^{\alpha}(\mathbf{n}), m_{\text{L}}^{\alpha}(\mathbf{n}, \boldsymbol{\mu})\}_{\alpha=1}^6 \quad (1.3.55)$$

which is made of the following states

$$\begin{aligned} |1\rangle &= |0, 0, 0\rangle, & |2\rangle &= \frac{|r, 0, g\rangle - |g, 0, r\rangle}{\sqrt{2}}, \\ |3\rangle &= \frac{|g, r, 0\rangle - |r, g, 0\rangle}{\sqrt{2}}, & |4\rangle &= \frac{|0, r, g\rangle - |0, g, r\rangle}{\sqrt{2}}, \\ |5\rangle &= |0, 2, 0\rangle, & |6\rangle &= \frac{|r, 2, g\rangle - |g, 2, r\rangle}{\sqrt{2}}. \end{aligned} \quad (1.3.56)$$

Similarly to the procedure in Sec. 1.3.4, the construction of the dressed-site operators and their expression in the 6-dimensional qudit basis in Eq. (1.3.56) follows:

$$\hat{Q}_{\mathbf{n},L} = \hat{Q}_{\mathbf{n},+\mu} = \sum_{\alpha} \hat{\zeta}_{\mathbf{n},+\mu}^{\dagger} \hat{\psi}_{\mathbf{n}} = \sqrt{2} |1\rangle\langle 4| + |2\rangle\langle 3| + |3\rangle\langle 6| + \sqrt{2} |4\rangle\langle 5|, \quad (1.3.57a)$$

$$\hat{Q}_{\mathbf{n},R} = \hat{Q}_{\mathbf{n},-\mu} = -i \sum_{\alpha} \hat{\zeta}_{\mathbf{n},-\mu}^{\dagger} \hat{\psi}_{\mathbf{n}} = \sqrt{2} |1\rangle\langle 3| + |2\rangle\langle 4| + \sqrt{2} |3\rangle\langle 5| + |4\rangle\langle 6|, \quad (1.3.57b)$$

$$\hat{N}_{\mathbf{n}} = \sum_{\alpha} \hat{\psi}_{\mathbf{n},\alpha}^{\dagger} \hat{\psi}_{\mathbf{n},\alpha} = |3\rangle\langle 3| + |4\rangle\langle 4| + 2 |5\rangle\langle 5| + 2 |6\rangle\langle 6|, \quad (1.3.57c)$$

$$\hat{\Gamma}_{\mathbf{n}} = \frac{1}{2} [\hat{E}_{\mathbf{n},+\mu}^2 + \hat{E}_{\mathbf{n},-\mu}^2] = 2 |2\rangle\langle 2| + |3\rangle\langle 3| + |4\rangle\langle 4| + 2 |6\rangle\langle 6|. \quad (1.3.57d)$$

For potential quantum simulation implementations, it is convenient to rewrite Eq. (1.3.54) solely in terms of Hermitian operators, introducing [143]

$$\begin{aligned} \hat{A}^{(1)} &= \hat{Q}_L + \hat{Q}_L^{\dagger}, & \hat{B}^{(1)} &= \hat{Q}_R + \hat{Q}_R^{\dagger}, \\ \hat{A}^{(2)} &= i [\hat{Q}_L - \hat{Q}_L^{\dagger}], & \hat{B}^{(2)} &= i [\hat{Q}_R - \hat{Q}_R^{\dagger}]. \end{aligned} \quad (1.3.58)$$

Noting that $(\hat{A}^{(1)} \otimes \hat{A}^{(1)} + \hat{A}^{(2)} \otimes \hat{A}^{(2)}) = 2(\hat{Q}_L \otimes \hat{Q}_R^{\dagger} + \hat{Q}_L^{\dagger} \otimes \hat{Q}_R)$ Finally, we map Eq. (1.3.54) to the following 6-dimensional qudit Hamiltonian [4]:

$$\hat{H}_{\text{SU}(2)}^{1\text{D}} = \frac{c\hbar}{4a_0} \sum_{\mathbf{n}} \sum_{k \in \{1,2\}} [\hat{A}_{\mathbf{n}}^{(k)} \hat{B}_{\mathbf{n}+\mu}^{(k)}] + m_0 c^2 \sum_{\mathbf{n}} (-1)^{\mathbf{n}} \hat{M}_{\mathbf{n}} + \frac{g^2 c\hbar}{4a_0} \sum_{\mathbf{n},\mu} \hat{\Gamma}_{\mathbf{n}}. \quad (1.3.59)$$

Since the basis in Eq. (1.3.56) is already gauge invariant, the Hamiltonian in Eq. (1.3.59) is tailored for TN simulations as well as to a six-level trapped-ion qudit quantum processor [166]. In [143], the authors discuss the experimental feasibility of using generalized Mølmer-Sørensen gates to efficiently simulate dynamics of Eq. (1.3.59). A shallow circuit with these resources is demonstrated to be sufficient for implementing scalable digital quantum simulations of the model. Numerical simulations of the corresponding dynamics manifest physically-relevant properties specific to non-Abelian field theories, such as baryon excitations [143], and compelling non-ergodic behaviors compatible with quantum many-body scars [4] and detailed in Sec. 4.4.

(2+1)D hardcore-gluon SU(2) LGT

In two spatial dimensions, where the logical site is structured as in Eq. (1.3.38), the previous 6-dimensional dressed-site basis becomes a 30-dimensional Hilbert space. The first 9 states are

combinations of only gauge fields:

$$\begin{aligned}
|0\rangle &= \begin{vmatrix} 0 \\ 0 & 0 & 0 \\ 0 \end{vmatrix} \\
|1\rangle &= \frac{1}{\sqrt{2}} \begin{vmatrix} g \\ 0 & 0 & r \\ 0 \end{vmatrix} - \frac{1}{\sqrt{2}} \begin{vmatrix} r \\ 0 & 0 & g \\ 0 \end{vmatrix} & |2\rangle &= \frac{1}{\sqrt{2}} \begin{vmatrix} g \\ 0 & 0 & 0 \\ r \end{vmatrix} - \frac{1}{\sqrt{2}} \begin{vmatrix} r \\ 0 & 0 & 0 \\ g \end{vmatrix} \\
|3\rangle &= \frac{1}{\sqrt{2}} \begin{vmatrix} g \\ r & 0 & 0 \\ 0 \end{vmatrix} - \frac{1}{\sqrt{2}} \begin{vmatrix} r \\ g & 0 & 0 \\ 0 \end{vmatrix} & |4\rangle &= \frac{1}{\sqrt{2}} \begin{vmatrix} 0 \\ 0 & 0 & g \\ r \end{vmatrix} - \frac{1}{\sqrt{2}} \begin{vmatrix} 0 \\ 0 & 0 & r \\ g \end{vmatrix} \\
|5\rangle &= \frac{1}{\sqrt{2}} \begin{vmatrix} 0 \\ r & 0 & g \\ 0 \end{vmatrix} - \frac{1}{\sqrt{2}} \begin{vmatrix} 0 \\ g & 0 & r \\ 0 \end{vmatrix} & |6\rangle &= \frac{1}{\sqrt{2}} \begin{vmatrix} 0 \\ r & 0 & 0 \\ g \end{vmatrix} - \frac{1}{\sqrt{2}} \begin{vmatrix} 0 \\ g & 0 & 0 \\ r \end{vmatrix} \\
|7\rangle &= \frac{1}{2} \left[\begin{vmatrix} g \\ r & 0 & r \\ g \end{vmatrix} - \begin{vmatrix} r \\ r & 0 & g \\ g \end{vmatrix} + \begin{vmatrix} g \\ g & 0 & r \\ r \end{vmatrix} + \begin{vmatrix} r \\ g & 0 & g \\ r \end{vmatrix} \right] \\
|8\rangle &= \frac{1}{2\sqrt{3}} \left[2 \begin{vmatrix} g \\ r & 0 & g \\ r \end{vmatrix} - \begin{vmatrix} g \\ r & 0 & r \\ g \end{vmatrix} - \begin{vmatrix} r \\ r & 0 & g \\ g \end{vmatrix} - \begin{vmatrix} g \\ g & 0 & r \\ r \end{vmatrix} - \begin{vmatrix} r \\ g & 0 & g \\ r \end{vmatrix} + 2 \begin{vmatrix} r \\ g & 0 & r \\ g \end{vmatrix} \right],
\end{aligned} \tag{1.3.60}$$

Then, 12 states including single-occupied matter sites and gauge fields:

$$\begin{aligned}
|9\rangle &= \frac{1}{\sqrt{2}} \begin{vmatrix} g \\ 0 & r & 0 \\ 0 \end{vmatrix} - \frac{1}{\sqrt{2}} \begin{vmatrix} r \\ 0 & g & 0 \\ 0 \end{vmatrix} & |10\rangle &= \frac{1}{\sqrt{2}} \begin{vmatrix} 0 \\ 0 & r & g \\ 0 \end{vmatrix} - \frac{1}{\sqrt{2}} \begin{vmatrix} 0 \\ 0 & g & r \\ 0 \end{vmatrix} \\
|11\rangle &= \frac{1}{\sqrt{2}} \begin{vmatrix} 0 \\ 0 & r & 0 \\ g \end{vmatrix} - \frac{1}{\sqrt{2}} \begin{vmatrix} 0 \\ 0 & g & 0 \\ r \end{vmatrix} & |14\rangle &= \frac{1}{\sqrt{2}} \begin{vmatrix} 0 \\ g & r & 0 \\ 0 \end{vmatrix} - \frac{1}{\sqrt{2}} \begin{vmatrix} 0 \\ r & g & 0 \\ 0 \end{vmatrix} \\
|12\rangle &= \frac{1}{2} \left[\begin{vmatrix} g \\ 0 & r & r \\ g \end{vmatrix} - \begin{vmatrix} r \\ 0 & r & g \\ g \end{vmatrix} + \begin{vmatrix} g \\ 0 & g & r \\ r \end{vmatrix} + \begin{vmatrix} r \\ 0 & g & g \\ r \end{vmatrix} \right] \\
|13\rangle &= \frac{1}{2\sqrt{3}} \left[2 \begin{vmatrix} g \\ 0 & r & g \\ r \end{vmatrix} - \begin{vmatrix} g \\ 0 & r & r \\ g \end{vmatrix} - \begin{vmatrix} r \\ 0 & r & g \\ g \end{vmatrix} - \begin{vmatrix} g \\ 0 & g & r \\ r \end{vmatrix} - \begin{vmatrix} r \\ 0 & g & g \\ r \end{vmatrix} + 2 \begin{vmatrix} r \\ 0 & g & r \\ g \end{vmatrix} \right] \\
|15\rangle &= \frac{1}{2} \left[\begin{vmatrix} g \\ g & r & r \\ 0 \end{vmatrix} - \begin{vmatrix} r \\ g & r & g \\ 0 \end{vmatrix} + \begin{vmatrix} g \\ r & g & r \\ 0 \end{vmatrix} + \begin{vmatrix} r \\ r & g & g \\ 0 \end{vmatrix} \right] \\
|16\rangle &= \frac{1}{2\sqrt{3}} \left[2 \begin{vmatrix} g \\ r & r & g \\ 0 \end{vmatrix} - \begin{vmatrix} g \\ g & r & r \\ 0 \end{vmatrix} - \begin{vmatrix} r \\ g & r & g \\ 0 \end{vmatrix} - \begin{vmatrix} g \\ r & g & r \\ 0 \end{vmatrix} - \begin{vmatrix} r \\ r & g & g \\ 0 \end{vmatrix} + 2 \begin{vmatrix} r \\ g & g & r \\ 0 \end{vmatrix} \right] \\
|17\rangle &= \frac{1}{2} \left[\begin{vmatrix} g \\ g & r & 0 \\ r \end{vmatrix} - \begin{vmatrix} r \\ g & r & 0 \\ g \end{vmatrix} + \begin{vmatrix} g \\ r & g & 0 \\ r \end{vmatrix} + \begin{vmatrix} r \\ r & g & 0 \\ g \end{vmatrix} \right] \\
|18\rangle &= \frac{1}{2\sqrt{3}} \left[2 \begin{vmatrix} g \\ r & r & 0 \\ g \end{vmatrix} - \begin{vmatrix} g \\ g & r & 0 \\ r \end{vmatrix} - \begin{vmatrix} r \\ g & r & 0 \\ g \end{vmatrix} - \begin{vmatrix} g \\ r & g & 0 \\ r \end{vmatrix} - \begin{vmatrix} r \\ r & g & 0 \\ g \end{vmatrix} + 2 \begin{vmatrix} r \\ g & g & 0 \\ r \end{vmatrix} \right] \\
|19\rangle &= \frac{1}{2} \left[\begin{vmatrix} 0 \\ g & r & g \\ r \end{vmatrix} - \begin{vmatrix} 0 \\ g & r & r \\ g \end{vmatrix} + \begin{vmatrix} 0 \\ r & g & g \\ r \end{vmatrix} + \begin{vmatrix} 0 \\ r & g & r \\ g \end{vmatrix} \right] \\
|20\rangle &= \frac{1}{2\sqrt{3}} \left[2 \begin{vmatrix} 0 \\ r & r & g \\ g \end{vmatrix} - \begin{vmatrix} 0 \\ g & r & g \\ r \end{vmatrix} - \begin{vmatrix} 0 \\ g & r & r \\ g \end{vmatrix} - \begin{vmatrix} 0 \\ r & g & g \\ r \end{vmatrix} - \begin{vmatrix} 0 \\ r & g & r \\ g \end{vmatrix} + 2 \begin{vmatrix} 0 \\ g & g & r \\ r \end{vmatrix} \right],
\end{aligned} \tag{1.3.61}$$

and finally 9 states with double-occupied matter sites coupled to gauge d.o.f.:

$$\begin{aligned}
|21\rangle &= \begin{vmatrix} 0 \\ 0 & 2 & 0 \\ 0 \end{vmatrix} \\
|22\rangle &= \frac{1}{\sqrt{2}} \begin{vmatrix} g \\ 0 & 2 & r \\ 0 \end{vmatrix} - \frac{1}{\sqrt{2}} \begin{vmatrix} r \\ 0 & 2 & g \\ 0 \end{vmatrix} & |23\rangle &= \frac{1}{\sqrt{2}} \begin{vmatrix} g \\ 0 & 2 & 0 \\ r \end{vmatrix} - \frac{1}{\sqrt{2}} \begin{vmatrix} r \\ 0 & 2 & 0 \\ g \end{vmatrix} \\
|24\rangle &= \frac{1}{\sqrt{2}} \begin{vmatrix} g \\ r & 2 & 0 \\ 0 \end{vmatrix} - \frac{1}{\sqrt{2}} \begin{vmatrix} r \\ g & 2 & 0 \\ 0 \end{vmatrix} & |25\rangle &= \frac{1}{\sqrt{2}} \begin{vmatrix} 0 \\ 0 & 2 & g \\ r \end{vmatrix} - \frac{1}{\sqrt{2}} \begin{vmatrix} 0 \\ 0 & 2 & r \\ g \end{vmatrix} \\
|26\rangle &= \frac{1}{\sqrt{2}} \begin{vmatrix} 0 \\ r & 2 & g \\ 0 \end{vmatrix} - \frac{1}{\sqrt{2}} \begin{vmatrix} 0 \\ g & 2 & r \\ 0 \end{vmatrix} & |27\rangle &= \frac{1}{\sqrt{2}} \begin{vmatrix} 0 \\ r & 2 & 0 \\ g \end{vmatrix} - \frac{1}{\sqrt{2}} \begin{vmatrix} 0 \\ g & 2 & 0 \\ r \end{vmatrix} \\
|28\rangle &= \frac{1}{2} \left[\begin{vmatrix} g \\ r & 2 & r \\ g \end{vmatrix} - \begin{vmatrix} r \\ r & 2 & g \\ g \end{vmatrix} + \begin{vmatrix} g \\ g & 2 & r \\ r \end{vmatrix} + \begin{vmatrix} r \\ g & 2 & g \\ r \end{vmatrix} \right] \\
|29\rangle &= \frac{1}{2\sqrt{3}} \left[2 \begin{vmatrix} g \\ r & 2 & g \\ r \end{vmatrix} - \begin{vmatrix} g \\ r & 2 & r \\ g \end{vmatrix} - \begin{vmatrix} r \\ r & 2 & g \\ g \end{vmatrix} - \begin{vmatrix} g \\ g & 2 & r \\ r \end{vmatrix} - \begin{vmatrix} r \\ g & 2 & g \\ r \end{vmatrix} + 2 \begin{vmatrix} r \\ g & 2 & r \\ g \end{vmatrix} \right].
\end{aligned} \tag{1.3.62}$$

The resulting dressed-site basis of Eqs. (1.3.60) to (1.3.62) is adopted in the simulations of [2] and detailed in Chap. 3.

1.4 U(1) Lattice Gauge Theory

In this section, we apply the dressed-site formalism developed in Sec. 1.2 to an Abelian scenario, focusing on the U(1) LGT including dynamical matter, i.e. the lattice realization of quantum-electrodynamics (QED). Again, for simplicity we will consider a (2+1)D system, where all the gauge (electric and magnetic) contributions play a non-trivial role.

1.4.1 The model

Within the Wilson and Kogut-Susskind formulation of LGTs [14, 144], the U(1) version of the general Hamiltonian in Eq. (1.1.65) reads:

$$\begin{aligned}
H_{U(1)} &= \frac{c\hbar}{2a_0} \sum_{\mathbf{n}} \left[-i\hat{\psi}_{\mathbf{n}}^\dagger \hat{U}_{\mathbf{n},\mu_x} \hat{\psi}_{\mathbf{n}+\mu_x} - (-1)^{n_x+n_y} \hat{\psi}_{\mathbf{n}} \hat{U}_{\mathbf{n},\mu_y} \hat{\psi}_{\mathbf{n}+\mu_y} + \text{h.c.} \right] \\
&\quad + m_0 c^2 \sum_{\mathbf{n}} (-1)^{\mathbf{n}} \hat{\psi}_{\mathbf{n}}^\dagger \hat{\psi}_{\mathbf{n}} + \frac{g^2 c\hbar}{2a_0} \sum_{\mathbf{n},\mu} \hat{E}_{\mathbf{n},\mu}^2 - \frac{c\hbar}{2g^2 a_0} \sum_{\square} \text{Tr}(\hat{U}_{\square} + \hat{U}_{\square}^\dagger),
\end{aligned} \tag{1.4.1}$$

where, since there is only one generator, the electric field is unique $\hat{L} = \hat{R} = \hat{E}$ and the parallel transporter acts as a raising operator:

$$\left[\hat{U}, \hat{E} \right] = \hat{U} \quad \hat{U}^\dagger \hat{U} = \mathbb{1} \quad \left[\hat{U}, \hat{U}^\dagger \right] = 0. \tag{1.4.2}$$

In the electric basis representation, where \hat{E} is diagonal, Eq. (1.4.2) can be obtained assuming the following behaviors: given the $|\ell\rangle$ electric state of the gauge link Hilbert space,

$$\begin{cases} \hat{E} |\ell\rangle = \ell |\ell\rangle \\ \hat{U} |\ell\rangle = |\ell-1\rangle \\ \hat{U}^\dagger |\ell\rangle = |\ell+1\rangle \end{cases} \quad \text{so that} \quad \begin{cases} \hat{E} \hat{U} |\ell\rangle = (\ell-1) |\ell-1\rangle \\ \hat{U} \hat{E} |\ell\rangle = \ell |\ell-1\rangle \end{cases}. \tag{1.4.3}$$

Correspondingly, U(1) Gauss law requires that $G_{\mathbf{n}} |\Psi_{\text{phys}}\rangle = 0 \forall \mathbf{n}$, where $G_{\mathbf{n}}$ is the local generator of the U(1) gauge symmetry, satisfies $[G_{\mathbf{n}}, \hat{H}] = 0$, and is defined as follows:

$$\hat{G}_{\mathbf{n}} = \hat{E}_{\mathbf{n},\mu} - \hat{E}_{\mathbf{n}-\mu,\mu} - \psi_{\mathbf{n}}^\dagger \psi_{\mathbf{n}} + \frac{1 - (-1)^{\mathbf{n}}}{2}. \quad (1.4.4)$$

1.4.2 Truncating the U(1) gauge group

To perform numerical simulations of Eq. (1.4.1), we need to perform a truncation of the infinite algebra of the U(1) gauge fields. As discussed in Sec. 1.2.1, one possible solution is to express the gauge operators \hat{E} and \hat{U} directly in terms of spin operators in the j representation of SU(2):

$$\hat{E} = \hat{S}^z(j) \quad \hat{U} = \frac{1}{j} \hat{S}^-(j). \quad (1.4.5)$$

Correspondingly, the gauge link Hilbert space $\mathcal{H}_{\text{link}}$ is made out of $(2j + 1)$ states $|\ell\rangle$, which can be labeled as $|j, m\rangle$, where $-j \leq m \leq j$ is the third component of the spin momentum j . According to the rules of angular momentum summation, we would have:

$$\begin{cases} \hat{E} |j, m\rangle = S^z |j, m\rangle = m |j, m\rangle \\ \hat{U} |j, m\rangle = \frac{S^-}{j} |j, m\rangle = \sqrt{(1 - \frac{1}{j}) - \frac{m}{j^2}(m-1)} |j, m-1\rangle \\ \hat{U}^\dagger |j, m\rangle = \frac{S^+}{j} |j, m\rangle = \sqrt{(1 + \frac{1}{j}) - \frac{m}{j^2}(m+1)} |j, m+1\rangle, \end{cases} \quad (1.4.6)$$

which yields to the following commutation relations:

$$\begin{aligned} [\hat{U}, \hat{E}] &= \frac{1}{j} [\hat{S}^-(j), \hat{S}^z(j)] = \frac{\hat{S}^-(j)}{j} = \hat{U} \\ [\hat{U}, \hat{U}^\dagger] &= \frac{1}{j^2} [\hat{S}^-(j), \hat{S}^+(j)] = -\frac{2\hat{S}^z(j)}{j^2} \xrightarrow{j \rightarrow \infty} 0. \end{aligned} \quad (1.4.7)$$

Such a definition of parallel transport provides a uniform convergence to Eq. (1.4.2) in the large- j limit. Similarly, we can define $\hat{U} = \text{diag}_{-1}(+1, \dots, +1)$ as a ladder operator, which is perfectly unitary in the core, yet badly converges in the (upper and lower) truncated states. In the limit of $j \rightarrow \infty$, both solutions recover Eq. (1.4.3). As we will discuss in Sec. 1.4.5, the error induced by the truncation is particularly relevant in the small coupling limit, while remaining negligible in most scenarios [46, 112]. Choosing the ladder operator can reveal optimal for qubit base quantum hardware [167], while Eq. (1.4.5) is preferable in case of quantum systems that allow for the implementation of interacting spin chains with large spins [168]. For completeness, we mention that there are mappings of the parallel transporter preserving unitarity [169–172].

1.4.3 Rishon decomposition of U(1) gauge fields

The next step towards the dressed-site formalism is decomposing the $(2j + 1)$ states of the link basis as a combination of two states, one per half-link: $|j, m\rangle_{\mathbf{n},\mu} = |j, m_{\mathbf{n},+\mu}, m_{\mathbf{n},+\mu,-\mu}\rangle$. Omitting the j -label, the truncated link Hilbert space reads:

$$\mathcal{H}_j = \{|+j, -j\rangle, |+j-1, -j+1\rangle, \dots, |m, m\rangle, \dots, |-j+1, +j-1\rangle, |-j, +j\rangle\}. \quad (1.4.8)$$

In the Euclidean basis, these gauge link states would read:

$$|+j, -j\rangle = \begin{pmatrix} 1 \\ 0 \\ \vdots \\ 0 \\ 0 \end{pmatrix} \quad |+j-1, -j+1\rangle = \begin{pmatrix} 0 \\ 1 \\ \vdots \\ 0 \\ 0 \end{pmatrix} \quad \dots \quad |-j+1, +j-1\rangle = \begin{pmatrix} 0 \\ 0 \\ \vdots \\ 1 \\ 0 \end{pmatrix} \quad |-j, +j\rangle = \begin{pmatrix} 0 \\ 0 \\ \vdots \\ 0 \\ 1 \end{pmatrix} \quad (1.4.9)$$

Then, we express the parallel transport \hat{U} as the product of two rishon modes $\hat{\zeta}_L$ and $\hat{\zeta}_R$:

$$\hat{U}_{\mathbf{n}, \boldsymbol{\mu}} = \hat{\zeta}_{A, \mathbf{n}} \hat{\zeta}_{B, \mathbf{n} + \boldsymbol{\mu}, -\boldsymbol{\mu}}^\dagger \quad (1.4.10)$$

where, in full generality, we assumed the two rishon modes of the $(\mathbf{n}, \boldsymbol{\mu})$ -link to belong to two different species, A and B³. A general definition for the rishon operators is

$$\hat{\zeta}_A = \begin{pmatrix} 0 & a_1 & & & \\ & 0 & a_2 & & \\ & & 0 & a_3 & \\ & & & & \ddots \\ & & & 0 & \ddots \end{pmatrix}_F \quad \hat{\zeta}_B = \begin{pmatrix} 0 & b_1 & & & \\ & 0 & b_2 & & \\ & & 0 & b_3 & \\ & & & & \ddots \\ & & & 0 & \ddots \end{pmatrix}_F, \quad (1.4.11)$$

where $\{a_i\}_{i=1\dots 2s}$ and $\{b_i\}_{i=1\dots 2s}$ are complex numbers to be determined in the specific spin- s representation of $U(1)$. To obtain an operative Hamiltonian that is fully bosonic in every term, we require the rishon modes to satisfy a fermionic algebra. Namely, $\hat{\zeta}$ -rishons must anti-commute among themselves and with matter fields:

$$\{\hat{\zeta}_{A, \mathbf{n}, \boldsymbol{\mu}}, \hat{\zeta}_{B, \mathbf{n} + \boldsymbol{\mu}, -\boldsymbol{\mu}}\} = 0 \quad \{\hat{\zeta}_{\mathbf{n}, \boldsymbol{\mu}}, \hat{\psi}_{\mathbf{n}}\} = 0. \quad (1.4.12)$$

Being fermions, $\hat{\zeta}$ -rishon must also satisfy (1.2.7). We define the rishon parity operator as

$$P_{\hat{\zeta}}^{U(1)} = \text{diag}(+1, -1, +1, -1, \dots), \quad (1.4.13)$$

where by convention we establish the first rishon state to be *even*, while the remaining ones are determined by alternating the sign of parity. Then, the last state is even (odd) if the spin- j representation is *integer* (*semi-integer*).

We can then properly express the parallel transport in (1.4.10) as follows:

$$\begin{aligned} \hat{U}_{\mathbf{n}, \boldsymbol{\mu}} &= \hat{\zeta}_{A, \mathbf{n}, +\boldsymbol{\mu}} \hat{\zeta}_{B, \mathbf{n} + \boldsymbol{\mu}, -\boldsymbol{\mu}}^\dagger = \left[\hat{\zeta}_{A, \mathbf{n}, +\boldsymbol{\mu}} \otimes \mathbb{1}_{\mathbf{n} + \boldsymbol{\mu}, -\boldsymbol{\mu}} \right] \times \left[\hat{P}_{\zeta, \mathbf{n}, +\boldsymbol{\mu}} \otimes \hat{\zeta}_{B, \mathbf{n} + \boldsymbol{\mu}, -\boldsymbol{\mu}}^\dagger \right] \\ &= \hat{\zeta}_{A, \mathbf{n}, +\boldsymbol{\mu}} \cdot \hat{P}_{\zeta, \mathbf{n}, +\boldsymbol{\mu}} \otimes \hat{\zeta}_{B, \mathbf{n} + \boldsymbol{\mu}, -\boldsymbol{\mu}}^\dagger \\ &= \begin{pmatrix} 0 & -a_1 & & & \\ & 0 & +a_2 & & \\ & & 0 & -a_3 & \\ & & & & \ddots \\ & & & & \ddots \end{pmatrix}_{\mathbf{n}} \otimes \begin{pmatrix} 0 & & & & \\ \bar{b}_1 & 0 & & & \\ & \bar{b}_2 & 0 & & \\ & & \bar{b}_3 & 0 & \\ & & & & \ddots \\ & & & & \ddots \end{pmatrix}_{\mathbf{n} + \boldsymbol{\mu}}. \end{aligned} \quad (1.4.14)$$

The correct matrix elements $\{a_i\}_{i=1\dots 2j_{\max}}$ and $\{b_i\}_{i=1\dots 2j_{\max}}$ of the two $\hat{\zeta}$ -rishon modes in the specific spin- j_{\max} representation for $U(1)$ are the ones matching the original choice of the parallel transporter (spin operator as in Eq. (1.4.5) or ladder operator).

³It is possible to prove that, in *semi-integer* spin-representations, the two species coincide.

Example: spin-1 representation of U(1)

As an example, we derive the expression of the gauge fields (in terms of rishons) for the $j = 1$ -spin representation. Such a truncation is the smallest non-trivial *integer* representation that gives access to non trivial features of the U(1) LGT [87, 90, 173].

Within this truncation, the gauge fields read:

$$\hat{E} = \hat{S}^z = \begin{pmatrix} +1 & & \\ & 0 & \\ & & -1 \end{pmatrix} \quad \hat{U} = \hat{S}^- = \sqrt{2} \begin{pmatrix} 0 & & \\ 1 & 0 & \\ & 1 & 0 \end{pmatrix}. \quad (1.4.15)$$

The corresponding link Hilbert space $\mathcal{H}^{j=1}$ defined in (1.4.9) is made out of the following states:

$$|1, 1\rangle = \begin{pmatrix} 1 \\ 0 \\ 0 \end{pmatrix} \quad |0, 0\rangle = \begin{pmatrix} 0 \\ 1 \\ 0 \end{pmatrix} \quad |-1, -1\rangle = \begin{pmatrix} 0 \\ 0 \\ 1 \end{pmatrix}. \quad (1.4.16)$$

Then, from the definition of \hat{U} in (1.4.15), the only relevant matrix elements of $\hat{\zeta}_A \hat{\zeta}_B^\dagger$ are the ones that correspond to the action on sites belonging to (1.4.9):

$$\begin{aligned} \hat{\zeta}_A \hat{\zeta}_B^\dagger |1, 1\rangle &= +a_2 \bar{b}_1 |0, 0\rangle \\ \hat{\zeta}_A \hat{\zeta}_B^\dagger |0, 0\rangle &= -a_1 \bar{b}_2 |-1, -1\rangle \\ \hat{\zeta}_A \hat{\zeta}_B^\dagger |-1, -1\rangle &= 0 \end{aligned} \quad \text{whose solution could be} \quad \begin{aligned} a_1 &= a_2 = 1 \\ b_1 &= +\sqrt{2} = -b_2. \end{aligned} \quad (1.4.17)$$

Summarizing, we have found

$$\hat{\zeta}_A = \begin{pmatrix} 0 & +1 & \\ & 0 & +1 \\ & & 0 \end{pmatrix} \quad \hat{\zeta}_B = \begin{pmatrix} 0 & +\sqrt{2} & \\ & 0 & -\sqrt{2} \\ & & 0 \end{pmatrix}. \quad (1.4.18)$$

Notice that, by using the ladder definition for the parallel transporter, the two rishons read:

$$\hat{\zeta}'_A = \begin{pmatrix} 0 & +1 & \\ & 0 & +1 \\ & & 0 \end{pmatrix}_F \quad \hat{\zeta}'_B = \begin{pmatrix} 0 & +1 & \\ & 0 & -1 \\ & & 0 \end{pmatrix}_F. \quad (1.4.19)$$

1.4.4 Constructing the dressed-site operators

We stress that the rishon decomposition is a general approach and can be applied to lattices of whatever dimension D . However, as discussed for SU(2), for a fixed D , the construction of the Hamiltonian operators requires attention in choosing an internal ordering of the dressed-site basis. Working in a $D = 2$ -dimensional lattice, the single dressed-site basis can be sketched as:

$$\left| \begin{array}{ccc} \hat{\zeta}_{A,\mathbf{n},+\mu_y} & & \\ \hat{\zeta}_{B,\mathbf{n},-\mu_x} & \psi_{\mathbf{n}} & \hat{\zeta}_{A,\mathbf{n},+\mu_x} \\ & \hat{\zeta}_{B,\mathbf{n},-\mu_y} & \end{array} \right\rangle \quad \text{where the d.o.f. are ordered as:} \quad \left| \begin{array}{ccc} 4 & & \\ 1 & 0 & 3 \\ & 2 & \end{array} \right\rangle. \quad (1.4.20)$$

Every dressed-site operator is then constructed as in (1.2.6) according to the previous order. We are then ready to express each Hamiltonian term in terms of dressed-site operators.

Hopping operators In the hopping Hamiltonian, the matter-gauge interaction (apart from the staggered factors) along the link $(\mathbf{n}, \boldsymbol{\mu})$ can be rewritten in terms of two bosonic *arrival* operators. Namely

$$\begin{aligned}\hat{H}_{\mathbf{n}, \boldsymbol{\mu}}^{\text{hopping}} &= \left[\hat{\psi}_{\mathbf{n}}^\dagger \hat{U}_{\mathbf{n}, \boldsymbol{\mu}} \hat{\psi}_{\mathbf{n}+\boldsymbol{\mu}} + \text{h.c.} \right] \\ &= \left[\hat{\psi}_{\mathbf{n}}^\dagger \hat{\zeta}_{A, \mathbf{n}+\boldsymbol{\mu}} \hat{\zeta}_{B, \mathbf{n}+\boldsymbol{\mu}, -\boldsymbol{\mu}}^\dagger \hat{\psi}_{\mathbf{n}+\boldsymbol{\mu}} + \text{h.c.} \right] \quad \text{where} \quad \begin{aligned} \hat{Q}_{\mathbf{n}, +\boldsymbol{\mu}}^\dagger &= \hat{\psi}_{\mathbf{n}}^\dagger \hat{\zeta}_{A, \mathbf{n}+\boldsymbol{\mu}} \\ \hat{Q}_{\mathbf{n}, -\boldsymbol{\mu}}^\dagger &= \hat{\psi}_{\mathbf{n}}^\dagger \hat{\zeta}_{B, \mathbf{n}, -\boldsymbol{\mu}} \end{aligned} \\ &= \left[\hat{Q}_{\mathbf{n}, +\boldsymbol{\mu}}^\dagger \hat{Q}_{\mathbf{n}+\boldsymbol{\mu}, -\boldsymbol{\mu}} + \text{h.c.} \right]\end{aligned}\tag{1.4.21}$$

Then, according to the internal ordering of dressed site defined in (1.4.20), we have for instance:

$$\begin{aligned}\hat{Q}_{\mathbf{n}, +\boldsymbol{\mu}_x}^\dagger &= \hat{\psi}_{\mathbf{n}}^\dagger \hat{\zeta}_{A, \mathbf{n}+\boldsymbol{\mu}_x} = \hat{\psi}_{\mathbf{n}}^\dagger \otimes \mathbb{1}_{\mathbf{n}, -\boldsymbol{\mu}_x} \otimes \mathbb{1}_{\mathbf{n}, -\boldsymbol{\mu}_y} \otimes \mathbb{1}_{\mathbf{n}, +\boldsymbol{\mu}_x} \otimes \mathbb{1}_{\mathbf{n}, +\boldsymbol{\mu}_y} \\ &\quad \times \hat{P}_{\psi, \mathbf{n}} \otimes \hat{P}_{\hat{\zeta}, \mathbf{n}, -\boldsymbol{\mu}_x} \otimes \hat{P}_{\hat{\zeta}, \mathbf{n}, -\boldsymbol{\mu}_y} \otimes \hat{\zeta}_{A, \mathbf{n}+\boldsymbol{\mu}_x} \otimes \mathbb{1}_{\mathbf{n}, +\boldsymbol{\mu}_y} \\ &= \hat{\psi}_{\mathbf{n}}^\dagger \cdot \hat{P}_{\psi, \mathbf{n}} \otimes \hat{P}_{\hat{\zeta}, \mathbf{n}, -\boldsymbol{\mu}_x} \otimes \hat{P}_{\hat{\zeta}, \mathbf{n}, -\boldsymbol{\mu}_y} \otimes \hat{\zeta}_{A, \mathbf{n}+\boldsymbol{\mu}_x} \otimes \mathbb{1}_{\mathbf{n}, +\boldsymbol{\mu}_y}.\end{aligned}\tag{1.4.22}$$

Number density operators Similarly, number density operators can be expressed as:

$$\hat{N}_{\mathbf{n}} = \hat{\psi}_{\mathbf{n}}^\dagger \hat{\psi}_{\mathbf{n}} = \hat{\psi}_{\mathbf{n}}^\dagger \cdot \hat{\psi}_{\mathbf{n}} \bigotimes_{\pm \boldsymbol{\mu}} \mathbb{1}_{\mathbf{n}, \boldsymbol{\mu}}.\tag{1.4.23}$$

Magnetic operators Let us rewrite the single plaquette interaction in terms of rishon modes. The idea is to perform a series of fermionic swaps to make the rishons of the same dressed site close in the internal ordering of the plaquette. We have then:

$$\begin{aligned}\hat{U}_{\square} &= \left[\hat{U}_{\mathbf{n}, \boldsymbol{\mu}_x} \hat{U}_{\mathbf{n}+\boldsymbol{\mu}_x, +\boldsymbol{\mu}_y} \hat{U}_{\mathbf{n}+\boldsymbol{\mu}_y, +\boldsymbol{\mu}_x}^\dagger \hat{U}_{\mathbf{n}, \boldsymbol{\mu}_y}^\dagger \right] \\ &= \left[\left(\hat{\zeta}_{A, \mathbf{n}+\boldsymbol{\mu}_x} \hat{\zeta}_{B, \mathbf{n}+\boldsymbol{\mu}_x, -\boldsymbol{\mu}_x}^\dagger \right) \left(\hat{\zeta}_{A, \mathbf{n}+\boldsymbol{\mu}_x, +\boldsymbol{\mu}_y} \hat{\zeta}_{B, \mathbf{n}+\boldsymbol{\mu}_x+\boldsymbol{\mu}_y, -\boldsymbol{\mu}_y}^\dagger \right) \times \right. \\ &\quad \left. \left(\hat{\zeta}_{A, \mathbf{n}+\boldsymbol{\mu}_y, +\boldsymbol{\mu}_x} \hat{\zeta}_{B, \mathbf{n}+\boldsymbol{\mu}_x+\boldsymbol{\mu}_y, -\boldsymbol{\mu}_x}^\dagger \right) \left(\hat{\zeta}_{A, \mathbf{n}, +\boldsymbol{\mu}_y} \hat{\zeta}_{B, \mathbf{n}+\boldsymbol{\mu}_y, -\boldsymbol{\mu}_y}^\dagger \right) \right] \\ &= \left[\left(\hat{\zeta}_{A, \mathbf{n}+\boldsymbol{\mu}_x} \hat{\zeta}_{B, \mathbf{n}+\boldsymbol{\mu}_x, -\boldsymbol{\mu}_x}^\dagger \right) \left(\hat{\zeta}_{A, \mathbf{n}+\boldsymbol{\mu}_x, +\boldsymbol{\mu}_y} \hat{\zeta}_{B, \mathbf{n}+\boldsymbol{\mu}_x+\boldsymbol{\mu}_y, -\boldsymbol{\mu}_y}^\dagger \right) \times \right. \\ &\quad \left. \left(\hat{\zeta}_{B, \mathbf{n}+\boldsymbol{\mu}_x+\boldsymbol{\mu}_y, -\boldsymbol{\mu}_x} \hat{\zeta}_{A, \mathbf{n}+\boldsymbol{\mu}_y, +\boldsymbol{\mu}_x}^\dagger \right) \left(\hat{\zeta}_{B, \mathbf{n}+\boldsymbol{\mu}_y, -\boldsymbol{\mu}_y} \hat{\zeta}_{A, \mathbf{n}, +\boldsymbol{\mu}_y}^\dagger \right) \right] \\ &= \left[\left(\hat{\zeta}_{A, \mathbf{n}+\boldsymbol{\mu}_x} \hat{\zeta}_{A, \mathbf{n}, +\boldsymbol{\mu}_y}^\dagger \right) \left(\hat{\zeta}_{B, \mathbf{n}+\boldsymbol{\mu}_x, -\boldsymbol{\mu}_x} \hat{\zeta}_{A, \mathbf{n}+\boldsymbol{\mu}_x, +\boldsymbol{\mu}_y}^\dagger \right) \times \right. \\ &\quad \left. \left(\hat{\zeta}_{B, \mathbf{n}+\boldsymbol{\mu}_x+\boldsymbol{\mu}_y, -\boldsymbol{\mu}_y} \hat{\zeta}_{B, \mathbf{n}+\boldsymbol{\mu}_x+\boldsymbol{\mu}_y, -\boldsymbol{\mu}_x}^\dagger \right) \left(\hat{\zeta}_{A, \mathbf{n}+\boldsymbol{\mu}_y, +\boldsymbol{\mu}_x} \hat{\zeta}_{B, \mathbf{n}+\boldsymbol{\mu}_y, -\boldsymbol{\mu}_y}^\dagger \right) \right] \\ &= \left[-\hat{C}_{\mathbf{n}, +\boldsymbol{\mu}_x, +\boldsymbol{\mu}_y} \hat{C}_{\mathbf{n}+\boldsymbol{\mu}_x, +\boldsymbol{\mu}_y, -\boldsymbol{\mu}_x} \hat{C}_{\mathbf{n}+\boldsymbol{\mu}_x+\boldsymbol{\mu}_y, -\boldsymbol{\mu}_x, -\boldsymbol{\mu}_y} \hat{C}_{\mathbf{n}+\boldsymbol{\mu}_y, -\boldsymbol{\mu}_y, +\boldsymbol{\mu}_x} \right],\end{aligned}\tag{1.4.24}$$

where we merged rishon modes belonging to the same dressed site into *corner* operators defined as $\hat{C}_{\mathbf{n}, \boldsymbol{\mu}_1, \boldsymbol{\mu}_2} = \hat{\zeta}_{\mathbf{n}, \boldsymbol{\mu}_1} \hat{\zeta}_{\mathbf{n}, \boldsymbol{\mu}_2}^\dagger$. For instance, from the internal order of the dressed-site basis in (1.4.20), we have for instance:

$$\begin{aligned}\hat{C}_{\mathbf{n}, -\boldsymbol{\mu}_y, +\boldsymbol{\mu}_x} &= \hat{\zeta}_{B, \mathbf{n}, -\boldsymbol{\mu}_y} \hat{\zeta}_{A, \mathbf{n}, +\boldsymbol{\mu}_x}^\dagger \\ &= \hat{P}_{\psi, \mathbf{n}} \otimes \hat{P}_{\hat{\zeta}, \mathbf{n}, -\boldsymbol{\mu}_x} \otimes \hat{\zeta}_{B, \mathbf{n}, -\boldsymbol{\mu}_y} \otimes \mathbb{1}_{\mathbf{n}, +\boldsymbol{\mu}_x} \otimes \mathbb{1}_{\mathbf{n}, +\boldsymbol{\mu}_y} \\ &= \times \hat{P}_{\psi, \mathbf{n}} \otimes \hat{P}_{\hat{\zeta}, \mathbf{n}, -\boldsymbol{\mu}_x} \otimes \hat{P}_{\hat{\zeta}, \mathbf{n}, -\boldsymbol{\mu}_y} \otimes \hat{\zeta}_{A, \mathbf{n}, +\boldsymbol{\mu}_x}^\dagger \otimes \mathbb{1}_{\mathbf{n}, +\boldsymbol{\mu}_y} \\ &= \mathbb{1}_{\mathbf{n}} \otimes \mathbb{1}_{\mathbf{n}, -\boldsymbol{\mu}_x} \otimes \hat{\zeta}_{B, \mathbf{n}, -\boldsymbol{\mu}_y} \cdot \hat{P}_{\hat{\zeta}, \mathbf{n}, -\boldsymbol{\mu}_y} \otimes \hat{\zeta}_{A, \mathbf{n}, +\boldsymbol{\mu}_x}^\dagger \otimes \mathbb{1}_{\mathbf{n}, +\boldsymbol{\mu}_y}.\end{aligned}\tag{1.4.25}$$

Electric field operators In the dressed-site formalism, as with the parallel transporter, the electric field contribution is equally divided across the two half-links, with each half contributing half the total electric energy. Namely, from (1.4.5) we have:

$$\hat{E}_{\mathbf{n},\boldsymbol{\mu}}^2 = \frac{1}{2} \left[\hat{S}_{\mathbf{n},\boldsymbol{\mu}}^z(j)^2 + \hat{S}_{\mathbf{n}+\boldsymbol{\mu},-\boldsymbol{\mu}}^z(j)^2 \right]. \quad (1.4.26)$$

In the operative Hamiltonian, we combine the $2D$ half-links contribution to the electric energy onto the same single dressed-site operator:

$$\hat{\Gamma}_{\mathbf{n}} = \frac{1}{2} \sum_{\pm\boldsymbol{\mu}} \hat{S}_{\mathbf{n},\boldsymbol{\mu}}^z(j)^2. \quad (1.4.27)$$

Operative dressed-site U(1) Hamiltonian

We can then rewrite the (2+1)D U(1) truncated Hamiltonian in Eq. (1.4.1) as follows:

$$\begin{aligned} H_{\text{U}(1)} = & \frac{c\hbar}{2a_0} \sum_{\mathbf{n}} \left[-i\hat{Q}_{\mathbf{n},+\boldsymbol{\mu}_x}^\dagger \hat{Q}_{\mathbf{n}+\boldsymbol{\mu}_x,-\boldsymbol{\mu}_x} - (-1)^{\mathbf{n}} \hat{Q}_{\mathbf{n},+\boldsymbol{\mu}_y}^\dagger \hat{Q}_{\mathbf{n}+\boldsymbol{\mu}_y,-\boldsymbol{\mu}_y} + \text{h.c.} \right] \\ & + m_0 c^2 \sum_{\mathbf{n}} (-1)^{\mathbf{n}} \hat{N}_{\mathbf{n}} + \frac{g^2 c\hbar}{4a_0} \sum_{\mathbf{n}} \hat{\Gamma}_{\mathbf{n}} - \frac{c\hbar}{2g^2 a_0} \sum_{\square} \text{Tr} \left(\hat{U}_{\square} + \hat{U}_{\square}^\dagger \right). \end{aligned} \quad (1.4.28)$$

U(1) Link-Symmetry operators

The equivalence between Eq. (1.4.1) and Eq. (1.4.28) is correct as long as the link symmetries are satisfied, i.e., as long as the rishon states of each link have opposite electric fields. This constraint reduces to a \mathbb{Z}_2 symmetry on each link that can be easily resolved with dedicated libraries [6, 174], or imposed as two-body penalty terms (one per link) in the Hamiltonian, in such a way to behave as the largest energy scale of the problem.

Open boundary conditions and half-integer representations

In the case of open boundary conditions (OBC), we may want to freeze the half links on the bordering dressed sites of the lattice to the ground of the electric field. For *integer* j -representations, this can be easily achieved by selecting the rishon configurations with $|j, 0\rangle$ on sites along the corresponding border $\boldsymbol{\mu}$. Equivalently, for each of these sites, we can add a penalty term like $\hat{H}_{\mathbf{n},\boldsymbol{\mu}}^{\text{border}} = \alpha \left(\hat{E}_{\mathbf{n},\boldsymbol{\mu}} - j \right)^2$. As for *semi-integer* representations, where the minimal electric field is degenerate, we can choose between one of the following penalties:

$$\hat{H}_{\mathbf{n},-\boldsymbol{\mu}}^{\text{border}} = \alpha \left(\hat{E}_{\mathbf{n},-\boldsymbol{\mu}} - [j] \right)^2 \quad \text{and} \quad \hat{H}_{\mathbf{n},+\boldsymbol{\mu}}^{\text{border}} = \alpha \left(\hat{E}_{\mathbf{n},+\boldsymbol{\mu}} - \lfloor j \rfloor \right)^2, \quad (1.4.29)$$

where $[j]$ ($\lfloor j \rfloor$) corresponds to the minimum upper (maximum lower) integer representation.

Projecting operators on the U(1) gauge-invariant dressed-site basis

As discussed in Sec. 1.2.3, all the previous operators need to be projected in the U(1) gauge-invariant subspace. Since we have chosen the staggered fermions formulation, we expect two gauge invariant bases, one for *even* and one for *odd* sites, respectively M_+ and M_- . Each one coincides with the kernel of the corresponding U(1) Gauss Law operator $\hat{G}_{\mathbf{n},p}$:

$$\hat{G}_{\mathbf{n},p} M_p = \left[\hat{N}_{\mathbf{n}} + \sum_{\boldsymbol{\mu}} \hat{E}_{\boldsymbol{\mu}} - \frac{1-p}{2} \mathbb{1}_{\mathbf{n}} \right] M_p = 0, \quad (1.4.30)$$

where $p = \pm 1$ is the parity of the lattice site.

ℓ	d			
	(2 + 1)-dimensions		(3 + 1)-dimensions	
	U(1)	SU(2)	U(1)	SU(2)
1	35	30	267	178
2	165	168	3437	3670
3	455	600	18487	35280
4	969	1650	64953	214958
5	1771	3822	177155	967466
6	2925	7840	408421	3509062
7	4495	14688	835311	10828494
8	6545	25650	1561841	29473038

Table 1.1: Dressed site Hilbert space dimension d for increasing number ℓ of allowed electric energy density levels in some (2+1)D and (3+1)D paradigmatic LGTs with dynamical matter and gauge groups U(1) and SU(2). Table from [5].

1.4.5 Scaling of the local basis dimension

Of course, the larger the gauge field truncation (i.e. the larger the spin- j representation), the larger the effective dressed-site Hilbert space. In Tab. 1.1, we list the dressed-site dimension $d = \dim \mathcal{H}_{\text{dress}}$ associated with the first few nontrivial gauge truncations of U(1) and SU(2), detailed in Sec. 1.3 in $D = 2, 3$ space dimensions. Both the considered LGTs include dynamical matter, represented by one fermionic field multiplet in the fundamental representation of the gauge group. The ℓ -th row of Tab. 1.1 is obtained keeping only the first ℓ nonzero electric energy levels (i.e., using the ℓ -th smallest quadratic Casimir eigenvalue as cutoff Θ , see Sec. 1.2.1). As Tab. 1.1 shows, the local dimension increases rapidly with ℓ . For (3+1)D non-Abelian LGTs, $d \sim O(10^4)$ is reached already within the first two truncations, making the study of the untruncated limit prohibitive.

As it will be discussed in Sec. 2.6, differently from the models typically encountered in condensed matter physics, the local dimension of LGTs can thus be a limiting factor for Tensor Network simulations | especially when d becomes comparable to commonly used TN bond dimensions ($100 \lesssim \chi \lesssim 500$ for TTN). In these cases, crucially for high-dimensional LGTs, strategies aimed at further compressing the local computational basis are needed (see Sec. 2.6.1).

Several numerical analyses suggest that, in some cases, a small-to-moderate truncation of the gauge group is enough for accurately approximating the continuum limits, at least for low-energy states [81, 82, 87, 175–177]. However, the optimal gauge truncation depends on the Hamiltonian parameters m_0 and g .

In order understand this behavior, we focus on a single QED plaquette in open boundary conditions, as it provides the minimal setting allowing for both electric and magnetic effects. Then, to characterize the convergence in the gauge truncation ℓ , we consider a candidate observable O and compute its ground state expectation value $\langle \hat{O} \rangle_\ell$ for increasing ℓ . We iterate until the relative deviation between consecutive truncations drops below some threshold ϵ_{trunc} : $|\langle \hat{O} \rangle_{\ell^*} - \langle \hat{O} \rangle_{\ell^*-1}| < \epsilon_{\text{trunc}} |\langle \hat{O} \rangle_{\ell^*}|$ for some ℓ^* . Fig. 1.3(a) shows the minimal truncation ℓ^* at which the magnetic energy operator $\hat{O} = \text{Re} \hat{U}_\square$ is converged to $\epsilon_{\text{trunc}} = 10^{-5}$. We explore a grid of model parameters, whose extent has been chosen according to standard MC literature [9, 29–31, 35, 36, 146, 178–183]. $\text{Re} \hat{U}_\square$ is used as a benchmark due to its relevance in the weak coupling

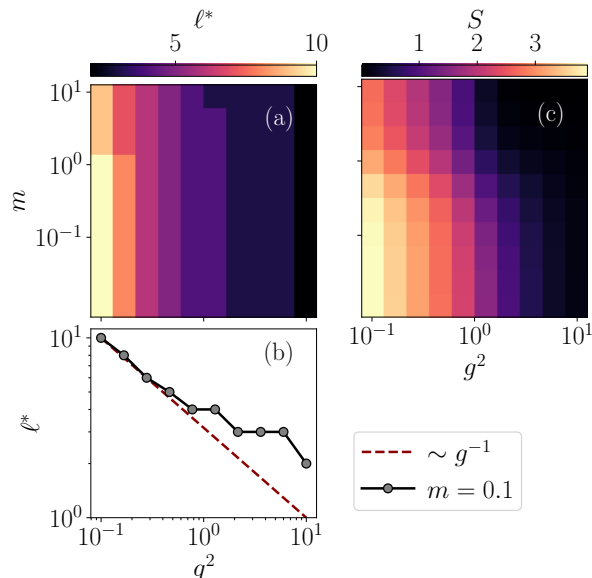


Figure 1.3: Exact diagonalization of a QED plaquette for a grid of masses $m \in [10^{-2}, 10^1]$ and couplings $g^2 \in [10^{-1}, 10^1]$. (a,b) Minimal gauge truncation ℓ^* required to reach a precision $\epsilon_{\text{trunc}} = 10^{-5}$ in the magnetic energy $\langle \text{Re} \hat{U}_{\square} \rangle$. (c) Corresponding entanglement entropy $S(\ell^*)$ associated with a symmetric bipartition of the plaquette. Figure from [5].

regime, where the continuum limit of $D < 3$ lattice QED is located [29]. As Fig. 1.3(b) shows, ℓ^* depends heavily on the coupling, growing asymptotically like $\ell^* \sim g^{-1}$ as g is decreased, while m_0 plays almost no role. An analogous inverse dependence of the minimal gauge truncation on the coupling is expected for non-Abelian LGT in arbitrary dimensions. Moreover, the continuum limit of non-Abelian LGTs in $D \leq 3$ is also expected at $g \rightarrow 0$ [29], further substantiating the need to compress the local dimension in TN simulations of LGT whenever extrapolation to the continuum is in order. Developments along this directions represent an ongoing research line we are considering towards more accurate simulations.

Apart from the growth of the local dimension, extrapolation to the continuum is further complicated by the fact that the continuum limit of a lattice quantum field theory corresponds to a critical point of the underlying lattice model [12]. Close to criticality, quantum correlations are boosted and violations of the entanglement area law are expected [184]. The higher entanglement entropy in the proximity of the continuum ($g, m_0 \ll 1$ regime) is already captured by the single-plaquette analysis of Fig. 1.3(c) (see [2] for the SU(2) case). Continuum limits of LGTs are thus an area of potential advantage for quantum computation over classical methods, as the former is not limited by entanglement. Nonetheless, quantum computation is also affected by the need to relax gauge truncations when $g^2 \rightarrow 0$, either by increasing the number of qubits used to encode a dressed site, which is at least $\lceil \log_2(d) \rceil$, or by using hybrid devices with both qubits and bosonic modes [185].

1.5 Summary

In this chapter, we provided a detailed exploration of Hamiltonian Lattice Gauge Theories (LGTs) with an emphasis on the discretization process for both fermionic and gauge fields. We began by reviewing the lattice discretization of fermions, highlighting the staggered fermion approach to mitigate the fermion doubling problem. The discretization of gauge fields was then discussed,

where the continuous gauge fields were replaced by parallel transporters, ensuring lattice gauge invariance. We detailed how the discretization of the electric and magnetic components of the gauge fields, leading to the construction of the lattice Hamiltonian. The dimensional analysis was carried out, emphasizing the role of the gauge coupling and its scaling with lattice spacing.

The second part of the chapter introduced the dressed-site formalism, which effectively integrates the gauge fields into matter sites, reducing the complexity of the gauge theory and making it more amenable to TN algorithms and quantum simulations. This formalism has been thoroughly applied to two exemplary cases, such as the non-Abelian $SU(2)$ Yang-Mills in Sec. 1.3 and the Abelian $U(1)$ LGTs in Sec. 1.4. The techniques and concepts introduced here for these two models will be foundational for understanding the numerical methods and physical results presented and investigated later in the subsequent chapters of this thesis.

Chapter 2

Tensor Networks methods for LGTs

The rich phenomenology of complex quantum many-body (QMB) systems is often explored using advanced numerical techniques. For many quantum Hamiltonians, exact solutions become computationally infeasible as the system size increases, due to the exponential growth of the Hilbert space. For a system with N particles and a local dimension d , the dimensionality of the Hilbert space grows as $\dim, \mathcal{H} = d^N$, leading to a $d^N \times d^N$ Hamiltonian matrix. Exact diagonalization (ED), while valuable for small systems, quickly becomes impractical, requiring memory beyond the limits of most hardware as system size increases.

Given these challenges, alternative numerical approaches have emerged, with two key methods standing out: Quantum Monte Carlo (QMC) simulations [186] and Tensor Network (TN) methods [48]. QMC techniques use stochastic methods to solve the Schrödinger equation as a diffusion problem, while TN approaches leverage the entanglement properties of quantum systems to efficiently represent low-energy states, retaining only the most relevant contributions to equilibrium properties and real-time dynamics.

Both QMC and TN methods have significantly advanced our ability to simulate QMB systems, providing insights into ground state properties, phase transitions, and dynamic behaviors across various domains. Their applications extend beyond condensed matter physics, with relevance in fields such as nuclear physics, chemistry [37], material science, and even machine learning [48]. However, these methods also face significant challenges when dealing with strongly correlated fermionic systems. For instance, QMC suffers from the notorious *sign problem* [13, 38, 187], which stems from the antisymmetric nature of fermionic wave functions, leading to highly oscillatory integrals that are difficult to compute.

On the other hand, TNs provide a powerful framework for bypassing the sign problem, but they require careful handling of entanglement and dimensionality issues, particularly when applied to higher-dimensional systems. In these contexts, optimizations that preserve locality, such as the use of space-filling curves like the Hilbert curve, become crucial for maintaining efficiency in TN algorithms on high-dimensional lattices. Such curves help reducing the computational overhead by minimizing long-range interactions when mapping 2D lattices into effective 1D structures [1].

The need for scalability becomes even more pressing when dealing with lattice gauge theories (LGTs), where large-scale simulations are necessary to access the continuum limit and explore complex phenomena such as non-perturbative dynamics and phase transitions. Here, TN methods, despite their successes, face challenges related to large bond dimensions and local basis truncations. Addressing these requires both theoretical innovations, such as optimized mappings

and geometries, and computational improvements, like parallelization and hybrid techniques leveraging modern high-performance computing (HPC) infrastructures.

The structure of this chapter reflects the key elements necessary for an efficient exploration of QMB systems via ED and TN methods. In Sec. 2.1, we begin with an introduction to exact diagonalization, discussing the importance of symmetry-based techniques like block diagonalization to reduce the effective size of the Hilbert space and the associated computational load. Next, in Sec. 2.2, we turn to TN methods, outlining the fundamental concepts and the role of entanglement in TN algorithms [48]. Loopless TN geometries, such as Matrix Product States (MPS) and Tree Tensor Networks (TTNs), are introduced in Sec. 2.2.2 as powerful tools for simulating one-dimensional and higher-dimensional finite-size systems. A key aspect of this section is the focus on the implementation of gauge symmetries within the TN structure, enabling a further reduction in computational costs. In Sec. 2.4, we detail the TTN variational ground-state search algorithm used for studying equilibrium properties, while Sec. 2.5 outlines time evolution algorithms, such as Time-Evolved Block Decimation (TEBD) and the Time-Dependent Variational Principle (TDVP).

The original contributions of this chapter are in Secs. 2.3 and 2.6. In the former, we analyze the effectiveness of different TN geometries in simulating high-dimensional systems, with a particular focus on 2D lattice models. Here, the importance of locality-preserving mappings like the Hilbert curve is highlighted, demonstrating their role in improving the accuracy and efficiency of TN simulations [1]. In the latter, we provide a roadmap for future developments, discussing both numerical and theoretical improvements that will enable TN methods to scale up to large LGT simulations, potentially reaching sizes and accuracies comparable to current Monte Carlo methods [5]. In conclusion, the chapter outlines a cohesive strategy for advancing the simulation of QMB systems, combining ED, efficient TN geometries, and a vision for overcoming the remaining computational barriers in large-scale LGT simulations.

2.1 Exact Representation of Quantum Many-Body Systems

Consider a QMB system defined on a D -dimensional lattice with $N = \prod_k^D L_k$ sites. A generic pure QMB state $|\Psi_{\text{QMB}}\rangle$ of the system lives in the tensor product of N local Hilbert spaces \mathcal{H}_j , each one being of finite dimension d_j ¹: $\mathcal{H} = \mathcal{H}_1 \otimes \mathcal{H}_2 \otimes \cdots \otimes \mathcal{H}_N$. The state $|\Psi_{\text{QMB}}\rangle$ can be exactly expanded in terms of a complete basis set of \mathcal{H} :

$$|\Psi_{\text{QMB}}\rangle = \sum_{i_1, \dots, i_N} T_{i_1, \dots, i_N} |i_1, \dots, i_N\rangle, \quad (2.1.1)$$

where $|i_1, \dots, i_N\rangle = |i_1\rangle \otimes \cdots \otimes |i_N\rangle$ represents the tensor product of the local basis vectors, while $\{i_s\}$ is the canonical basis for the s^{th} subsystem. As the state is pure, it is uniquely determined by the coefficient tensor T_{i_1, \dots, i_N} , whose entries are in general complex scalars and their number scales as d^N , i.e., exponentially with the system size N .

In these terms, providing an exact description of the state entails knowing all the d^N complex coefficients. This is a fundamental limitation when solving a QMB problem on a classical computer, since an exponential scaling with the number of degrees of freedom implies that the exact representation described in Eq. (2.1.1) is computationally unfeasible for intermediate-large values of N , especially when the local basis becomes large as in the case of dressed-site formulated LGTs (see Secs. 1.2 and 1.4.5). Nonetheless, ED simulations for small lattices are crucial for

¹For the moment, we are still considering the general case where system sites can have in principle different local dimension and different local Hilbert space. Later on, we will restrict to the case of $d_j = d \forall j \in \{1, \dots, N\}$.

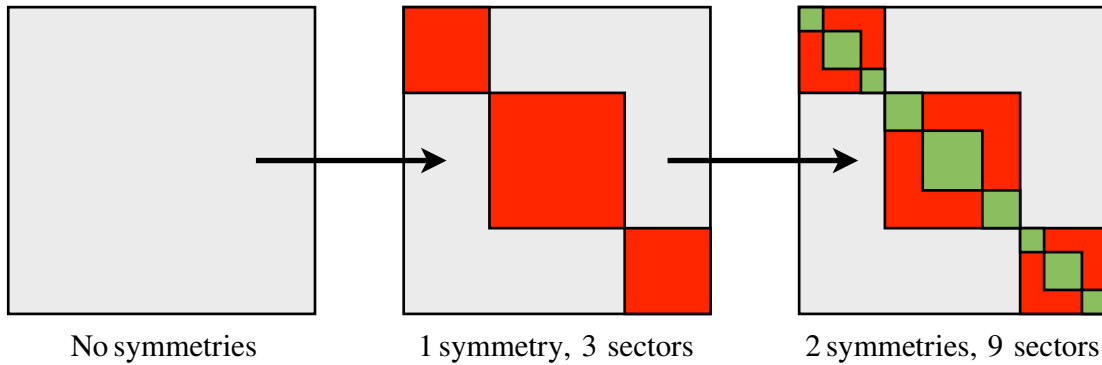


Figure 2.1: Illustration of block diagonalization. In absence of symmetries, we have to diagonalize the whole Hamiltonian, which explores the whole Hilbert space $\sim d^N$. If the Hamiltonian has one symmetry, by constructing states labeled by the corresponding conserved quantum number, the Hamiltonian matrix breaks up into blocks that can be diagonalized independently of each other (middle). Applying another symmetry, the blocks can be further broken up into smaller blocks (right) labeled by two different quantum numbers, etc [188].

validating other methods such as Tensor Networks, and offer a concrete way to understand key aspects of quantum mechanics, especially the symmetry of many-body states [188].

2.1.1 Block Diagonalization

In the special case where the QMB system has a set of symmetries (as in LGTs), the computational cost of ED algorithms can be significantly reduced (while still remaining exponential in the system size) by using *block diagonalization*, allowing for a more efficient numerical treatment of the problem. Indeed, when a symmetry group G is present in the system, the total Hilbert space \mathcal{H} can be decomposed into a direct sum of smaller subspaces \mathcal{H}_α labeled by an irreducible representation (or quantum number) α . Correspondingly, the QMB Hamiltonian, which is invariant under these symmetry transformations, can be written as follows:

$$\hat{H} = \bigoplus_{\alpha} \hat{H}_{\alpha}, \quad (2.1.2)$$

where each \hat{H}_{α} is a block corresponding to a specific symmetry sector α . Instead of diagonalizing the full Hamiltonian in the entire Hilbert space, one can diagonalize each block \hat{H}_{α} independently. This drastically reduces the computational cost, as the size of each block is much smaller than the full Hilbert space.

In the following, we review two main cases of symmetries: U(1) invariance, related to particle-number conservation, and translational invariance, related to momentum conservation. Both symmetries are currently employed in the ED-LGT Python library [6] and exploitable for simulating any QMB system or LGT in the dressed-site formalism.

Particle-number conservation

The presence of a global U(1) symmetry (not local as in LGTs) is associated with the conservation of a globally conserved quantity, such as the total number of particles, charge, or spin (along a certain direction) in a QMB system. Formally, this means that the Hamiltonian \hat{H} commutes

with a total operator \hat{A} :

$$\left[\hat{H}, \hat{A}\right] = 0 \quad \text{where} \quad \hat{A} = \sum_{\mathbf{n}} \hat{a}_{\mathbf{n}} \quad (2.1.3)$$

and $\hat{a}_{\mathbf{n}}$ is the particle number operator on lattice site \mathbf{n} . This implies that \hat{A} is conserved under the time evolution generated by the Hamiltonian. For instance, in the case of the Ising model without transverse field, the conserved quantity \hat{A} is the magnetization along z and $\hat{a}_{\mathbf{n}} = \hat{\sigma}_{\mathbf{n}}^z$. In bosonic or fermionic systems like in Hubbard Hamiltonians (see Sec. 5.2), the conserved quantity is the total particle number and $\hat{a}_{\mathbf{n}} = \hat{n}_{\mathbf{n}}$ is the operator that counts the number of particles at site \mathbf{n} . For fermions, $\hat{n}_{\mathbf{n}}$ can only take values 0 or 1 (due to the Pauli exclusion principle), while for bosons $\hat{n}_{\mathbf{n}}$ can take any non-negative integer value. As for LGTs such as the ones described in Chap. 1 and simulated in Chaps. 3 and 4, there is a global U(1) symmetry related to the invariants of the matter fields under rotations $\hat{\psi}_{\mathbf{n}} \rightarrow e^{i\theta} \hat{\psi}_{\mathbf{n}}$ and corresponds to the conservation of charge: baryon number for non-Abelian LGTs such as SU(2) Yang Mills in Sec. 1.3 and electric charge for Abelian ones such as QED in Sec. 1.4. In the former case, $\hat{a}_{\mathbf{n}}$ corresponds to the baryon number density b defined in Eq. (3.1.8); in the latter case, $\hat{a}_{\mathbf{n}} = \hat{q}_{\mathbf{n}} \equiv \hat{\psi}_{\mathbf{n}}^\dagger \hat{\psi}_{\mathbf{n}} - ((1)^{\mathbf{n}} - 1)/2$ [87, 89, 90]. Due to the aforementioned sign-problem, accessing sectors with finite baryon number density b or finite electric charge is challenging for MC based algorithms, while being straightforward for ED simulations (by exploiting block diagonalization) [6] or TN methods, where the U(1) sector is directly selected in the TN ansatz, ensuring that the symmetry is preserved throughout the simulation [47, 49, 189, 190].

Momentum conservation

In a QMB system with translational symmetry, as in the case of periodic boundary conditions (PBC), the corresponding Hamiltonian \hat{H} is invariant under translations of particle positions or lattice sites. This means shifting all particles or lattice sites by a unit (or a set of units) leaves the physical properties of the system unchanged [188]. For simplicity, let us focus on a 1D lattice, whose sites are labeled by $n \in \{0, \dots, N\}$.

We define a translation operator \hat{T} which moves every particle from site n to site $n + 1$, i.e., $\hat{T}|n\rangle = |n + 1\rangle$, with $\hat{T}^N = \mathbb{1}$. Due to translational symmetry, $\hat{T}\hat{H} = \hat{H}\hat{T}$, meaning that \hat{H} and \hat{T} admit a common set of eigenstates. Thanks to Bloch's theorem, these eigenstates can be expressed as wave functions with a definite momentum, characterized by a wave vector $p = 2\pi n/N$:

$$|\varphi_p\rangle = \frac{1}{\sqrt{N_\varphi}} \sum_{n=0}^{N_\varphi-1} e^{-ipn} \hat{T}^n |\varphi\rangle, \quad (2.1.4)$$

where $|\varphi\rangle$ is a reference state. To construct the momentum basis for given p , we need a set of reference states resulting in a complete set of normalizable orthogonal states. Clearly, for two states $|\varphi_p\rangle$ and $|\varphi_{p'}\rangle$ to be orthogonal, the corresponding representatives must obey $\hat{T}^r |\varphi\rangle \neq |\varphi'\rangle \forall r \in \{1, \dots, N\}$. Therefore, for each set of translated states $\{|\varphi(r)\rangle = \hat{T}^r |\varphi\rangle\}$, only one of them should be used as a reference state [188]. The normalization factor N_φ in Eq. (2.1.4) takes into account the periodicity of the reference state $|\varphi\rangle$, which in general could be smaller to N : $\hat{T}^{N_\varphi} |\varphi\rangle = |\varphi\rangle$ for some $N_\varphi < N$.

Once we have selected an orthonormal set of reference states, we can build the corresponding momentum basis via Eq. (2.1.4) and express the Hamiltonian as follows:

$$\hat{H}_{pp'} = \langle \psi_p | \hat{H} | \psi_{p'} \rangle, \quad (2.1.5)$$

where, due to the translational invariance, $\hat{H}_{pp'} = 0$ for $p \neq p'$. Eigenvalues and eigenstates of the Hamiltonian in a particular momentum sector p are obtained diagonalizing the block \hat{H}_{pp} .

When dealing with QMB systems where translational invariance involves a logical basis of $N^b > 1$ sites, the translational symmetry unit is expanded from a single site to N^b sites. Correspondingly, we have to update the momentum vector definition in Eq. (2.1.4) with a normalization factor that matches the total number of unit cells $L = \frac{N}{N^b}$ or a smaller periodicity L_φ :

$$|\varphi_p\rangle = \frac{1}{\sqrt{L_\varphi}} \sum_{n=0}^{L_\varphi-1} e^{-ipn} \hat{T}^{N^b n} |\varphi\rangle. \quad (2.1.6)$$

For instance, in LGTs employing the staggered fermion solution, the corresponding Hamiltonian is invariant under translations of two sites along each spatial direction. For instance, ED simulations of the (1+1)D SU(2) Yang-Mills LGT in PBC (see Sec. 4.4 and [4]) have been obtained in the zero momentum, since the scarred initial states of the dynamics belong to that sector.

2.1.2 Basic Tensor Operations

Aside by block diagonalization and the use of symmetries, by accurately manipulating the coefficient tensor T in Eq. (2.1.1), we can further extract a lot of information, such as quantum correlations, entanglement, and few-body observables, sometimes accessing only a portion of all its entries. The main operations which can be performed over T_{i_1, \dots, i_N} involve the indices labelling its links. In particular, it is possible to distinguish among at least three different kinds of operations affecting links: manipulations, contractions, and decompositions. Below, we briefly discuss each of them. For an equivalent pictorial representation, see Fig. 2.2.

Manipulations

Link manipulations involve operations like permutation, which reorders tensor indices, fusion, which combines adjacent links into a single index, and splitting, which breaks down a link into multiple smaller indices.

Link permutation It reorders the links $i_1 \dots i_N$ of the tensor T by moving the link at position ℓ into $k = \sigma(\ell)$ of the permuted tensor $T^{[p]}$:

$$T_{i_{\sigma(1)} \dots i_{\sigma(N)}}^{[p]} = T_{i_1 \dots i_N}. \quad (2.1.7)$$

Link fusion It combines $m - k + 1$ adjacent links ($i_k \dots i_m$) of dimensions ($d_k \dots d_m$) into a fused link j defined as follows:

$$\begin{aligned} j = \text{fuse}(i_k \dots i_m) &= 1 + \sum_{r=k}^m (i_r - 1) \prod_{j=1}^{r-k} d_j \quad \text{where } j \in \mathbb{J} = \mathbb{1}_k \times \dots \times \mathbb{1}_m \\ &= 1 + (i_k - 1)d_k^0 + (i_{k+1} - 1)d_{k+1} + \dots + (i_m - 1)d_m^{m-k}. \end{aligned} \quad (2.1.8)$$

Link splitting It replaces a given link k with index j_k and dimension d_k with $m - k + 1$ links $i_k \dots i_m$ of dimensions $d_{k'} \dots d_{m'}$ such that $d_k = d_{k'} \times \dots \times d_{m'}$:

$$T'_{i_1 \dots i_{k-1} (i_{k+1} \dots i_m) i_{m+1} \dots i_N} = T_{i_1 \dots i_{k-1}, j_k, i_{m+1} \dots i_N}. \quad (2.1.9)$$

Link fusion and splitting are very useful for decomposing large tensors into manageable parts.

Contractions

Whenever two tensors A and B, with links $\{a_1, \dots, a_n\}$ and $\{b_1 \dots b_m\}$ of dimensions respectively $\{d_{1\dots n}^A\}$ and $\{d_{1\dots m}^B\}$, have a set of k common links s_j (where $\{d_{n-k+j}^A\} = \{d_j^B\} = \{d_j^s\}$ for $j = 1 \dots k$), we can contract them over $\{s_1 \dots s_k\}$, obtaining a single tensor C:

$$C_{ab} \stackrel{\text{split}}{=} C_{a_1, \dots, a_{n-k} b_{k+1} \dots b_m} = \sum_{s_1 \dots s_k} A_{a_1, \dots, a_{n-k} s_1 \dots s_k} B_{s_1 \dots s_k b_{k+1} \dots b_m} \stackrel{\text{fuse}}{=} \sum_s A_{as} B_{sb}, \quad (2.1.10)$$

where in the 1st and in the 3rd equalities we exploited the link splitting and fusing operations respectively, obtaining the single links s , a , and b , with dimensions respectively:

$$d_s = d_1^s \times \dots \times d_k^s \quad d_a = d_1^a \times \dots \times d_{n-k}^a \quad d_b = d_{k+1}^b \times \dots \times d_m^b. \quad (2.1.11)$$

Decompositions

A tensor decomposition replaces a single input tensor with two or more output tensors, connected through a certain number of auxiliary links; correspondingly, it preserves with a given distribution, all the physical links of the input tensor. To perform a decomposition we need to:

1. choose a *bipartition* of the physical links of the input tensor T : $(i_1 \dots i_r) (i_{r+1} \dots i_N)$.
2. fuse these latter into two single row and column links: $T_{(i_1 \dots i_r)(i_{r+1} \dots i_N)} = T_{ab}$
3. decompose the obtained tensor into two factor matrices and (eventually) a diagonal one:

$$T_{ab} = \sum_{k=1}^{d_k} A_{ak} \lambda_k B_{kb}; \quad (2.1.12)$$

4. split the links initially fused to restore the initial network geometry.:

$$T_{(i_1 \dots i_N)} = \sum_k A_{(i_1 \dots i_r), k} \lambda_k B_{k, (i_{r+1} \dots i_N)}. \quad (2.1.13)$$

Noticeable examples are the QR decomposition and the SVD decomposition.

QR decomposition We can split T into two tensors, namely Q and R :

$$T_{(i_1 \dots i_r)(i_{r+1} \dots i_N)} = T_{ab} \stackrel{\text{QR}}{=} \sum_{k=1}^{d_k} Q_{ak} R_{kb} = \sum_{k=1}^{d_k} Q_{(i_1 \dots i_r)k} R_{k(i_{r+1} \dots i_N)}. \quad (2.1.14)$$

The matrix R_{kb} is an *upper trapezoidal matrix*, whereas Q_{ak} is a *semi-unitary matrix* w.r.t. k , that is $\sum_a Q_{ak} Q_{ak'}^* = \delta_{kk'}$. The minimal dimension d_k is such that

$$d_k = \min \{a, b\} = \min \{(i_1 \dots i_r), (i_{r+1} \dots i_N)\}. \quad (2.1.15)$$

Singular value decomposition (SVD) In this case, we split T into three tensors:

$$T_{(i_1 \dots i_r)(i_{r+1} \dots i_N)} = T_{ab} \stackrel{\text{SVD}}{=} \sum_{k=1}^{d_k} S_{ak} V_{kk} D_{kb} = \sum_{k=1}^{d_k} S_{ak} \lambda_k D_{kb} = \sum_{k=1}^{d_k} S_{(i_1 \dots i_r)k} \lambda_k D_{k(i_{r+1} \dots i_N)}, \quad (2.1.16)$$

where V is a diagonal and positive real matrix, whereas S and D are *semi unitary matrices* ($S^\dagger S = \mathbb{1} = DD^\dagger$). This decomposition is quite useful to mention the possibility of *truncation* for an index. Indeed, since the diagonal elements of V are real, positive, and hence lower bounded from below by 0, they can be ordered (for instance) in *descending order*:

$$[V_{11} = \lambda_1 \geq V_{22} = \lambda_2 \cdots \geq 0]. \quad (2.1.17)$$

Moreover, if $\lambda_k < \epsilon \forall k > \chi$ for $\chi \in \{1, \dots, d_k\}$, it is possible to disregard some of the singular values λ_k with a precision ϵ . In other words, whenever the singular values decay fast enough after some λ_χ , we can neglect them. Correspondingly, the matrices S and D can be truncated, and d_k reduced to χ . Such a reduction introduces an error in the original representation of the tensor T_{ij} , which can be estimated as follows:

$$\left\| T_{ij} - \sum_{k=1}^{\chi} S_{ik} \lambda_k D_{kj} \right\| = \left\| \sum_{k=m+1}^{d_k} S_{ik} \lambda_k D_{kj} \right\| < \sum_{k=\chi+1}^{d_k} \|S_{ik} D_{kj}\| < \epsilon C \quad (2.1.18)$$

for a finite constant C . As we will see in Sec. 2.2, in the context of Tensor Networks, the parameter χ will correspond to the *bond dimension*.

Schmidt Decomposition Let us consider a bipartition according to which the first N_A particles belong to a subsystem A with Hilbert space $\mathcal{H}_A = \bigotimes_{k=1}^{N_A} \mathcal{H}_k$, whereas, the remaining $N_B = N - N_A$ particles belong to the subsystem B with Hilbert space $\mathcal{H}_B = \bigotimes_{k=1}^{N_B} \mathcal{H}_k$; globally, we have $\mathcal{H} = \mathcal{H}_A \otimes \mathcal{H}_B$. Assuming all system sites with the same d -dimensional Hilbert space, i.e. $\dim \mathcal{H}_k = d \forall k$, then the QMB state and its coefficient tensor can be arranged as a *linear superposition* of products of states of the two sub-partitions:

$$|\Psi_{\text{QMB}}\rangle = \sum_{n=1}^{N_A} \sum_{m=1}^{N_B} C_{nm} |a_n\rangle |b_m\rangle, \quad (2.1.19)$$

where $\{|a_n\rangle\}_{n=1}^{N_A} \in \mathcal{H}_A$ and $\{|b_m\rangle\}_{m=1}^{N_B} \in \mathcal{H}_B$ are orthonormal basis of A and B . The corresponding density matrix ρ associated to (2.1.19) reads

$$\begin{aligned} \rho &= |\Psi_{\text{QMB}}\rangle \langle \Psi_{\text{QMB}}| = \sum_{n,n'} \sum_{m,m'} C_{nm} C_{n'm'}^* |a_n\rangle |b_m\rangle \langle a_{n'}| \langle b_{m'}| \\ &= \sum_{n,n'} \sum_{m,m'} \rho_{nm}^{n'm'} |a_n\rangle \langle a_{n'}| \otimes |b_m\rangle \langle b_{m'}|, \end{aligned} \quad (2.1.20)$$

where we grouped the coefficient matrix C_{nm} and its complex conjugate $C_{n'm'}^*$ into a single 4-order coefficient tensor $\rho_{nm}^{n'm'}$. The *reduced density matrix* of subsystem A is then given by tracing ρ over all the states of B :

$$\begin{aligned} \rho_A &= \sum_{\ell=1}^{N_B} \langle b_\ell | \rho | b_\ell \rangle = \sum_{n,n'} \sum_{\ell} \sum_{m,m'} \rho_{nm}^{n'm'} |a_n\rangle \langle a_{n'}| \otimes \langle b_\ell | b_m \rangle \langle b_{m'} | b_\ell \rangle \\ &= \sum_{n,n'=1}^{N_A} \sum_{\ell=1}^{N_B} \rho_{n\ell}^{n'\ell} |a_n\rangle \langle a_{n'}|, \end{aligned} \quad (2.1.21)$$

where we recall the partial trace not to depend on the choice of the basis of the partition we trace out. Then, if $\lambda_1, \lambda_2, \dots, \lambda_{N_A}$ are the eigenvalues of ρ_A and $|\alpha_1\rangle \dots |\alpha_{N_A}\rangle$ are the corresponding eigenvectors, we can rewrite $|\Psi_{\text{QMB}}\rangle$ in terms of $\{|\alpha_n\rangle\}_{n=1}^{N_A}$ as follows:

$$|\Psi_{\text{QMB}}\rangle = \sum_{n,m} C_{nm} |\alpha_n\rangle |b_m\rangle, \quad (2.1.22)$$

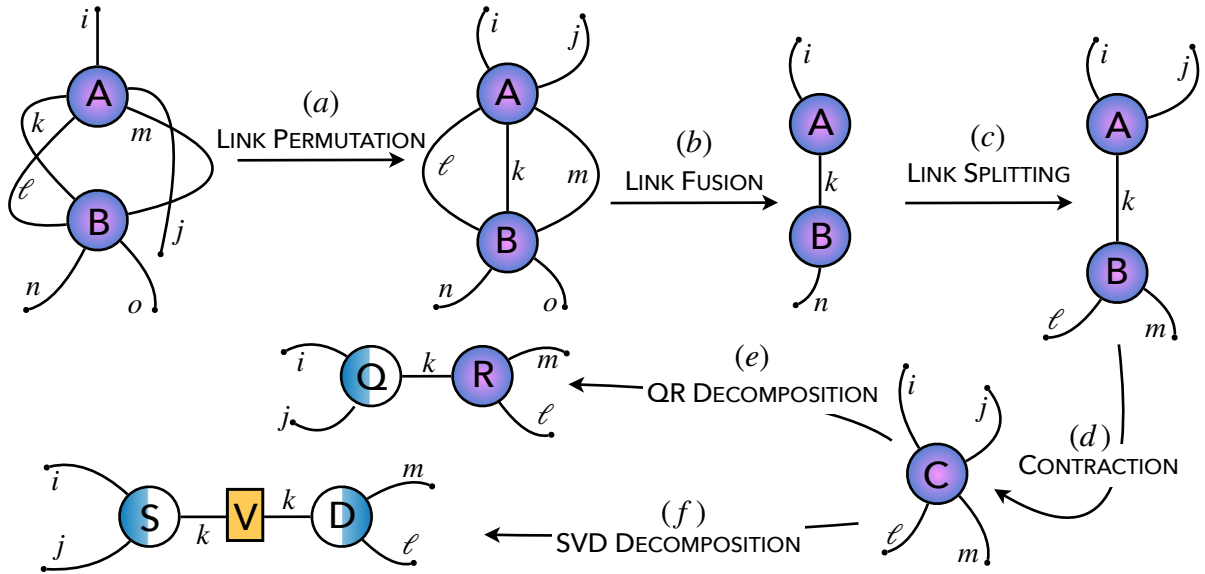


Figure 2.2: Pictorial representation of the main manipulations (a)-(c), contractions (d), and decompositions (e)-(f) which can be performed on the tensor coefficient in Eq. (2.1.1).

where \mathcal{C}_{nm} is a new coefficient tensor. We can then build up a new basis also for the subsystem B, in such a way that each vector is a clever superposition of vectors of the old basis:

$$|\beta_k\rangle = \sum_{m=1}^{N_B} \frac{\mathcal{C}_{km}}{\lambda_k} |b_m\rangle. \quad (2.1.23)$$

Since the matrix $\mathcal{C}_{km}/\lambda_k$ is unitary for each k , then $\{|\beta_k\rangle\}$ is an orthonormal basis, and we can rewrite (2.1.19) and (2.1.20) in terms of the *Schmidt decomposition*:

$$|\Psi_{\text{QMB}}\rangle = \sum_{n,m} \mathcal{C}_{nm} |\alpha_n\rangle |b_m\rangle = \sum_n \lambda_n |\alpha_n\rangle |\beta_n\rangle \quad \rho = \sum_{n,m} \lambda_n \lambda_m^* |\alpha_n\rangle \langle \alpha_m| \otimes |\beta_n\rangle \langle \beta_m|. \quad (2.1.24)$$

It is then clear that both the reduced density matrices ρ_A and ρ_B are diagonal in the Schmidt basis, and display the same positive spectrum:

$$\rho_A = \sum_q \langle \beta_q | \rho | \beta_q \rangle = \sum_{n,m} \sum_q \lambda_n \lambda_m^* \langle \beta_q | \beta_n \rangle |\alpha_n\rangle \langle \alpha_m| \langle \beta_m | \beta_q \rangle = \sum_q |\lambda_q|^2 |\alpha_q\rangle \langle \alpha_q| \quad (2.1.25a)$$

$$\rho_B = \sum_k \langle \alpha_k | \rho | \alpha_k \rangle = \sum_k |\lambda_k|^2 |\beta_k\rangle \langle \beta_k|. \quad (2.1.25b)$$

Such a Schmidt decomposition is very exploitable when computing quantum correlations between bipartitions of a system in a pure state. Conversely, it reveals useless for multipartite descriptions or when applied to mixed states, where no expression in terms of single partitions is available.

Physical perspective

What may appear as just a series of algebraic or technical manipulations on purely mathematical objects, is firmly connected to the control of quantum correlations and *entanglement* in a QMB system [191, 192]. From a purely physical perspective, if the coefficient tensor $T_{(i_1 \dots i_N)}$ describes the state of a N -body system, then, every decomposition or contraction allows to move from a

many-body description (with a single large tensor), to a single site or partite description (made of several small physical tensors) and the other way around, with eventual intermediate steps. The auxiliary link k along which decompositions/contractions are performed deserves special regard: in absence of loops in the TN structure, its dimension d_k quantifies the number of shared degrees of freedom between the arisen subsystems (e.g. QR in Eq. (2.1.15), SVD in Eq. (2.1.16), or Schmidt in Eq. (2.1.24) decompositions). In turn, these shared d.o.f. provide the amount of quantum correlations through which the partitions are mutually entangled. Therefore, the larger the truncation performed on $d_k \rightarrow \chi$ (see Eq. (2.1.18)), the smaller the entanglement between the partition we keep in track. For instance, exploiting the entanglement entropy [50], we have:

$$\mathcal{S}_A = - \sum_{k=1}^{\chi} \lambda_k \log \lambda_k. \quad (2.1.26)$$

2.1.3 Entanglement area law

As anticipated in Sec. 2.1, ED simulations of a QMB system, even resolving all its symmetries, are not feasible for a large number system size N , as the total Hilbert space grows exponentially with N . Nonetheless, a great variety of natural QMB systems happens to be described by ground and thermal equilibrium states that own little-to-moderate entanglement content. The physical states of these systems live in a small corner of the total Hilbert space, which can be efficiently targeted and parameterized without the exponential cost required by an exact representation.

This property is formally described as *entanglement area law*, fulfilled by low-energy states of local QMB Hamiltonians [50]: the entanglement between a partition of the system and the rest is proportional to the area of the boundary between them, instead of its volume, as happens for the majority of states in the Hilbert space. Thus, a state obeying area law contains much fewer quantum correlations than expected for a generic (or random) QMB state². From a theoretical point of view, the entanglement area law has been rigorously proven for (i) one-dimensional gapped local Hamiltonians, where the locality means that a lattice site interacts only with neighboring sites, without two-body all-to-all interactions [194–196]; (ii) for quantum states at thermal equilibrium, independently from the dimensionality of the system [197]. Even though rigorous proof for QMB systems in higher dimensions is lacking, several numerical and phenomenological shreds of evidence suggest that area law still holds in the presence of local interactions [50, 59, 198–200].

2.2 Tensor Networks Methods

We are then ready to present a general overview of Tensor Networks (TN), which are based on controlled wave-function variational ansätze exploiting the area-law entanglement bounds satisfied by locally interacting QMB systems. Thus, TN admit an efficient representation of the low-energy sectors contributing to the equilibrium properties and (low-entangled) time evolution [50], without suffering from the aforementioned sign problem [187]. Before looking at specific TN realizations, it is convenient to provide the general idea behind a TN geometry.

2.2.1 Tensor Network state

The area law described in Sec. 2.1.3 has important implications on the numerical simulation of QMB models: indeed, for ground-states and first excited states of local Hamiltonians where the

²Small corrections to the area law exist for instance close to a transition point for one-dimensional quantum systems (logarithmic corrections). However, the entanglement remains overall moderate [193].

entanglement content is low-to-moderate, it is possible to obtain an approximate but efficient representation capable of describing the main properties of these states [50]. TNs give a natural language for this representation, by replacing the complete rank- N tensor T_{i_1, \dots, i_N} of Eq. (2.1.1) with a chain of Q smaller tensors $T^{[q]}$ with $q \in \{1, \dots, Q\}$ connected via *auxiliary links* $\{\alpha\}_q$:

$$T_{i_1 \dots i_N} = \sum_{\alpha_1, \dots, \alpha_L} T_{\{i\}_1, \{\alpha\}_1}^{[1]} T_{\{i\}_2, \{\alpha\}_2}^{[2]} \cdots T_{\{i\}_Q, \{\alpha\}_Q}^{[Q]}. \quad (2.2.1)$$

Each single tensor $T^{[q]}$ has a set of physical indices $\{i\}_q$ of dimension d (one for each lattice site), whereas the dimension of the auxiliary indices $\{\alpha\}_q$ is upper bounded by a control parameter χ that is called *maximal bond dimension*.

The advantage of passing from the exact representation of Eq. (2.1.1) to a TN representation like Eq. (2.2.1) is that the number of TN parameters is of the order $O(\text{poly}(d)\text{poly}(N)\text{poly}(\chi))$, e.g., $\mathcal{O}(N\chi \max(\chi, d)^2)$ for the TTN [5]. The scaling with the system size and consequently the computational complexity is now *polynomial* and not exponential, as in the exact representation of the QMB state. It is worth noting that the bond dimension χ determines the degree of entanglement and quantum correlations encoded in the TN. Namely, for $\chi = 1$, the TN describes a *separable* state (product state, no entanglement), whereas one recovers the exact but inefficient representation in the limit $\chi \lesssim d^N$ assuming the system to be strongly entangled. Tuning χ properly allows interpolating between these two extreme regimes, efficiently reproducing the entanglement of the quantum state by exploiting decompositions like Schmidt/QR/SVD discussed in Sec. 2.1.2 [49, 60]. For example, dynamical problems characterized by a slow entanglement entropy growth, as in the many-body scars dynamics observed in Sec. 4.4, can be efficiently and accurately described by MPS ansatz with small or intermediate bond dimensions [46, 55].

Gauge invariance

More in general, the employment of auxiliary links clearly adds in the TN state some *information redundancy* with respect to the quantum state it describes. Such a redundancy corresponds to a set of linear transformations of the TN, which leave the quantum state unchanged. We usually refer to these transformations as *gauge transformations*, as they correspond to *local and invertible manipulations* on the auxiliary TN links $\{\alpha\}_q$ without affecting the physical degrees of freedom.

To give an example, let us focus on the following portion of Eq. (2.2.1)

$$T_{\{i\}, \{i'\}}^{[q+q']} = \sum_{\alpha_\eta} T_{\{i\}, \{\alpha\}_{|\eta}, \alpha_\eta}^{[q]} T_{\{i'\}, \{\alpha'\}_{|\eta}, \alpha_\eta}^{[q']}, \quad (2.2.2)$$

where $\{\alpha\}_{|\eta}$ collects the auxiliary links of the tensor except for η connecting the nodes q and q' with dimension χ_η . Then, given a $\chi'_\eta \times \chi_\eta$ left-invertible matrix $Y_{\alpha_\eta \alpha'_\eta}$, such that

$$\sum_{\alpha'} (Y^{-1})_{\alpha \alpha'} Y_{\alpha' \alpha''} = \delta_{\alpha \alpha''} \neq \sum_{\alpha'} Y_{\alpha \alpha'} (Y^{-1})_{\alpha' \alpha''}, \quad (2.2.3)$$

the TN state in Eq. (2.2.2) is left unchanged if the tensors $T^{[q]}$ and $T^{[q']}$ transform as follows:

$$\begin{aligned} T_{\{i\}, \{\alpha\}_{|\eta}, \alpha_\eta}^{[q]} &\longrightarrow \tilde{T}_{\{i\}, \{\alpha\}_{|\eta}, \alpha_\eta}^{[q]} = \sum_{\beta} Y_{\alpha_\eta \beta_\eta} T_{\{i\}, \{\alpha\}_{|\eta}, \beta_\eta}^{[q]} \\ T_{\{i'\}, \{\alpha'\}_{|\eta}, \alpha_\eta}^{[q']} &\longrightarrow \tilde{T}_{\{i'\}, \{\alpha'\}_{|\eta}, \alpha_\eta}^{[q']} = \sum_{\gamma} (Y^{-1})_{\alpha_\eta \gamma_\eta} T_{\{i'\}, \{\alpha'\}_{|\eta}, \gamma_\eta}^{[q']}. \end{aligned} \quad (2.2.4)$$

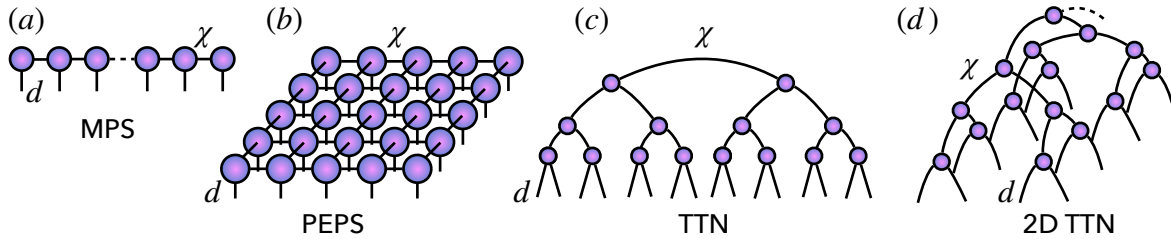


Figure 2.3: Examples of tensor network structures [5]: (a) Matrix Product States (MPS); (b) Projected Entangled Pair States (PEPS); (c) Tree Tensor Networks (TTN) for an underlying one-dimensional system; (d) TTN for an underlying two-dimensional square lattice. The physical links with local dimension d and the auxiliary links with bond dimension χ are highlighted in all the figures.

Overall, these contractions on the two edges of the link η leaves the composite tensor $T^{[q+q']}$ in Eq. (2.2.2) invariated. Therefore, since the state $|\Psi_{\text{QMB}}\rangle$ in Eq. (2.2.1) depends on $T^{[q]}$ and $T^{[q']}$ via $T^{[q+q']}$, it is insensitive to such a transformation. The intrinsic presence of gauge invariances arising from the TN prescription is going to be numerically exploited when contracting $|\Psi_{\text{QMB}}\rangle$ with its corresponding $\langle\Psi_{\text{QMB}}|$ through the Hamiltonian or other many-body operators.

2.2.2 Loopless Tensor Networks ansätze

The most widely used TN architectures are represented in Fig. 2.3. For 1D systems, Matrix Product States (MPS) [52, 53, 60, 201, 202] represent the landmark of TN simulations, and are largely employed for Density Matrix Renormalization Group's (DMRG) techniques [203, 204]. Beyond one dimension, there are Projected Entangled Pair States (PEPS) [46, 64–67, 205, 206], Tree Tensor Networks (TTN) [49, 69–71] and Multi-scale Entanglement Renormalization Ansatz (MERA) [73, 74, 207].

In this thesis, we focus on TTNs, which together with MPS, are *loopless Tensor Networks* [49], a special class of TN geometries which have found increasing applications for QMB and LGT simulations on finite lattices [1, 2, 46, 47, 76, 77, 89, 90, 100, 106, 136, 208]. Of course, the main concepts and ideas of these two ansätze can be easily generalized and applied to other TN structures, such as PEPS or MERA, which we briefly outline in Sec. 2.2.5.

Loopless Tensor Network attributes

Before exploring MPS and TTN geometries, it is convenient to review all the TN attributes linked to an intrinsic loopless geometry, which hold for the all the loopless TN realizations. As the name says, loopless TNs can be thought as network graphs which contain no circles among the single tensors. The main consequences of the absence of loops for TNs are the followings: first, they can exploit the full power of gauge transformations in Eq. (2.2.4), reducing the number of needed contractions and enhancing the computational speed. Secondly, the maximal entanglement between two given subsystems of the TN depends on the chosen bipartition of the system, and hence on the bond dimension χ of the auxiliary link over which the bipartition is performed. Such a feature is known as *entanglement clustering* [184]. More in detail, any loopless TN geometry admits the following attributes.

A distance $dist(a, b)$ between two tensor nodes a, b of the network: it corresponds to the number of links encountered along the *shortest path* between them. For a loopless TN, such a

path is unique: all the nodes which share the same distance d w.r.t. a central node c form a *level* $L(d; c)$. This gives the loopless TN geometry a well defined layered structure w.r.t. each tensor.

A bipartition of the QMB system: every (auxiliary) link η between two nodes q and q' induces a bipartition of state of the whole model. The Hilbert states of the two partitions are spanned by the canonical basis states

$$\{|i_s\rangle : \text{dist}(s, q) < \text{dist}(s, q')\} \quad \text{and} \quad \{|i_s\rangle : \text{dist}(s, q) > \text{dist}(s, q')\} \quad (2.2.5)$$

respectively, that is by fusing all links s ultimately connected either to q or q' once removed the bipartition link from the network. Then, if A and B are the resulting TN subportions, we can rewrite any pure state $|\Psi_{\text{QMB}}\rangle$ using the Schmidt decomposition in Eq. (2.1.24):

$$|\Psi_{\text{QMB}}\rangle = \sum_{k=1}^{\chi_\eta} |A_k\rangle |B_k\rangle \lambda_k \quad (2.2.6)$$

for λ_k sorted in a descending order. In these terms, a loopless TN can be seen as a simultaneous Schmidt decomposition over all the auxiliary links. For each network bipartition over a link η , the bond dimension χ_η provides an *upper bound* to the Schmidt rank, which in turn contributes to define the *bipartite entanglement* between the two subsystems (see Eq. (2.1.26)). Obviously, the larger the bond dimension, the larger is the amount of quantum correlations encoded by the TN structure for the given bipartition. In these terms, by exploiting the SVD in Eq. (2.1.16), it is possible to reduce the dimension of the auxiliary link η simply by discarding the smallest values λ_k and truncating the sum up to a given threshold χ'_η , obtaining a truncated state:

$$|\Psi_{\text{QMB}}^{\text{trunc}}\rangle = \frac{1}{\mathcal{N}_{\text{kept}}} \sum_{k=1}^{\chi'_\eta} |A_k\rangle |B_k\rangle \lambda_k, \quad \text{where} \quad \mathcal{N}_{\text{kept}} \equiv \sqrt{\sum_{k=1}^{\chi'_\eta} \lambda_k}. \quad (2.2.7)$$

The error provided by the truncation, is estimated as in Eq. (2.1.18).

The computational complexity of a given TN ansatz is then expressed as a polynomial function of the *maximal bond dimension* $\chi = \max_\eta \chi_\eta$ among all the TN auxiliary links, which represents the maximal level of entanglement between any two partitions formed over an auxiliary link. In these terms loopless TN ansätze display a smother scalings ($\mathcal{O}(\chi^3)$ for MPS and $\mathcal{O}(\chi^4)$ for TTN) w.r.t. PEPS [60] or MERA [72], where the presence of loops strongly increase computational costs, at least with $\mathcal{O}(\chi^8)$.

Gauges in loopless Tensor Networks

The absence of loops in the TN geometry allows for a strong speed up of tensor contractions between the network and its conjugate (like the ones in expectation values $\langle \Psi_{\text{QMB}} | O | \Psi_{\text{QMB}} \rangle$ for any observable O) by installing and exploiting gauge transformations like Eq. (2.2.4).

Among all the possible choices of local symmetries, we select the *unitary gauge*, which will be exploited in the ground state search algorithm of Sec. 2.4. The unitary gauge is defined w.r.t. a single node $T^{[c]}$ of the TN, named *current gauge center*. Starting from nodes of *maximal distance* $d = d_{\text{max}}$ from $T^{[c]}$, we can install unitary gauges on each level $\{L(d; c) : d = 1 \cdots d_{\text{max}}\}$ of the network as follows:

1. for each node $q \in L(d; c)$, perform a QR decomposition with respect to the link η which leads towards the center node c (see Fig. 2.4a):

$$T_{\{s\}\{\alpha\}_{1\eta}, \alpha_\eta}^{[q]} = \sum_{b_\eta=1}^{\chi_\eta} Q_{\{s\}\{\alpha\}_{1\eta}, b_\eta}^{[q]} R_{b_\eta \alpha_\eta}^{[q]}. \quad (2.2.8)$$

2. update $T^{[q]} \longrightarrow \tilde{T}^{[q]} \equiv Q^{[q]}$ with the *semi unitary isometry* of the QR decomposition, and contract the upper trapezoidal matrix $C^{[\eta]} \equiv R^{[q]}$ over the corresponding auxiliary link η into the adjacent tensor $T^{[q']}$ from the inner layer $L(d-1; c)$ (see Fig. 2.4a). Do it for all the nodes of the level $L(d; c)$.
3. advance inwards $d \longrightarrow d-1$ and repeat the previous steps for all the tensors of $L(d-1; c)$, up to reach $d = 1$ (see Fig. 2.4b). Notice that this iterative procedure implements a *global gauge transformation* which does not change the physical state of the network. The computational complexity of such a proceeding (QR decompositions plus R contractions over auxiliary links) is dominated by the QR decomposition $\sim \mathcal{O}(\chi^{Z+1})$, where Z is the maximal number of links of a single tensor in the network (maximal degree of a tensor).
4. move the center from a node c to a node c' . This corresponds to the implementation of steps 1 and 2 for each node along the path connecting c to c' . Obviously, the non unitary matrix $C^{[\eta]}$ out coming from the QR decomposition of a node close to c has to be contracted with the next node on the path towards c' . For example, if $c = q_1$ and $c' = q_3$ as in Fig. 2.4c, we should have the following steps

$$\begin{aligned}
& T_{\{s_1\}\{\alpha_1\}_{|\eta}^{\alpha_\eta}}^{[q_1]} \xrightarrow{\text{QR}} \sum_{\alpha_\eta} \tilde{T}_{\{s_1\}\{\alpha_1\}_{|\eta}^{\alpha_\eta} C_{\alpha_\eta b_\eta}^{[\eta]} \\
& \sum_{b_\eta} C_{\alpha_\eta b_\eta}^{[\eta]} T_{\{s_2\}\{\alpha_2\}_{|\eta, \eta^*}^{b_\eta \alpha_{\eta^*}}^{[q_2]} \longrightarrow T_{\{s_2\}\{\alpha_2\}_{|\eta, \eta^*}^{\alpha_\eta \alpha_{\eta^*}}^{[q_2]} \\
& T_{\{s_2\}\{\alpha_2\}_{|\eta^*}^{\alpha_{\eta^*}}^{[q_2]} \xrightarrow{\text{QR}} \sum_{\alpha_{\eta^*}} \tilde{T}_{\{s_2\}\{\alpha_2\}_{|\eta^*}^{\alpha_{\eta^*}} C_{\alpha_{\eta^*} b_{\eta^*}}^{[\eta^*]} \\
& \sum_{b_{\eta^*}} C_{\alpha_{\eta^*} b_{\eta^*}}^{[\eta^*]} T_{\{s_3\}\{\alpha_3\}_{|\eta^*}^{b_{\eta^*}}^{[q_3]} \longrightarrow T_{\{s_3\}\{\alpha_3\}_{|\eta^*}^{\alpha_{\eta^*}}^{[q_3]}
\end{aligned} \tag{2.2.9}$$

where $C^{[\eta]}$ and $C^{[\eta^]}$ are the non unitary upper trapezoidal matrices respectively defined on any two links η and η^* connecting $q_1 \rightarrow q_2$ and $q_2 \rightarrow q_3$.

Aside of the gauge isometrization w.r.t a single tensor node, any loopless TN ansatz admits a *canonical form* where all the tensors are concurrently isometrized, allowing for multipartite representation of QMB states (see [209–211]). However, such a canonical form is not suitable for the practical TN contractions that are performed during the variational algorithms, where the whole TN structure is sequentially optimized w.r.t each single tensor (see Sec. 2.4), which can be more conveniently chosen as the unique gauge center.

Aware of all these features of loopless TN geometries, we can look at two specific realizations: Matrix product states in Sec. 2.2.3 and (binary) Tree Tensor Networks in Sec. 2.2.4.

2.2.3 Matrix product states

The simplest yet most diffused and powerful loopless TN ansatz in one dimension, is represented by Matrix product states (MPS), which reproduces the structure of the lattice with a network of tensors, one for each lattice site [211]. As shown in Fig. 2.3(a), each tensor in the bulk of the network has three indices: one physical leg i of dimension d , representing the local degrees of freedom, and two auxiliary legs a s of dimension χ connected to the neighboring sites.

More formally, the MPS representation consists in reshaping the generic QMB pure state $|\Psi_{\text{QMB}}\rangle$

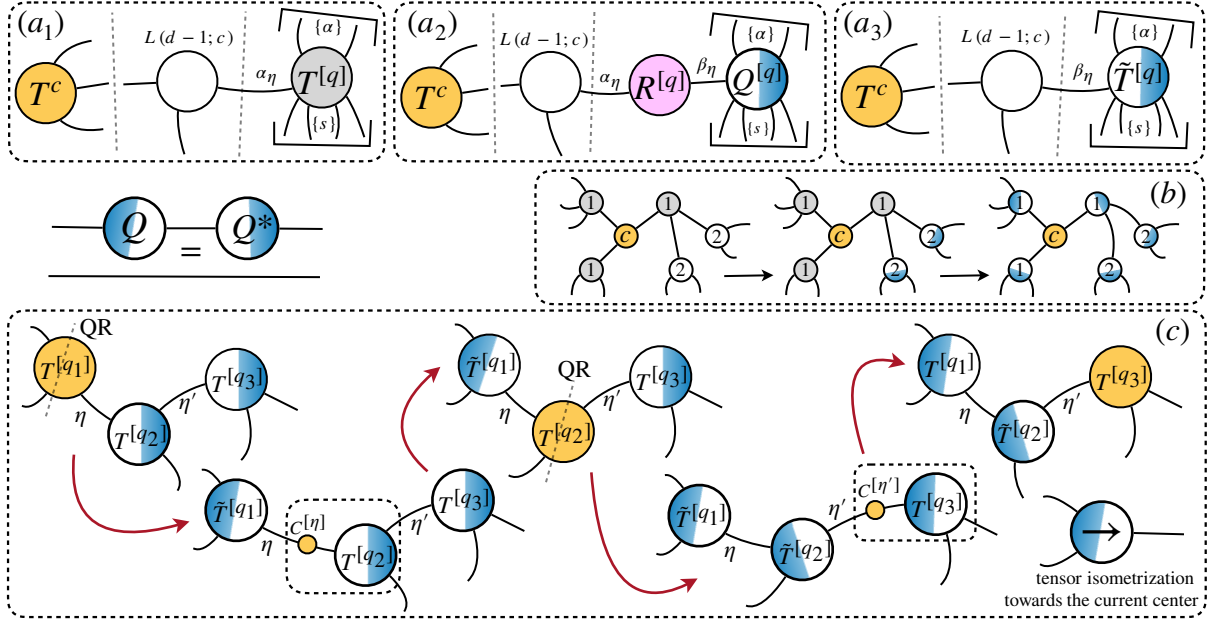


Figure 2.4: Pictorial representation of the employment of unitary gauges on a TN structure making use of QR decompositions. (a) QR decomposition of a node q of the level $L(d; c)$. (b) Iterative gauge transformations of TN nodes with respect to the chosen (red) center one from the highest to the lowest level L of the TN structure. (c) Iterative gauge transformation of the TN tensors in between of two successive center nodes.

in Eq. (2.1.1) as follows [51, 52, 212]:

$$|\Psi_{\text{QMB}}\rangle = \sum_{i_1, \dots, i_N=1}^d \sum_{\alpha_1, \dots, \alpha_N=1}^{\chi} A_{\alpha_1, \alpha_2}^{[1], i_1} A_{\alpha_2, \alpha_3}^{[2], i_2} \dots A_{\alpha_{N-2}, \alpha_{N-1}}^{[N-1], i_{N-1}} A_{\alpha_{N-1}, \alpha_1}^{[N], i_N} |i_1, i_2, \dots, i_N\rangle, \quad (2.2.10)$$

where each 3-rank tensor $A_{\alpha_k, \alpha_{k+1}}^{[k], i_k}$ describes the local k^{th} lattice site with the index i_k and the amount of quantum correlations shared its neighbors through the indices α_k, α_{k+1} . In open boundary conditions (OBC), the tensors at the boundaries of an MPS have one trivial auxiliary link $\alpha_1 = \alpha_N = 1$. Fixing the physical index i_k , the tensor $A_{\alpha_k, \alpha_{k+1}}^{[k], i_k}$ is a $\chi \times \chi$ complex matrix. In this perspective, Eq. (2.2.10) is a sum of basis elements weighted by matrix products.

In principle, every state of a one-dimensional QMB system can be written exactly in the MPS form, with bond dimension $\chi = d^{N/2}$ growing exponentially with the lattice sites N [209]. However, since MPS intrinsically satisfies area law, when dealing with low-energy states of local Hamiltonians, and their real-time dynamics for small-to-intermediate time, an approximate but efficient representation at fixed maximal bond dimension is usually very accurate in capturing the essential features of the systems [50, 66].

In this case, the number of parameters in the MPS representation grows only polynomially with the system size, drastically reducing the overall computational complexity. More in detail, the MPS ground state searching algorithm (based on DMRG) scales like $\mathcal{O}(Nd\chi^3 + Nd^2\chi^2)$ or $\mathcal{O}(Nd^3\chi^3)$, depending if the algorithm optimizes a single MPS tensor at a time, or two-tensors simultaneously [53, 55]. Two-site optimization is usually important to avoid local minima or meta-stable configurations during the energy variational minimization [213]. The subspace expansion is an intermediate approach with the benefits of the two-tensor update and a tunable computational cost between the two approaches [49].

2.2.4 Tree Tensor Networks

The other important family of loopless TNs is represented by Tree Tensor Networks (TTN), in which the wave function is decomposed into a hierarchical network of tensors that do not contain internal loops [49, 69]. This way, the network can be efficiently contracted and manipulated in polynomial time by exploiting the unitary gauge transformations detailed in Sec. 2.2.2.

A particular class of TTN is represented by binary TTN (bTTN), reported in Fig. 2.3c and Fig. 2.3d for one- and two-dimensional lattices. In these structures, tensors in the lowest layer have two physical legs of dimension d (representing two lattice sites) and an auxiliary leg of dimension χ , whereas, in the upper layers, they have three auxiliary legs of dimensions up to χ . The network intrinsically encodes a renormalization procedure, in which, at each layer, two sites are mapped into a single effective one.

More in detail, bTTN are quite useful for a series of reasons:

1. thanks to their loopless TN geometry, in finite-range models, ground searching algorithms for bTTNs display a numerical complexity of the order $\mathcal{O}(Nd^2\chi^2 + N\chi^4)$ [49] (see also Sec. 2.4). This is a much more favorable scaling concerning equivalent algorithms for other TN structures, and allows reaching quite large values of bond dimensions ($\chi \approx 500$) [72] to keep the variational TTN optimization under control.
2. similarly to MPS, they provide an efficient basis for DMRG-based algorithms, which represent the state-of-the-art technique for the numerical simulation of 1D QMB systems with both short and long-range interactions [203, 204].
3. they can handle both open (OBC) and periodic (PBC) boundary conditions, without the typical limitations of DMRG for periodic systems.
4. any D-dimensional realization of a bTTN admits an equivalent realization in 1D [1, 2, 89, 90]. For instance, to move from a 2D bTTN to the corresponding 1D version (see Fig. 2.3), we just need to rotate each layer of the tree with alternate clockwise and anti-clockwise $\pi/2$ rotations in the xy plane. This procedure requires the application of a 2D-1D site-ordering that generates a mapping between the 2D physical system and a 1D chain [1] (see Sec. 2.3). Once the 2D physical model is modeled on a 1D chain, one can apply the TTN variational algorithm discussed in Sec. 2.4 by using 1D bTTNs.
5. due to their hierarchical structure, bTTNs offer a strong connectivity: rather than MPS, the distance between two physical lattice sites is *logarithmically* rescaled in the network. As a result, they reveal particularly advantageous to reproduce properly long-range interactions (see also Sec. 2.3).

Augmented Tree Tensor Networks

The drawback of loopless structures like binary TTN, is that the area law may not be explicitly reproduced in dimensions higher than one [214], which becomes a limiting factor when large systems are addressed. Nonetheless, it is possible to explicitly encode the area law of high dimensional systems in the TTN ansatz by introducing an additional layer of independent disentanglers, acting on different couples of lattice sites and connected to the corresponding physical legs. This process augments the expressive power of TTN, and the resulting ansatz is known as augmented Tree Tensor Network (aTTN) [173]. The computational complexity of variationally optimizing an aTTN structure, which means optimizing both the tensors and the disentanglers, is of the order $\mathcal{O}(N\chi^4d^4 + N\chi d^7)$. We point out that the scaling of the computational costs

with the local dimension d is particularly severe in the case of aTTN due to the presence of the disentangler layer.

2.2.5 Tensor Network ansätze with loops

Beyond loopless TN structures like MPS and TTN, there exist other ansätze, which despite their higher computational costs in contractions, offer unique advantages for describing complex QMB systems beyond one dimensions. Below we briefly outline two realizations of these TN ansätze.

Projected Entanglement Pair States (PEPS) displayed in Fig. 2.3b, represent a generalization of the MPS ansatz to two- or higher-dimensional lattices which directly encode in their structure the area law of entanglement [60]. In this case, each tensor in the bulk has a physical leg of dimension d , and a number of χ -dimensional auxiliary legs depending on the coordination number of the considered lattice. For example, this coordination number is four in the case of a two-dimensional square lattice, as shown in Fig. 2.3(b). Despite the area law implementation, due to the presence of loops in the TN geometry, an exact contraction of PEPS is an exponentially hard problem, meaning that PEPS can not be efficiently contracted for numerical computing, e.g. scalar products of states or physical observables [58]. To circumvent this problem, approximate contraction methods have been developed during the last years, and are still at the center of current research efforts [60]. But even with exploiting these approximate techniques, the computational complexity for ground state optimization remains quite high, e.g. of the order of $\mathcal{O}(Nd^2\chi^8)$ [67, 184], limiting the maximum reachable bond dimensions (typical values are of the order $\chi \approx 10$).

Multi-scale Entanglement Renormalization Ansatz (MERA) displayed in Fig. 2.3, extends the capabilities of MPS and TTN by efficiently representing QMB systems with long-range correlations, particularly at criticality. While TTN can capture certain entanglement structures beyond what MPS can handle, they are limited by their tree-like structure, which lacks the loops necessary to efficiently encode the entanglement scaling of critical systems. MERA addresses this limitation by introducing a layered, hierarchical network with loops, allowing for a logarithmic scaling of entanglement entropy and revealing suitable for critical ground states [73, 74].

Unlike TTN, where contractions can be performed in a straightforward and computationally inexpensive manner as detailed in Secs. 2.2.2 and 2.4, MERA introduces additional complexity through its disentanglers and isometric tensors, which are necessary for accurately capturing the multi-scale entanglement in critical systems. The presence of loops in MERA increases the complexity of the network and consequently the cost of tensor manipulations. For 1D systems, the scaling of MERA contractions and optimizations is accessible $\mathcal{O}(N\chi^4)$ but more expensive than TTNs. Beyond one dimension, e.g. for 2D systems, optimizing MERA is much more challenging and scales with $\mathcal{O}(N\chi^8)$. Current research is focusing on developing more efficient contraction and optimization algorithms to enhance its applicability to complex QMB systems [207]. Nonetheless, despite its higher computational, MERA's ability to capture the intricate entanglement patterns of critical systems makes it a powerful tool in the study of QMB physics.

2.3 Efficient Tensor Network geometries beyond one dimension

If MPS are the established TN ansatz for one-dimensional systems, the development of efficient TN algorithms for higher-dimensional systems is still ongoing [205, 215–219]. On one side, a possible and frequently used approach lies in the application of consolidated numerical methods based on DMRG (MPS) by suitably mapping the high-dimensional problem onto an

equivalent one-dimensional one. Indeed, the DMRG algorithm is often used for analyzing quasi-one-dimensional systems, such as ladder structures [55], and two-dimensional systems, obtaining reliable numerical results in a wide variety of condensed-matter problems [220–223].

However, using MPS/DMRG on high-dimensional lattices generally involves a significant increase in computational complexity. When adapting an MPS to two dimensions, it requires a careful arrangement of the 2D lattice into a 1D structure. Two main strategies can be implemented: the first one consists in considering the $n \times n'$ 2D lattice as an n' -legs ladder, then grouping all the n' sites of each column in a single numerical site, and finally applying the one-dimensional algorithms to the resulting chain [224]. The cost of this approach is the exponential growth with n' of the local basis dimension, which usually limits the application of this strategy to quasi-two-dimensional systems, in which the number of ladder legs is small with respect to the longitudinal extension.

The second strategy, which we discuss here, lies in covering the two-dimensional lattice by a one-dimensional curve and then applying one-dimensional algorithms to the resulting effective chain. The drawback at this approach is that even if the original model contains only nearest-neighbor interactions, the resulting model on the effective one-dimensional chain shows long-range interactions, that have an influence on the numerical approach efficiency [225]. In detail, the latter strategy induces a specific one-dimensional site-ordering in the 2D lattice, generating a mapping between the 2D physical system and a 1D chain. This procedure can be defined for any mapping

$$\mathcal{M} : i \in [1, n] \times [1, n'] \rightarrow \mu \in [1, nn'] \quad (2.3.1)$$

from a $n \times n'$ lattice onto a chain with nn' sites, through which it is possible to translate a two-dimensional model into a one-dimensional one. Finally, one can apply 1D TN algorithms, such as DMRG or the TTN variational one discussed in Sec. 2.4, while accounting for the long-range interactions introduced by the mapping. Long-range interactions eventually require a larger bond dimension to properly describe the system. It follows that the performance of the simulation depends on the capability of the mapping to preserve the locality of the interactions from the original 2D Hamiltonian to the effective new 1D one.

In this section, we quantify the importance of the choice of the site-ordering curve based on the numerical results obtained in [1]. In particular, we consider a square $n \times n$ lattice and compare the numerical precision achieved using the standard snake curve (see Fig. 2.5d) and the Hilbert curve (see Fig. 2.5c) detailed in Sec. 2.3.2. We demonstrate that, compared to other space-filling curves, the locality-preserving properties of the Hilbert curve leads to a clear improvement of numerical precision, especially for large system sizes, and turns out to provide the best performances for the simulation of 2D lattice systems via 1D TN structures.

2.3.1 Preserving the locality of interactions

Before effectively comparing different $2D \rightarrow 1D$ mappings, let us deepen the concept of preserving the interaction range (i.e. locality). In the context of numerical simulations with TN algorithms, it would be extremely useful to map a 2D lattice into a 1D chain in a way that preserves locality at most, avoiding long-range interactions of sites that are very far apart from each other. However, it is straightforward to prove that it is impossible to map a D -dimensional lattice into a D' -dimensional one, with $D' < D$, so that two neighboring sites in the D -lattice are always close together in the D' -lattice. Let us consider, for instance, nearest neighbour sites: each point of the D -dimensional square lattice has $2D$ nearest neighbours, while only $2D'$ nearest neighbours in the D' -dimensional one. Thus, after the mapping, at least $2(D - D')$ sites will be placed at a distance larger than one unit. For the specific case of a 2D square lattice and a 1D

chain, this implies that the optimal solution would be a mapping such that two out of four nearest neighbours in the 2D lattice remain nearest neighbours in the 1D chain. If we strictly follow this argument, the best choice would be the frequently used snake curve, shown in Fig. 2.5d. However, in this way, the other two nearest neighbours of a generic site of the 2D lattice would be rather far away from each other in the one-dimensional setup, with their distance increasing up to $2n$. If our goal is to preserve the locality also for these two other nearest neighbours, the curve that tends to globally satisfy these constraints, outperforming other types of mapping, is exactly the Hilbert curve.

2.3.2 Hilbert curve

Without going into much detail (see [226–228] for an exhaustive description), the Hilbert curve is a 1D fractal-like self-similar *space-filling* curve with Hausdörrff dimension $\delta = 2^3$ introduced for the first time in 1891 by the mathematician David Hilbert [230]. Notably, among other interesting properties, it allows to create a mapping between a 1D and a 2D space by keeping and preserving the locality: this implies that two points that are close to each other in the 1D space are close to each other also after folding on the 2D space. The converse is not always strictly true, as unavoidable when passing from two-dimensions to one-dimension. However, even in this case, the curve shows a tendency to preserve the locality as much as possible [226–228]. For this reason, it finds several applications in computer science [231] and bioinformatics [232].

Effective construction The basic element of the Hilbert curve is obtained by connecting the elements of a 2×2 lattice starting from the bottom-left (BL) to the bottom-right (BR) corner as shown in Fig. 2.5a. From this we can now construct the $n = 4$ Hilbert curve via the following procedure: draw the $n = 2$ Hilbert curve into the top-left (TL) and top-right (TR) quadrants, while rotating it clockwise and counterclockwise by 90 degrees in the BL and BR quadrants respectively. Then, by joining these different curve replicas, we end up with the $n = 4$ curve shown in Fig. 2.5b. The generalization to the level n for covering the $n \times n$ lattice is then straightforward: the $2n$ curve is obtained by drawing the n curve in the four main quadrants of the $2n \times 2n$ lattice and by applying the just mentioned rules for the rotations in the BL and BR quadrants. In Fig. 2.5c, for example, we report the Hilbert curve for the 8×8 lattice.

Comparing space filling curves

To get an intuition of how different curves preserve locality, we report in Fig. 2.5c the Hilbert mapping of a generic site of the 2D lattice (within a given quadrant) and its four nearest neighbours: it is evident that all these points that are close on the two-dimensional plane remain fairly close on the one-dimensional chain. On the contrary, this property does not hold for the standard snake mapping, where, as expected, two out of four nearest neighbours are almost always mapped at large distance, as shown in Fig. 2.5d. The only regions in which the Hilbert mapping does not preserve the locality are the inner borders of the main quadrants. In this case, nearest neighbor sites belonging to two adjacent quadrants turn out to be mapped quite far away from each other. Nonetheless, in the limit of large lattices, the number of these points becomes negligible $\sim \mathcal{O}(n)$ w.r.t the total number of sites.

³The fractal or Hausdörrff dimension δ is a measure of roughness (or smoothness) for a smooth, differentiable D -dimensional surface $S \in \mathbb{R}^{D+1}$ with topological dimension D . If the surface is nondifferentiable and rough, the fractal dimension δ of S takes values between the topological dimension D and $D + 1$ [229]. The closer δ to $D + 1$, the better the ability of S in covering the \mathbb{R}^{D+1} manifold space where the surface is embedded.

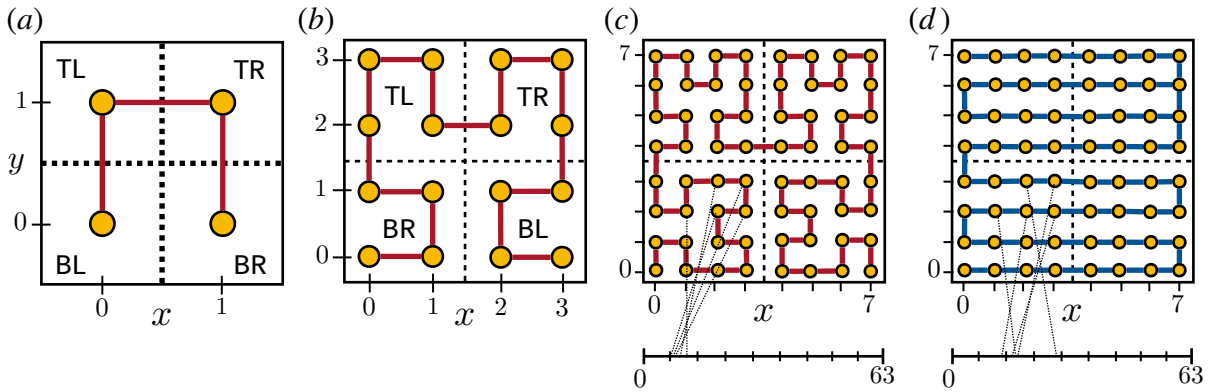


Figure 2.5: Iterative construction of the space-filling Hilbert curve on an $n = 4, 8, 16$ (a)-(c) square lattice. Examples of nearest-neighboring 2D lattice points mapped into 1D points making use of the Hilbert curve (c) and the Snake curve (d) respectively. Figure from [1].

2.3.3 Numerical evidences

In [1], we compare the performance obtained from the Hilbert and the snake curve on MPS and TTN simulations. We focus on the ground state properties of the 2D Ising model at zero temperature in presence of a uniform transverse magnetic field along the z -direction [233] with the following Hamiltonian:

$$\hat{H} = J \sum_{\langle i,j \rangle} \hat{\sigma}_i^x \hat{\sigma}_j^x + \lambda \sum_i \hat{\sigma}_i^z, \quad (2.3.2)$$

where $\langle i, j \rangle$ refers to the nearest neighbour sites and $\hat{\sigma}_i^\alpha$ is the Pauli matrix in the α -direction defined on the site i . The coefficient J represents the strength of the interaction between nearest neighbour spins along the x -axis, whereas λ determines the strength of the external magnetic field along the z -axis. In the following, we consider the antiferromagnetic (AF) scenario for $J > 0$, and, without loss of generality, we fix the energy scale by setting $J = 1$.

Ground-state energy density

We simulate the Hamiltonian in Eq. (2.3.2) on a square lattice $n \times n$ with different sizes, up to $n = 64$, and both boundary conditions. To compare the Hilbert and the snake mappings, we express Eq. (2.3.2) as a long-range, one-dimensional Hamiltonian $\hat{H}_{S(H)}$ where sites are sorted according to the snake (S) or the Hilbert (H) curve. As shown in [1], for both MPS and TTN simulations, the Hilbert curve mapping provides more accurate ground state energies, especially close to the second order critical point [234, 235], stressing the relevance of our analysis for the study of quantum phase transitions. More in detail, as shown in Fig. 2.6, the Hilbert curve shows a faster convergence of the energy as the bond dimension χ is increased.

Local Magnetization

Additionally, it is possible to understand which regions of the lattice contribute to the energy improvement by studying the expectation values of the local magnetization. We measure the local expectation values of the magnetization $\{\langle \hat{\sigma}_k^z \rangle\}_{1 \leq k \leq n^2}$ on both the ground states of the two Hamiltonians \hat{H}_H and \hat{H}_S and compute the difference $\Delta \hat{\sigma}_k^z = |\langle \hat{\sigma}_k^z \rangle_H - \langle \hat{\sigma}_k^z \rangle_S|$. As shown in Fig. 2.7, $\Delta \hat{\sigma}_k^z$ seems to be significant all over the lattice quadrants, while vanishing on their edges (the black lines in Fig. 2.5c), where the magnetization values obtained from the two methods are similar. This result aligns with the fact that the Hilbert curve excels at preserving the locality

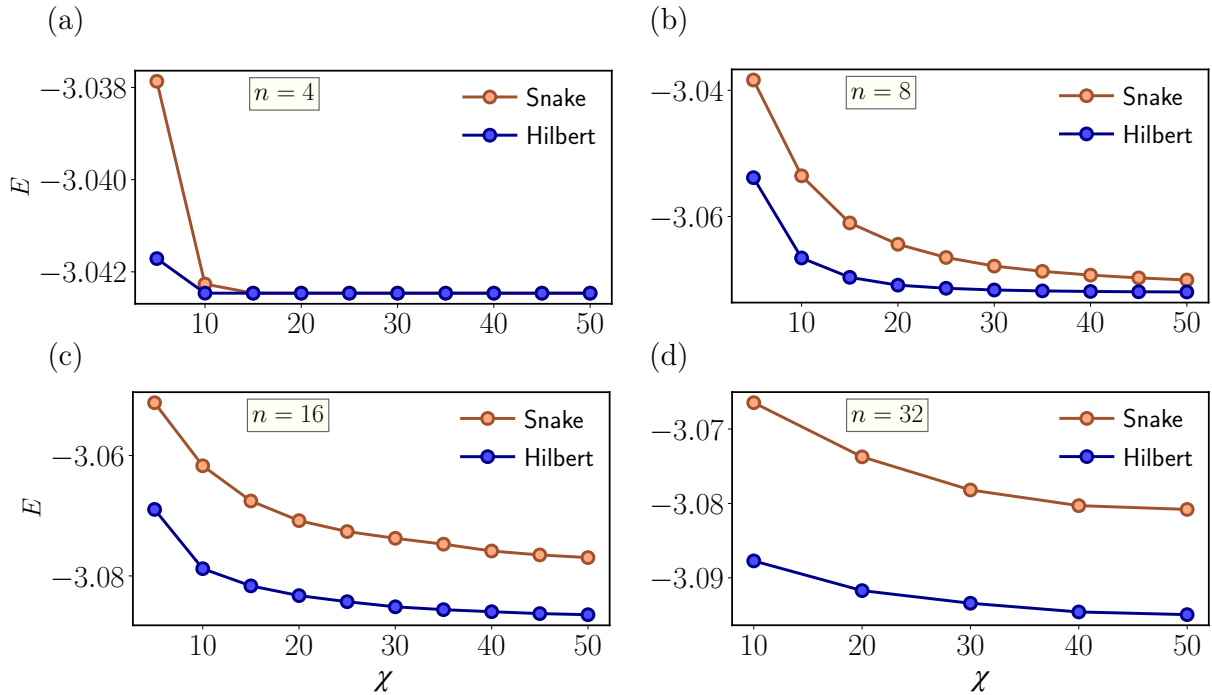


Figure 2.6: Numerical simulations of the 2D quantum Ising Hamiltonian at $\lambda = 2.9$, i.e. close to the quantum critical point. Ground-state energy density measurements obtained via TTN at different system sizes n employing the Snake and the Hilbert ordering for incremental values of the bond dimension χ . Similar results are obtained via MPS and discussed in [1].

of interactions within the core of the quadrants, while its performance near the edges becomes comparable to that of other orderings, such as the snake. In these terms, we expect to observe similar results also when considering other observables, such as two-point correlation functions.

2.3.4 Distance distributions

For a more rigorous explanation of the previous numerical results, let us introduce two distances d_{MPS} and d_{TTN} , defined as the number of links connecting two different lattice sites within the MPS and TTN network geometries respectively. Namely, we consider the interaction terms of the 1D Hamiltonians $\hat{H}_{\mathcal{S}}$ and $\hat{H}_{\mathcal{H}}$ of Eq. (2.3.2) and compute the distances d_{MPS} and d_{TTN} between all the relative couples of sites. We obtain then four sets of distances, each of them labeled by the relative mapping (snake and Hilbert) and the TN geometry (MPS and TTN).

Different curves In Fig. 2.8, we fix $n = 16$ and plot the distributions of d_{MPS} and d_{TTN} for the snake (left column) and the Hilbert (right column) mappings: one can qualitatively see that the probabilities at large distances are larger for the snake mapping than for the Hilbert one. This feature is particularly evident in the TTN case, due to the logarithmic scaling of distances within the network.

Different Tensor Network Geometries Remarkably, when focusing on the same space filling curve (e.g. the Hilbert curve) we can compare the MPS and TTN method the distributions of d_{MPS} and d_{TTN} on different values of n . As shown in Fig. 2.9, the fraction of interaction terms with largest distances changes when we move from $n = 16$ to $n = 32$ and decreases faster in the MPS case than in the TTN one. This explains why the improvement achievable with the

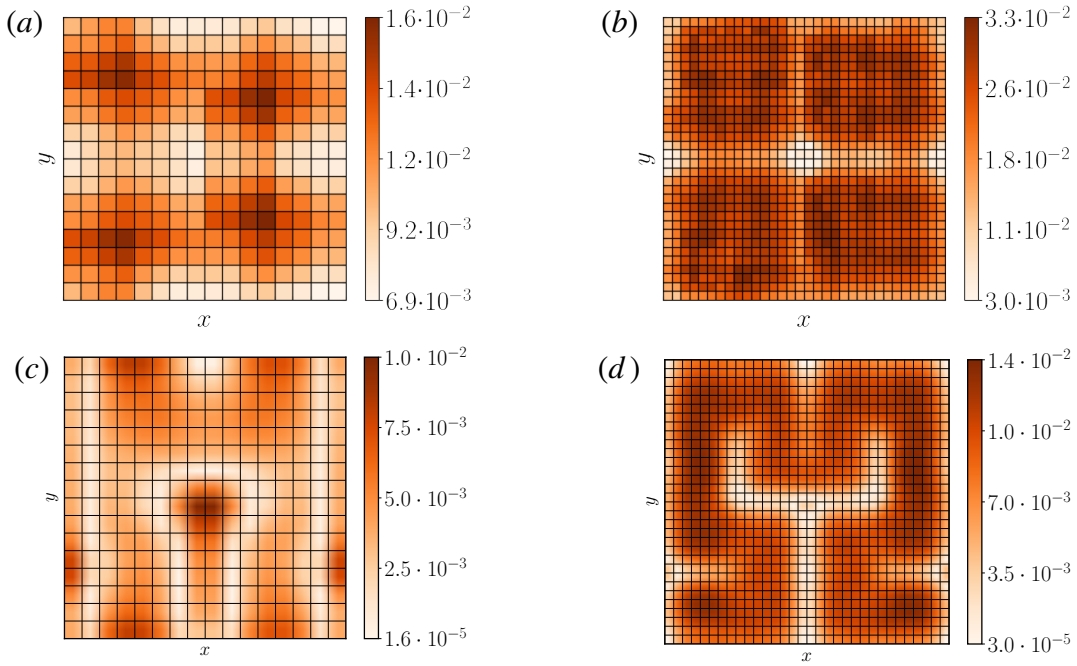


Figure 2.7: Local magnetization difference between the Hilbert and the snake ground states for $n = 16$ (left panel) and $n = 32$ (right panel) computed by using TTNs (upper row) and MPS (lower row) for $\lambda = 2.9$, $\chi = 50$, and PBC. The regions with similar expectation values (i.e. the quadrants borders) are those where neither the Hilbert nor the snake curve are able to properly preserve the locality of the interactions.

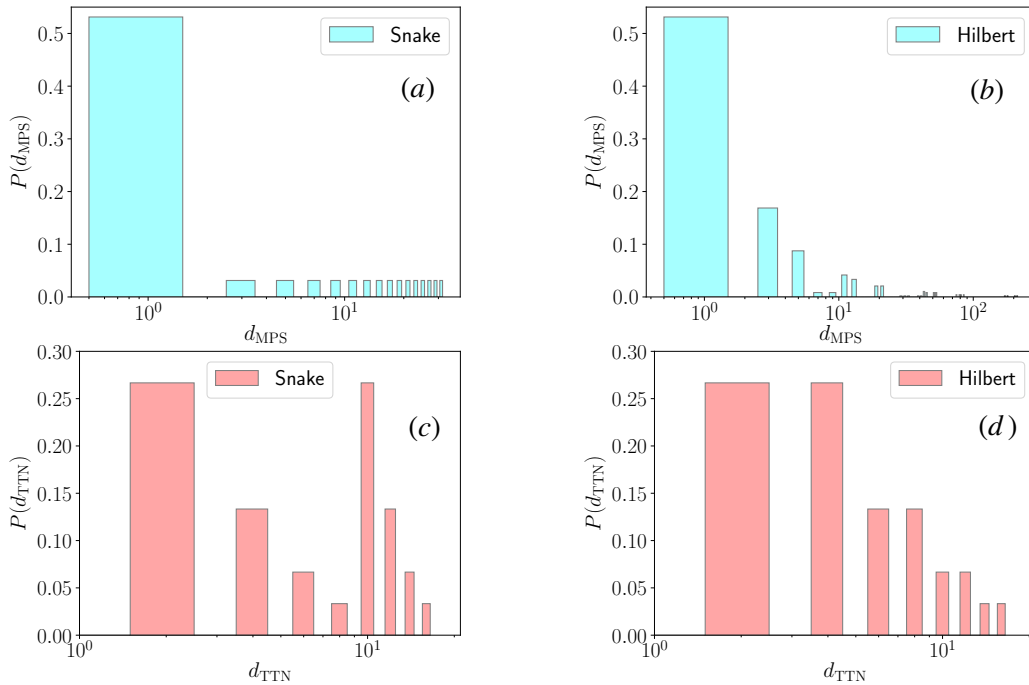


Figure 2.8: Distributions of the number of TN links separating physically adjacent lattice sites in the 2D lattice d_{MPS} (first row) and d_{TTN} (second row) relative to the pairs of sites connected by an interaction term in the Hamiltonians \hat{H}_S (first column) and \hat{H}_H (second column), for $n = 16$.

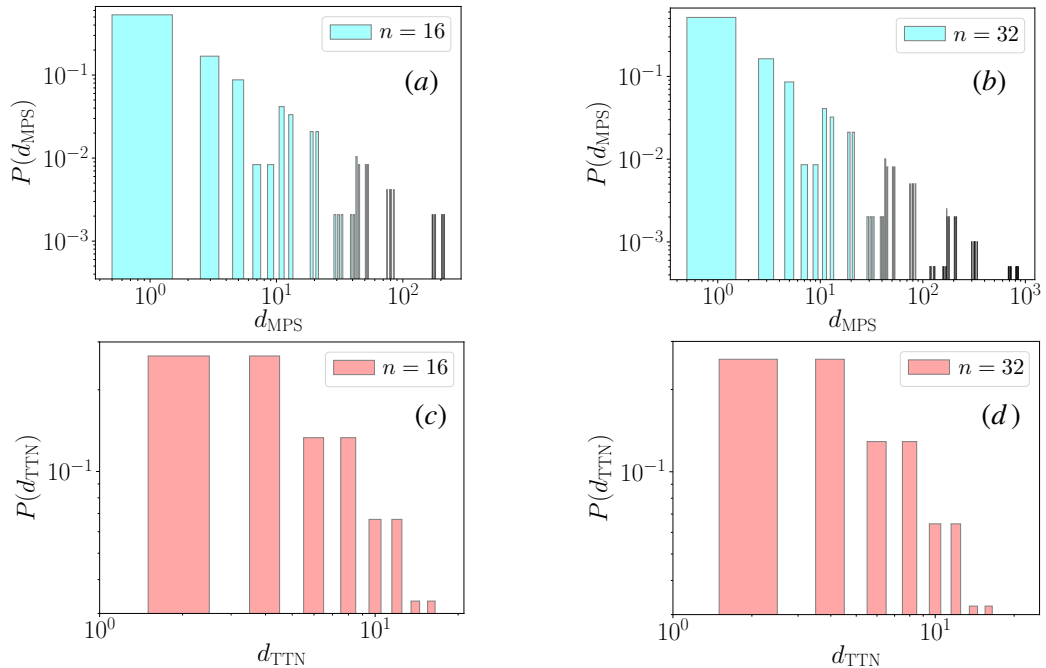


Figure 2.9: Distributions of the distances d_{MPS} (first row) and d_{TTN} (second row) relative to the pairs of sites connected by an interaction term in the Hamiltonian $\hat{H}_{\mathcal{H}}$ computed for $n = 16$ (first column) and $n = 32$ (second column).

MPS and the Hilbert curve is larger than the one achievable with TTNs, even though the TTN simulations are overall more accurate than the MPS ones.

2.3.5 Conclusions

These results are particularly interesting, as they provide useful hints for simulating QMB systems and LGTs beyond one spatial dimension. In particular, the choice of an optimal space filling curve, such as the Hilbert one, to map a d -dimensional lattice onto a one-dimensional one, reveals fundamental to minimize long-range interactions on both MPS and TTN ansätze.

While the locality-preserving properties of the Hilbert ordering are directly mapped onto the MPS chain, in the case of TTNs they are enhanced by the logarithmic scaling of distances within the TTN structure. By recalling that the standard TTN methods for two-dimensional systems rely on the construction of a 2D bTTN [173], it is worth noting that the 2D bTTN and the Hilbert curve mapping generate the same long-range interactions within the corresponding networks. Therefore, the former benefits from the mathematical locality-preserving properties of the Hilbert curve.

We have then obtained a systematic strategy to evaluate, given a QMB system defined on a two-dimensional lattice, the more efficient site-ordering to perform simulations by using TNs, based on the analysis of the effective, one-dimensional system generated by the mapping. Our results suggest that 1D variational ground state searching algorithms, such as DMRG, strongly benefit from the choice of the Hilbert curve for treating 2D systems. This can be easily extended to rectangular lattices, such as long narrow cylinders, or on 3D cubic lattice, since it is possible to generalize the Hilbert curve definition also in these cases. Other possible outlooks include the application of this strategy to the study of systems characterized by non-trivial lattice structures and interactions, as for example in spin glasses [236] and quantum chemistry [237].

2.4 Variational ground state search algorithm

We now present the ground-state search algorithm for TTN simulations which has been used for simulating LGTs [2, 89, 90] such as the (2+1)D SU(2) theory in Chap. 3. A pictorial explanation of the algorithm is sketched in Fig. 2.10a. Let us suppose to search for the ground state properties of a QMB Hamiltonian \hat{H}_{QMB} . Formally, if $|\Psi_{\text{QMB}}\rangle$ is the target state, any observable requires the contraction of the Hamiltonian tensor operator with the TN state and its hermitian conjugate: $\langle\Psi_{\text{QMB}}|\hat{H}|\Psi_{\text{QMB}}\rangle$. To reduce the complexity of the minimization problem, we use a *variational* approach that optimizes a single tensor T_{var} of $|\Psi_{\text{QMB}}\rangle$ per step⁴. We fix a T_{var} as the *optimization center* and treat all its parameters as variational. Correspondingly, all the other tensors of the TN are kept fixed to form the so-called *TN environment*. We then contract the environment with the Hamiltonian operator, obtaining an *effective Hamiltonian* \hat{H}_{eff} which acts only on T_{var} . Properly, this is just a *local optimization problem*, which involves only two single tensors, respectively T_{var}^* from $\langle\Psi_{\text{QMB}}|$ and T_{var} from $|\Psi_{\text{QMB}}\rangle$ ⁵. Then, if we sequentially solve the reduced optimization problem for each TN node, (i.e. by moving the optimization center following the numbered tensors in Fig. 2.10a), the energy expectation value is gradually reduced up to a certain fixed minimal value. The whole series of local optimizations in $|\Psi_{\text{QMB}}\rangle$ is also known as *sweep sequence*.

2.4.1 High level operations

We then focus on a single local optimization problem [49]. Let us consider a TTN geometry of tensors $T^{[q]}$ whose nodes $q \in \{1 \dots Q\}$ are mutually joined by auxiliary links ζ of dimension χ_ζ . We suppose to use *unitary gauges* and fix an arbitrary center node T_{var} w.r.t. which each tensor of the environment is gauge transformed. Correspondingly, we assume the Hamiltonian as a sum of P different contributions (e.g. the kinetic energy, the interaction potential, or an external magnetic field):

$$\hat{H} = \sum_{p=1}^P \hat{H}_p, \quad (2.4.1)$$

where each term \hat{H}_p is a Tensor Product Operator (TPO) like the following (see Fig. 2.10b):

$$\left[\hat{H}_p\right]_{\{i_s\}\{j_s\}} = \sum_{\{\gamma_\mu\}} \prod_s \left[\hat{h}_{p,k(s)}^{[s]}\right]_{i_s j_s}^{\{\gamma_\mu\}_{k(s)}}. \quad (2.4.2)$$

In this expression, $\{i_s\}$ and $\{j_s\}$ label the sets of physical links which connect the Hamiltonian interaction \hat{H}_p with $\langle\Psi_{\text{QMB}}|$ and $|\Psi_{\text{QMB}}\rangle$ respectively; $\hat{h}_{p,k(s)}^{[s]}$ is the k^{th} *local operator* of the specific TPO \hat{H}_p acting on the physical site s of the TN.

Local operators such as $\hat{h}_{p,k(s)}^{[s]}$ and $\hat{h}_{p,k'(s')}^{[s']}$, concurrently acting on the physical sites s and s' , are connected among each other through TPO links like $\gamma_{\mu=(k,k')}$ (see Fig. 2.10b). The sum $\sum_{\{\gamma_\mu\}}$ runs over all the TPO links $\{\mu\}$ and we define $\{\mu\}_{k(s)} \subseteq \{\mu\}$ as the set of all the links μ attached to the k^{th} TPO operator $\hat{h}_{p,k(s)}^{[s]}$.

Renormalization

At this point, once fixed a center node c of the TTN structure defining $|\Psi_{\text{QMB}}\rangle$, we associate to each auxiliary link ζ of the TTN a *renormalized Hamiltonian* $\hat{h}_{p,k(\zeta)}^{[\zeta]}$, which describes the effective

⁴In practice, we exploit the Krylov sub-space expansion technique to numerically solve the local eigenvalue problem for each tensor [49].

⁵This step is efficiently carried out by applying the Arnoldi method of the ARPACK library [238]

action of the single Hamiltonian TPO in Eq. (2.4.2) onto the subsystem (or partition) S_ζ , made of all the environmental sites of the TN separated by ζ from the current network center c .

To figure out the situation, let us consider a given node $q \neq c$ with a proper set of auxiliary links $\{\eta\}_q$. We can suppose that, among these links, the link ζ is the one through which the node q communicates with c (see Fig. 2.10c). All the remaining links are then denoted with $\{\xi\}_q$, in such a way that $\{\eta\}_q = \zeta + \{\xi\}_q$. Then, we define the renormalized Hamiltonian associated to the link ζ in the following recursive way:

$$\left[\hat{h}_{p, \mathbb{K}(\zeta)}^{[\zeta]} \right]_{\{\alpha_\xi\} \{\beta_\xi\}}^{\{\gamma_\mu\}_{\mathbb{K}(\zeta)}} = \sum_{\substack{\text{paired } \xi \neq \zeta \\ \{\gamma_\mu\}}} \prod \left[\hat{h}_{p, \mathbb{K}(\xi)}^{[\xi]} \right]_{\alpha_\xi \beta_\xi}^{\{\gamma_\mu\}_{\mathbb{K}(\xi)}} \quad \text{where} \quad \mathbb{K}(\zeta) = \bigcup_{\xi \neq \zeta} \mathbb{K}(\xi). \quad (2.4.3)$$

In $\mathbb{K}(\zeta)$, we collect all the physical renormalized Hamiltonians defined on all the links $\{\xi\}_q$ of the TN node q with $\xi \neq \zeta$ (we recall that both ζ and ξ are auxiliary links of the TN structure, not of the Hamiltonian TPO). These terms are generally connected by some TPO links $\{\mu\}$, over which the contractions are performed (and the sum is taken).

The fundamental unit of a renormalized Hamiltonian $\hat{h}_{p, \mathbb{K}(\xi)}^{[\xi]}$ is a single renormalized Hamiltonian operator $\hat{h}_{p, \mathbb{K}}^\xi$, where \mathbb{K} is the set of all local operators of the TPO $\hat{h}_{p, k(s)}^{[s]}$ involved the renormalization:

$$\mathbb{K}(\xi) = \bigcup_{s \in S_\xi} k(s) \quad (2.4.4)$$

Properly, in order to effectively obtain the renormalized Hamiltonian over the link ζ , we must additionally contract the Hamiltonian operators $\hat{h}_{p, \mathbb{K}(\xi)}^{[\xi]}$ over the links $\xi \neq \zeta$ with the node tensor $T^{[q]}$ and its complex conjugate $T^{[q]*}$:

$$\left[\hat{h}_{p, \mathbb{K}(\zeta)}^{[\zeta]} \right]_{\alpha_\zeta \beta_\zeta}^{\{\gamma_\mu\}_{\mathbb{K}(\zeta)}} = \sum_{\{\alpha_\xi\}} \sum_{\{\beta_\xi\}} T^{[q]}_{\alpha_\zeta \{\alpha_\xi\}} \left[\hat{h}_{p, \mathbb{K}(\zeta)}^{[\zeta]} \right]_{\{\alpha_\xi\} \{\beta_\xi\}}^{\{\gamma_\mu\}_{\mathbb{K}(\zeta)}} T^{[q]*}_{\{\beta_\xi\} \beta_\zeta} \quad (2.4.5)$$

In the unitary gauge, the tensor $T^{[q]}$ appears as an isometry (see Eq. (2.2.8) et seq.) over the links $\xi \neq \zeta$. Therefore, it is immediately clear that if Eq. (2.4.3) holds 1, so Eq. (2.4.5) does. Obviously, such renormalized Hamiltonians are defined for each kind of interaction $p = 1 \dots P$.

Effective Hamiltonian

At this point, we exploit the variational feature of the algorithm: for a given center node c (i.e. the unitary gauge center), we define the *effective Hamiltonian* $\hat{H}_{\text{eff}}^{[c]} = \langle \Psi_{\text{env}}^{[c]} | \hat{H} | \Psi_{\text{env}}^{[c]} \rangle$ where $\Psi_{\text{env}}^{[c]}$ stands for the result of the TN contractions over all the tensors of the TN except $T^{[c]}$, i.e. over the environment of the center node. Then, the energy expectation value $E_{[c]}$ of the TN state with respect to the given center node c reads

$$E_{[c]} = \langle \Psi_{\text{QMB}}^{[c]} | \hat{H} | \Psi_{\text{QMB}}^{[c]} \rangle = \langle T^{[c]} | \langle \Psi_{\text{env}}^{[c]} | \hat{H} | \Psi_{\text{env}}^{[c]} \rangle | T^{[c]} \rangle = \langle T^{[c]} | \hat{H}_{\text{eff}}^{[c]} | T^{[c]} \rangle. \quad (2.4.6)$$

Basically, in order to obtain $\hat{H}_{\text{eff}}^{[c]}$, we do not need to contract the entire environment if we have already computed the renormalized Hamiltonians over all the available links of c . We should have:

$$\hat{H}_{\text{eff}}^{[c]} = \sum_{p=1}^P \hat{h}_{p, \text{eff}}^{[c]} \quad \text{where} \quad \left[\hat{h}_{p, \text{eff}}^{[c]} \right]_{\{\alpha_\eta\} \{\beta_\eta\}} = \sum_{\{\gamma_\mu\}} \prod_{\eta} \left[\hat{h}_{p, \mathbb{K}(\eta)}^{[\eta]} \right]_{\alpha_\eta \beta_\eta}^{\{\gamma_\mu\}_{\mathbb{K}(\eta)}}. \quad (2.4.7)$$

are the renormalized Hamiltonian terms defined over all links $\{\eta\}_c$ of the node c with corresponding indices $\{\alpha_\eta\}$ and $\{b_\eta\}$. Hence, the effective Hamiltonian involves the contraction of all renormalized Hamiltonian terms over each tensor link $\eta \in \{\eta\}_c$ of the center node c . Plugging together all the previous steps, we can rewrite the energy expectation value $E_{[c]}$ as following:

$$\begin{aligned}
E_{[c]} &\equiv \langle \Psi_{\text{QMB}}^{[c]} | \hat{H} | \Psi_{\text{QMB}}^{[c]} \rangle = \langle \Psi_{\text{QMB}}^{[c]} | \sum_{p=1}^P \hat{H}_p | \Psi_{\text{QMB}}^{[c]} \rangle \\
&\stackrel{(2.4.6)}{=} \langle T^{[c]} | \langle \Psi_{\text{env}}^{[c]} | \hat{H} | \Psi_{\text{env}}^{[c]} \rangle | T^{[c]} \rangle = \langle T^{[c]} | \hat{H}_{\text{eff}}^{[c]} | T^{[c]} \rangle \\
&= \langle T^{[c]} | \sum_{p=1}^P \hat{h}_{p,\text{eff}}^{[c]} | T^{[c]} \rangle = \sum_{\{\beta_\zeta\}} \sum_{\{\alpha_\zeta\}} T_{\{\beta_\zeta\}}^{[c]*} \left(\sum_{p=1}^P \left[\hat{h}_{p,\text{eff}}^{[c]} \right]_{\{\beta_\zeta\}, \{\alpha_\zeta\}} \right) T_{\{\alpha_\zeta\}}^{[c]} \\
&\stackrel{(2.4.7)}{=} \sum_{\{\beta_\zeta\}} \sum_{\{\alpha_\zeta\}} T_{\{\beta_\zeta\}}^{[c]*} \sum_{p=1}^P \left[\sum_{\{\gamma_\mu\}} \prod_{\zeta} \left[\hat{h}_{p,\mathbb{K}(\zeta)}^{[\zeta]} \right]_{\beta_\zeta, \alpha_\zeta}^{\{\gamma_\mu\}_{\mathbb{K}(\zeta)}} \right] T_{\{\alpha_\zeta\}}^{[c]} \\
&\stackrel{(2.4.5)}{=} \sum_{\{\beta_\zeta\}} \sum_{\{\alpha_\zeta\}} T_{\{\beta_\zeta\}}^{[c]*} \sum_{p=1}^P \left[\sum_{\{\gamma_\mu\}} \prod_{\zeta} \left[\sum_{\{\beta_\xi\}} \sum_{\{\alpha_\xi\}} T_{\beta_\zeta, \{\beta_\xi\}}^{[q]*} \left[\left[\hat{h}_{p,\mathbb{K}(\zeta)}^{[\zeta]} \right]_{\{\beta_\xi\}, \{\alpha_\xi\}}^{\{\gamma_\mu\}_{\mathbb{K}(\zeta)}} \right] T_{\{\alpha_\xi\}, \alpha_\zeta}^{[q]} \right] \right] T_{\{\alpha_\zeta\}}^{[c]} \\
&\stackrel{(2.4.3)}{=} \sum_{\{\beta_\zeta\}} \sum_{\{\alpha_\zeta\}} T_{\{\beta_\zeta\}}^{[c]*} \sum_{p=1}^P \sum_{\{\gamma_\mu\}} \prod_{\zeta} \sum_{\{\beta_\xi\}} \sum_{\{\alpha_\xi\}} T_{\beta_\zeta, \{\beta_\xi\}}^{[q]*} \sum_{\substack{\text{paired } \xi \neq \zeta \\ \{\gamma_\mu\}}} \prod_{\xi} \left[\hat{h}_{p,\mathbb{K}(\xi)}^{[\xi]} \right]_{\beta_\xi, \alpha_\xi}^{\{\gamma_\mu\}_{\mathbb{K}(\xi)}} T_{\{\alpha_\xi\}, \alpha_\zeta}^{[q]} T_{\{\alpha_\zeta\}}^{[c]}.
\end{aligned} \tag{2.4.8}$$

2.4.2 Ground state reach algorithm in details

We can then schedule the algorithm as follows:

Initialization

1. **TN geometry** Define a TN geometry which is compatible with both the physical system and the Hamiltonian interactions. On the same time, such a geometry should be capable of hosting (through auxiliary links) the necessary quantum correlations of the ground state (a reasonable maximal bond dimension should be assigned). Moreover, dealing with loopless TNs, the TN geometry must be chosen according to these constraints:
 - (a) The number of physical links has to be adequate for the Hamiltonian in Eq. (2.4.1).
 - (b) The network has to be *acyclic*: for each pair of nodes, namely q and q' , there has to exist a *unique (shortest) path* connecting them.
 - (c) The dimension χ_η of any auxiliary link η has not to exceed the maximal bond dimension χ of the TN.
 - (d) Each tensor have at least 3 links.
2. **Sweep sequence** Choose the sequence with which the optimization centers are used for the local optimization problem (follow the numbers in the tensors of Fig. 2.10a). Any sequence that visits every tensor of the TN is allowed. However, if the TN has a proper hierarchical structure (as for TTNs), the sweep sequence is based on the distance from a given physical link s . An *optimization precedence* $p \equiv \min_s [\text{dist}(c, s)]$ is assigned to every

optimization center c : in this way, optimization centers with smaller p take precedence over centers with larger p .

3. **Initialize the TN state** A typical choice is to start from a *random* state, as it reduces the possibilities of ending up in local energy minima leading the convergence criteria to fail. For other useful TN initializations, look at Sec. 2.6.2.
4. **Initial optimization center** Select the first optimization center c and transform the network with the unitary gauge w.r.t. c . Contract the two TN environments with the Hamiltonian obtaining the effective Hamiltonian $\hat{H}_{\text{eff}}^{[c]}$. In particular, once the optimization center has been prepared, the effective Hamiltonian is made of contributions like Eq. (2.4.7), while the expectation value of $E_{[c]}$ is given by Eq. (2.4.8). Repeat the local optimization problem for all the other TN nodes up to the end of the chosen sweep sequence.

Optimization loop

1. Optimize $T^{[c]}$ finding the eigenvector associated to the lowest eigenvalue $E_{[c]}$ of $\hat{H}_{\text{eff}}^{[c]}$.
2. Target the next optimization center c' according to the *sweep sequence*; move the isometry center from c to c' by gauge transforming (as in Fig. 2.4c) and updating the renormalized Hamiltonian terms between c and c' . When moving the effective Hamiltonian form the center c to the center c' , only the renormalized Hamiltonian terms defined on the links located along the path from c to c' have to be updated. All the other renormalized Hamiltonians are left unchanged by this movement and do not need to be computed again.
3. Back to step 1. and repeat the optimization with respect to the new center c' up to the end of the sweep sequence.

Convergence in energy

Perform at least 3 different sweep sequences of local optimization. Exploiting the variational definition of the algorithm, we expect that the energy of successive sweep progressively decreases. Then, for each successive couple among the last three sweep sequences s , s' and s'' , with the corresponding energies $E(s)$, $E(s')$ and $E(s'')$, compare both their absolute and relative deviations to reasonable thresholds ϵ and δ respectively⁶. The simulation halts when at least one of the following constraint sets is satisfied:

$$E(s) - E(s') < \epsilon \quad \& \quad E(s') - E(s'') < \epsilon \quad (2.4.9a)$$

$$-\frac{E(s) - E(s')}{E(s')} < \delta \quad \& \quad -\frac{E(s') - E(s'')}{E(s'')} < \delta. \quad (2.4.9b)$$

2.5 Time Evolution Algorithms for Tensor Network

Besides variational optimization for ground state searching, the previous loopless TN families can also be exploited to simulate the real-time dynamics of local Hamiltonians [239], such as the one studied in Sec. 4.4 for detecting QMB scars in non-Abelian SU(2) LGTs. Below, we briefly outline two of the most relevant methods: the Time Evolved Block Decimation (TEBD) and the Time-Dependent Variational Principle (TDVP). These algorithms represent important and efficient tools for simulating with TN the real-time dynamics of QMB systems. While equilibrium

⁶In all the simulations provided in Chap. 3, we fixed $\epsilon = 4 \cdot 10^{-8}$ and $\delta = 8 \cdot 10^{-7}$.

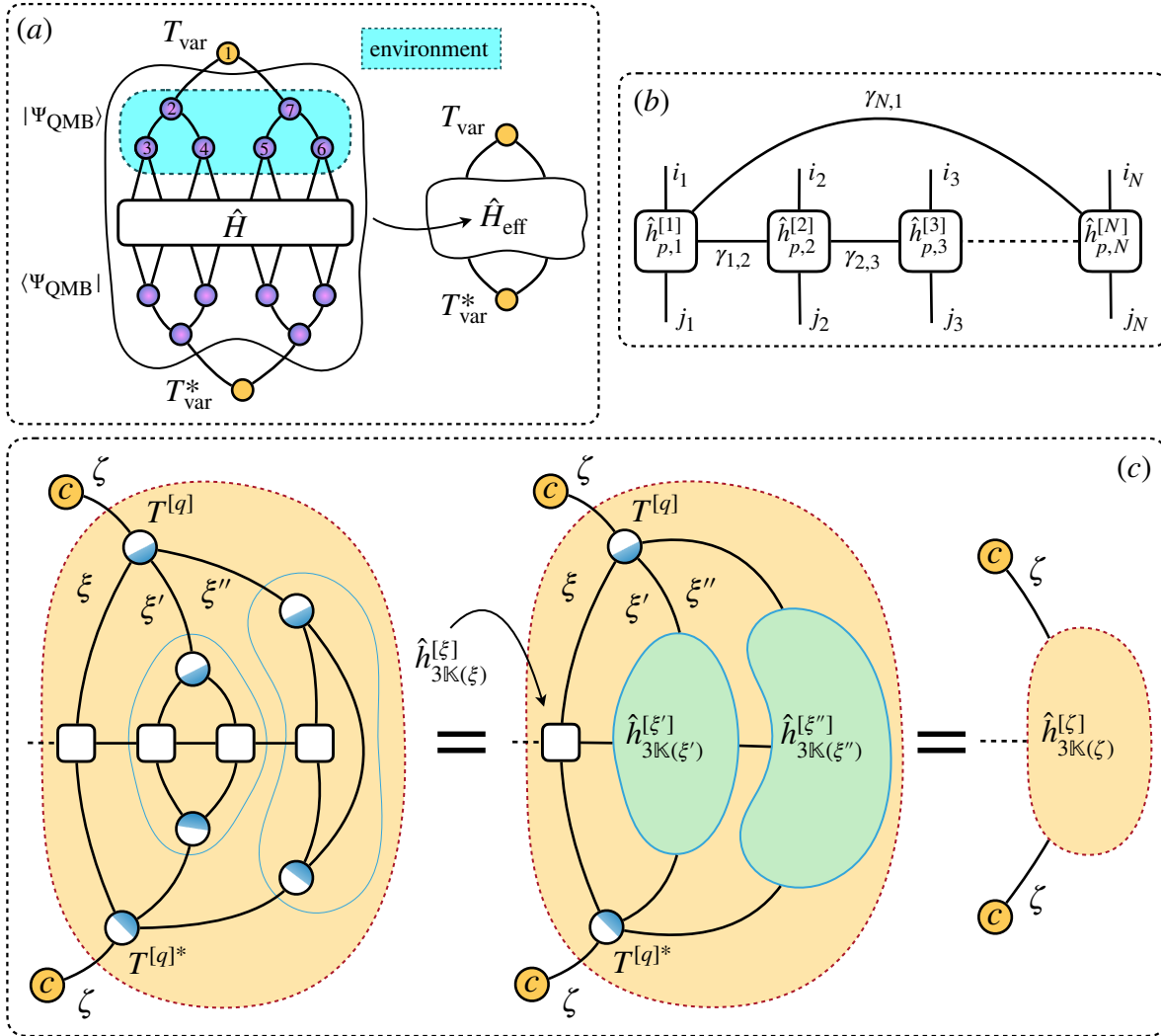


Figure 2.10: (a) Pictorial representation of the variational ground-state search algorithm w.r.t a given node of the TTN geometry. By contracting the environments of $|\Psi_{\text{QMB}}\rangle$ and $\langle\Psi_{\text{QMB}}|$ with the Hamiltonian TPO, one obtains an *effective Hamiltonian* and a *local optimization problem* with respect to T_{var} . Iterating this procedure along the black arrow, one globally minimizes the TPO Hamiltonian with respect to the whole TN structure. (b) Representation of a 1D TPO Hamiltonian in PCB. Each single-site operator $\hat{h}_{p,k}$ display both physical i_k, j_k and auxiliary links γ . The former ones connect the operator respectively to the physical sites of $|\Psi_{\text{QMB}}\rangle$, $\langle\Psi_{\text{QMB}}|$; the latter ones to the other local operators. (c) Iterative Renormalization proceeding with respect to a given auxiliary link ζ of the TN structure. For more details, see [49].

states satisfy the aforementioned area law [50], out-of-equilibrium time evolution can generate a linear growth of entanglement. In such cases, the bond dimension of the time-evolved state grows exponentially with total time [240]. For this reason, TN methods are currently limited to studying the dynamics for low-to-moderate times, close-to-equilibrium phenomena [54], and typically on 1D systems. In this framework, further developments are extremely important to avoid or at least mitigate this barrier, by devising new algorithms or optimizing existing strategies [241, 242].

2.5.1 Time Evolved Block Decimation

One of the most widely used approaches, the Time Evolved Block Decimation (TEBD) algorithm, is based on a Suzuki-Trotter decomposition of the time evolution exponential [210]. The total evolution time is discretized in small time steps. The corresponding evolution operator is computed as products of local terms, such as two-body operators, and repeatedly applied to the TN wave function to generate the time-evolved state. Each application can determine an increase in the bond dimension of the network, so an optimized truncation is needed to maintain an efficient and manageable description of the quantum state. This truncation reduces the bond dimension back to χ and is performed through a singular value decomposition that minimizes the distance between the evolved and the truncated state. In general, the method allows the simulation of the real-time dynamics for nearest-neighbor or finite-range Hamiltonians; one time-step with an MPS for a one-dimensional system with local interactions comes with a computational cost that is below a two-tensor sweep for the ground-state search algorithm.

2.5.2 Time-Dependent Variational Principle

Another method for simulating the evolution of quantum states via TN is the Time-Dependent Variational Principle (TDVP), which does not rely on the Suzuki-Trotter decomposition [243, 244]. In general, TDVP constrains the time evolution to the specific TN manifold considered, such as MPS or TTN, of a given initial bond dimension [245]. This is obtained by projecting the action of the Hamiltonian into the tangent space of the TN manifold and then solving the time-dependent Schrödinger equation within this manifold. This approach automatically preserves the energy and the norm of the quantum states during the time evolution. The TDVP algorithm and the variational ground state search rely both on a set of Krylov vectors and therefore have the same computational scaling for one time step compared to one sweep.

2.6 Roadmap for advanced LGT simulations via tensor networks

As discussed in Chap. 1 and particularly in Sec. 1.2, LGT models present some peculiar features that make TN simulations particularly challenging, especially for large system sizes and for studying the continuum limits in terms of gauge field truncation, lattice spacing, and volume. State-of-the-art techniques, such as TTN methods, have been successfully applied for simulating ground state properties of QED in (2+1)- and (3+1)-dimensions for small-to-intermediate sizes (still well far beyond the standards of ED and quantum simulations) [89, 90]. Very recently, as reported in Chap. 3, TTN have been also applied to the SU(2) Yang-Mills model in (2+1)-dimensions [2], exploring a rich phase diagram at both zero and finite baryon density. In all these simulations, small non-trivial representations of the gauge groups have been exploited, e.g. three electric field levels for QED (see the $j = 1$ example in Sec. 1.4.3), and the first two irreducible representations of SU(2) for the Yang-Mills model (see the *harcure-gluon* approximation in Sec. 1.3.5).

Nowadays, lattice computations with MC-based techniques are performed on large lattices, e.g. of the order $64^3 \times 128$ sites (space and time discretization), and with no truncation of the gauge fields. These large sizes are required to control finite-volume effects and to perform extrapolations toward the continuum limits [246]. In the last decades, the impressive progress in algorithmic development, high-performance optimizations, and the availability of increasingly powerful supercomputer facilities have played a major role in the advancement of MC-based LGT computations. Indeed, this progress has opened the doors to large-scale simulations, that currently represent the standard approach for studying non-perturbative phenomena in QFT.

However, MC techniques are generally based on computations of path integrals in which the integrand functions are overall positive. Many physically relevant scenarios, such as finite baryon density regimes or real-time dynamics of quarks, give rise to a change in the sign of the integrands and highly oscillating behaviors. Thus, numerical evaluations suffer from the near cancellation of the opposite-sign contributions to the integrals. This is the essence of the infamous sign problem, a long-standing issue of LGT simulations with MC methods [13, 38, 39, 187]. Hence the quest lies in conceiving, developing, and optimizing alternative approaches that enable simulating these regimes, being the latter at the heart of many open problems related to our understanding of high-energy physics.

As described in the previous sections, TNs represent a promising complementary method, which found the first applications in simulating non-trivial instances of high-dimensional LGTs on small-to-intermediate lattice sizes. TNs are intrinsically sign-problem-free, enabling the simulation of both static properties at equilibrium, such as low-energy states, and real-time dynamics, even in the presence of finite chemical potentials or non-trivial topological terms. It is worth noting that, in addition to local observables and correlation functions, TNs allow the numerical computations of entanglement properties and central charges, that could potentially shed new light on LGT phenomena [87].

Nevertheless, TN simulations of high-dimensional LGTs still represent a challenging problem, especially for large lattice sizes or higher representations of gauge groups needed for analyzing continuum limits. In this framework, further and intensive developments are required to tackle TNs' current problems related to LGTs, such as QCD's non-perturbative effects on lattices of sizes comparable with MC simulations. In this regard, we note that sign-problem-free TN ansätze can also be used in combination with variational MC methods to tackle high-dimensional lattice gauge theories with arbitrary gauge groups [247].

In the following, we present a possible roadmap [5] in terms of algorithmic development and optimization strategies that we foresee to be crucial for making the TN approach competitive as a complementary method to MC techniques. Therein, Secs. 2.6.1 and 2.6.2, can be approached with existing TN algorithms and a good intuition on LGT problems; then, Sec. 2.6.3 and Sec. 2.6.4 outline optimization for existing algorithms to leverage HPC systems; finally, we discuss new classes of ansätze to tackle finite temperature problems in Sec. 2.6.5. In some parts, we focus on TTNs, but the vast majority of the presented concepts and techniques can be straightforwardly applied to other TN ansätze.

2.6.1 Local basis truncation

One of the main issues in simulating LGTs with TN methods lies in the very large local basis dimension d that one needs to handle to represent matter and gauge-field degrees of freedom properly (see Sec. 1.4.5). To some extent, this situation is very similar to some condensed matter models, e.g. the Holstein model, involving lattice fermions coupled with phonons [248], or bosonic systems coupled to optical cavities [249, 250]. Also in these cases, the local Hilbert space

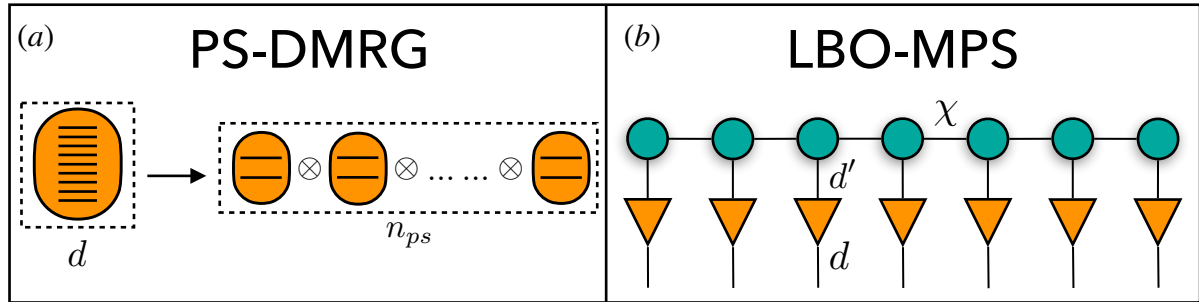


Figure 2.11: Graphical representation of (a) the pseudo site DMRG (PS-DMRG) approach, in which a single site having large local dimension d is replaced with N_{ps} pseudo sites with a smaller local dimension, e.g two; (b) the local basis optimization embedded in the MPS ansatz (LBO-MPS), so that an additional layer of tensors connected to the physical legs of the MPS performs the reduction from a large local basis with dimension d into an effective basis with smaller dimension d' .

is in principle infinite-dimensional, and a truncation to a fixed cutoff is needed for performing TN simulations. For one-dimensional systems of this type, some efficient algorithms based on MPS have been developed in the last years [251], e.g. the pseudosite DMRG (PS-DMRG) method [252], and the DMRG with local basis optimization (DMRG-LBO) [201, 253, 254].

PS-DMRG

The key idea of the PS-DMRG is to replace a single site having large local dimension d with $N_{ps} \approx \log_2(d)$ pseudo sites of local dimension $d = 2$, as shown Fig. 2.11(a). Since a large class of optimization algorithms for TNs scale at least quadratically with the local dimension but linearly with the total number of sites, as detailed in Sec. 2.2, one obtains a more efficient and manageable representation according to this procedure.

The price to pay lies in the range of the interactions: short-range interactions in the Hamiltonian are transformed into long-range operators due to the pseudo-site encoding of the local degrees of freedom. As a consequence, PS-DMRG should require a larger bond dimension χ and a larger number of variational steps to converge; in these terms, the benefits offered by the pseudo-sites could progressively fade for increasing values of N_{ps} at fixed χ . PS-DMRG has been applied to one-dimensional QMB systems with d up to $O(100)$ [251].

DMRG-LBO

The core of the DMRG-LBO algorithm, instead, lies in a local basis optimization protocol which enables a controlled and efficient truncation of the local Hilbert space [255]. For each site \mathbf{n} of the lattice, the optimized local basis is computed by starting from its reduced density matrix:

$$\rho_{\mathbf{n}} = \text{Tr}_{\mathbf{n} \neq \mathbf{n}'} |\psi\rangle\langle\psi|, \quad (2.6.1)$$

where $|\psi\rangle$ is a general state of the whole system and the trace is over all the degrees of freedom which do not involve the site \mathbf{n} . By performing the diagonalization procedure, the eigenvalues λ_{α} and the eigenvectors v_{α} of $\rho_{\mathbf{n}}$ can be easily determined. The set of values λ_{α} represent the probabilities associated with the states v_{α} . If λ_{α} is small, e.g. below a certain numerical threshold, the related eigenvector v_{α} can be discarded from the local basis of the site \mathbf{n} , with a controllable loss of accuracy for the state $|\psi\rangle$. Thus, for reducing the local basis dimension of \mathbf{n} from d to a smaller value d' , an optimal choice is keeping the d' eigenvectors of $\rho_{\mathbf{n}}$ with the

largest probabilities. Then, the original state $|\psi\rangle$ can be projected on the new basis, without losing the relevant physical information. Let us notice that the site \mathbf{n} can also be a generic unit cell of the system, composed of a certain number of lattice sites.

A crucial point of the LBO procedure is the knowledge of the original state $|\psi\rangle$, generally the ground state of the system, that is not known prior. This issue can be overcome in several ways: by performing ED of the system Hamiltonian with local dimension d for small lattice sizes, to determine $|\psi\rangle$, and then truncating the basis from d to d' for increasing values of the cutoff d' . From this procedure, we can obtain an optimized local basis ensuring a controlled approximation of the original ground state. This optimized basis can then be exploited in optimization algorithms for simulating larger lattice sizes, such as DMRG. Another strategy directly incorporates the LBO procedure in the TN ansatz, as shown Fig. 2.11(b): by inserting an additional tensor on each physical leg of the MPS, the large local basis with dimension d is transformed into an effective basis with smaller dimension d' . In this way, the MPS tensors only see the effective basis in the optimization procedures, with a significant reduction of the computational costs described in Sec. 2.2. This method has been used for both static DMRG and time evolution algorithms, such as , for the study of one-dimensional quantum impurity models and correlated electron-phonon systems [201, 253, 256].

Local basis truncation for LGTs

In the context of LGTs, the dimension of the local basis d can easily go beyond values of the order of 10^6 , especially for higher-dimensional non-Abelian models and large representations of the gauge groups, as shown in Sec. 1.4.5 and Tab. 1.1. In this scenario, numerical simulations with TNs are practically infeasible without an optimized scheme for truncating the local degrees of freedom. Techniques like PS-DMRG might offer some benefits for small system sizes, such as unveiling the most relevant degrees of freedom in the low-energy states, but it is difficult to scale them up for large sizes due to the long-range interactions induced between the pseudo-sites. Also, the local constraints imposed by Gauss law would become highly non-local when splitting a single site into multiple pseudo-sites representing the matter and link fields.

In principle, LBO-based procedures could instead represent a well-grounded route for addressing the problem. Their use in condensed matter, e.g. bosonic systems, is a rather consolidated approach, whereas their application to TN simulations of LGTs currently is an uncharted but promising territory. The main steps that we foresee as needed and important in this direction are the following:

- (i) Employing ED [6], testing the convergence of LBO procedures for one-dimensional systems, such as the φ^4 -theory or the Schwinger model, for which analytical solutions, at least in some regimes of the phase diagram, and numerical results are widely available, also in the limit of no gauge field truncations. In this way, we can obtain valuable information about the scaling of the basis cutoffs concerning the final accuracy of the state representation for small system sizes.
- (ii) Performing the same analysis on (2+1)-dimensional LGTs, such as QED or $SU(N)$ models, for one unit cell, like a single lattice-plaquette, to systematically study the effects of the magnetic interactions on the local degrees of freedom. Indeed, finite truncations of gauge fields as the ones detailed in Sec. 1.4.2 and Sec. 1.3.2, generally exploits the *electric field* basis, in which the electric field terms of the Hamiltonian and Gauss law are diagonal (see the dressed-site formalism in Sec. 1.2). In this scheme, the magnetic interactions correspond to non-diagonal operators which can increase the number of local electric states to include for

an accurate description of the system, especially for small values of the coupling constant g of Eq. (1.1.65), as highlighted in the numerical analysis in Sec. 1.4.5 [5].

- (iii) Exploiting the optimized local bases obtained from ED as input of TN simulations for larger sizes, testing the effects on the global ground state accuracy and in computing physically relevant quantities, such as the mass gap [146].
- (iv) In the same spirit of LBO-MPS, implementing LBO protocols directly in TN ansätze that are more suitable for simulating high-dimensional LGT models, such as TTN. This step could be of great benefit in particular for aTTNs [173], which encode the area law for the entanglement but are severely limited by large local bases (see Sec. 2.2).

By following and combining all these steps, we expect to reduce the effective local basis of LGT models, potentially enabling TN simulations for large representations of Abelian and non-Abelian gauge groups.

It is worth noting that constructing optimal bases for numerical and quantum computation of LGTs is an active area of research. Several approaches that have been recently proposed involve performing canonical transformations of the gauge degrees of freedom before truncation [109, 110, 112, 257]. By exploiting a resource-efficient protocol of this type, Ref. [112] has shown that the number of local states required to reach a 1% accuracy level when computing the expectation value of the plaquette operators in two-dimensional (2+1)-dimensional QED can be reduced by more than 94% compared to the unoptimized truncation. Integrating these approaches into TN algorithms could greatly benefit LGT simulations.

2.6.2 Tailored initial states

In TN algorithms for ground state searching, the optimization procedure generally starts from a random TN initial state $|\psi_{\text{init}}\rangle$, i.e. the tensors in the network are filled with random coefficients at the beginning. This strategy usually guarantees that the probability of overlapping with the true ground state $|\langle\psi_{\text{init}}|\psi_{\text{gs}}\rangle|^2$ is not vanishing. To reach a small error in the final energy, this procedure typically requires from 10 to 50 optimization sweeps for LGTs simulations, depending on the specific models, the Hamiltonian parameters, and the lattice size. Since the time for completing a sweep can be very long, especially for large bond dimensions, strategies for reducing the number of needed sweeps could be beneficial for scaling up system sizes. From this perspective, constructing appropriate states to be used as initial guesses can speed up the convergence, similar to the choice of the trial wave function for variational MC simulations. We consider the following options:

- (i) *Physical insight*: Initial states can be constructed by following physical intuition, at least in those regimes in which analytical or partial numerical results are available. For instance, initial guesses can be constructed by starting from the TN ground states numerically obtained for a lower representation to simulate large spin representations of the gauge fields.
- (ii) *Machine learning*: Machine learning-assisted protocols can improve the construction of tailored initial states in the different regimes of the model parameters. For instance, feed-forward neural networks have been proposed as trial wave functions for quantum MC simulations [258], and machine learning techniques have been used to feed TN simulations [259]. Similarly, neural networks might reveal great potential in constructing initial states for LGTs to be used in large-scale TN simulations, in which reducing the number of sweeps is a key point for feasibility.
- (iii) *Tensor network results*: Following the idea of the physical insight, it is also possible to feed

neighboring ground states as initial guesses into a ground state search. This option exists especially when scanning a phase diagram and varying parameters in a small increment such that the overlap between neighboring wave functions is sufficient; this overlap decreases for two points on the opposite sides of a quantum critical point. The same idea can be implemented by preparing an initial guess quenching from an easily accessible ground state to the target parameters; the quench itself does not have to be adiabatic or free of numerical errors, but must only have sufficient overlap with the ground state. The advantage is that one quench can generate multiple initial guesses along the quench for different parameters.

2.6.3 Leverage HPC techniques for local optimization

We dedicate the two following sections to the numerical optimization of the TN algorithms. In this one, we give an overview of the topic and discuss possible strategies to improve the optimization. The more technical steps are discussed in the following Sec. 2.6.4.

To scale up TN simulations of LGTs, in particular regarding lattice sizes, another important factor is the number of optimization steps to be carried out. The number of optimization steps scales linearly with the number of sweeps as well as with the system size for MPS, PEPS, and TTN. The choice of the number of sweeps is set so that the algorithm reaches convergence when computing ground or low energy states. Let us briefly describe the general procedure for ground state searches. We will focus on the TTN optimization, even if the main points described here can be applied to other TN ansätze, such as MPS or PEPS. For a complete and technical description of the algorithms and implementation details, see Ref. [49].

Consider a generic QMB Hamiltonian \hat{H} and a generic normalized state $|\psi\rangle$, defined on the same Hilbert space. To numerically determine the ground state of \hat{H} , the following global minimization problem has to be solved:

$$\min_{|\psi\rangle} \{E(|\psi\rangle)\} = \min_{|\psi\rangle} \langle\psi|\hat{H}|\psi\rangle. \quad (2.6.2)$$

If $|\psi\rangle$ is written in terms of the TTN ansatz introduced in Sec. 2.2, the variational parameters are the coefficients in the TTN. In this case, the global optimization problem of Eq. (2.6.2) is broken down into a sequence of smaller optimizations, each of which involves only a minimal subset of tensors in the TTN. The algorithm solves the optimization via an eigenproblem searching for the eigenvector with the lowest eigenvalue. Without any loss of generality, one single tensor at a time is optimized in the simplest case, as shown in Fig. 2.12(a). In detail, the energy is computed by contracting the Hamiltonian between the TTN and its complex conjugate. Then, we start the optimization procedure from a target tensor T , by computing its environment, i.e. the network without the tensors T and T^\dagger , which represents the effective Hamiltonian \hat{H}_{eff} for the local problem. At this stage, an eigenproblem of \hat{H}_{eff} is solved, and the tensor T is updated with the newly found ground state. The whole procedure is sequentially iterated for all the tensors in the network, performing an optimization sweep.

For each operation, efficient algorithms from linear algebra are typically used, e.g. the Arnoldi algorithm implemented in the ARPACK library [238, 260]. We recall that the numerical complexity of this procedure for a single TTN-tensor is $O(d^2\chi^2 + \chi^4)$ ⁷. Therefore, a single optimization can be time-consuming when χ is very large, e.g. $\chi \approx 1000$, as for simulating high-dimensional LGTs. We point out the established and promising future parallelization schemes for the single tensor optimization:

⁷As reported in [5], the scaling presented here does not consider the bond dimension of the MPO representing the hamiltonian. The bond dimension of the mpo depends on the dimensionality of the system. In a simplified argument holding for the TTN, the maximum number of interactions cut for any bipartition gives a first intuition.

- (i) *openMP*: An efficient openMP implementation of the contraction between the effective operators with the tensor can speed up simulations. Moreover, the Arnoldi algorithm of ARPACK is optimized for large-scale linear algebra operations and supports intra-node multi-core parallelization based on openMP [261]; thus, ARPACK does not become a bottleneck in the openMP implementation. Nonetheless, many simulations remain expensive in computation time even with 64 or more cores available in HPC facilities; therefore, we consider more approaches beyond the well-established openMP path.
- (ii) *Accelerators*: Graphics Processing Units (GPU) and Tensor Processing Units (TPU) offer a path to accelerate linear algebra routines, where both have demonstrated their usefulness: GPUs have reported speedups of up to a factor of 10 due to the efficient tensor manipulations [262–265]; TPU have shown great potential in large-scale simulations of several quantum systems, e.g. drastically reducing the computational time of DMRG calculations with very large bond dimensions from months to hours [266–269]. TPU are application-specific integrated circuits originally introduced for machine learning; we then consider the integration and tuning of TPUs as a step after the successful integration of GPUs. While single GPUs can solve TTN-problems up to a bond dimension of $\chi < 1000$, multi-GPU support is available for libraries; HPC systems typically provide hardware with four GPUs per node.
- (iii) *Multi-node approaches to local tensor optimizations*: Both CPU and GPU algorithms can be further scaled by using multiple nodes. The underlying linear algebra routines of the local eigenvalue problem are parallelizable via libraries such as ScaLAPACK or MAGMA. Both libraries provide routines for distributed memory machines [270]; MAGMA supports moreover CPU and GPUs. In this way, the workload of the eigenproblem procedure can be split into several computation nodes. Then, it is important to analyze the performances as a function of the bond dimension χ , to test the effectiveness of this approach against the latency of the inter-node communications.
- (iv) *Tuning of parameters and algorithms*: accelerators developed for machine learning applications have excellent support for lower and real precision. Tuning parameters over the different sweeps is beneficial, e.g. increasing the precision towards the end of the sweep. This approach profits from faster single-precision implementations during the first sweeps. Selecting algorithms like random SVD can also bring benefits [271].

2.6.4 Sweeps and HPC parallelization

So far, we have parallelized single tensor optimizations within a sweep, but the sweep itself was sequential, i.e. serial. Recent works formulated parallel versions of MPS algorithms for ground state search and time evolution, e.g. via the Message Passing Interface (MPI) [272–274]. The main difference between the serial and parallel algorithms is the effective operators used in the optimization. In the serial version, the effective operators contain the information of the most recent version of all other tensors. This update is delayed in the parallel version, i.e. the tensor that entered the effective operator is not necessarily the one of the current sweep but can be the version of an earlier sweep.

If the delay becomes an obstacle to convergence, there is the option to modify parameters during the sweeps. Typically, ten to fifty sweeps are necessary to converge to a solution. As the initial state is usually random, MPI can be used especially at the beginning. To ensure convergence, one can consider serial steps at the end; even a gradual reduction of the MPI processes as the sweeps proceed is possible and gradually reduces the delays.

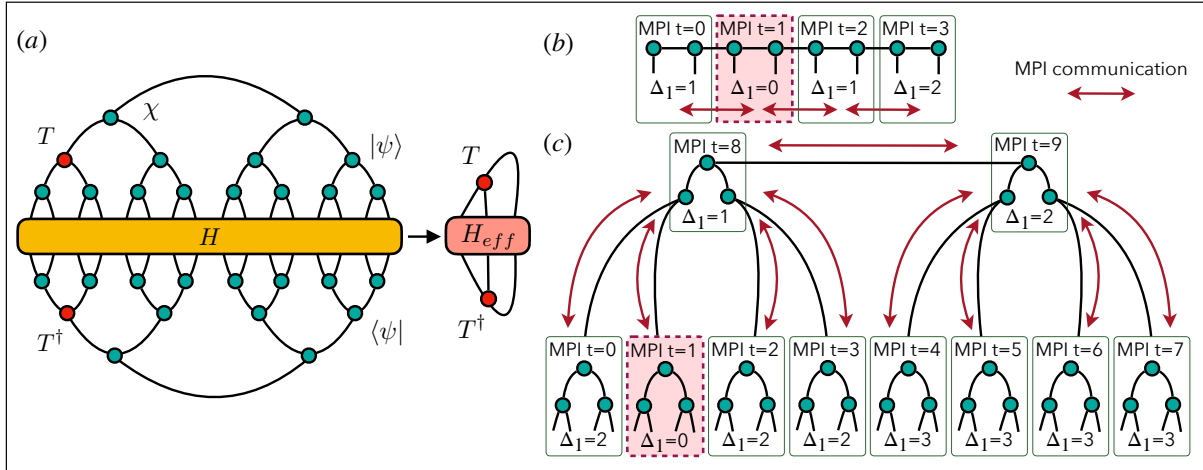


Figure 2.12: *Effective operators and parallel tensor networks.* (a) Procedure for optimizing a TTN to find the ground state of a QMB system: the energy is computed by contracting the Hamiltonian \hat{H} (yellow tensor) with the TTN, representing the state $|\psi\rangle$, and its hermitian conjugate, representing $\langle\psi|$. The variational optimization starts from a target tensor T (red tensor), by computing its effective Hamiltonian \hat{H}_{eff} and then solving the local eigenvalue problem for the latter. The tensor T is then updated with the newly found ground state, and the procedure iterates over all the tensors in the network (sweep). (b) The workload itself consists of optimizing each tensor held by the MPI thread t , which requires effective operators calculated by other MPI threads. We dub *delays* Δ_i the number of optimization cycles needed to obtain the information of tensors in the i -th MPI thread in another MPI thread via MPI communication. MPS naturally split into sub-chains which communicate with one or two neighboring MPI threads to obtain updated effective operators. Delays for updates scale with the distance between two MPI threads along the chain. Each MPI thread can use threading or openMP, e.g. in a hybrid openMP-MPI approach. (c) Similarly, TTNs can be split into sub-trees for each MPI thread allowing for optimizing the sub-tree without communication with other MPI threads. Delays due to updating scale logarithmically as any distance in a tree network.

Considering the MPS scenario of a chain in Fig. 2.12(b), we split the chain into equal parts of $(N/n_{\text{MPI-threads}})$ sites. Each part of the chain communicates with its two neighbors apart from the two boundaries. The effective operators take into account the tensors of the same MPI process with zero delay as in the serial case. The tensors of the i -th neighboring MPI process have a delay of i . The worst-case scenario of the delay scales linearly with the number of MPI processes. The delay can be avoided by communicating the effective operators after each update through the chain, which is a quasi-serial step with no more than two MPI processes active at the same time.

The problem becomes more complicated for the TTNs suggested for LGT, but we expect a benefit for the parallelization of a TTN versus an MPS for higher dimensional systems. Fig. 2.12(c) shows an example of how each MPI process gets assigned a sub-tree within the complete TTN. Unlike the MPS, the number of neighboring MPI processes for communication is at least three and increases with $(N/n_{\text{MPI-threads}})$ tensors per thread. Assuming equally shaped subtrees for all MPI processes, the delay of the tensor update is $2 \cdot \log_2(N)$ in the worst-case scenario.

One-dimensional systems with nearest-neighbor interactions thus exhibit a delay of 1 in the worst-case scenario in the MPS, while the delay is up to $2 \cdot \log_2(N)$ for the nearest neighbors in the center of the TTN. Rather, higher dimensional systems change this aspect, e.g., for an $N \times N$ two-dimensional system mapped to 1D via a zig-zag mapping. The MPS has a worst-case delay of the tensor update of N for the slow index. In contrast, the TTN has the same log behavior and a maximum delay at the center of the TTN as $2 \cdot \log_2(N^2)$. Thus, the worst-case delay is equal for 16×16 systems; increasing N further, TTNs exhibit smaller maximum delays during parallel sweeps. Moreover, the TTN is unaffected by the type of mapping used; in contrast, the worst-case delay for the MPS grows to $2N$ for the snake mapping and to at least $N^2/2$ for the Hilbert curve [1]. Equal arguments hold for 3D systems and delays of N^2 (MPS, zig-zag) versus $2\log_2(N^3)$ (TTN, any mapping).

To get an intuition of what parallelized simulations can solve, we sketch out the specifications for a parallel simulation on the pre-exascale cluster *Leonardo* hosted by *Cineca*. We choose an MPI approach together with the GPUs. *Leonardo* has 3456 nodes with four GPUs totaling 13824 GPUs available for the complete cluster. Bond dimensions on the order of $\chi = 450$ consume 54GB of memory without effective operators (assuming double complex precision, 40 Lanczos vectors) and allow to solve the eigenproblem on the GPU without temporarily storing data on the CPU. We use the single-tensor per MPI-thread with $\chi = 450$ as a baseline where we extract a rough empirical estimate with *Leonardo*; in detail, we use a 2D quantum Ising model with \mathbb{Z}_2 symmetry in the vicinity of the quantum critical point and the initial tensor optimizations [275]. Due to the delay of the tensor in the effective operators, the minimum number of sweeps must be beyond 24. Then, we consider the scaling of the TTN previously introduced and generate Tab. 2.1 with an overview of different system sizes and bond dimensions. These results provide a coarse-grained estimate, since plaquette terms, different symmetries, entanglement generation, and optimization time within later sweeps could further impact the computational time.

Our estimate predicts that a system of 256×256 sites takes about two months for bond dimension $\chi = 450$ on 1024 GPU nodes of *Cineca's leonardo*. Future improvements are likely to bring this simulation time down, e.g., the next-generation GPUs in comparison to the A100 or further optimization in data movement. In contrast, a three-dimensional system with large entanglement and many sites requires three to four orders of magnitude improvement, where cluster size and other improvements have to come together to reach this challenge. Furthermore, Tab. 2.1 provides an estimate of the boundary for a potential quantum advantage in simulating lattice gauge theories with quantum computers or simulators.

System size	χ	Factor	Estimated walltime
64×64	450	T_{base}	4.16 days
64×64	900	$16 \cdot T_{\text{base}}$	66.6 days
256×256	450	$28 \cdot T_{\text{base}}$	116.5 days
256×256	900	$448 \cdot T_{\text{base}}$	5.1 years
$16 \times 16 \times 16$	450	$4 \cdot T_{\text{base}}$	16.6 days
$16 \times 16 \times 16$	900	$64 \cdot T_{\text{base}}$	266 days
$64 \times 64 \times 64$	450	$1984 \cdot T_{\text{base}}$	23 years
$64 \times 64 \times 64$	900	$31744 \cdot T_{\text{base}}$	362 years

Table 2.1: *Estimated simulation time.* We derive the baseline from a single-tensor optimization of a 64×64 quantum Ising simulation with \mathbb{Z}_2 symmetry taking 7192s on a A100 GPU. Further, we assume that single-tensor update, one tensor and one GPU per MPI thread, and 50 sweeps for the baseline. To extrapolate to larger systems, we assume a scaling with $\mathcal{O}(\chi^4 N^{D-1})$ as well as seven (thirty-one) tensors per MPI thread for 256×256 ($64 \times 64 \times 64$) systems. The empirical scalings are approximately a factor of 2.3 for doubling the system size and 13 for doubling the bond dimension, which we obtain from smaller simulations with $\chi = 225$ and for 32×32 qubits. The times are valid for any $d < \chi$.

2.6.5 Finite temperature regime

To date, TN simulations of high-dimensional LGTs including dynamical matter are exploring zero temperature regimes, which are important to understand the low-energy properties of the models. To explore finite temperature phenomena, particularly relevant for open research problems such as the QCD phase diagram, technical and numerical challenges have to be tackled, e.g. devising and testing efficient TN algorithms for targeting quantum states at equilibrium. As suggested in the next paragraph, we foresee two possible paths toward finite temperature TN states.

Matrix product density operators (MPDOs) and locally purified tensor networks (LPTNs) provide already today the option to tackle finite temperature regimes via an imaginary time evolution [276–278]. Herein, the algorithm starts at the infinite temperature state and starts *cooling* the system via a specified number of time steps and specified step size to reach a given temperature. In its original formulation, both approaches are one-dimensional chains. Matrix product density operator can be formulated as TTN but faces some challenges in terms of the question of positivity [202] or integrating symmetries. In contrast, tree tensor operators (TTO) are the tree-equivalent of an LPTN; they are also a positive loopless representation of density matrices, recently introduced in [279]. However, TTOs cannot represent the infinite temperature state necessary for the imaginary time evolution approach. Instead, a possible use of the TTO employed in LGT simulations consists of a variational algorithm to target finite-temperature states or reconstruct open-system quantum dynamics, by efficiently compressing the relevant information. The TTO enables useful measures, e.g. computing the entanglement of formation as already shown for representative one-dimensional models at finite temperature [279].

2.7 Summary

In this chapter, we have provided a comprehensive exploration of Tensor Network (TN) methods applied to Lattice Gauge Theories (LGTs), highlighting their relevance as a complementary approach to traditional numerical techniques like Monte Carlo simulations. We began by addressing the limitations of exact diagonalization (ED) for quantum many-body (QMB) systems, empha-

sizing the importance of block diagonalization for computational efficiency in high-dimensional systems [6].

The chapter then shifted focus to TN methods, with a detailed explanation of how they efficiently capture quantum correlations, particularly through Matrix Product States (MPS) and Tree Tensor Networks (TTN), characterized by a loopless geometry. We underscored the critical role of preserving locality in high-dimensional simulations, discussing the superiority of space-filling curves like the Hilbert curve in optimizing TN algorithms [1]. Additionally, we reviewed key algorithms for equilibrium and time-evolution simulations, such as the TTN ground-state variational search and TEBD/TDVP techniques.

Finally, we laid out a roadmap for improving TN simulations, particularly in large-scale LGTs beyond one dimension, focusing on addressing computational challenges such as bond dimension growth and local basis truncation [5]. These improvements offer promising pathways for enhancing the scalability of TN methods and making them competitive with Monte Carlo techniques in simulating complex LGT models.

Chapter 3

Equilibrium properties of SU(2) LGT

In this chapter, we collect the numerical simulations of [2] concerning the ground-state properties of the (2+1)D SU(2) Yang-Mills Hamiltonian LGT within the *hardcore-gluon approximation* of Sec. 1.3.5 and obtained by using the variational ground-state search algorithm¹ for Tree Tensor Networks (TTN) discussed in Sec. 2.4. Given the inherent complexity of the model, simulations range from small to intermediate system sizes, up to 32 matter sites, well beyond the capabilities of Exact Diagonalization (ED) and state-of-the-art quantum computing. Indeed, due to the rich structure of the quantum degrees of freedom, the analysis of the ground state properties of the system, for lattice sizes up to 4×8 as performed here, would require >160 qubits to describe on a quantum computer.

The results explore several regimes of the model at equilibrium, including finite baryon number density. We characterize the model phase diagram by evaluating multiple observables, such as energy gaps, matter/antimatter and color-charge densities, gauge field distributions, and topological invariants. Whenever it is possible, we highlight the role of dynamical matter out of the behavior observed in the simpler pure theory.

3.1 The model

Let us start recalling the SU(2) Hamiltonian in Eqs. (1.3.7) and (1.3.8) on a (2+1)D spatial lattice Λ and rescale it in dimensionless energy scale units $\hat{H} \rightarrow \hat{H}' = \frac{a_0}{c\hbar} \hat{H}$ so that the hopping term has constant coupling $\frac{1}{2}$. Correspondingly, the other Hamiltonian terms acquire the rescaled dimensionless couplings:

$$m = a_0 \frac{m_0 c}{\hbar} = \frac{a_0}{a_m} \text{ (mass)} \quad \frac{g^2}{2} = \frac{a_0}{2a_g} \text{ (electric)} \quad \frac{1}{2g^2} = \frac{a_g}{2a_0} \text{ (magnetic)}, \quad (3.1.1)$$

where $a_m \equiv \hbar/(m_0 c)$, while, from the gauge coupling in Eq. (1.1.57) in two spatial dimensions, $a_g \equiv (c\hbar\epsilon_0)/q^2$. By doing so we obtain a fixed dimensionless *quark ratio* $\alpha_c = g^2/2m = (a_m/2a_g)$ which does not scale with the lattice spacing and is solely determined by the color charge and

¹As for the single-node TN optimization, we set the Arnoldi algorithm to discard eigenvalues smaller than 10^{-4} . The convergence of the whole variational algorithm is established for absolute $\Delta\varepsilon_{abs} = 10^{-5}$ and relative convergence thresholds $\Delta\varepsilon_{rel} = 10^{-5}$ defined in Eq. (2.4.9) for consecutive optimization sweeps $s-1$ and s . The maximal bond dimension χ adopted in the reported TN simulations is always obtained by looking at the single-site energy relative convergence of 10^{-4} (for more details, see [2]).

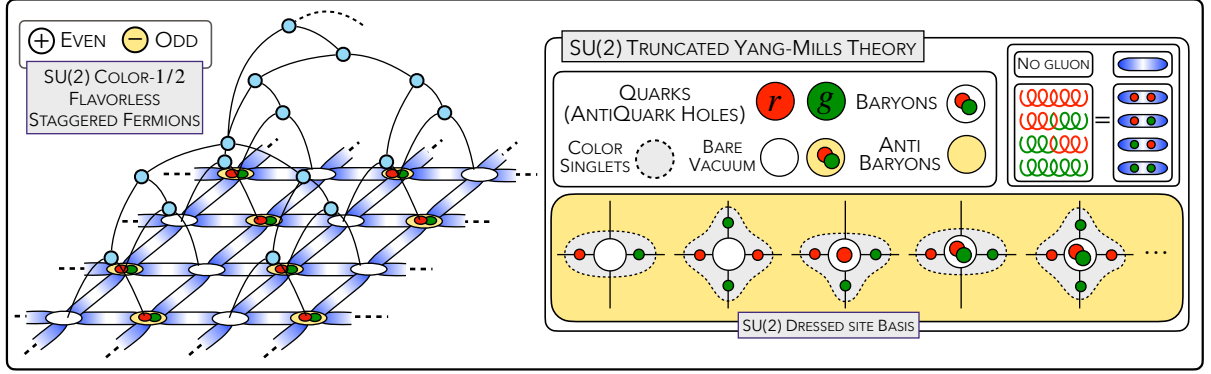


Figure 3.1: TTN approach to (2+1)D SU(2) Yang-Mills LGT. Lattice sites host flavorless SU(2)-color-1/2 fermionic fields (red and green) in a staggered configuration (white and yellow). Lattice (blue) links describe gauge degrees of freedom from a 5-dimensional truncated Hilbert space (*hardcore-gluon approximation*). SU(2) Gauss Law is implemented at each lattice site.

the bare mass of the quark (see Sec. 1.1.4). Then, the (dimensionless) Hamiltonian reads:

$$\begin{aligned} \hat{H}' = & + \frac{1}{2} \sum_{\alpha, \beta} \sum_{\mathbf{n}} \left[-i \hat{\psi}_{\mathbf{n}, \alpha}^{\dagger} \hat{U}_{\mathbf{n}, \mu_x}^{\alpha \beta} \hat{\psi}_{\mathbf{n}+\mu_x, \beta} - (-1)^{n_x+n_y} \hat{\psi}_{\mathbf{n}, \alpha}^{\dagger} \hat{U}_{\mathbf{n}, \mu_y}^{\alpha \beta} \hat{\psi}_{\mathbf{n}+\mu_y, \beta} + \text{h.c.} \right] \\ & + m \sum_{\mathbf{n}} (-1)^{n_x+n_y} \sum_{\alpha} \hat{\psi}_{\mathbf{n}, \alpha}^{\dagger} \hat{\psi}_{\mathbf{n}, \alpha} + \frac{g^2}{2} \sum_{\mathbf{n}, \mu} \hat{E}_{\mathbf{n}, \mu}^2 - \frac{1}{2g^2} \sum_{\square} \text{Tr}(\hat{U}_{\square} + \hat{U}_{\square}^{\dagger}), \end{aligned} \quad (3.1.2)$$

where $\alpha, \beta \in \{r, g\}$. Expressing in Eq. (3.1.2) in terms of the dressed site operators from Sec. 1.3.4 in the *hardcore-gluon* approximation (see Sec. 1.3.5), we obtain:

$$\begin{aligned} \hat{H}' = & + \frac{1}{2} \sum_{\mathbf{n}} \left[-i \hat{Q}_{\mathbf{n}}^{\dagger} \hat{Q}_{\mathbf{n}+\mu_x} - (-1)^{n_x+n_y} \hat{Q}_{\mathbf{n}} \hat{Q}_{\mathbf{n}+\mu_y} + \text{h.c.} \right] \\ & + m \sum_{\mathbf{n}} (-1)^{n_x+n_y} \hat{N}_{\mathbf{n}, \text{tot}} + \frac{g^2}{4} \sum_{\mathbf{n}} \hat{\Gamma}_{\mathbf{n}}^2 - \frac{1}{2g^2} \sum_{\square} \text{Tr}(\hat{U}_{\square} + \hat{U}_{\square}^{\dagger}), \end{aligned} \quad (3.1.3)$$

Assuming that the SU(2) LGT is super-renormalizable in two spatial dimensions [280] and excluding quantum corrections to the scaling (see anomalous dimension [281]), then the continuum limit of Eq. (3.1.2) is located at $g^2 = \alpha_c m \rightarrow 0$ (more quantitatively, at $a_0 \ll a_g, a_m$).

3.1.1 Local Observables

Together with the ground-state energy density $\varepsilon = \langle \hat{H} \rangle / N$, we evaluate the expectation values $\langle \cdot \rangle$ of several local observables onto the computed ground states. Regarding gauge fields, we track the color-electric and color-magnetic energy densities

$$\langle E^2 \rangle = \frac{1}{N} \sum_{\mathbf{n}, \mu} \langle \hat{E}_{\mathbf{n}, \mu}^2 \rangle \quad \text{and} \quad \langle B^2 \rangle = -\frac{1}{N_{\square}} \sum_{\square} \langle \text{Tr}(\hat{U}_{\square} + \hat{U}_{\square}^{\dagger}) \rangle + c', \quad (3.1.4)$$

where N and N_{\square} correspond to the total number of sites and lattice plaquettes. The constant factor $c' = \frac{1}{2}$ in Eq. (3.1.4) sets the minimum of the magnetic energy density to 0. Correspondingly, we define the electric and magnetic fluctuations as follows:

$$\delta E^2 = \sqrt{\langle E^4 \rangle - \langle E^2 \rangle^2} \quad \delta B^2 = \sqrt{\langle B^4 \rangle - \langle B^2 \rangle^2}. \quad (3.1.5)$$

When considering matter fields, it is useful to separately measure the staggered fermion density for even (+) and odd (-) sites

$$n_{\pm} = \frac{1}{N_{\pm}} \sum_{\mathbf{n} \in \Lambda_{\pm}} \sum_{\alpha=r,g} \langle \hat{\psi}_{\mathbf{n},\alpha}^{\dagger} \hat{\psi}_{\mathbf{n},\alpha} \rangle \quad (3.1.6)$$

where Λ_+ , (Λ_-) is the even (odd) sub-lattice, while N_+ , (N_-) is the corresponding number of sites. Tracking these two quantities gives us immediate access to the density of quarks (n_+) and the density of anti-quarks ($2 - n_-$) separately, according to the staggered fermion formalism. Similarly, we can define the total *particle density* (quarks plus anti-quarks)

$$\varrho = n_+ + (2 - n_-) \quad \text{with} \quad 0 \leq \varrho \leq 4, \quad (3.1.7)$$

as well as the *baryon number density*, (quarks minus anti-quarks divided by two)

$$b = \frac{1}{2}(n_+ - (2 - n_-)) \quad \text{with} \quad 0 \leq b \leq 1, \quad (3.1.8)$$

which is a good quantum number, as it is a conserved quantity tied to the global staggered fermion number conservation. We stress that, unlike quantum chromodynamics, SU(2) Yang-Mills baryons – colorless bound states of matter particles – are made by two, not three, quarks. Similarly, anti-baryons are made by two anti-quarks. Correspondingly, mesons are made by one quark and one anti-quark as normal.

Both mesons and standalone quarks can be detected by looking at the average *matter color density* $\langle S_{\text{matt}}^2 \rangle$ defined in Eq. (1.3.6):

$$\langle S_{\text{matt}}^2 \rangle = \frac{1}{N} \sum_{\mathbf{n}} \langle \hat{S}_{\text{matt},\mathbf{n}}^2 \rangle = \frac{1}{N} \sum_{\mathbf{n},a} \langle \hat{Q}_{\mathbf{n}}^a \hat{Q}_{\mathbf{n}}^a \rangle = \frac{1}{2N} \sum_{\mathbf{n},a} \left\langle \sum_{\alpha\beta} \left(\hat{\psi}_{\mathbf{n},\alpha}^{\dagger} \hat{\psi}_{\mathbf{n},\beta} \sigma_{\alpha\beta}^a \right)^2 \right\rangle. \quad (3.1.9)$$

Our quantitative analysis also includes the von Neumann entanglement entropy [50]

$$\mathcal{S}_A = -\text{Tr} \rho_A \log_2 \rho_A, \quad (3.1.10)$$

where ρ_A is the reduced density matrix of the partition A , which we choose exactly to be the bottom (or top) half of the system.

3.2 Magneto-electric transition in the pure theory

We first focus on the pure theory (corresponding to the $m \rightarrow \infty$ of Eq. (3.1.2)) under Open Boundary Conditions (OBC). According to the results shown in Fig. 3.2, the pure Hamiltonian displays two phases driven by g and characterized by strong fluctuations of the electric and magnetic fields.

In detail, for the small- g (magnetic) phase, the plaquette interaction provides the largest contribution to the energy in Eq. (3.1.2). As such, magnetic fields are depleted, and electric fields display large quantum fluctuations $\delta \hat{E}^2$ and compensate for any electric activity. Conversely, in the large- g (electric) phase, electric fields are energetically expensive and thus depleted in the ground state, while magnetic fields show large fluctuations $\delta \hat{B}^2$.

Unlike the electric phase, which displays marginal entanglement as the ground state is almost a product state, the magnetic phase reveals an entanglement that scales with the length of the bipartition: this behavior, signaling a sharp area-law of entanglement, suggests that the magnetic

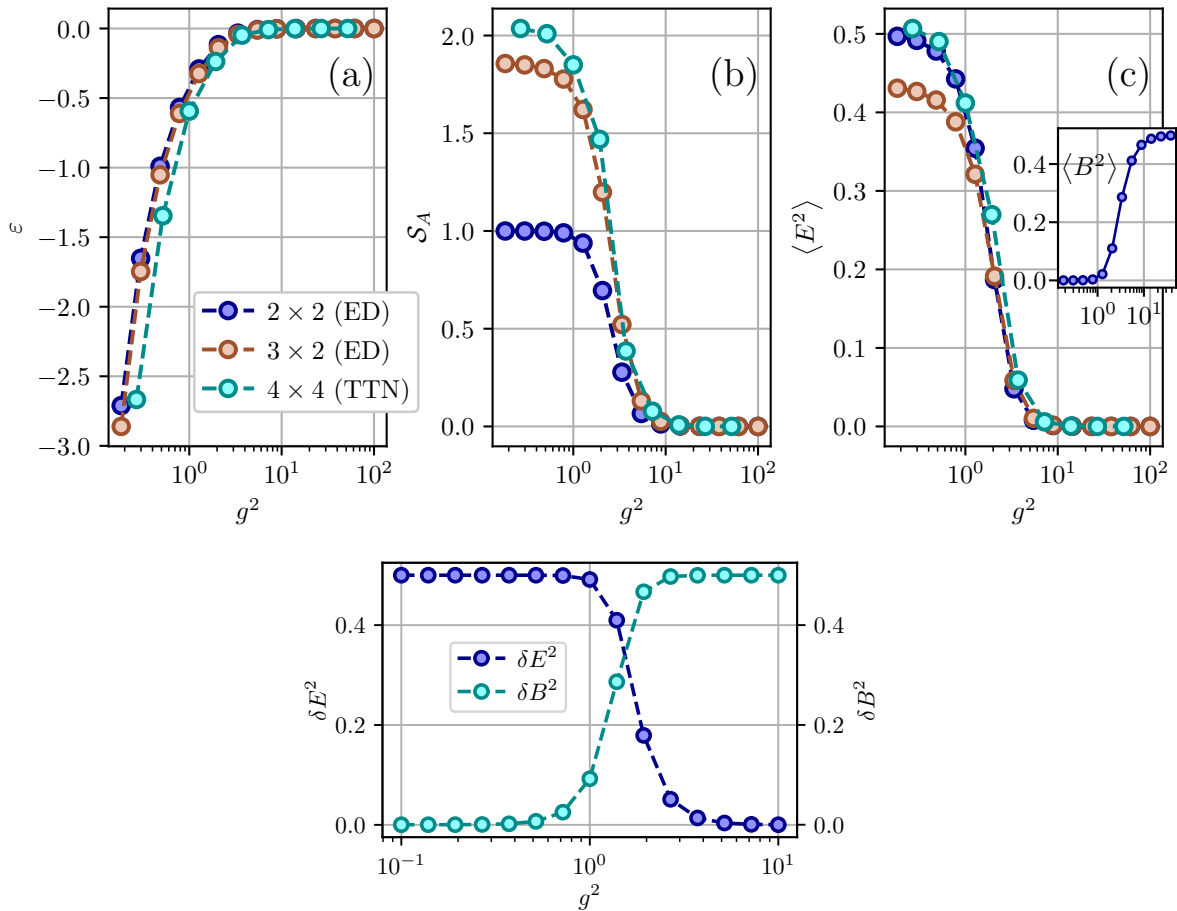


Figure 3.2: Numerical simulations of the pure Hamiltonian in Eq. (3.1.2) with OBC for different lattice sizes. The plots display respectively (a) the ground-state energy density ε , (b) the entanglement entropy S_A of half the system, (c) the average electric energy contribution $\langle E^2 \rangle$, with the magnetic energy density $\langle B^2 \rangle$ shown in the inset. (bottom line) Fluctuations of the gauge observables in Eq. (3.1.4) as a function of the g -coupling for a 2×2 lattice. Figures from [2].

phase is likely approximated by a resonant-valence bond (RVB) state of plaquettes, akin to the local structure of the ground state of the Toric Code [282].

The entanglement entropy approximates a monotonic function along g , without any peak in the transition between the two phases. This observation suggests that, for large bare masses m , this quantum phase transition is either *first order* or a *crossover*. Conversely, as shown in Fig. 3.5, the small- m scenario of the full theory peaks close to the transition, and the peak is wider and larger for smaller masses. We stress that the magneto-electric transition is compatible with the *roughening transition* [10, 283, 284] observed via MC simulations [18, 19, 28] and Cluster Expansion Methods (CEM) [280, 285].

3.3 Baryonic spectrum

For finite m , fermionic matter displays a dynamical role in the Hamiltonian of Eq. (3.1.2). The baryon number density b in Eq. (3.1.8) is a quantum number associated with global symmetry, and can thus be directly encoded in the TTN ansatz as well as in ED simulations. In this way,

we directly target the ground state within a selected baryon number density sector [6, 93, 158].

The model is symmetric under CP, that is, mirror spatial reflection ($n_x \rightarrow N_x - n_x$) times particle-hole exchange ($\hat{\psi}_\alpha \rightarrow i\sigma_{\alpha\beta}^y \hat{\psi}_\beta^\dagger$) of staggered fermions. Then, at negative baryon densities $b < 0$, the ground state is the CP-reflected of the ground state at positive baryon density $|b|$.

We numerically verified that the global ground state is found at null baryon density $b = 0$ for any g and m . As we can directly tune the baryon number of each TTN simulation, we have immediate access to the inter-sector energy gap by calculating the difference

$$\begin{aligned} \Delta_{|b|} &= (\varepsilon_b - \varepsilon_0)N = (\varepsilon_{-b} - \varepsilon_0)N \geq 0 \\ &= m|b|N + \Delta_{|b|}^*, \end{aligned} \quad (3.3.1)$$

where we also defined the *binding energy* $\Delta_{|b|}^*$ by subtracting the bare mass of the corresponding excess quarks or anti-quarks ($|b|N$).

A simple yet illustrative analysis is to study the energy density gap between the one-baryon sector ($b = 2/N$) and the vacuum sector ($b = 0$) and then approach the continuum limit $a_0 \rightarrow 0$ at fixed ratio $\alpha_c = g^2/2m \propto q^2/m_0$ (see Sec. 1.1.4).

As shown in Fig. 3.3(a), the gap $\Delta_{2/N}$ displays a clear linear scaling with $m = \frac{m_0 c}{\hbar} a_0$. Namely:

$$\Delta_{2/N} = \kappa(\alpha_c)m = \kappa(\alpha_c)\frac{m_0 c}{\hbar} a_0, \quad (3.3.2)$$

implying that the actual baryon mass is $m_b = \kappa(\alpha_c)m_0$. As for all hadrons, its mass is always greater than the bare mass of its quark components, thus $\kappa \geq 2$. We show this observation in Fig. 3.3(b), where we display κ as a function of α_c . More interestingly, in the case of the binding energy $\Delta_{2/N}^*$ displayed in the inset of Fig. 3.3(b), we observe a power-law scaling of κ^* in α_c :

$$\kappa^* = \frac{\Delta_{2/N}^*}{m} = \kappa - 2 \quad \text{with} \quad \kappa^*(\alpha_c) \sim 0.13 \cdot \alpha_c^{0.96}, \quad (3.3.3)$$

that is compatible with linear scaling. Such relations confirm that baryons are actual *quasi-particles* of the continuum theory and provide a connection to the bare quark properties (α_c, m_0). We carried out this analysis for a finite-size sample, but the baryon-to-quark mass ratio κ is expected to stay finite even at the thermodynamical limit.

3.4 Baryon-liquid phase

Beyond energy gaps, other phase properties can be inferred when probing the observables in Sec. 3.1.1. As shown in Figs. 3.4 and 3.5, by varying $m \in [10^{-1}, 10^0]$, the magneto-electric transition, driven by g^2 , gets sharper for larger masses m , while remaining almost unaltered at finite baryon densities b .

Correspondingly, for fixed m -values, the entanglement entropy of half the lattice is constant in the magnetic phase, peaked in the g -transition, and tending to a default value (0 for $b = 0$ and 1 for $b = 0.5$) in the electric phase. In the limit of large masses, this peak in the entropy progressively vanishes, and we recover the (*crossover/first-order*) transition observed in Fig. 3.2 for the pure theory.

As for the particle density ρ , it reveals an exciting behavior as the rescaled quark mass m is lowered (see Fig. 3.5). As long as m is the largest energy scale of the model ($m \gg 1, g^2, g^{-2}$) the emergent behavior is relatively trivial, as a system of gapped hardcore bosons.

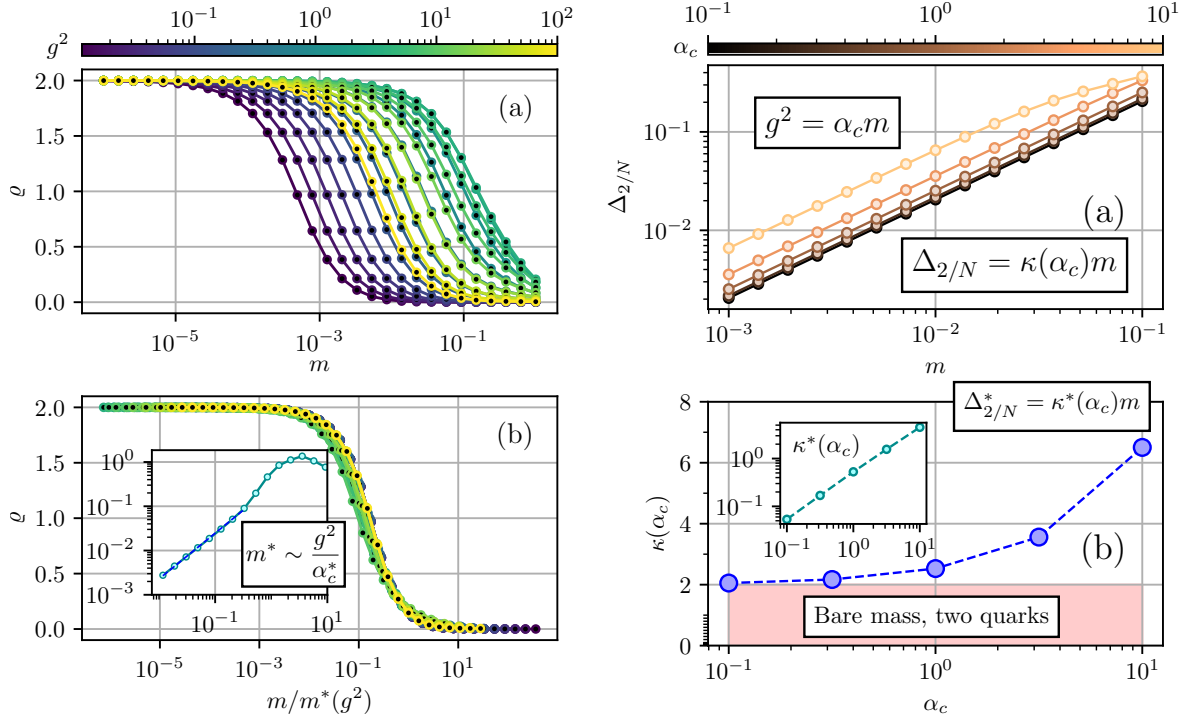


Figure 3.3: (a) Scaling of the particle density defined in Eq. (3.1.7) as a function of m for different values of the gauge coupling g . (b) All the $\rho(m)$ curves of the particle density collapse on a single one simply by re-scaling the mass m by a factor m^* displaying a power-law scaling in g^2 (see the inset). By fitting this scaling we extract Eq. (3.4.1), whose error bars have been computed exploiting error propagation onto the covariance matrix of the fit. Results obtained from simulations on a 2×2 lattice in OBC at baryon density $b = 0$. (a) Scaling of the inter-sector gap $\Delta_{2/N}$ in Eq. (3.3.1) as a function of m , for different choices of the g -coupling $g^2 = \alpha_c m$. By fitting the power-law scaling of $\Delta_{2/N}$ in the small- m limit, we obtain the linear dependence on m shown in Eq. (3.3.2), whose slope κ depends on α_c as shown in (b). The inset displays the corresponding κ^* of the binding energy $\Delta_{2/N}^*$ in Eq. (3.3.3). Results have been obtained from simulations of a 2×2 lattice in PBC, where $\Delta_{2/N} = \Delta_{|b|=0.5}$. Figure from [2].

More precisely, if $b \geq 0$ ($b \leq 0$) the antimatter (matter) sites are fully empty, while the matter (antimatter) sites host exactly b quark-pair hardcore bosons, mass gapped and with almost flat-band dynamics. The particle density ϱ confirms this interpretation, as it stays at its minimum possible value of $\varrho \simeq \varrho_{\min}(b) = 2|b|$ and without fluctuations $\delta\varrho \simeq 0$ (see Fig. 3.6).

As shown in Fig. 3.3, this behavior drastically changes at low masses m , in relative proximity of the transition line $g^2 \sim 2(1)$. In fact, for m lower than a critical value $m^*(g)$, we see a sharp growth of the particle density ϱ and its on-site fluctuations $\delta\varrho$, which become similar in magnitude (see Fig. 3.6). Even though we do not have access to long-range correlation functions at these limited system sizes, this observation is a strong hint of superfluidity of the phase, where we expect the quasi-particle excitations to be gapless (in the rescaled units).

To deeper investigate the nature of these quasi-particles we track the matter-color density S_{matt} defined in Eq. (3.1.9) (see Figs. 3.6 and 3.10). There is a very narrow region around the magneto-electric g -transition where colored matter emerges (maybe a possible deconfined critical boundary) with fluctuations δS_{matt} of the same order of magnitude of the observable itself. Elsewhere, especially towards the continuum limit, the color density is vanishing $S_{\text{matt}} = 0$. We must conclude that the gapless quasi-particles must be made by on-site pairs of quarks or anti-quarks. As such, we can regard the low-mass phase, $m < m^*(g)$, as a *gapless baryon liquid*. Using a finite-size scaling technique shown in Fig. 3.3(b), we are able to characterize m^* as a power-law function of g^2 , where a numerical regression yields

$$m^*(g^2) \simeq 0.267(4) \cdot (g^2)^{1.03(2)}, \quad (3.4.1)$$

which is less than 2σ deviation from a linear scaling. Now, if we assume that the linear scaling holds, then there must be a critical quark ratio $\alpha_c^* = 3.75(6)$ that determines the behavior when approaching the continuum limit (recall that α_c^* depends only on quark color-charge and bare mass, see Sec. 1.1.4). Namely, for strong color charges $\alpha_c > \alpha_c^*$ the baryon fluid at $a_0 \rightarrow 0$ is gapless, while for weak charges $\alpha_c < \alpha_c^*$ the baryon fluid is gapped. We recall that we are working with energy scales rescaled by a_0 , thus only quasiparticles that we identify as gapless at the continuum limit will survive as finite energy excitations in natural units.

3.5 Non-local/Topological properties

Another relevant analysis that can be carried out in Yang-Mills theories is the characterization of topological properties at the critical point and the investigation of whether some form of topological order emerges within or without deconfined phases [286, 287]. While the simplified model we considered does not support the existence of a deconfined phase in proximity to the continuum limit, it is still possible to characterize some topological properties by evaluating non-local order parameters.

In this section, we address the topological properties of the (2+1)D *hardcore-gluon* SU(2) Hamiltonian in Eq. (3.1.2). In particular, we show that its pure theory displays a non-local $\mathbb{Z}_2 \times \mathbb{Z}_2$ symmetry which exists only under periodic boundary conditions (PBC) and whose topological sectors close as approaching the g -transition. Such a topological structure is completely *independent* of the chosen truncation of the SU(2) gauge Hilbert space developed throughout Sec. 1.3.2. The presence of dynamical matter removes such a symmetry from the full Hamiltonian in Eq. (3.1.2), but it can be recovered in the infinite mass limit.

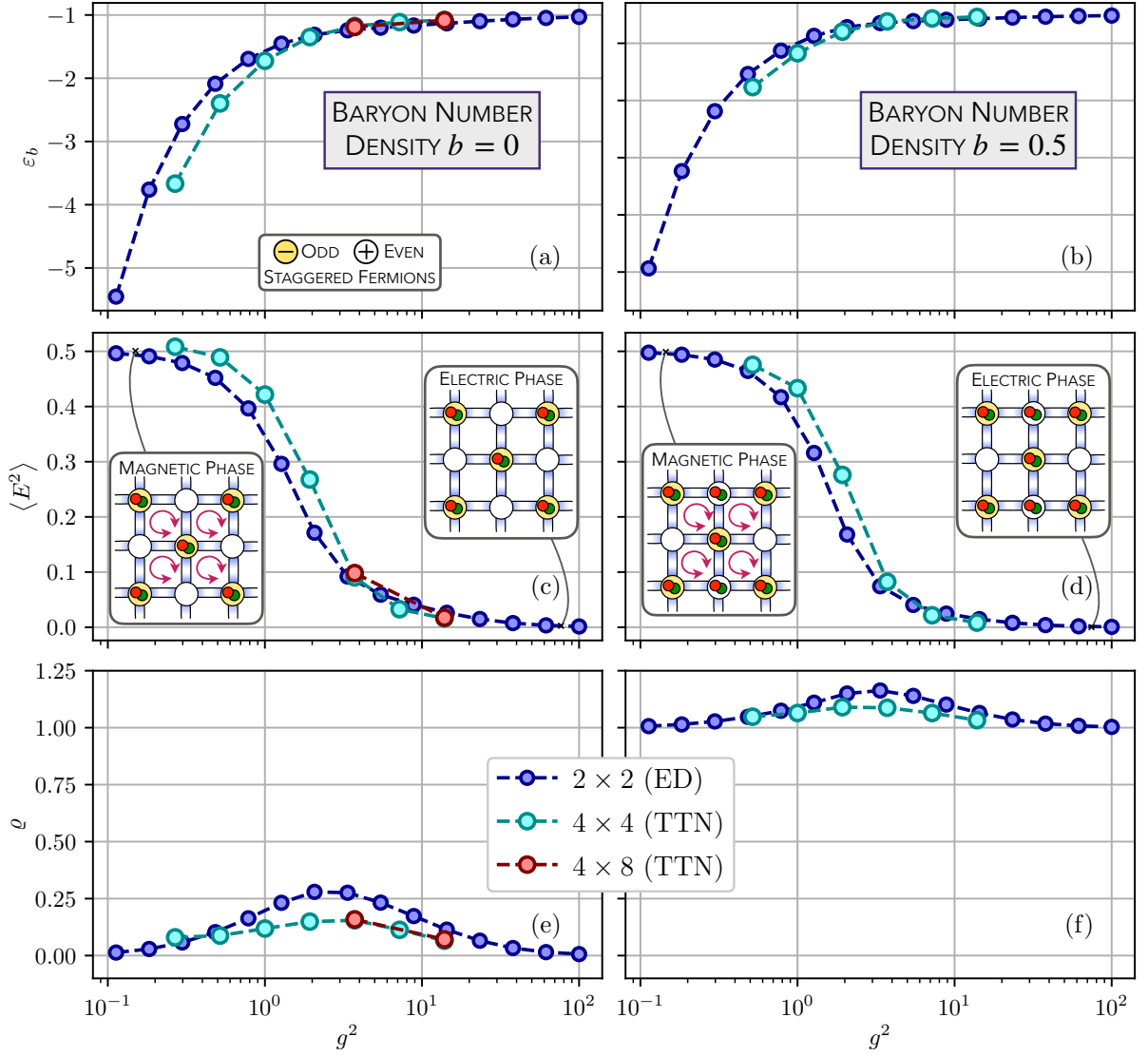


Figure 3.4: Numerical results of the full SU(2) Hamiltonian in Eq. (3.1.2) with OBC and baryon number density $b = 0$ (left column) and $b = 0.5$ (right column). The plots display respectively: (a)-(b) the ground-state energy density ε_b , (c)-(d) the average electric energy contribution $\langle E^2 \rangle$ in Eq. (3.1.4), enlightening the transition between the magnetic (purple fluxes) and the electric (no fluxes) phases discussed in Sec. 3.2, and (e)-(f) the average particle density ρ in Eq. (3.1.7), which appears peaked in the g -transition. The pictorial lattice configurations in the finite baryon density $b = 0.5$ represent states with b extra gapped hardcore local bosons with low dynamics compatible with the two electric/magnetic phases. Figure from [2].

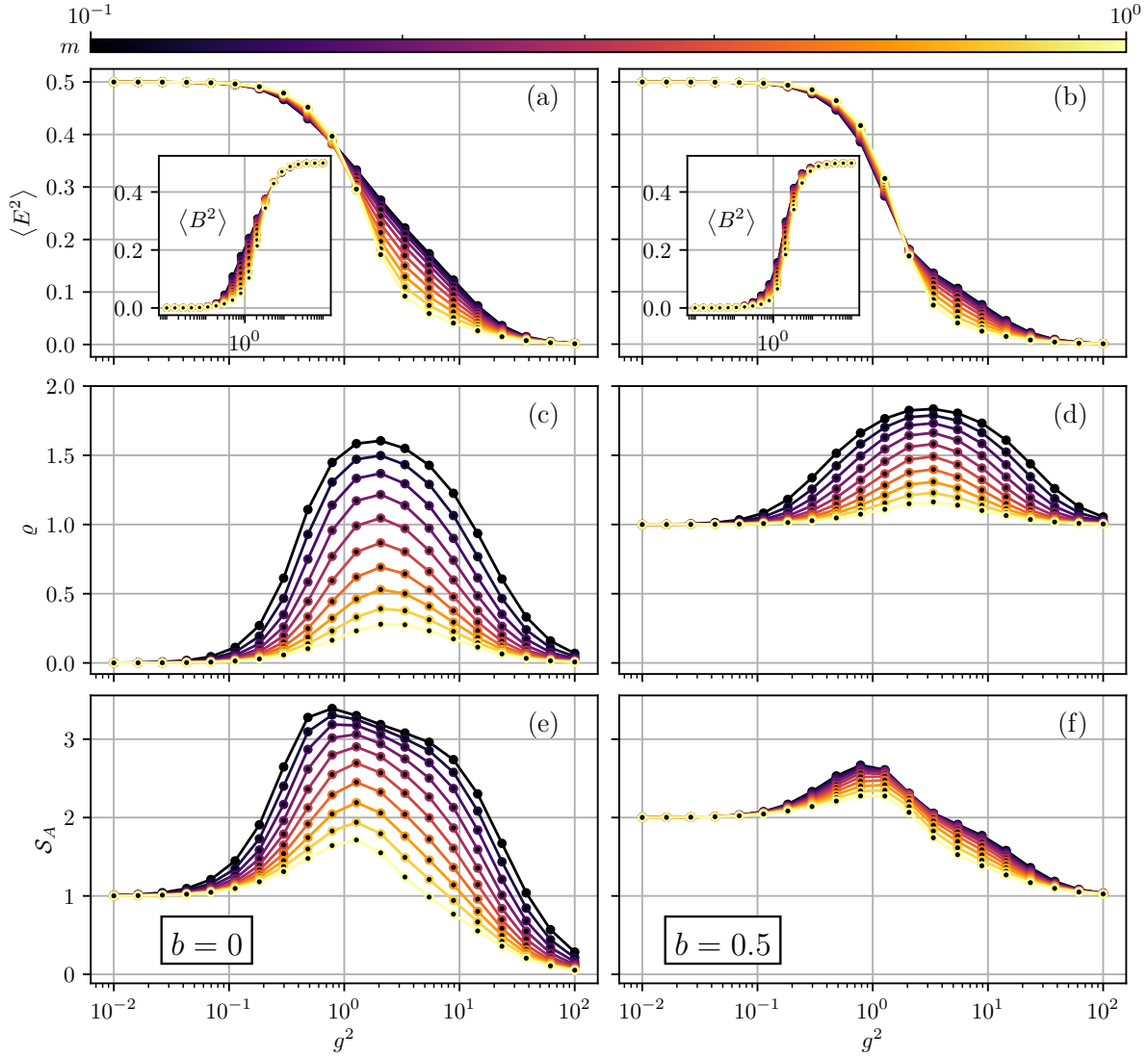


Figure 3.5: Simulations of the full $SU(2)$ Hamiltonian in Eq. (1.3.45) on a 2×2 lattice with OBC in the $b = 0$ (a)-(c)-(e) and $b = 0.5$ (b)-(d)-(f) baryon number density sectors. The plots display respectively: (a)-(b) the average electric and magnetic energy contributions $\langle E^2 \rangle$ and $\langle B^2 \rangle$ (inset) enlightening the transition between the magnetic and the electric phases discussed in Sec. 3.2; (c)-(d) the average particle density ρ in Eq. (3.1.7), which appears peaked in the g -transition; (e)-(f) the entanglement entropy \mathcal{S}_A of half the system, with a peak in the g -transition which is larger for smaller m while disappearing for large ones. Figure from [2].

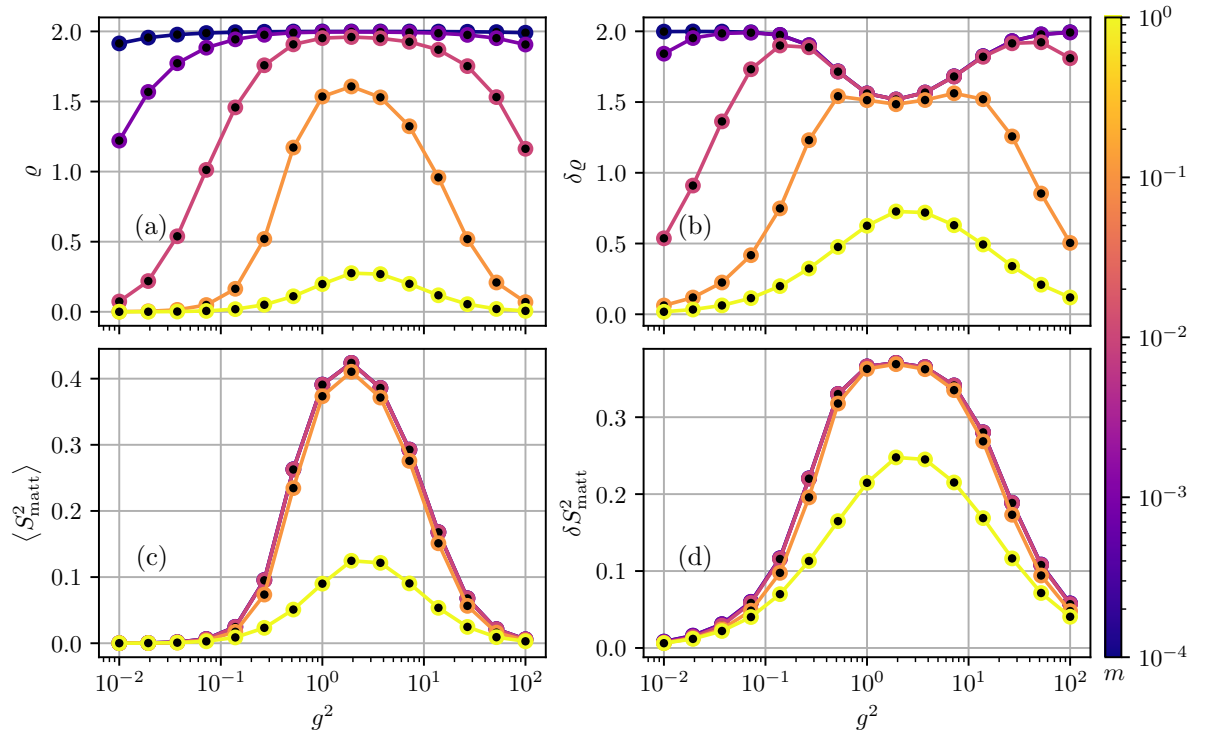


Figure 3.6: Simulations of a 2×2 lattice in PBC. The plots display respectively: (a) the average particle density ρ and (b) its quantum fluctuations $\delta\rho$; (c) the matter color density $\langle S_{\text{matt}}^2 \rangle$ and (d) its quantum fluctuations δS_{matt}^2 . All the observables are studied as a function of the square coupling g^2 for different mass values $m \in [10^{-4}, 10^1]$.

3.5.1 Topological Invariants

In order to properly characterize a topological symmetry, we need to introduce some topological *invariants*: string operators whose action commutes with pure gauge Hamiltonian terms of Eq. (3.1.2). The right candidates involve the rishon parity operators \hat{P}_ζ introduced in Eq. (1.3.51). Thanks to the link symmetry in Eq. (1.3.36), we can extend such a definition to the whole link $(\mathbf{n}, \boldsymbol{\mu})$ and consider the corresponding parity operator $\hat{P}_{\mathbf{n}, \boldsymbol{\mu}}$. As aforementioned, it returns $(+1)$ for *integer* and (-1) for *semi-integer* SU(2) representations. In the *hardcore-gluon* approximation of Sec. 1.3.5, such an operator reads:

$$\hat{P}_{\mathbf{n}, \boldsymbol{\mu}} = \text{diag}(+1, -1, -1, -1, -1) \quad \forall \mathbf{n}, \forall \boldsymbol{\mu}. \quad (3.5.1)$$

Since the Casimir operator in Eq. (1.3.47) is diagonal in the link basis, it commutes with $\hat{P}_{\mathbf{n}, \boldsymbol{\mu}}$:

$$\left[\hat{P}_{\mathbf{n}, \boldsymbol{\mu}}, \hat{E}_{\mathbf{n}, \boldsymbol{\mu}}^2 \right] = 0 \quad \forall \mathbf{n}, \forall \boldsymbol{\mu} \in \Lambda. \quad (3.5.2)$$

Rather, $\hat{P}_{\mathbf{n}, \boldsymbol{\mu}}$ anti-commutes with the parallel transport \hat{U} (and \hat{U}^\dagger), as its action on the link decreases (respectively increases) the SU(2) link-representation by $1/2$:

$$\left\{ \hat{P}_{\mathbf{n}, \boldsymbol{\mu}}, \hat{U}_{\mathbf{n}, \boldsymbol{\mu}}^{(\dagger)} \right\} = 0 \quad \forall \mathbf{n}, \forall \boldsymbol{\mu} \in \Lambda. \quad (3.5.3)$$

Then, we define the *string* operator $\hat{\mathbb{P}}_y$ as the consecutive action of the horizontal link parity operators along a vertical loop of Λ in PBC (see orange links in Fig. 3.7):

$$\hat{\mathbb{P}}_y \equiv \bigotimes_{k=0}^{|\Lambda_y|} \hat{P}_{\mathbf{n}+k\boldsymbol{\mu}_y, \boldsymbol{\mu}_x} = \hat{P}_{\mathbf{n}, \boldsymbol{\mu}_x} \otimes \hat{P}_{\mathbf{n}+\boldsymbol{\mu}_y, \boldsymbol{\mu}_x} \otimes \dots \quad (3.5.4)$$

Correspondingly, $\hat{\mathbb{P}}_x$ is the consecutive action of the vertical link parity operator along a horizontal loop in Λ (see green links in Fig. 3.7):

$$\hat{\mathbb{P}}_x \equiv \bigotimes_{k=0}^{|\Lambda_x|} \hat{P}_{\mathbf{n}+k\boldsymbol{\mu}_x, \boldsymbol{\mu}_y} = \hat{P}_{\mathbf{n}, \boldsymbol{\mu}_y} \otimes \hat{P}_{\mathbf{n}+\boldsymbol{\mu}_x, \boldsymbol{\mu}_y} \otimes \dots \quad (3.5.5)$$

Within the SU(2) dressed site formalism developed in Sec. 1.3, Eqs. (3.5.4) and (3.5.5) can be expressed just as chains of single-site operators along one of the two sides of the links. Indeed, as long as the SU(2) link-symmetry in Eq. (1.3.36) is satisfied, the information about every link-parity is present in both the attached neighboring sites.

3.5.2 Topological properties the pure theory

It is clear that both the $\hat{\mathbb{P}}_x$ and $\hat{\mathbb{P}}_y$ operators remain unaffected by the action of the electric field along any of their steps, as their parity does not get flipped. Correspondingly, any plaquette term \hat{U}_\square of the magnetic interaction applied on the chain where $\hat{\mathbb{P}}_x$ or $\hat{\mathbb{P}}_y$ is evaluated flips the parity of two consecutive steps of the chain so that the overall sign is left unchanged. Namely:

$$\left[\hat{\mathbb{P}}_{\mathbf{n}}, \hat{E}_{\mathbf{n}, \boldsymbol{\mu}}^2 \right] = 0 = \left[\hat{\mathbb{P}}_{\mathbf{n}}, \hat{U}_\square \right] \quad \forall \mathbf{n}, \square \in \Lambda \quad (3.5.6)$$

Therefore, $\hat{\mathbb{P}}_x$ and $\hat{\mathbb{P}}_y$ are the generators of two \mathbb{Z}_2 symmetries of the pure theory in Eq. (3.1.2):

$$\left[\hat{\mathbb{P}}_x, \hat{H}_{\text{pure}} \right] = 0 \quad \left[\hat{\mathbb{P}}_y, \hat{H}_{\text{pure}} \right] = 0 \quad (3.5.7)$$

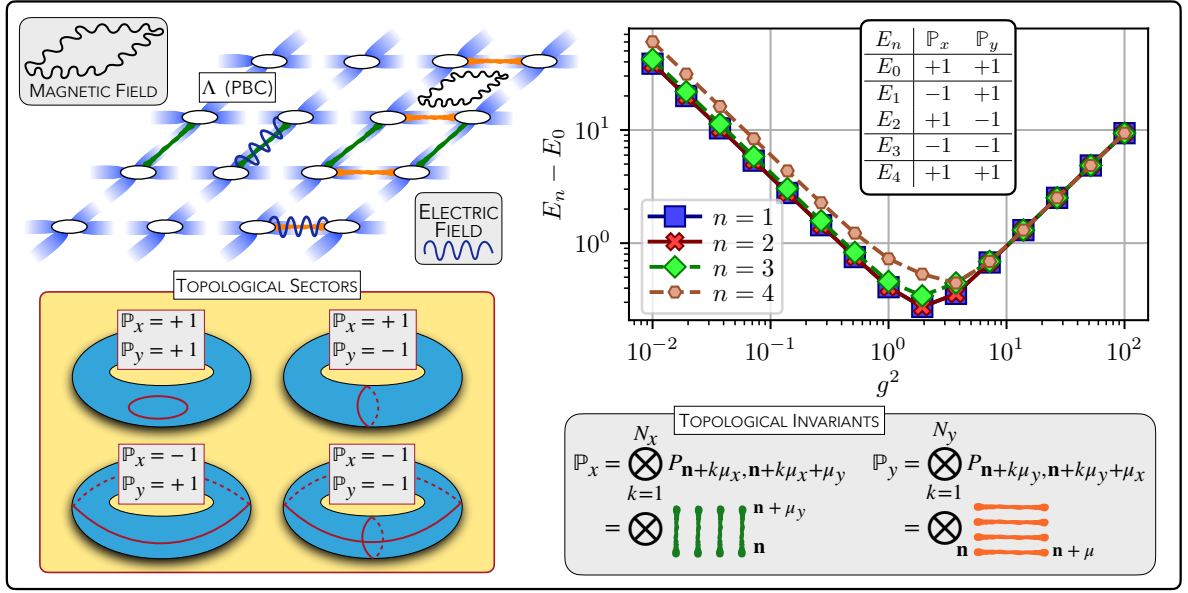


Figure 3.7: Pictorial representations of the topological invariants defined in Eqs. (3.5.4) and (3.5.5) on the lattice Λ in PBC (i.e. a torus). The topological sectors of Eq. (3.5.8) are sketched in the yellow panel: closed red curves on the blue torus Λ correspond to SU(2) loop excitations. Energy gaps between the first excited levels and the ground state of Eq. (3.1.2) in PBC, for a 2×2 lattice. Figure from [2]

and justify labeling them as *topological invariants*. The whole symmetry group is then $\mathbb{Z}_2 \times \mathbb{Z}_2$, as we have $[\hat{\mathbb{P}}_x, \hat{\mathbb{P}}_y] = 0 \forall x, y \in \Lambda$. Therefore, any physical state $|\Psi\rangle$ of the pure theory in Eq. (3.1.2) lies in one of the sectors of $\hat{\mathbb{P}}_x$ and $\hat{\mathbb{P}}_y$ sketched in the yellow panel of Fig. 3.7. The distinction between different symmetry sectors is in terms of the number of *non-removable loop excitations* displayed by the state. With *loop excitations*, we refer to closed magnetic strings (red circles in the blue torus of the yellow panel of Fig. 3.7) displayed by the state on its topological geometry. In particular, *non-removable* loops are the ones that cannot be removed through homotopies, i.e. without modifying the topology of the system.

Then, any state with an *even* number of horizontal (vertical) non-removable loop excitations lies in the *even* sector of the vertical $\hat{\mathbb{P}}_y$ (horizontal $\hat{\mathbb{P}}_x$) topological invariant. Correspondingly, any state with an *odd* number of non-removable loop excitations lies in the *odd* sector of the proper topological invariant. Hence, $\forall k \in \{x, y\}$:

$$\langle \Psi | \hat{\mathbb{P}}_k | \Psi \rangle = \lambda \quad \text{where} \quad \lambda \in \frac{\hat{\mathbb{P}}_x}{\hat{\mathbb{P}}_y} \begin{array}{cc|cc} +1 & +1 & -1 & -1 \\ +1 & -1 & +1 & -1 \end{array} \quad (3.5.8)$$

By selecting each quantum number(s) for this symmetry group, we can evaluate inter-sector and intra-sector energy gaps, and verify the presence of quasi-degeneracies, signatures of a potential spontaneous breaking of the topological symmetry group, and thus of topological order.

To check numerically the previous statements, we would need to measure the topological invariants on the low energy states of the Hamiltonian in Eq. (1.3.45). As shown in Fig. 3.7, the topological sectors of the first 4 lowest eigenstates of the pure theory in PBC belong to a different topological sector of Eq. (3.5.8). Moreover, the eigenstates are sorted in increasing energy according to the table in Eq. (3.5.8). In particular, $E_1 = E_2$ only in the case of isotropic geometries, as non-removable loop excitations along the two directions are equally expensive in energy. In

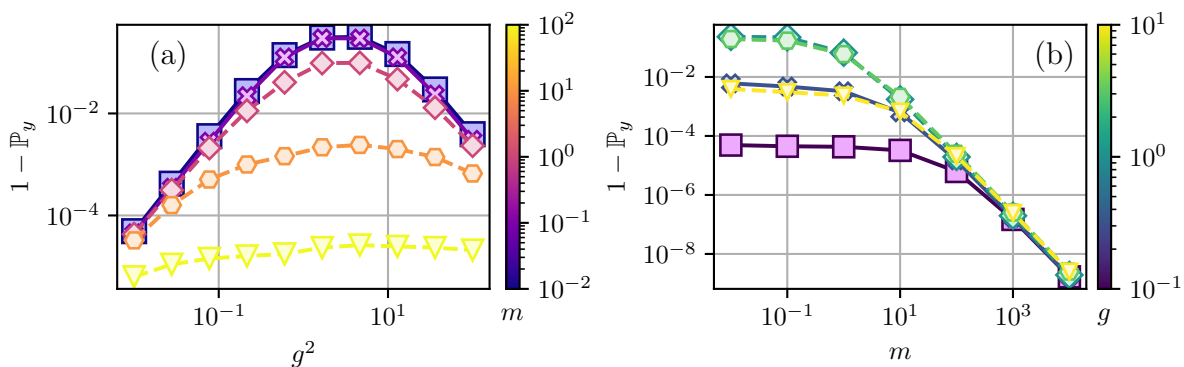


Figure 3.8: Distance between the ground-state \mathbb{P}_y -topological invariant in the full theory and the corresponding one of the pure theory for different m -values (a) and g -couplings (b). Results from simulations in a 2×2 lattice with PBC at $b = 0$. Figure from [2].

the case of an-isotropic lattices, where $N_x \neq N_y$, non-removable loop excitations along different axes are shifted in energy. Remarkably, when approaching the transition point from the large- g phase, inter-sector and intra-sector gaps reach a minimum, signaling a possible degeneracy lifted by finite-size effects. However, both gaps re-open while moving towards the small- g phase. This observation suggests topological order not to survive for $g^2 \ll 2$.

3.5.3 Dynamical matter removes the topological symmetry

The addition of dynamical matter removes the topological invariants $\mathbb{P}_{x,y}$ from being symmetries of the model because of the hopping terms inverting the string parity. Indeed, each of them includes a single parallel transport \hat{U} that flips one link parity along the line where \mathbb{P}_x or $\hat{\mathbb{P}}_y$ are defined. In the large- m limit, where the particle density vanishes, the Hamiltonian in Eq. (3.1.2) reduces to the only pure theory, and the topological invariants become good quantum numbers again (at least in the ground-state).

Such a behavior is exactly reproduced in Fig. 3.8, where we look at the distance between the exact *even* topological sector of $\hat{\mathbb{P}}_y$ (+1) and the corresponding value measured on the ground state. That gap gets larger when approaching the g -transition while vanishing far from the latter. Moreover, in the large-mass m limit, we recover the full symmetry sector of the pure theory.

3.6 Large-coupling phase via perturbation theory

In the large- g limit, the zero-density sector of the truncated SU(2) Hamiltonian can be studied via perturbation theory in $1/g^2$. In this scenario, the full theory can be mapped to a good approximation into a spin-like Hamiltonian similar to an anisotropic Heisenberg model in two spatial dimensions [288, 289]. Let us start rewriting the Hamiltonian in Eq. (1.3.45) as

$$H \sim \left[\hat{H}_0 + \left(\hat{H}_{\text{matt}} + \hat{H}_{\text{x-hop}} + \hat{H}_{\text{y-hop}} + \hat{H}_{\text{plaq}} \right) \right] = \sum_{\mathbf{n}} \left[\hat{H}_{\mathbf{n}}^0 + \hat{H}_{\mathbf{n}}^{\text{matt}} + \hat{H}_{\mathbf{n}}^{\text{x-hop}} + \hat{H}_{\mathbf{n}}^{\text{y-hop}} + \hat{H}_{\mathbf{n},\square}^{\text{plaq}} \right] \quad (3.6.1)$$

where \hat{H}_0 is the single-site unperturbed Hamiltonian:

$$\hat{H}_{\mathbf{n}}^0 = \frac{g^2}{4} \hat{\Gamma}_{\mathbf{n}}, \quad (3.6.2)$$

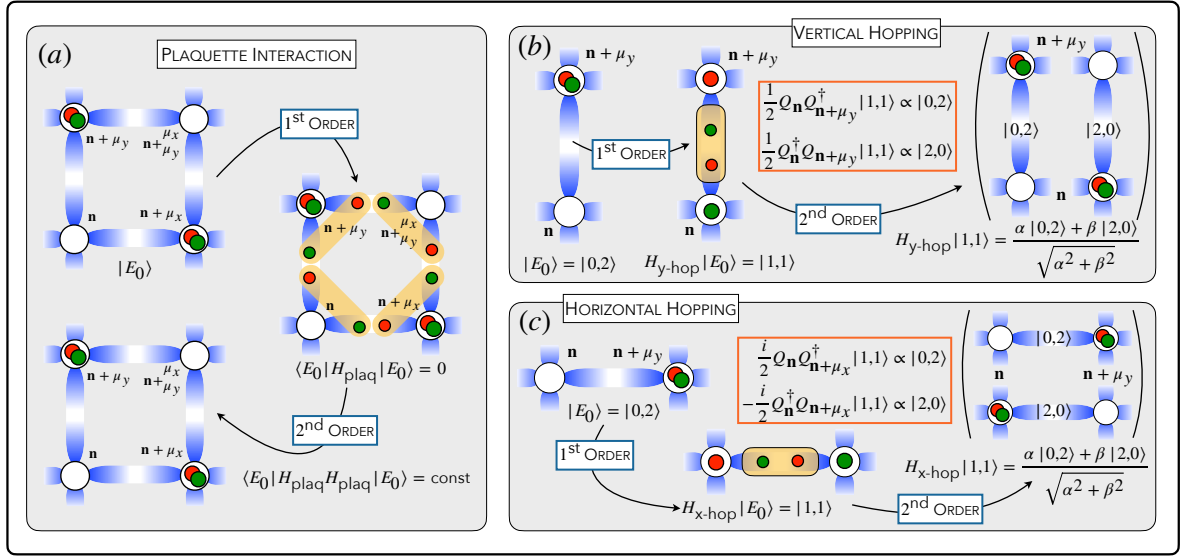


Figure 3.9: Graphical representation of the 1st and 2nd order perturbative effects of the magnetic (a) and the hopping terms (b)-(c) to the ground state of Eq. (3.6.2).

while the perturbative terms read:

$$\hat{H}_{\mathbf{n}}^{\text{matt}} = m(-1)^{n_x+n_y} \hat{N}_{\mathbf{n},\text{tot}} \quad (3.6.3a)$$

$$\hat{H}_{\mathbf{n}}^{\text{x-hop}} = \frac{1}{2} \left[-i \hat{Q}_{\mathbf{n},+\mu_x}^\dagger \hat{Q}_{\mathbf{n}+\mu_x,-\mu_x} + \text{h.c} \right] \quad (3.6.3b)$$

$$\hat{H}_{\mathbf{n}}^{\text{y-hop}} = \frac{1}{2} \left[-(-1)^{n_x+n_y} \hat{Q}_{\mathbf{n},+\mu_y}^\dagger \hat{Q}_{\mathbf{n}+\mu_y,-\mu_y} + \text{h.c} \right] \quad (3.6.3c)$$

$$\hat{H}_{\mathbf{n},\square}^{\text{plaq}} = -\frac{1}{2g^2} \begin{pmatrix} \hat{C}_r & \hat{C}_l \\ \hat{C}_l & \hat{C}_r \end{pmatrix}. \quad (3.6.3d)$$

where for simplicity, we replaced the two species of *arrival operators* in Eq. (1.3.39) and *corner operator* in Eq. (1.3.43) with a unique version, \hat{Q} and \hat{C} respectively.

In the large- g limit, we expect the 0th order ground-state $|E_0\rangle$ not to display gauge activity, as the electric interaction is energetically penalized. Then, the effective Hilbert state of the dressed sites reduces just to states with singlets in the matter fields. Namely, in terms of the sectors of the local charge density operator, we have only

$$|0\rangle \equiv \begin{pmatrix} 0 \\ 0 \\ 0 \\ 0 \end{pmatrix} \quad \text{and} \quad |2\rangle \equiv \begin{pmatrix} 0 \\ 0 \\ rg \\ 0 \end{pmatrix}. \quad (3.6.4)$$

Therefore, at the 0th-order, the single-site ground-state $|E_0\rangle$ can be expressed as a linear combination of Eq. (3.6.4) with energy $E_0 = 0$:

$$|E_0\rangle = \alpha |0\rangle + \beta |2\rangle \quad \text{with} \quad \sqrt{\alpha^2 + \beta^2} = 1 \quad (3.6.5)$$

At the 1st perturbative order, we have to separately consider the action of every single term in Eq. (3.6.3a)-Eq. (3.6.3d). As for the plaquette term in Eq. (3.6.3d), we expect it to yield a vanishing contribution. Indeed, if we refer to $|E_0\rangle$ as a single-plaquette ground state, then we have:

$$\langle E_0 | \hat{H}^{\text{plaq}} | E_0 \rangle = \langle E_0 | \left(-\frac{1}{2g^2} \right) \left(\frac{1}{\sqrt{2}} \right)^4 | E_1 \rangle = -\frac{1}{8g^2} \langle E_0 | E_1 \rangle = 0 \quad (3.6.6)$$

since the plaquette-state $|E_1\rangle$ is orthogonal to the ground state $|E_0\rangle$, as all its links are electrically active (see Fig. 3.9). The factor $1/\sqrt{2}$ is due to each single corner operator \hat{C} acting on the corresponding empty corner of the plaquette state $|E_0\rangle$.

As for the hopping terms, we focus on the effective Hilbert space of the neighboring sites \mathbf{n} and $\mathbf{n} + \boldsymbol{\mu}$:

$$\mathcal{H}_{\mathbf{n},\boldsymbol{\mu}}^{\text{eff}} = \{|0,0\rangle, |0,2\rangle, |2,0\rangle, |2,2\rangle\} \quad \forall \mathbf{n}, \forall \boldsymbol{\mu} \quad (3.6.7)$$

where we labeled the states $|\mathbf{n}, \mathbf{n} + \boldsymbol{\mu}\rangle$ in terms of the only two possible single-site states in Eq. (3.6.4). First of all, we notice that $|0,0\rangle$ and $|2,2\rangle$ are completely decoupled from the other two states, since $\forall \boldsymbol{\mu}$:

$$\hat{Q}_{\mathbf{n},+\boldsymbol{\mu}}^\dagger \hat{Q}_{\mathbf{n}+\boldsymbol{\mu},-\boldsymbol{\mu}} |0,0\rangle = \hat{Q}_{\mathbf{n},+\boldsymbol{\mu}}^\dagger \hat{Q}_{\mathbf{n}+\boldsymbol{\mu},-\boldsymbol{\mu}} |2,2\rangle = 0 \quad (3.6.8)$$

Then, the only relevant matrix elements of the effective (perturbed) hopping-Hamiltonian are:

$$\begin{aligned} \hat{Q}_{\mathbf{n},+\boldsymbol{\mu}}^\dagger \hat{Q}_{\mathbf{n}+\boldsymbol{\mu},-\boldsymbol{\mu}} |0,2\rangle &= (-1)^2 |1,1\rangle \\ \hat{Q}_{\mathbf{n},+\boldsymbol{\mu}} \hat{Q}_{\mathbf{n}+\boldsymbol{\mu},-\boldsymbol{\mu}}^\dagger |2,0\rangle &= (-1)^2 |1,1\rangle \end{aligned} \quad \forall \mathbf{n}, \forall \boldsymbol{\mu} \quad (3.6.9)$$

where $|1,1\rangle$ is figured in Fig. 3.9, while the (-1) factor is due to the action of a single arrival operator $\hat{Q}_{\mathbf{n},\boldsymbol{\mu}}^{(\dagger)}$ defined in Eq. (1.3.39) on the states in Eq. (3.6.4). Since $\langle 0,2|1,1\rangle = 0 = \langle 2,0|1,1\rangle$, none of the hopping Hamiltonians Eq. (3.6.3b)-(3.6.3c) do provide any 1^{st} -order correction to \hat{H}_0 in Eq. (3.6.2).

The only relevant 1^{st} order term is the one related to \hat{H}_{matt} , as it acts just on the matter fields without yielding any gauge activity. Moreover, it removes the ground-state degeneracy of Eq. (3.6.5) by favoring a staggered configuration to the lattice, namely:

$$|E_1(n)\rangle = \delta_{1,(-1)^{n_x+n_y}} |0\rangle + \delta_{-1,(-1)^{n_x+n_y}} |2\rangle \quad (3.6.10)$$

where δ_{ij} is the Kronecker delta function. However, for sufficiently small values of the mass m , the staggering effect is irrelevant, and the degeneracy of Eq. (3.6.5) is restored. Therefore, in the small- m limit, the first relevant perturbative order is the 2^{nd} one.

As for the plaquette interaction, the 2^{nd} order does not remove the ground-state degeneracy, as it completely restores $|E_0\rangle$ providing just an energy shift. Namely, the 2^{nd} order perturbative corrections to the single-site ground-state energy reads:

$$\begin{aligned} E_2^{\text{plaq}} &= \frac{1}{4} \langle E_0 | \hat{H}_{\text{plaq}} [E_0 - H_0]^{-1} \hat{H}_{\text{plaq}} | E_0 \rangle \\ &= \frac{1}{4} \left(-\frac{1}{2g^2} \right) \langle E_0 | \hat{H}_{\text{plaq}} [E_0 - H_0]^{-1} | E_1 \rangle \\ &= -\frac{1}{8g^2} \langle E_0 | \hat{H}_{\text{plaq}} \left[-\frac{g^2}{4} \sum_{\mathbf{n} \in \square} \hat{\Gamma}_{\mathbf{n}} \right]^{-1} | E_1 \rangle \\ &= -\frac{1}{8g^2} \left(-\frac{g^2}{4} \cdot \frac{3}{4} \right)^{-1} \langle E_0 | \hat{H}_{\text{plaq}} | E_1 \rangle = -\frac{2}{3g^4} \left(-\frac{1}{2g^2} \right) \langle E_0 | E_0 \rangle = \boxed{\frac{1}{3g^6}} \end{aligned} \quad (3.6.11)$$

where $[O]^{-1}$ is the Moore-Penrose inverse and the initial $1/4$ factor is put to get the single-site energy out of the one of a plaquette.

As for the hopping terms, because of Eq. (3.6.8)-(3.6.9), $\forall k \in \{x, y\}$, the only relevant terms are the diagonal ones

$$\frac{1}{2} \langle 0, 2 | \hat{H}^{\text{hop}} [E_0 - \hat{H}_0]^{-1} \hat{H}^{\text{hop}} | 0, 2 \rangle = \frac{1}{2} \langle 2, 0 | \hat{H}^{\text{hop}} [E_0 - \hat{H}_0]^{-1} \hat{H}^{\text{hop}} | 2, 0 \rangle \quad (3.6.12)$$

and the off-diagonal ones:

$$\frac{1}{2} \langle 0, 2 | \hat{H}^{\text{hop}} [E_0 - \hat{H}_0]^{-1} \hat{H}^{\text{hop}} | 2, 0 \rangle = \frac{1}{2} \langle 2, 0 | \hat{H}^{\text{hop}} [E_0 - \hat{H}_0]^{-1} \hat{H}^{\text{hop}} | 0, 2 \rangle. \quad (3.6.13)$$

The factor 1/2 is put to take into account just the single-site energy out of the corresponding two-site energy. As for the hopping along the x -axis, we have:

$$\begin{aligned} & \frac{1}{2} \langle 0, 2 | \hat{H}^{\text{x-hop}} [E_0 - \hat{H}_0]^{-1} \hat{H}^{\text{x-hop}} | 0, 2 \rangle \\ &= \frac{1}{2} \langle 0, 2 | h^{\text{x-hop}} [E_0 - \hat{H}_0]^{-1} \left(-\frac{i}{2} \right) | 1, 1 \rangle \\ &= \left(\frac{-i}{4} \right) \langle 0, 2 | \hat{H}^{\text{x-hop}} \left[-\frac{1g^2}{4} (\hat{\Gamma}_{\mathbf{n}} + \hat{\Gamma}_{\mathbf{n}+\mu_x}) \right]^{-1} | 1, 1 \rangle \\ &= \left(\frac{-i}{4} \right) \langle 0, 2 | \hat{H}^{\text{x-hop}} \left(-\frac{8}{3g^2} \right) | 1, 1 \rangle \\ &= \frac{2i}{3g^2} \langle 0, 2 | \left(\frac{i}{2} \right) | 0, 2 \rangle = \boxed{-\frac{1}{3g^2}}. \end{aligned} \quad (3.6.14)$$

Analogously proceeding, we have:

$$\frac{1}{2} \langle 2, 0 | \hat{H}^{\text{x-hop}} [E_0 - \hat{H}_0]^{-1} \hat{H}^{\text{x-hop}} | 0, 2 \rangle = \boxed{\frac{1}{3g^2}}. \quad (3.6.15)$$

Then, the 2^{nd} -order perturbative x -hopping term reads:

$$\hat{H}_{\text{x-hop}}^{\text{eff}} = -\frac{1}{3g^2} \begin{pmatrix} 0 & 0 & 0 & 0 \\ 0 & +1 & -1 & 0 \\ 0 & -1 & +1 & 0 \\ 0 & 0 & 0 & 0 \end{pmatrix} = -\frac{1}{6g^2} \left[\hat{\sigma}_{\mathbf{n}}^x \hat{\sigma}_{\mathbf{n}+\mu_y}^x + \hat{\sigma}_{\mathbf{n}}^y \hat{\sigma}_{\mathbf{n}+\mu_y}^y - \hat{\sigma}_{\mathbf{n}}^z \hat{\sigma}_{\mathbf{n}+\mu_y}^z \right]. \quad (3.6.16)$$

As for the y -hopping Hamiltonian, one can prove that:

$$\hat{H}_{\text{y-hop}}^{\text{eff}} = \frac{1}{3g^2} \begin{pmatrix} 0 & 0 & 0 & 0 \\ 0 & +1 & +1 & 0 \\ 0 & +1 & +1 & 0 \\ 0 & 0 & 0 & 0 \end{pmatrix} = -\frac{1}{6g^2} \left[\hat{\sigma}_{\mathbf{n}}^x \hat{\sigma}_{\mathbf{n}+\mu_y}^x + \hat{\sigma}_{\mathbf{n}}^y \hat{\sigma}_{\mathbf{n}+\mu_y}^y + \hat{\sigma}_{\mathbf{n}}^z \hat{\sigma}_{\mathbf{n}+\mu_y}^z \right]. \quad (3.6.17)$$

Summarizing, in the large- g limit, the Hamiltonian in Eq. (1.3.45) can be approximated as:

$$\hat{H}^{\text{eff}} \sim -\frac{1}{6g^2} \sum_{\mathbf{n}} \left[\left[\hat{\sigma}_{\mathbf{n}}^x \hat{\sigma}_{\mathbf{n}+\mu_x}^x + \hat{\sigma}_{\mathbf{n}}^y \hat{\sigma}_{\mathbf{n}+\mu_x}^y - \hat{\sigma}_{\mathbf{n}}^z \hat{\sigma}_{\mathbf{n}+\mu_x}^z \right] + \left[\hat{\sigma}_{\mathbf{n}}^x \hat{\sigma}_{\mathbf{n}+\mu_y}^x + \hat{\sigma}_{\mathbf{n}}^y \hat{\sigma}_{\mathbf{n}+\mu_y}^y + \hat{\sigma}_{\mathbf{n}}^z \hat{\sigma}_{\mathbf{n}+\mu_y}^z \right] \right] \quad (3.6.18)$$

which looks similar to a 2D quantum Heisenberg Hamiltonian apart from the staggering factor in the kinetic term $\hat{\sigma}^z \hat{\sigma}^z$ [288, 289].

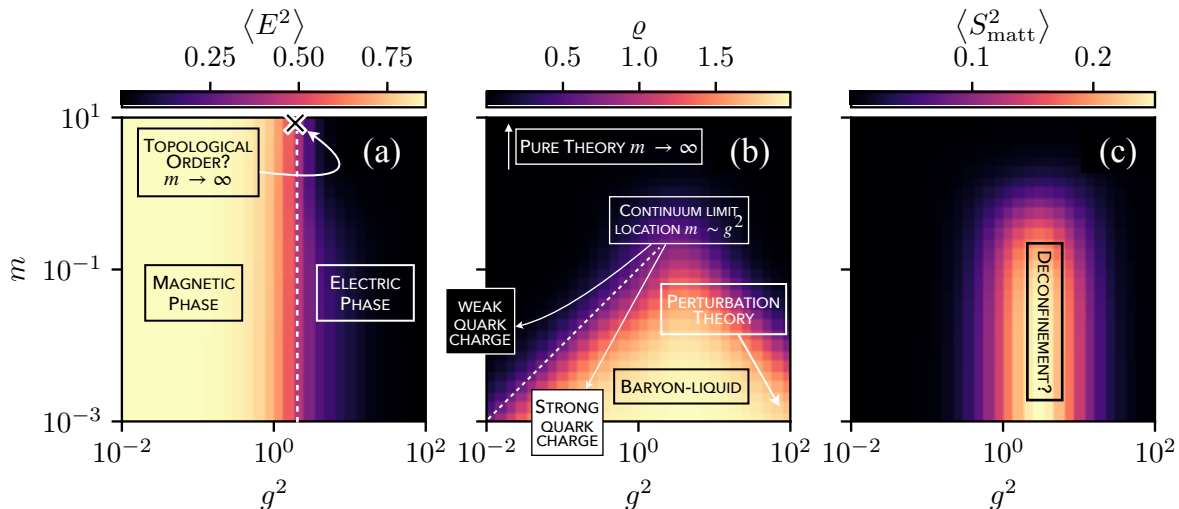


Figure 3.10: Phase diagram (g^2, m) of the full SU(2) Hamiltonian in Eq. (3.1.2) in the sector with zero baryon number density from (a) the average electric energy density in Eq. (3.1.4), (b) the average particle density in Eq. (3.1.7), and (c) the matter color density defined in Eq. (3.1.9). Phases are marked according to all the discussions throughout the entire chapter.

3.7 Phase Diagram

By collecting and summarizing all the previous observations, we can outline in Fig. 3.10 the full phase diagram of the (2+1)D SU(2) Yang-Mills Hamiltonian in Eq. (3.1.2) around zero baryon density $b = 0$ (where the baryon mass gap opens).

We observed that the presence of fermionic degrees of freedom affects only marginally the behavior of the gauge degrees of freedom of Eq. (3.1.4), albeit the magneto-electric transition becomes smoother at lower m values.

For sufficiently large masses, $m > m^*(g)$, matter fields play a minor role (trivial phase). In the infinite mass limit, the Hamiltonian recovers the topological properties of the pure theory of Sec. 3.5, but no spontaneous topological order survives outside the magneto-electric transition $g^2 \sim 2(1)$.

Conversely, for small masses, $m < m^*(g)$ [17], we observe an emergent color-density of the matter fields, only in the proximity of the magneto-electric transition. Such observation is compatible with the existence of a deconfined critical phase (i.e. where color particles may appear) in the region where electric and magnetic fields are maximally frustrated. Elsewhere, the system shows the free emergence of a liquid of colorless baryons and anti-baryons. The collective behavior towards the continuum limit is particularly intriguing, as it can exhibit both trivial or baryon superfluid phase depending on the quark ratio α_c .

3.8 Summary

In this chapter, we reviewed the numerical results obtained from TN simulations of a non-Abelian SU(2) Yang-Mills LGT in two spatial dimensions, with dynamical matter and hardcore gluons [2]. Our focus on this physical setting is motivated by the wide use of the latter as a paradigmatic model to address fundamental properties that could be relevant for high-dimensional QCD. For instance, standard MC simulations of such an LGT have highlighted intriguing effects, such

as the *dimensional reduction* [18, 19], the compatibility with *string theory* [290, 291], and the possibility of accessing features of the *continuum theory* already at small correlation lengths [28].

In summary, we have investigated in detail both the zero and finite baryon number density regimes, where MC methods are severely limited due to the sign problem. Our results confirm TN methods as a reliable approach to addressing the non-perturbative phenomena of LGTs, capable of accessing strong coupling regimes as well as finite baryon number densities.

Despite the truncation of the gauge field, by exploiting numerical estimations of various observables, we inferred quite a few qualitative and quantitative observations concerning the zero-temperature phase diagram of the model. First, when approaching the continuum limit ($a_0 \rightarrow 0$ at fixed m_0, α_c) SU(2) baryons and anti-baryons become the actual quasiparticles of the theory. Interestingly, if their color charge is strong enough, i.e. for a sufficiently large quark ratio $\alpha_c \geq \alpha_c^*(m_0)$, baryons seem to be able to condense into a superfluid phase.

In the parameter regime at $g^2 \sim 2(1)$, where the electric term and the magnetic term are maximally frustrated, and electric and magnetic field fluctuations are proportional, we witnessed more exotic physics: at low quark masses, the system manifests colorful matter sites, possibly indicating a quark-deconfined regime, such as a quark-gluon plasma. At high quark masses, the system encounters a degeneracy between topological sectors (string symmetries in periodic boundary conditions), possibly signaling the emergence of a topological order reminiscent of the Toric code.

From a theoretical perspective, the simulated Hamiltonian describes the interaction between flavorless 2-color fermionic matter and gauge fields in the *hardcore-gluon* approximation of Sec. 1.3.5. Considering larger representations in the gauge Hilbert space (following the prescription detailed in Sec. 1.3) would be a natural extension of these simulations and an improved approximation of the continuous gauge field theory. A larger truncation becomes substantial in the small coupling limit, where the Hamiltonian is dominated by the magnetic interaction, which is non-local and non-diagonal in the representation basis developed in Sec. 1.3.2. This makes the model significantly entangled and challenging to be numerically attacked via TNs.

As an outlook of this study, we plan to develop an analogous formalism in the magnetic basis, where plaquette terms are diagonal [112, 167, 292]. This change of basis should ease TN simulations, which in our case are limited to finite system sizes, but anyway larger than the state-of-the-art of quantum-inspired or quantum simulations of non-Abelian LGTs [134, 175, 293]. Accessing larger system sizes would be a substantial advantage, as it would enable the characterization of correlation functions not distorted by finite-size effects. Correspondingly, larger sizes would allow for studying magnetic effects at small coupling, as in MC simulations [294–296].

To overcome these limitations (finite gauge representation and finite system sizes), further developments of the numerical simulation architecture are also required: on the hardware side, the possibility of running the computation on a (pre)exascale HPC environment, while on the software side the development of new and improved TN-based algorithms. The latter will be achieved by exploiting the augmented TTN ansatz, which drastically enhances the capability of representing area law-states in high dimensions [173]. These steps will be fundamental for the long-term goal of applying TN methods to large-scale (3+1) lattice QCD and ultimately address open, secular research problems, such as confinement and asymptotic freedom.

From an experimental viewpoint, similarly to the one-dimensional case [143], the dressed-site formalism developed for the (2+1)D SU(2) Hamiltonian could be encoded on quantum hardware. In this perspective, the results presented in this chapter and in [2] represent essential benchmarks

for validating current and future experimental implementations [136, 297-299].

Chapter 4

Non-Ergodic dynamics of LGTs

The nature of equilibration in a isolated interacting quantum many-body (QMB) systems is a fundamental question in physics [300]. Whereas open quantum systems are expected to thermalize due to exchanging energy with a bath [301], the conditions under which an isolated QMB system thermalizes are less intuitive. While the classical counterpart can be easily figured out by using the Liouville theorem and applying the statistical mechanics ensemble on the phase space [302], thermalization in quantum systems is stipulated by the Eigenstate Thermalization Hypothesis (ETH) [302–305]. According to the ETH, for an *ergodic* Hamiltonian, the expectation values of observables in individual energy eigenstates match thermal ensemble averages, and through the process of *dephasing*, the system’s long-time behavior averages out to these thermal values, leading to thermalization.

So far, ETH has been widely confirmed and numerically verified in several contexts, from strongly correlated models of condensed matter and ultracold atom gases of (softcore and hardcore) bosons [306–310], spins [311–314], and fermions [315–318]. However, in recent years, a new paradigm of weak ergodicity breaking has emerged violating the ETH. In certain ergodic Hamiltonians, there is a polynomial (in system size) number of special non-thermal *scar* eigenstates that are roughly equally spaced in energy over the whole spectrum [319–321] and exhibit anomalously low bipartite entanglement entropy [322]. Upon initializing the system in an initial state with a high overlap with these scar eigenstates, the subsequent quench dynamics gives rise to *quantum many-body scarring* (QMBS), which manifests as prominent oscillations in local observables and persistent revivals in the (local and global) Loschmidt fidelity that last longer than all relevant timescales, thereby circumventing expected thermalization [320, 323–328]. QMBS has received a lot of attention since its initial discovery in [323] and has been the subject of several quantum simulation experiments [299, 329–332].

After the discovery of QMBS, it has been shown that the effective model quantum-simulated in [323] is a spin-1/2 U(1) lattice gauge theory (LGT), where the electric field is represented by a spin-1/2 z -operator [333]. In detail, the robustness of QMBS has been shown to depend on the stability of an underlying gauge symmetry of this model [334]. Later, QMBS have been further observed in spin- S U(1) LGTs [335, 336] and other Abelian LGTs [337–339], even in two spatial dimensions [340–344]. Nonetheless, none of these studies tried to explore QMBS in the non-Abelian scenario. Recently, Ref. [345] has shown the emergence of scarring dynamics on a pure (without dynamical matter) (2+1)D SU(2) LGT. In detail, looking at the bipartite entanglement entropy, [345] identified a few scar-eigenstate candidates in a certain parameter regime. However, no experimentally feasible scarred initial states have been proposed, and the type of exhibited scarring vanishes beyond the crudest truncation of the electric field basis.

In this chapter, we bridge this gap discussing the emergence of QMBS in non-Abelian LGTs with dynamical matter and connect the presence of the latter at the origin of such an exotic dynamics. We start from Sec. 4.1, with a pedagogical introduction to classical thermalization. Then, in Sec. 4.2, we switch to the corresponding quantum version and expose in Sec. 4.2.1 the Eigenstate Thermalization Hypothesis (ETH) for isolated QMB systems in terms of their spectral and dynamical properties. After this introduction, we devote Sec. 4.3 to the first experimental and numerical observations of *scarring* dynamics in Rydberg atom chains. In Sec. 4.3.2, we highlight the strong connection QMB scars and fundamental mechanisms appearing in Abelian LGTs. The original part is in Sec. 4.4, where we extend such a relation to non-Abelian LGTs by simulating a one-dimensional truncated SU(2) Yang-Mills LGT and observing all the spectral and dynamical properties of a scarring dynamics [4].

4.1 Thermalization in Classical Systems

Before introducing the concept of thermalization in quantum physics, it is useful to first consider its classical counterpart and gain a physical intuition of the mechanism. Thermalization in isolated classical systems refers to the process by which a system evolves over time to reach a state where its macroscopic properties become consistent with those predicted by statistical mechanics. This concept is closely tied to the behavior of the system in its phase space, particularly when the system's total energy is conserved.

Let us consider a classical system of N particles without any exchange of energy or matter with the environment. The corresponding phase space Σ of the system is defined by a set of $2N$ variables $\Gamma = \{\mathbf{r}, \mathbf{p}\} = \{r_1, \dots, r_N, p_1, \dots, p_N\}$ identifying position and momentum of each particle on a point of the phase space Γ . Since the system is isolated, $\Gamma(t)$ moves on a hypersurface of the whole phase space Σ_E characterized by constant energy E .

Then, in principle, the dynamics of the system requires to follow the evolution of $\Gamma(t)$ at each time step along that hypersurface. Namely, for any observable O , we need to evaluate $O(\Gamma(t)) \forall t$. Correspondingly, the long-time average of such an observable is given by:

$$\bar{O} = \lim_{T \rightarrow \infty} \frac{1}{T} \int_0^T O(\Gamma(t)) dt. \quad (4.1.1)$$

If the system is *ergodic*, we expect that, given enough time, the trajectory $\Gamma(t)$ will pass arbitrarily close to every point of the hypersurface Σ_E at energy E . More in detail, thanks to the Liouville theorem, we then assume that the time spent in any small region of Σ_E is proportional to the phase space volume of that region. This implies that the time average of a function over a long period is statistically equivalent to the predictions made by statistical mechanics, where all accessible microstates at a given energy are equally probable.

In statistical mechanics, the microcanonical ensemble (ME) describes a system with fixed total energy E and number of particles N . Then, the ensemble average of an observable O corresponds to the uniform average over all possible microstates with energy E , because all accessible microstates are equally probable:

$$\langle O \rangle_{\text{ME}} = \frac{\int_{\Sigma_E} O(\Gamma) d\Gamma}{\int_{\Sigma_E} d\Gamma}. \quad (4.1.2)$$

Let us then assume the system to be in a non-equilibrium initial state where its macroscopic properties do not match the predictions of statistical mechanics. According to classical ergodicity, as the system evolves, the interactions between particles lead to a redistribution of energy and

momentum, causing the system to explore the whole hypersurface Σ_E of the phase space. Over time, the system “forgets” its initial conditions (except for conserved quantities like energy) and its macroscopic observables settle down to values that match the microcanonical ensemble predictions [302]. Once thermalization is complete, the long-time average in Eq. (4.1.1) matches the microcanonical ensemble average in Eq. (4.1.2) and $\bar{O} = \langle O \rangle_{\text{ME}}$. The system is then said to be in *thermal equilibrium*.

While a robust proof of ergodicity is typically challenging, a few examples have been demonstrated to display thermalization, such as gases in hard spheres in some volumes, a.k.a. Sinai billiards [346], and the Bunimovich Stadium [347], describing a free particle inside a stadium with hard walls that are circular on the sides and straight in the middle.

Of course, for an *integrable* system, i.e. with an extensive number of conserved quantities $\sim N$, its motion is constrained in a very small subportion of the hypersurface Σ_E which strongly depends on the initial conditions, and the whole dynamics reveals (quasi-)periodic. In such cases, ergodicity does not hold, as the statistical mechanics average is not applicable.

4.2 Thermalization in Quantum Systems

While for classical systems the connection between ergodicity of isolated systems and statistical mechanics is quite straightforward, a more accurate analysis is needed to understand how isolated quantum systems reaches thermal equilibrium, as in these case position r and momentum p do not commute and we cannot rely on the phase space.

Let us consider a finite non-integrable¹ N -body quantum system with N sufficiently large and a non-degenerate Hamiltonian spectrum:

$$\hat{H} = \sum_{\alpha=1}^N E_{\alpha} |\Phi_{\alpha}\rangle\langle\Phi_{\alpha}|, \quad (4.2.1)$$

where $\{E_{\alpha}\}_{\alpha=1\dots N}$ and $\{|\Phi_{\alpha}\rangle\}_{\alpha=1\dots N}$ are the corresponding eigenvalues and eigenvectors. Let us then assume to quench the system with an initial pure² state $|\Psi(0)\rangle = \sum_{\alpha} C_{\alpha} |\Phi_{\alpha}\rangle$, whose energy is well defined, extensive in N ³ and robust under (subextensive) fluctuations:

$$E = \langle H \rangle = \langle \Psi(0) | H | \Psi(0) \rangle \sim N \quad \Delta E = \sqrt{\langle H^2 \rangle - \langle H \rangle^2} \sim N^{\nu} \quad \text{with } \nu < 0. \quad (4.2.2)$$

In the Schrödinger picture, the system can be described in terms of the state

$$|\Psi(t)\rangle = \sum_{\alpha} C_{\alpha} e^{-itE_{\alpha}/\hbar} |\Phi_{\alpha}\rangle \quad \text{where} \quad \sum_{\alpha} |C_{\alpha}|^2 = 1. \quad (4.2.3)$$

Correspondingly, any generic (local) observable O can be instantaneously measured as follows

$$\begin{aligned} O(t) &= \langle \Psi(t) | O | \Psi(t) \rangle = \sum_{\alpha, \beta} C_{\alpha}^* C_{\beta} e^{it(E_{\alpha} - E_{\beta})} O_{\alpha\beta} \\ &= \sum_{\alpha} |C_{\alpha}|^2 O_{\alpha\alpha} + \sum_{\alpha, \alpha \neq \beta} C_{\alpha}^* C_{\beta} e^{it(E_{\alpha} - E_{\beta})} O_{\alpha\beta} \end{aligned} \quad (4.2.4)$$

¹If the system has a set of symmetries, we assume that all of them are resolved.

²Generalizations of ETH to mixed states are discussed in [302].

³This corresponds to assume that each d.o.f. has a finite amount of energy, and the system energy is far above the ground state energy.

where $O_{\alpha\beta} = \langle \Phi_\alpha | O | \Phi_\beta \rangle$. In analogy to the classical counterpart, we can formally define the *long time average* resulting from the unitary dynamics of the observable, which is well described by the average value predicted by the *diagonal ensemble* [306]:

$$\begin{aligned}
\bar{O} &\equiv \lim_{T \rightarrow \infty} \frac{1}{T} \int_0^T dt \langle \Psi(t) | O | \Psi(t) \rangle \\
&= \lim_{T \rightarrow \infty} \frac{1}{T} \int_0^T dt \sum_{\alpha, \beta} C_\alpha^* C_\beta \langle \Phi_\alpha | e^{it\hat{H}} O e^{-it\hat{H}} | \Phi_\beta \rangle \\
&= \sum_\alpha |C_\alpha|^2 O_{\alpha\alpha} + \sum_{\alpha, \alpha \neq \beta} C_\alpha^* C_\beta O_{\alpha\beta} \lim_{T \rightarrow \infty} \frac{1}{T} \int_0^T e^{i(E_\alpha - E_\beta)t} dt \\
&= \sum_\alpha |C_\alpha|^2 O_{\alpha\alpha} \equiv \langle O \rangle_{\text{DE}},
\end{aligned} \tag{4.2.5}$$

where the canceled term is exactly due to the dephasing, while $\langle O \rangle_{\text{DE}}$ is the average from the diagonal ensemble. Therefore, after enough time, we expect the observable $O(t)$ to approach long-time average $\langle O \rangle_{\text{DE}}$ which however depends on the initial quench of the system through the probabilities $|C_\alpha|^2$, as the latter are conserved in time.

This clearly differs from the expected *thermalization*, according to which the system relaxes to states whose macroscopic quantities are stationary, universal with respect to different initial conditions, and predictable using statistical mechanics [306]. Namely, thermalization in quantum system requires the long-time average in Eq. (4.2.5) to match the prediction of the *microcanonical ensemble* (ME), which relies on a superposition within the energy shell $[E - \Delta E, E + \Delta E]$ around the system energy E in Eq. (4.2.2) and containing $N_{E, \Delta E}$ eigenstates:

$$\langle O \rangle_{\text{ME}} = \frac{1}{N_{E, \Delta E}} \sum_{\substack{\alpha; \\ |E_\alpha - E| < \Delta E}} O_{\alpha\alpha}. \tag{4.2.6}$$

4.2.1 The Eigenstate Thermalization Hypothesis (ETH)

In order to prove the equivalence between the two ensemble averages (diagonal and microcanonical) and show ergodicity as an emerging property out of the microscopical properties of realistic QMB systems, we rely on the Eigenstate Thermalization Hypothesis (ETH), originally proposed by Deutsch [303] and Srednicki [304] and later widely confirmed [306]. For a detailed review, we recommend the reader to see [302, 305].

According to the ETH, the matrix elements of the observables displaying thermalization can be expressed in the Hamiltonian eigenbasis by the following ansatz:

$$O_{\alpha\beta} = O(E_{\alpha\beta}) \delta_{\alpha\beta} + e^{-S(E_{\alpha\beta})/2} f_O(E_{\alpha\beta}, \omega_{\alpha\beta}) R_{\alpha\beta} \tag{4.2.7}$$

where $E_{\alpha\beta} = (E_\alpha + E_\beta)/2$, $\omega_{\alpha\beta} = (E_\alpha - E_\beta)$, and $S(E) \sim N$ is the thermodynamic entropy at energy E . Correspondingly, $O(E_{\alpha\beta})$ and $f_O(E_{\alpha\beta}, \omega_{\alpha\beta}) = f_O(E_{\alpha\beta}, -\omega_{\alpha\beta})$ are smooth functions of their arguments, and $O(E_{\alpha\beta})$ equals the expectation value of the microcanonical ensemble at energy $E_{\alpha\beta}$. Ultimately, $R_{\alpha\beta} = R_{\beta\alpha}^{(*)}$ is a real (complex) variable with zero mean and unit variance ($\langle |R_{\alpha\beta}|^2 \rangle = 1$). Right candidates for observables that are proven to satisfy Eq. (4.2.7) are n -body observables, with $n \ll N$.

No matter of C_α , if the fluctuations of the system energy (and correspondingly the energy window of the microcanonical ensemble) are sufficiently small, i.e. $\Delta E \ll 1$, then, applying Eq. (4.2.7),

we can assume $O(E_{\alpha\beta})$ to be almost constant $\sim O(E)$ and approximate the long-time average in Eq. (4.2.5) as:

$$\langle O \rangle_{\text{DE}} = \sum_{\alpha}^N |C_{\alpha}|^2 O_{\alpha\alpha} \sim O(E) \sum_{\alpha}^N |C_{\alpha}|^2 = O(E). \quad (4.2.8)$$

Similarly, the thermal average given by the microcanonical ensemble reads:

$$\langle O \rangle_{\text{ME}} = \sum_{\alpha}^{N_{E,\Delta E}} \frac{O_{\alpha\alpha}}{N_{E,\Delta E}} \sim O(E) \sum_{\alpha}^{N_{E,\Delta E}} \frac{1}{N_{E,\Delta E}} = O(E), \quad (4.2.9)$$

so that, in the end, the long-time average matches the microcanonical ensemble prediction. Furthermore, using ETH, we can compute the long-time average of the temporal fluctuations of the observable expectation value:

$$\begin{aligned} \sigma_O^2 &= \lim_{T \rightarrow \infty} \frac{1}{T} \int_0^T dt [O(t)^2] - \langle O \rangle_{\text{DE}}^2 \\ &= \lim_{T \rightarrow \infty} \frac{1}{T} \int_0^T dt \sum_{\alpha, \beta, \gamma, \delta} O_{\alpha\beta} O_{\gamma\delta} C_{\alpha}^* C_{\beta} C_{\gamma}^* C_{\delta} e^{it(E_{\alpha} - E_{\beta} + E_{\gamma} - E_{\delta})} - \langle O \rangle_{\text{DE}}^2 \\ &= \sum_{\alpha, \alpha \neq \beta} O_{\alpha\beta} C_{\alpha}^* C_{\beta} \sum_{\gamma, \gamma \neq \delta} O_{\gamma\delta} C_{\gamma}^* C_{\delta} \lim_{T \rightarrow \infty} \frac{1}{T} \int_0^T dt e^{it(E_{\alpha} - E_{\beta} + E_{\gamma} - E_{\delta})} \\ &= \sum_{\alpha, \alpha \neq \beta} |O_{\alpha\beta}|^2 |C_{\alpha}|^2 |C_{\beta}|^2 \leq \max_{\alpha, \beta} |O_{\alpha\beta}|^2 \sum_{\alpha, \beta} |C_{\alpha}|^2 = \max_{\alpha, \beta} |O_{\alpha\beta}|^2 \propto e^{-S(E)}. \end{aligned} \quad (4.2.10)$$

Therefore, time fluctuations of the observable expectation values are exponentially small in the system size. Namely, $O(t)$ is almost equal at any time to the diagonal ensemble average and no time average is needed. In other words, ETH ansatz implies the ergodicity in the strong sense.

The equivalence between the long-time average and the statistical mechanics prediction is similar to the classical counterpart, where ergodicity can be explained in terms of particle collisions and energy redistribution between different d.o.f.. However, in isolated quantum systems, chaos, ergodicity, and thermalization are hidden in the nature of the Hamiltonian eigenstates. In other words, the information of the eventual thermal state is already encoded in the system from the initial quench, and relaxation of observables to their equilibrium values results from the *dephasing* originated in time evolution [302, 305, 306].

Numerical evidence of ETH has been found in several strongly correlated nonintegrable lattice models of condensed matter and ultracold atom gases, such as hard-core bosons [306, 307], soft-core bosons [308–310], interacting spin chains [311–314], and spinless and spinful fermions [315–318]. Nowadays, ETH is also applied in contexts like quantum gravity and warmholes [348, 349].

Nevertheless, despite a wide variety of QMB systems were observed displaying ergodicity and thermalization via ETH, some experiments have recently pointed out strong and weak violations of ETH. Apart from integrable systems, strong violations of ETH have been displayed by more interesting phenomena such as *many-body localization* (MBL) [350], where thermalization is strongly avoided by means of localized quench disorder.

4.3 Quantum Many-Body Scars and Lattice Gauge Theories

Here, we are interested in cases of *weak* ergodicity breaking, i.e. referred to a small portion of the spectrum violating ETH, while the overall system behaving ergodically. Such peculiar eigenstates

are called *scars* (like defects of the spectrum) and have been shown to be at the origin of slow dynamics for cold atoms experiments for some initial states [323, 326, 329]. In the following, we review the main features of such an exotic dynamics, starting from the observations in Rydberg atoms chains in Sec. 4.3.1 to the intimate connection with Abelian LGTs in Sec. 4.3.2.

4.3.1 Experimental observations of scars in Rydberg atoms

Experimental observation of slow dynamics, have been remarkably encountered in 1D Rydberg atom arrays of N optical traps, each of them hosting a atom [323]. Every atom is trapped in its electronic ground state (denoted with $|\downarrow\rangle_{\mathbf{n}}$), which is quasirenonantly coupled to a single Rydberg state, i.e. a highly excited electronic level (denoted with $|\uparrow\rangle_{\mathbf{n}}$). Overall, the Rydberg atom array behaves like a chain of qubits $\{|\uparrow, \downarrow\rangle\}_{\mathbf{n}=1\dots N}$, whose dynamics is ruled by the following Hamiltonian:

$$\hat{H}_{\text{Ryd}} = \sum_{\mathbf{n}} (\Omega \hat{\sigma}_{\mathbf{n}}^x + \delta \hat{\sigma}_{\mathbf{n}}^z) + \sum_{\mathbf{n}, \mathbf{n}' \neq \mathbf{n}} V_{\mathbf{n}, \mathbf{n}'} \hat{n}_{\mathbf{n}} \hat{n}_{\mathbf{n}'}, \quad (4.3.1)$$

where $\hat{\sigma}_{\mathbf{n}}^{\alpha}$ are Pauli matrices at site \mathbf{n} , while the operator $\hat{n}_{\mathbf{n}} = (\hat{\sigma}_{\mathbf{n}}^z + 1)/2$ measures the presence of a Rydberg excitation ($|\uparrow\rangle_{\mathbf{n}}$) at site \mathbf{n} . The coefficients Ω and δ are the Rabi frequency and the detuning of the laser excitation scheme respectively; the former one describes the coupling between the ground and Rydberg states due to an external driving field, while the second one represents the difference between the driving field frequency and the atomic transition frequency. Correspondingly, $V_{\mathbf{n}, \mathbf{n}'}$ couples the interaction between atoms in their Rydberg states at sites \mathbf{n} and \mathbf{n}' .

In typical experimental realizations of Rydberg arrays made by optical lattices or optical tweezers, the interaction is strong at short range and decays as $1/|\mathbf{n} - \mathbf{n}'|^6$ as in the Van der Waals scenario [323, 351, 352]. Such an interaction is typically approximated with the Rydberg-blockade effect, which assumes $V_{\mathbf{n}, \mathbf{n}'}$ as the largest energy scale of the system, avoiding atoms on neighboring sites to be simultaneously excited to Rydberg states $\hat{n}_{\mathbf{n}} \hat{n}_{\mathbf{n}+\mu} = 0$ [323]. Within this approximation, the Hamiltonian in Eq. (4.3.1) can be approximated as done by Fendley, Sengupta, and Sachdev (FSS) in [353]:

$$\hat{H}_{\text{FSS}} = \sum_{\mathbf{n}} (\Omega \hat{\sigma}_{\mathbf{n}}^x + 2\delta \hat{n}_{\mathbf{n}}) \quad (4.3.2)$$

plus the blockade constraint on neighboring sites. In the limit of zero detuning, Eq. (4.3.2) is equivalent to the PXP model [354]:

$$\hat{H}_{\text{PXP}} = \sum_{\mathbf{n}} \hat{P}_{\mathbf{n}-\mu} \hat{\sigma}_{\mathbf{n}}^x \hat{P}_{\mathbf{n}+\mu}, \quad (4.3.3)$$

where $\hat{P}_{\mathbf{n}}$ is a projector enforcing the state in \mathbf{n} to be in the groundstate. In both these realizations of the Rydberg Hamiltonian, the experimental and numerical observations of the corresponding dynamics pointed out two different behaviors according to the initial quench of the time evolution [323, 326, 329, 333]. Namely, starting from a configuration with all the Rydberg atoms in their groundstate, i.e. $|\downarrow, \downarrow, \dots, \downarrow, \downarrow\rangle$ (empty), the system thermalize, as expected from the ETH discussed in Sec. 4.2.1, and the average value of observables such as the local density \hat{n} matches the corresponding statistical mechanics predictions. Correspondingly, the return fidelity with the initial state $|\langle \Psi(0) | \Psi(t) \rangle|^2$ quickly vanishes. Conversely, quenching the dynamics from staggered configurations like the following charge-density wave (CDW) states [333]

$$|\downarrow, \uparrow, \downarrow, \uparrow, \downarrow, \uparrow, \dots\rangle \text{ (CDW1)} \quad |\uparrow, \downarrow, \uparrow, \downarrow, \uparrow, \downarrow, \dots\rangle \text{ (CDW2)}, \quad (4.3.4)$$

the system undergoes an oscillatory behavior of the local density operator $\hat{n}(t)$ (the return fidelity) between the two states $\{\downarrow, \uparrow\}$ (between CDW1 and CDW2) and escapes quantum thermalization

(see Fig6b of [323] and Fig1 of [333]). Such a pattern has also been detected by measuring the half-chain entanglement entropy, whose growth in time is slow and oscillating with the same period of density oscillations (see Fig10 of [323]). Moreover, the energy spectrum has revealed the presence of some scar states characterized by a high overlap with the initial quench state [326]. As we will see, the oscillating behavior between CDW1 and CDW2 passing from the full ground state, can be mapped into a process of particle-antiparticle pairs creation and annihilation, which is a foundational mechanism occurring in high-energy [333].

4.3.2 Scars in Abelian Lattice Gauge Theories

Indeed, it has been recently demonstrated that the experimental model of Rydberg atoms can be mapped into a spin-1/2 Quantum Link Model (QLM) version of a U(1) LGT [333] and correspondingly, the observation of scarring dynamics can be associated to high-energy physics phenomena such as the Schwinger mechanism [355]. In particular, we can then identify the computational basis of configurations allowed by the Rydberg blockade with the classical configurations of the electric field allowed by Gauss law.

In detail, a Rydberg atom chain in the Rydberg-blockade approximation can be mapped into a (1+1)D realization of the QED Hamiltonian in Eq. (1.4.1):

$$\hat{H} = -w \sum_{\mathbf{n}} \left[\hat{\psi}_{\mathbf{n}}^{\dagger} \hat{U}_{\mathbf{n},\mu} \psi_{\mathbf{n}+\mu} + \text{h.c.} \right] + m \sum_{\mathbf{n}} (-1)^{\mathbf{n}} \hat{\psi}_{\mathbf{n}}^{\dagger} \hat{\psi}_{\mathbf{n}} + J \sum_{\mathbf{n}} \hat{E}_{\mathbf{n},\mu}^2, \quad (4.3.5)$$

where $w = 1/2$, $m = m_0 c / \hbar$, and $J = g^2 / 2$ are adimensional parameters⁴. In the finite truncation of U(1) discussed in Sec. 1.4.2, the gauge fields can be represented by spin- j variables [96, 98]:

$$\hat{E}_{\mathbf{n},\mu} = \hat{S}_{\mathbf{n},\mu}^z(j) \quad \hat{U}_{\mathbf{n},\mu} = \hat{S}_{\mathbf{n},\mu}^+(j) \quad \left[\hat{E}_{\mathbf{n},\mu}, \hat{U}_{\mathbf{n},\mu} \right] = \hat{S}_{\mathbf{n},\mu}^+(j). \quad (4.3.6)$$

At any finite truncation, U(1) Gauss law always requires that $\hat{G}_{\mathbf{n}} |\Psi_{\text{phys}}\rangle = 0 \forall \mathbf{n}$, where $\hat{G}_{\mathbf{n}}$ is the local generator of the U(1) gauge symmetry defined in Eq. (1.4.4) and constrains the electric fields incoming and outgoing from a local site to match the corresponding amount of charge:

$$\hat{G}_{\mathbf{n}} = \hat{E}_{\mathbf{n},\mu} - \hat{E}_{\mathbf{n}-\mu,\mu} - \hat{\psi}_{\mathbf{n}}^{\dagger} \hat{\psi}_{\mathbf{n}} + \frac{1 - (-1)^{\mathbf{n}}}{2}. \quad (4.3.7)$$

In particular, due to the use of staggered fermions, an empty *odd* site corresponds to the presence of an anti-particle of charge \bar{q} , while occupied *odd* sites implies to the presence of a particle of charge q (assuming that U(1) $q < 0$, as it refers to the electron). Namely, indicating with $|\Omega\rangle_{\mathbf{n}}$ an empty matter state in site \mathbf{n} , and with $|\emptyset\rangle_{\mathbf{n}}$ the corresponding absence of charge, we have:

$$\begin{aligned} |\Omega\rangle_{\mathbf{n},\text{even}} &= |\emptyset\rangle_{\mathbf{n},\text{even}} & |\Omega\rangle_{\mathbf{n},\text{odd}} &= |\bar{q}\rangle_{\mathbf{n},\text{odd}} \\ \hat{\psi}^{\dagger} |\Omega\rangle_{\mathbf{n},\text{even}} &= |q\rangle_{\mathbf{n},\text{even}} & \hat{\psi}^{\dagger} |\Omega\rangle_{\mathbf{n},\text{odd}} &= |\emptyset\rangle_{\mathbf{n},\text{odd}}. \end{aligned} \quad (4.3.8)$$

Mapping the Rydberg blockade into the U(1) Gauss law

To understand the connection between the two models, let us reconsider from the Rydberg blockade. When the latter holds, such as in Eqs. (4.3.2) and (4.3.3), the total Hilbert space is restricted to those states without double occupancies on neighboring sites. Then, the effective

⁴Similarly to Eq. (3.1.2), for numerical simulations, we made the Hamiltonian in Eq. (1.4.1) adimensional by multiplying it by $a_0 / (c\hbar)$.

Hilbert space of each pair of neighboring Rydberg atoms along the chain within the Rydberg-blockade approximation is

$$|1\rangle_{\text{Ryd}} = |\uparrow, \downarrow\rangle \quad |2\rangle_{\text{Ryd}} = |\downarrow, \downarrow\rangle \quad |3\rangle_{\text{Ryd}} = |\downarrow, \uparrow\rangle. \quad (4.3.9)$$

Correspondingly, in the $j = 1/2$ finite truncation of U(1) gauge fields, the effective Hilbert space of a matter site coupled with its attached (left and right) gauge links is made of configurations like $|\hat{E}_{\mathbf{n}, -\boldsymbol{\mu}}, q_{\mathbf{n}}, \hat{E}_{\mathbf{n}, +\boldsymbol{\mu}}\rangle$. Denoting $\hat{E} = +1/2$ ($\hat{E} = -1/2$) with \rightarrow (\leftarrow), in the staggered fermion solution we have

$$|1\rangle_{\text{U}(1)}^{\text{even}} = |\rightarrow, \emptyset, \rightarrow\rangle \quad |2\rangle_{\text{U}(1)}^{\text{even}} = |\leftarrow, q, \rightarrow\rangle \quad |3\rangle_{\text{U}(1)}^{\text{even}} = |\leftarrow, \emptyset, \leftarrow\rangle \quad (4.3.10a)$$

$$|1\rangle_{\text{U}(1)}^{\text{odd}} = |\rightarrow, \emptyset, \rightarrow\rangle \quad |2\rangle_{\text{U}(1)}^{\text{odd}} = |\rightarrow, \bar{q}, \leftarrow\rangle \quad |3\rangle_{\text{U}(1)}^{\text{odd}} = |\leftarrow, \emptyset, \leftarrow\rangle. \quad (4.3.10b)$$

One can then associate the effective Hilbert space of neighboring Rydberg atoms in Eq. (4.3.9) with the U(1) gauge invariant configurations of Eq. (4.3.10) (for even and odd sites respectively). Correspondingly, states violating Gauss law are exactly mapped into the nearest-neighbor occupied sites which are strongly suppressed by the Rydberg blockade. A pictorial representation of such a correspondence is given in Fig1 of [333].

We can further identify the Hamiltonian parameters $\Omega = -w$, $\delta = -m$ and the operators

$$\hat{\sigma}_{\mathbf{n}}^z \leftrightarrow (-1)^{\mathbf{n}} 2\hat{S}_{\mathbf{n}-\boldsymbol{\mu}, \boldsymbol{\mu}}^z \quad \hat{\sigma}_{\mathbf{n}}^x \leftrightarrow \left[\hat{\psi}_{\mathbf{n}-\boldsymbol{\mu}}^\dagger \hat{S}_{\mathbf{n}-\boldsymbol{\mu}, \boldsymbol{\mu}}^+ \hat{\psi}_{\mathbf{n}} + \text{h.c.} \right] \quad \hat{\sigma}_{\mathbf{n}}^y \leftrightarrow -i(-1)^{\mathbf{n}} \left[\hat{\psi}_{\mathbf{n}-\boldsymbol{\mu}}^\dagger \hat{S}_{\mathbf{n}-\boldsymbol{\mu}, \boldsymbol{\mu}}^+ \hat{\psi}_{\mathbf{n}} + \text{h.c.} \right], \quad (4.3.11)$$

so that the two Hamiltonians in Eqs. (4.3.2) and (4.3.5) are equivalent.

4.3.3 Gauge theory interpretation of slow dynamics

Remarkably, beyond providing a direct link between Gauss law and the Rydberg blockade mechanism, the connection between Eq. (4.3.2) and Eq. (4.3.5) with the mapping in Eq. (4.3.11) provides an immediate connection between Rydberg-blockade chains experiments and the U(1) LGT. We can then interpret the slow dynamics observed in Rydberg atoms [323] in terms of particle-antiparticle pairs production in high-energy physics. In particular, the two charge density wave states CDW1 and CDW2 of [333] can be mapped into the two uniform electric field states $\hat{E}_{\mathbf{n}, \boldsymbol{\mu}} = \pm 1/2$. Namely, we can map the empty Rydberg configuration and the ones in Eq. (4.3.4) into the following states:

$$\begin{aligned} (\text{CDW1}) &\longleftrightarrow |\rightarrow, \emptyset, \rightarrow, \emptyset, \rightarrow, \emptyset, \rightarrow, \emptyset, \rightarrow\rangle \quad (\text{String}) \\ (\text{empty}) &\longleftrightarrow |\leftarrow, q, \rightarrow, \bar{q}, \leftarrow, q, \rightarrow, \bar{q}, \leftarrow\rangle \quad (\text{Pairs}) \\ (\text{CDW2}) &\longleftrightarrow |\leftarrow, \emptyset, \leftarrow, \emptyset, \leftarrow, \emptyset, \leftarrow, \emptyset, \leftarrow\rangle \quad (\text{anti-String}), \end{aligned} \quad (4.3.12)$$

where the *string* (*anti-string*) refers to a uniform rightward (leftward) electric flux, while *pairs* refers to the state filled by adjacent particle-antiparticle pairs.

Then, the long-lived oscillations between the CDW1 and CDW2 states observed in the Rydberg-blockade chain are related to the rightward-leftward switch of the electric flux passing through the intermediate production of particle-antiparticle pairs. Such a pattern is called *string inversion* and is directly tied to string breaking [355–357] prototypical of gauge theories including dynamical matter.

Remarkably, this mechanism is disturbed by quantum fluctuations, which are controlled by the dimensionless ratio m/w . In detail, for $m < 0.655w = m_c$, particle-antiparticle pairs are

created, which accelerates in an electric field and gradually screens it. Eventually, coherent pair annihilation takes place, leading to a state with an opposite electric flux. Such an inversion happens several times, causing the slow dynamics in the system. This leads to a significant slowdown of thermalization and limits quantum information propagation. Conversely, when the particle mass exceeds a critical value ($m > m_c$), pair production becomes a virtual process and string inversion does not occur. This marks a different phase of the system's evolution, preventing the formation of real particle pairs. This transition is related to a quantum phase transition observed in the FSS model in Eq. (4.3.2) at a critical detuning δ_c [353] and corresponds to the spontaneous breaking of chiral symmetry in the U(1) LGT [76, 333].

4.4 Scars in Non-Abelian Lattice Gauge Theories

Given the intimate connection between QMBS and LGTs, and the current large effort to quantum simulate the latter [106, 109, 110, 130, 133, 135, 297, 334, 358–361], it is important to investigate the origin of QMBS in connection to gauge symmetry by exploring its possible occurrence in non-Abelian LGTs with dynamical matter. In particular, investigating a high-energy context of QMBS requires the inclusion of dynamical matter, as demonstrated in the Abelian scenario.

In this section, we report and discuss the exact diagonalization (ED) and matrix product state (MPS) results of [4] that showcase robust QMBS dynamics in a non-Abelian SU(2) LGT with dynamical matter starting in simple initial product states (Sec. 4.4.1). We show how the QMBS dynamics involve state transfer through meson and baryon-anti-baryon bare states, highlighting the non-Abelian nature of this scarred behavior. In addition to the exotic dynamics observed in Sec. 4.4.2 and the spectral properties of the model discussed in Sec. 4.4.3, we enrobust our results with further analyses. In Sec. 4.4.4, we observe that log-time average of local observables displayed in Fig. 4.1 are not compatible with the thermal relaxation expected for other initial states at the same energy. In Sec. 4.4.5, we demonstrate how, for other parameter regimes, the spectral and dynamical properties of the two initial product states are compatible with the ergodic behavior predicted by statistical mechanics (microcanonical ensemble). Conversely, we further illustrate how the scars-induced revivals of Fig. 4.1 persist for large gauge-field truncations (Sec. 4.4.6), at larger system sizes (Sec. 4.4.7), and over longer timescales (Sec. 4.4.8) for the candidate initial states. These results confirm the overall ergodic nature of the model and regard the observed scarring behavior as a weak violation of ETH and the expected thermalization.

4.4.1 The model

As a prototypical model to probe non-ergodic dynamics in non-Abelian gauge theories, we consider a (1+1)D matter-coupled *hardcore-gluon* SU(2) LGT [2, 4, 49, 116, 143, 155] such as the one derived in Sec. 1.3.5. The model describes a matter quark field of mass m , living on lattice sites \mathbf{n} , coupled to a truncated SU(2) gauge field, defined on lattice links | see Fig. 4.1. The quark field is a staggered fermion doublet $\hat{\psi}_{\mathbf{n},\alpha}$, obeying the anticommutation relations in Eq. (1.3.4): $\{\hat{\psi}_{\mathbf{n},\alpha}, \hat{\psi}_{\mathbf{n}',\beta}^\dagger\} = \hbar \delta_{\mathbf{n},\mathbf{n}'} \delta_{\alpha,\beta}$ [148], where $\alpha, \beta \in \{r, g\}$ span SU(2) colors. A basis for matter sites is

$$\left\{ |0\rangle, |r\rangle = \hat{\psi}_r^\dagger |0\rangle, |g\rangle = \hat{\psi}_g^\dagger |0\rangle, |2\rangle = \hat{\psi}_r^\dagger \hat{\psi}_g^\dagger |0\rangle \right\}. \quad (4.4.1)$$

Gauge link states can be expanded in the basis $|j, m_L, m_R\rangle$, where $m_L, m_R \in \{-j, \dots, +j\}$ index spin- j states, and the link energy density operator is diagonal and coincides with the quadratic Casimir, $\hat{E}^2 |j, m_L, m_R\rangle = j(j+1) |j, m_L, m_R\rangle$ [160]. Adopting a hardcore-gluon truncation, we restrict j to $\{0, 1/2\}$, namely keep only basis states reachable from the singlet $|00\rangle$ via at

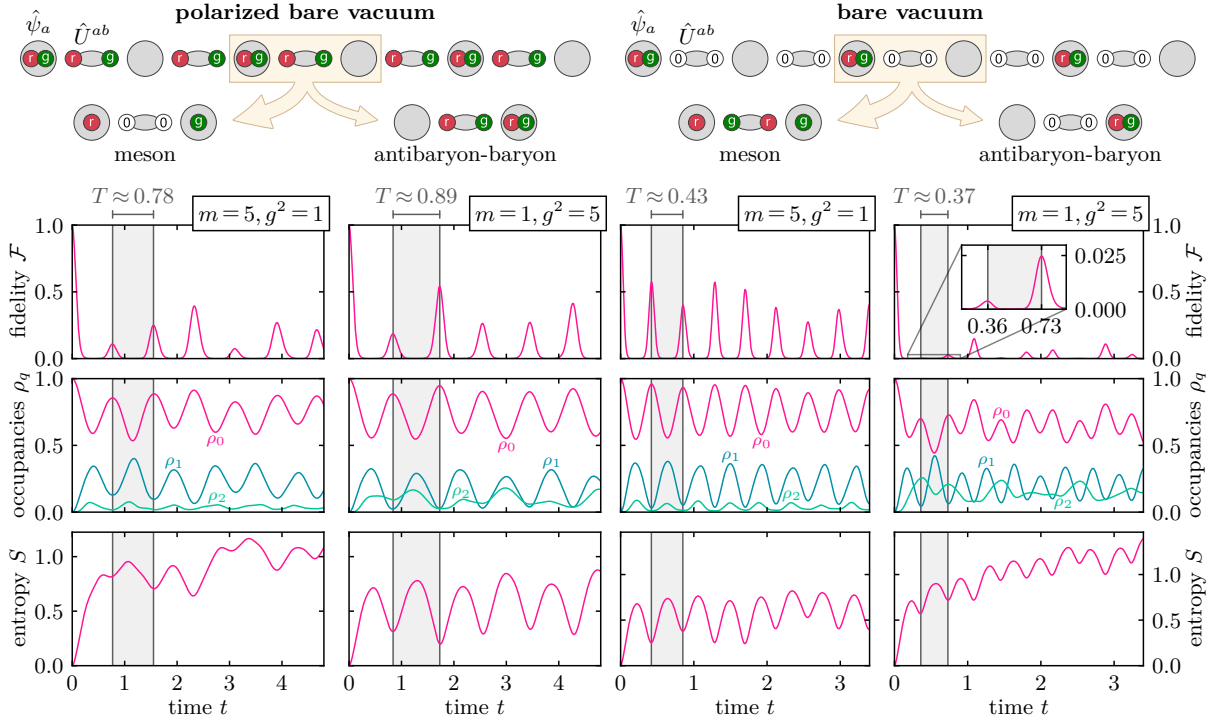


Figure 4.1: Many-body scattering dynamics of the polarized bare vacuum (left) and the bare vacuum (right) initial states. *Top*: cartoons depicting the classical configurations that give the leading contribution to the dynamics; with circles and ellipses denoting matter sites and gauge links respectively. *Bottom*: return fidelity, average quark occupancy, and bipartite entanglement entropy as a function of time, for different mass and coupling regimes, reported in Figure. MPS simulation with $N = 30$ sites in open boundary conditions (OBC), maximum bond dimension $\chi_{\max} = 350$, and truncation tolerance $\text{tol} = 10^{-7}$.

most a single application of the parallel transporter $\hat{U}^{\alpha\beta}$: $\{|00\rangle, |rr\rangle, |gg\rangle, |gr\rangle, |rg\rangle\}$, where $r(g) = +(-)1/2$.

Correspondingly, non-Abelian Gauss law mandates that physical states are local gauge singlets, $\hat{G}_{\mathbf{n}}^{\nu}|\Psi_{\text{phys}}\rangle \equiv 0$, $\forall \mathbf{n}$, $\nu \in \{x, y, z\}$, where $\hat{G}_{\mathbf{n}}^{\nu}$ are the generators of local rotations at site \mathbf{n} and defined in Eq. (1.3.5). In numerical simulations, we enforce this constraint using a dressed site approach, which yields a deformed qudit model with a 6-dimensional local basis discussed of Eq. (1.3.56) [143].

The dynamics is governed by the Kogut-Susskind (adimensional) Hamiltonian [144] employing staggered fermions and defined in Eq. (1.3.54) on an N -site lattice with spacing a_0

$$\hat{H} = \frac{1}{2} \sum_{\mathbf{n}} \sum_{\alpha, \beta} \left[-i \hat{\psi}_{\mathbf{n}, \alpha}^{\dagger} \hat{U}_{\mathbf{n}, \mu}^{\alpha\beta} \hat{\psi}_{\mathbf{n}+\mu, \beta} + \text{h.c.} \right] + m \sum_{\mathbf{n}, \alpha} (-1)^{\mathbf{n}} \hat{\psi}_{\mathbf{n}, \alpha}^{\dagger} \hat{\psi}_{\mathbf{n}, \alpha} + \frac{g^2}{2} \sum_{\mathbf{n}} \hat{E}_{\mathbf{n}, \mu}^2. \quad (4.4.2)$$

where, similarly to Eq. (3.1.2), for the sake of numerical simulations, we rescaled the Hamiltonian with dimensionless couplings such as $m = m_0 c / \hbar$ and $g^2 = q^2 a_0^2 \cdot (c \hbar \epsilon_0)^{-1}$. Values reported in the Figures refer to these rescaled quantities.

4.4.2 Observing scarred dynamics

To investigate the presence of non-ergodic behavior in this model, we consider the Schrödinger time evolution of different initial states $|\Psi(t=0)\rangle$, across various parameter regimes. The time evolution is performed on a chain of $N = 30$ sites via MPS methods⁵. As initial configuration, we first consider the *polarized bare vacuum* (PV), which consists of the matter sites in the bare vacuum configuration, while the gauge sites in the excited electric field state,

$$|\Psi_{\text{PV}}\rangle = |\dots 2020 \dots\rangle_{\text{m}} |\dots \frac{rg - gr}{\sqrt{2}} \dots \frac{rg - gr}{\sqrt{2}} \dots\rangle_{\text{g}}, \quad (4.4.3)$$

where $|\cdot\rangle_{\text{m}}$ and $|\cdot\rangle_{\text{g}}$ refer to the matter and gauge subsystems, respectively. Here $(m_{\text{R}})_{\mathbf{n}-\mu, \mathbf{n}}$ and $(m_{\text{L}})_{\mathbf{n}, \mu}$ around each bulk site \mathbf{n} are valence-bonded in a singlet. In the qudit formulation of the model (see Sec. 1.3.5 and [143]), the state in Eq. (4.4.3) becomes a product state:

$$|\Psi_{\text{PV}}\rangle = |6\rangle |2\rangle \dots |6\rangle |2\rangle, \quad (4.4.4)$$

We identify two regimes avoiding thermalization: the large-mass one, $m \gg (g^2, 1)$, and the large-coupling one, $g^2 \gg (m, 1)$. For each regime, we compute the return fidelity between the initial state and the evolved state, $\mathcal{F}(t) = |\langle \Psi(t) | \Psi(0) \rangle|^2$, shown in Fig. 4.1. After an initial complete system relaxation, we observe persistent revivals, signaling a clear deviation from the expected ergodic behavior. The revivals occur approximately periodically, with the period indicated in the figure for both the considered regimes.

The observed dynamics can be understood as a process of persistent particle pair creation out of an initial false vacuum [77, 86, 127]. To see this, we define the (staggered) site occupancy operator,

$$\hat{\mathcal{N}}_{\mathbf{n}} = (-1)^{\mathbf{n}} \sum_{\alpha} \left[\hat{\psi}_{\mathbf{n}, \alpha}^{\dagger} \hat{\psi}_{\mathbf{n}, \alpha} - \frac{1 - (-1)^{\mathbf{n}}}{2} \right], \quad (4.4.5)$$

which counts the number of quarks (on even sites) or antiquarks (on odd sites). Then, we compute the average occupancy $\varrho_q(t)$ of each $\mathcal{N}_{\mathbf{n}}$ eigenvalue (single site quark occupancy, $q \in \{0, 1, 2\}$), projecting on the corresponding eigensubspace of $\mathcal{N}_{\mathbf{n}}$ and averaging over all sites n :

$$\varrho_q(t) = \frac{1}{N} \sum_{\mathbf{n}} \langle \Psi(t) | \delta_{\mathcal{N}_{\mathbf{n}}, q} | \Psi(t) \rangle. \quad (4.4.6)$$

As lately discussed in Sec. 4.4.4, they oscillate around average values that do not coincide with the ones predicted by thermal ensembles, confirming deviations from ergodic behavior. Large values of either mass or coupling confine the system dynamics close to the initial state, creating few particle pair excitations in the system. In the large-mass regime, most of the excitations are meson-like (quark and antiquark adjacent pairs with an excited shared gauge link). In the large-coupling regime, the formation of pairs of baryon- (quark pair) and antibaryon- (antiquark pair) like excitations becomes likely as well, as shown by the enhanced double occupancy with respect to the large-mass regime.

Finally, the last row of Fig. 4.1 shows the evolution of the bipartite entanglement entropy defined as $\mathcal{S} = -\text{Tr}[\varrho_A \log \varrho_A]$, where A and B indicate the two halves of the chain and $\varrho_A = \text{Tr}_B[\varrho_{AB}]$ is the reduced density operator of subsystem A . In both cases, we observe a slow growth of the entanglement entropy after an initial fast increase up to the first fidelity revival peak. The oscillations on top of the growth are driven by the successive fidelity revivals, which indeed have the same period.

⁵In detailed, simulations we obtained from the iTensor Library [362, 363].

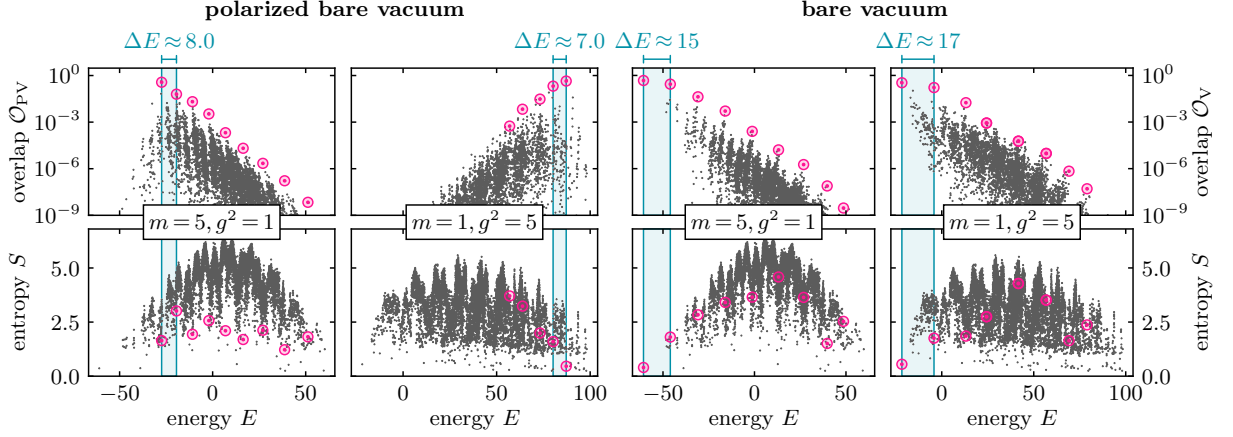


Figure 4.2: Spectrum analysis for a lattice chain of $N = 10$ sites in OBC, in the two parameter regimes of Fig. 4.1. Red circles highlight the scar states. *First row*: the overlap of the many-body spectrum with the polarized bare vacuum (left) and the bare vacuum (right); only states with $\mathcal{O}_{(P)V} > 10^{-9}$ are included. *Second row*: bipartite entanglement entropy of each eigenstate.

In addition to the polarized bare vacuum initial state, we also observe similar scarred-like dynamics for the *bare vacuum* (V) state: the ground state of the Hamiltonian in Eq. (4.4.2) without the hopping term, made of alternated doubly occupied and empty sites, and trivial links,

$$|\Psi_V(t=0)\rangle = |\dots 2020 \dots\rangle_m |\dots 0000 \dots\rangle_g. \quad (4.4.7)$$

which in the qudit formulation (see Sec. 1.3.5 and [143]) reads:

$$|\Psi_V\rangle = |5\rangle |1\rangle \dots |5\rangle |1\rangle. \quad (4.4.8)$$

The resulting non-ergodic dynamics is displayed on the right-side of Fig. 4.1. Compared to the polarized vacuum case, the oscillation's period in the fidelity revivals and occupancy is smaller. As discussed in the following section, it can be explained by the many-body spectrum. The large coupling regime is characterized by a faster entanglement growth, consistently with a corresponding lower return fidelity. Although in the regimes considered this product state is energetically close to the true ground state of the model, the observed dynamics is driven by nontrivial physics. This is evident from the significant oscillations observed in the average occupancy, which lead the system significantly away from its initial configuration.

4.4.3 Tower of scar states

To determine whether the observed non-ergodic dynamics originates from QMB scars, we perform ED up to $N = 10$ sites and, for each eigenstate in the many-body spectrum $\{|\Phi_s\rangle\}$, we compute the overlap

$$\mathcal{O}_{PV/V} = |\langle \Psi_{PV/V} | \Phi_s \rangle|^2 \quad (4.4.9)$$

and the bipartite entanglement entropy S with the two considered initial states (polarized, PV, and unpolarized bare vacua, V). These quantities are plotted in Fig. 4.2, for both regimes where we observe revivals in the return fidelity. For each candidate QMBS regime, we find a ‘tower of scar states’ (highlighted by red circles) characterized by a high overlap with the initial product states and entanglement low enough (compared to the rest of the many-body spectrum) to give rise to scarring behavior. In each case, the energy gap between the scar states in the tower, ΔE (reported in Fig. 4.2), approximately matches the frequency of the revivals observed in the return

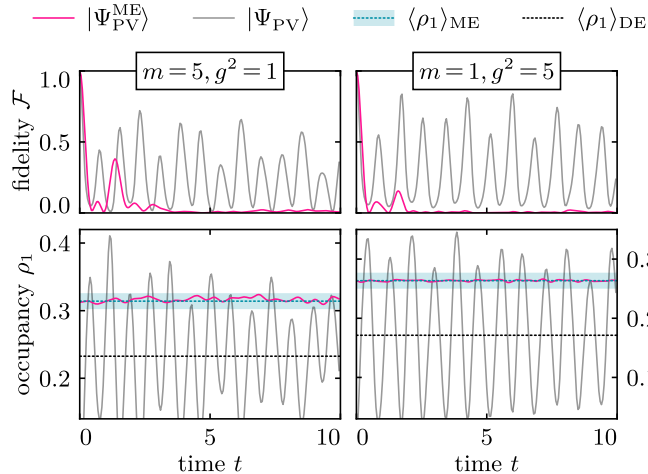


Figure 4.3: Dynamics of the *microcanonical* state in Eq. (4.4.10) for the same parameter regimes of Fig. 4.1. Gray curves reproduce the polarized bare vacuum dynamics, for comparison. The blue horizontal lines reproduce the thermal ϱ_1 occupancy, obtained via microcanonical ensemble (ME). The black ones show the diagonal ensemble (DE) results for the long-time average of ϱ_1 on $|\Psi_{\text{PV}}(t)\rangle$, highlighting its lack of thermalization. ED results for $N = 10$ sites in PBC.

fidelity from Fig. 4.1, $\Delta E \approx 2\pi/T$. The correspondence between spectral and dynamical features allows us to conclude that QMBS is indeed the underlying mechanism behind the non-ergodic dynamics shown in Fig. 4.1.

4.4.4 Ergodic dynamics for other initial states

In order to prove the scarring behavior as a specific feature of the configurations in Eqs. (4.4.3) and (4.4.7) and not of all the initial states, we consider the *microcanonical* ensemble (ME) state constructed as a uniform coherent superposition of all eigenstates lying within a small energy window around the quench energy of the polarized vacuum state $E_{\text{PV}} = \langle \Psi_{\text{PV}} | \hat{H} | \Psi_{\text{PV}} \rangle$. Namely, we define the thermal state

$$|\Psi_{\text{PV}}^{\text{ME}}\rangle = \frac{1}{\sqrt{N_{E_{\text{PV}}, \delta E}}} \sum_{s, |E_s - E_{\text{PV}}| < \delta E} |\Phi_s\rangle, \quad (4.4.10)$$

where $\delta E = \sqrt{\langle \Psi_{\text{PV}} | \hat{H}^2 | \Psi_{\text{PV}} \rangle - E_{\text{PV}}^2}$ defines the energy shell $[E_{\text{PV}} - \delta E, E_{\text{PV}} + \delta E]$, and $N_{E_{\text{PV}}, \delta E}$ is the number of eigenstates in this energy shell [306].

In Fig. 4.3, we compare the evolution of this state to that of $|\Psi_{\text{PV}}\rangle$, in the identified scarred regimes. As the plot illustrates, the *microcanonical* state exhibits ergodic behavior: return fidelities relax toward zero (up to minor oscillations attributable to the finite lattice size) and the single occupancy ϱ_1 remains close to its microcanonical ensemble average $\langle \varrho_1 \rangle_{\text{ME}}$ [306]. In contrast, for the polarized vacuum, ϱ_1 widely oscillates around its long-time average (diagonal ensemble) $\langle \varrho_1 \rangle_{\text{DE}}$ largely deviates from the thermal result. We thus conclude that the observed non-ergodic dynamics strictly depends on the initial conditions and escapes an otherwise thermal behavior through the occurrence of scar states in the many-body spectrum.

4.4.5 Ergodic dynamics for other parameter regimes

We have shown that the two considered initial product states polarized bare vacuum (PV) and bare vacuum (V), escape thermalization for the two regimes ($m = 5, g^2 = 1$) and ($m = 1, g^2 = 5$).

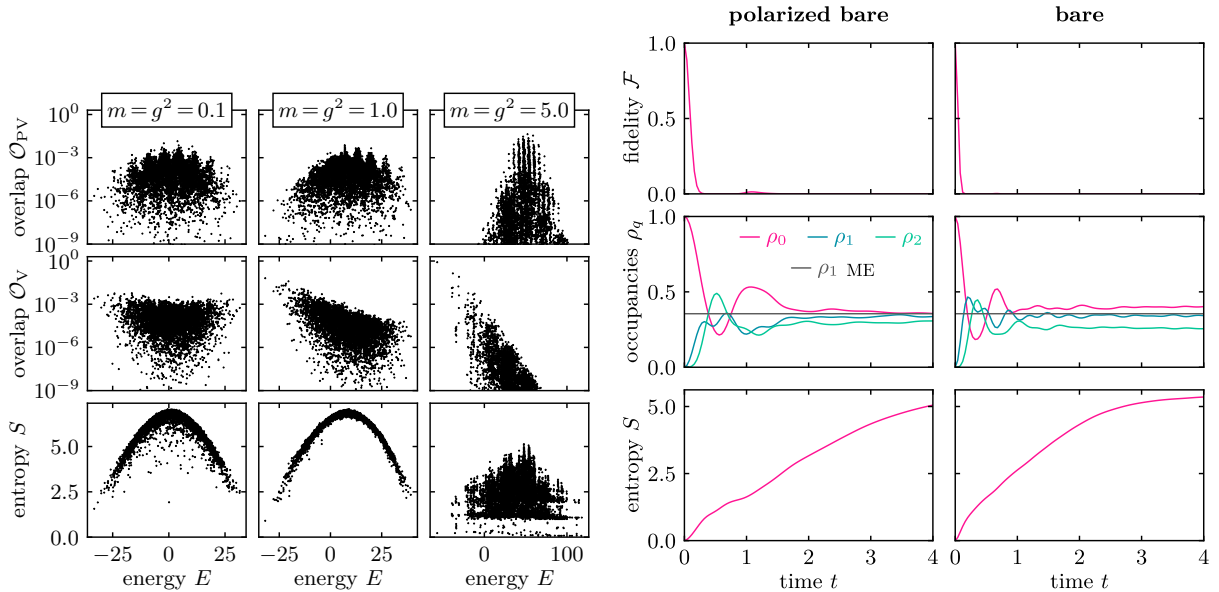


Figure 4.4: [Left]: *Many-body spectrum*. Spectrum analysis for a lattice chain of $N = 10$ sites with open boundary conditions in a few paradigmatic regimes (corresponding to different columns) where we observe ergodic dynamics. The first and second rows show the overlap of the many-body spectrum with the bare vacuum and polarized bare vacuum state, respectively. Only states with $\mathcal{O}_{PV} > 10^{-9}$ are included in the plot. In the third row, we display the bipartite entanglement entropy of all eigenstates in the energy spectrum as a function of their respective eigenvalues. [Right]: *Ergodic dynamics*. First to third row: return fidelity, average quark occupancy, and bipartite entanglement entropy as a function of time for the two considered initial states, polarized bare vacuum (PV), and bare vacuum (V) at $m = g^2 = 1$. The horizontal lines in the occupancy panels indicate the thermal expectation value of the single particle occupancy density obtained through ED of a lattice of $N = 10$ with PBC for the microcanonical ensemble. The simulation was performed with MPS for $N = 20$ sites by setting open boundary conditions, maximum bond dimension $\chi_{\max} = 350$, and truncation tolerance $\text{tol} = 10^{-7}$.

To confirm the scarring nature of the observed non-ergodic dynamics, we investigate the absence of scars states in the many-body spectrum for other parameter regimes. In Fig. 4.4[Left], we look at the overlap of the full many-body spectrum with the two considered initial states PV and V and the corresponding bipartite entanglement entropy for different values of $g^2 = m$. Rather than in Fig. 4.2, we do not observe a clear emergence of a tower of states, and thus, we expect ergodic dynamics for the two considered states. This is also confirmed by the time evolution of the two initial states for $g^2 = m = 1$ displayed in Fig. 4.4[Right]. In this case, the fidelity does not exhibit persistent revivals, and the entanglement entropy shows rapid growth compared to the previously observed scarred dynamics. Moreover, as expected for thermalization, the occupancy relaxes to a steady value compatible with the microcanonical averages.

We leave any further investigations on scarring dynamics for other candidate initial states to future work. To this extent, it could be interesting to investigate the $g^2 = m = 0.1$ case, whose many-body spectrum contains extremely low entanglement entropy states.

4.4.6 Scars at higher gauge link truncation

It is interesting to highlight that the scarring dynamics observed for the minimal truncation in Fig. 4.1, is not a feature of the truncation itself. Indeed, a similar behavior is displayed in the

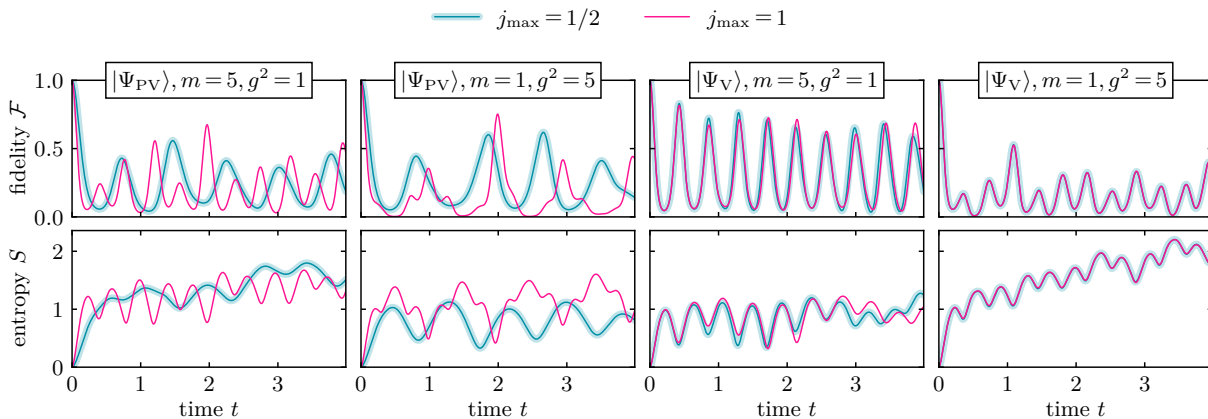


Figure 4.5: *Scarring at higher gauge truncation.* Many body scarring dynamics for the polarized bare vacuum (PV) and the bare vacuum (V) for the truncated SU(2) YM LGT at $j_{\max} = 1$ (pink line) in comparison with the corresponding one at $j_{\max} = 1/2$ (cyan line). Each column reports the fidelity and bipartite entanglement entropy as a function of time for the same two cases (m, g) considered in Fig. 4.1. The simulations are obtained via ED for $N = 10$ sites.

next gauge truncation $j_{\max} = 1$, which leads to a dressed-site basis of 10 gauge invariant states. As shown in Fig. 4.5, where we return the fidelity and the entanglement entropy for the same two cases discussed in the main text. Analogously with what has been observed in Abelian LGTs, these results remarkably suggest that the scars dynamics of non-Abelian theories also persist at higher gauge truncations.

4.4.7 Scaling with the system size

Many-body scars represent a polynomial (in number) subset of special non-thermal eigenstates within the full many-body spectrum. This implies that the overlap with the initially considered product states decreases as the system size increases. To investigate this behavior, in Fig. 4.6(a), we plot the return fidelity between the evolved state and two initial scarring states: the polarized bare vacuum (PV) and the bare vacuum (V). Exploiting the slow entanglement growth in the many-body scars regime, we considered system sizes ranging from $N = 10$ to $N = 50$. Although the fidelity peaks decrease with increasing N as expected, pronounced revivals are still visible even for large chains with $N = 50$ sites. The peaks become sharper, with the fidelity minima approaching zero, accordingly with the expected revivals induced by scars. The maximum amplitude of these peaks follows an exponential scaling in the system size, $\mathcal{F}_N = f^N$, with the extrapolated peak fidelity per site being $f = 0.97$ and $f = 0.98$ for the PV and V states, respectively. This estimate further demonstrates the robustness of the observed scar dynamics even at large system sizes.

4.4.8 Long-time dynamics

To illustrate how the observed non-ergodic dynamics persist over longer times, we conducted simulations for an extended duration. In Fig. 4.7, we present the same dynamics presented in Fig. 4.1, now up to $t = 30$, nearly ten times longer than previously shown. At this extended duration, we continue to observe persistent revivals and oscillations in both the return fidelity and occupancy. Moreover, in addition to the rapid oscillations with a period $T < 1$ previously discussed, we observe a beating with frequency $T \sim 1$ attributed to the non-uniform distribution of scars in energy spacing. Finally, we still observe a slow growth in entanglement at such

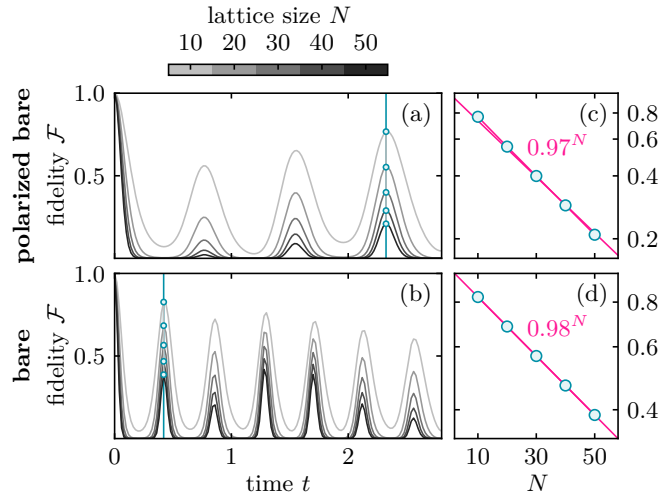


Figure 4.6: *Finite-size scaling*. Return fidelity during the evolution of the polarized bare vacuum (a) and bare vacuum (b) initial states, for $m = 5$, $g^2 = 1$, open boundary conditions, and various systems sizes N . The side plots (c) and (d) show the finite-size scaling of the highest fidelity peak, highlighted by a blue line in (a) and (b). Notice the log y -scale. The pink line is an exponential fit $\mathcal{F}_N = f^N$, and the extrapolated peak fidelity per site f is reported in the Figure. Simulations performed with maximum MPS bond dimension $\chi_{\max} = 350$, and truncation tolerance $\text{tol} = 10^{-7}$.

extended times, consistent with dynamics constrained to the many-body scars subset of the spectrum.

4.5 Summary

In this chapter, we reviewed the foundational concepts of thermalization in isolated quantum many-body (QMB) systems. We discussed how quantum thermalization is governed by the Eigenstate Thermalization Hypothesis (ETH) [302], which connects the equilibration over time to the dephasing mechanism of the spectrum eigenstates, as seen in a wide variety of models including bosonic, fermionic, and spin systems.

After this introduction, we highlighted the emergence of weak ergodicity breaking in recent studies [323, 326, 329], where a novel class of special non-thermal eigenstates, known as quantum many-body scars (QMBS), was identified. These scarred eigenstates exhibit anomalously low entanglement entropy and result in the system displaying long-lived oscillations and persistent revivals in quench dynamics, effectively violating the predictions of ETH.

This behavior was first observed experimentally in systems of Rydberg atoms, where scarred dynamics manifest in the form of coherent oscillations in local observables and revivals in state fidelity. Furthermore, we explored how this phenomenon extends to LGTs, particularly in $U(1)$ models, where QMBS arise in both spin-1/2 [333] and spin- S formulations [335, 336, 343, 354, 364]. These Abelian gauge theories show robust scarring dynamics, tied to the stability of the underlying gauge symmetry. Scars in these systems are deeply connected to the gauge structure and reveal an interplay between the gauge constraints and non-thermal eigenstates.

The original part was the extension of these results to the non-Abelian scenario. In detail, we presented strong numerical evidence for the occurrence of QMB scars in a non-Abelian $SU(2)$ lattice gauge theory with dynamical matter [4]. In particular, starting from simple experimentally

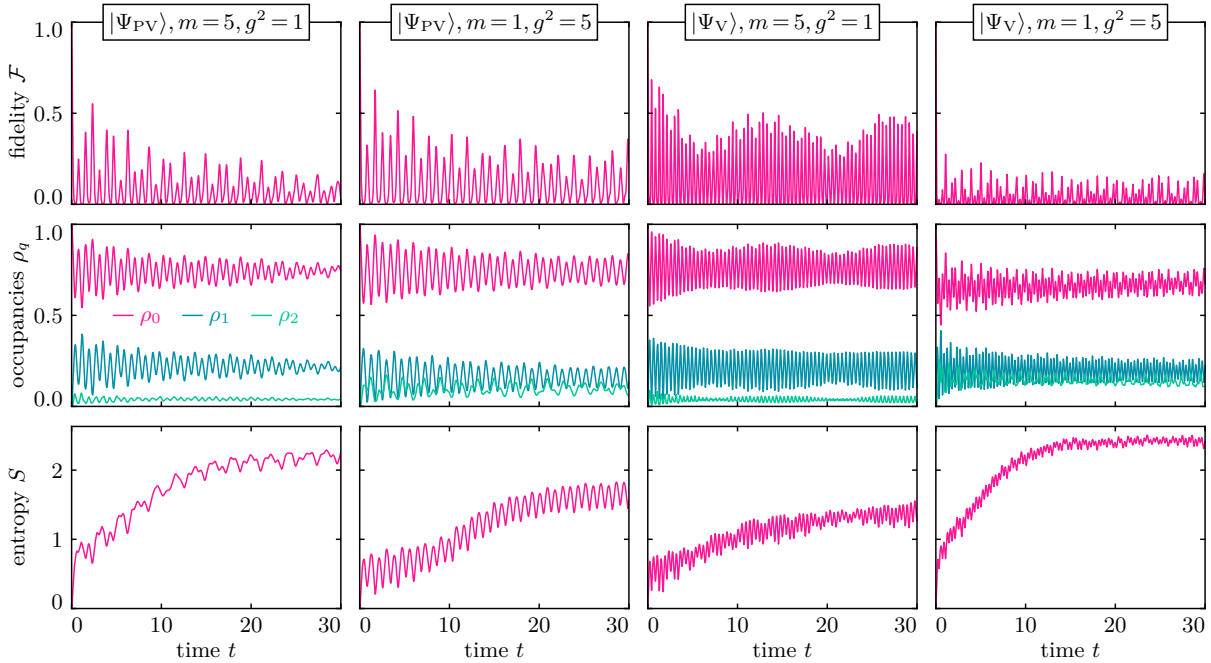


Figure 4.7: *Long time dynamics*. First to third row: return fidelity, average quark occupancy, and bipartite entanglement entropy as a function of time for the two initial states: polarized bare vacuum, and bare vacuum. We considered different values of mass and coupling as indicated in the Figure. The simulation was performed with MPS for $N = 30$ sites by setting open boundary conditions, maximum bond dimension $\chi_{\max} = 350$, and truncation tolerance $\text{tol} = 10^{-7}$.

friendly vacuum product states, scarred dynamics manifests as persistent oscillations in local observables and periodic revivals in the state fidelity. This dynamics arises from a state transfer through meson and baryon-antibaryon bare states, which allow the system to escape otherwise expected thermalization.

Even though the results were obtained for a non-Abelian lattice gauge theory model with the gauge-link truncated at the lowest nontrivial irreducible representations, we provided evidence that the observed scar dynamics persists even at higher gauge-link truncations, similar to what has recently been observed for Abelian models [336], hinting at the possible survival of QMBS in the Kogut-Susskind limit of the $SU(2)$ model under consideration. These findings demonstrate that the strong connection between QMBS and LGTs persists even for non-Abelian gauge groups, raising the intriguing question of whether such behavior represents an intrinsic feature of more fundamental theories such as quantum chromodynamics.

All the results we presented open the door to exciting future directions. Given the numerical evidence of scar eigenstates with very low bipartite entanglement entropy throughout the entire spectrum, even in regimes where both m and g are quite small, it would be interesting to find simple product states showing large overlap with these eigenstates. Additionally, it would be interesting to map the scarring phase diagram for this model as has been done for the PXP model [365], and see how driving protocols can enhance non-Abelian scarring dynamics [354]. Another venue to pursue is exploring the robustness of the non-Abelian scarring uncovered here in two spatial dimensions, as it has been recently done for Abelian gauge theories [343, 344]. This can shed further light on the nature of this non-Abelian scarring and its possible occurrence in the QFT limit. Furthermore, scarring is known to give rise to complex periodicities in the corresponding dynamical quantum phase transitions of Abelian LGTs [366, 367], and it would

be interesting to see if this carries over to the non-Abelian case.

Finally, we stress that, as addressed in [143], the qudit formulation of the proposed model is well-suited for conducting a digital quantum simulation on a recently demonstrated trapped-ion qudit quantum processor [166]. This opens up the intriguing possibility to experimentally observe this exotic non-ergodic dynamics in the near future.

Chapter 5

Simulating Lattice Fermion Theories

The quest for quantum simulation of interacting fermionic models [368–370] is necessary to reach a novel understanding of collective phenomena both at low and high energies [371–375], but it is hindered by fundamental challenges [38, 376, 377]. While analog quantum simulation, e.g. with optical lattices, has advanced greatly in recent decades [378–396], it presents limitations in tailoring exotic interactions. And while fermionic digital quantum processors are still at an early stage of development [114, 397], the well-established *conventional* digital quantum simulation platforms (e.g. superconducting qubits, trapped ions, Rydberg arrays, quantum dots) [117–121] are built on distinguishable, spatially localized qubits (qudits). In this framework, a *Fermion Encoding* is the analytical process to exactly convert a fermionic algebra (mutually-anticommuting operations) into a genuinely local algebra (mutually-commuting operations) of qudits.

Such encoding can not be carried out free of cost. Traditional strategies focused on encoding N Dirac orbitals into N qubits. By construction, these strategies can not preserve locality and, as a result, end up encoding the ubiquitous two-body interactions into cumbersome W -body interactions (with W often addressed as *Pauli weight*). Alongside recent efforts, which were able to reduce W from linear to logarithmic in N [122, 124], a separate sector of strategies arose: encodings attempting to preserve locality [157, 398–400]. They exhibit a flat Pauli weight (W does not scale with N) at the price of requiring a number of qubits larger (but still linear scaling) than the number N of fermion orbitals. For non-gauge lattice fermion theories, Ref. [282] showed that it is sufficient to add one qubit for each lattice bond to achieve local encoding (a generalization to lattice gauge fermionic theories was also recently introduced [115, 116]). The extra qubits play the role of an effective, discrete lattice gauge field with pure gauge dynamics akin to the Toric Code Hamiltonian [401]. The formal mapping is well understood [402], but evidence of practical feasibility of the local encoding for numerical simulation or digital quantum simulation is still the subject of active research [403, 404].

This chapter is based on the twofold study of Ref. [3] on the feasibility of the local fermion encoding for classical and quantum simulation, as summarized in Fig. 5.1: on one hand side, we investigate its performance for ground-state numerical simulations based on tensor network (TN) ansatz states. On the other side, we numerically test its applicability and scalability for digital quantum simulation on a generic platform (considering standard 1-qubit and 2-qubit programmable dynamical resources), by numerically emulating the noiseless quantum simulation processing in real-time. Equipped with these methods, we investigate the equilibrium and out-of-equilibrium properties of the spin- $\frac{1}{2}$ Hubbard model on a two-dimensional square lattice, with TN simulations. At zero temperature, we can access system sizes that allow us to identify the transition between liquid and insulating (crystalline spin-lattice) phases. In real-time dynamics,

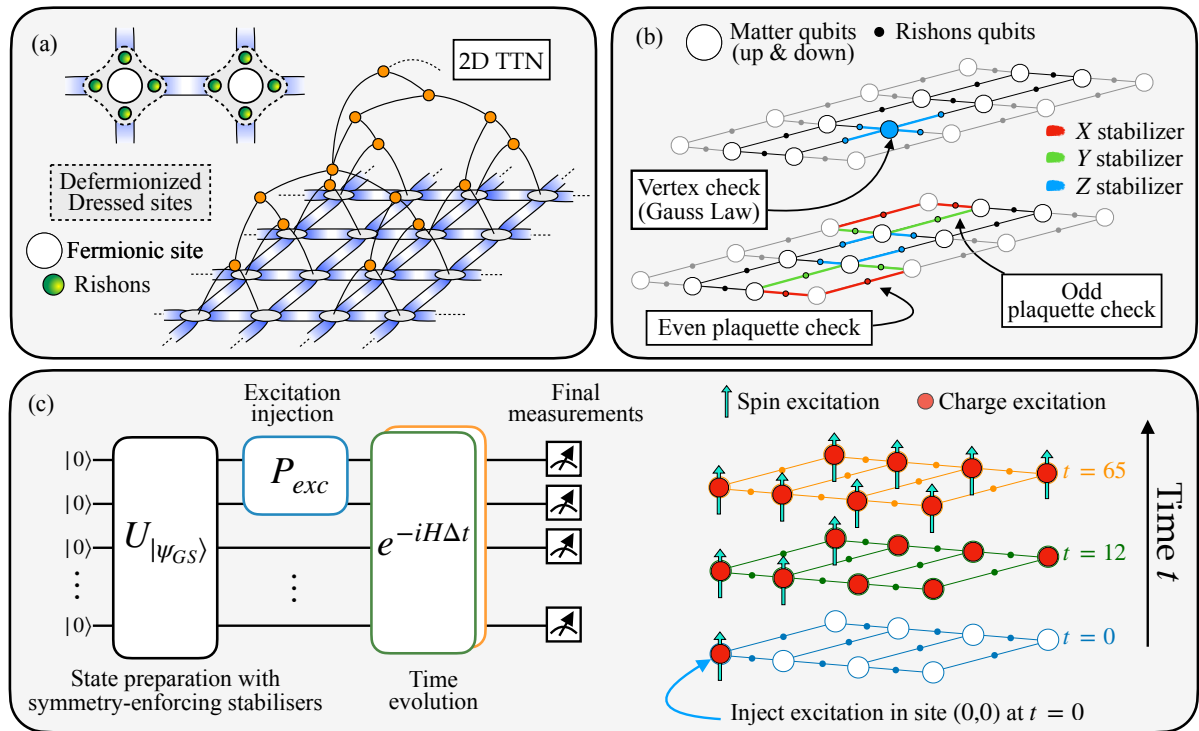


Figure 5.1: Simulation of the Hubbard model in 2D with tensor networks (equilibrium) and quantum circuits (out-of-equilibrium). (a) Schematic of the tree-tensor network (TTN) installed on the 2D lattice: the fermionic degrees of freedom are removed with the gauge defermentation and encoded in a dressed site (dashed closed line) comprising fermionic matter and rishons. With TTN, the ground state of the defermentation model is computed for up to 4×4 lattice. (b) To run the digital quantum simulation, dressed sites are decomposed into qubits and Hamiltonian terms in Pauli strings. The symmetries of the system are here enforced through the stabilizer formalism. (c) (left) Quantum circuit for simulating out-of-equilibrium dynamics: adiabatic preparation of the initial state (half-filling, repulsive U), injection of charge (spin) excitation, and time evolution with Hubbard Hamiltonian. (right) Spin-charge dynamics schematic: the charge excitation propagates faster than the spin one.

for a ladder in the $t-J$ model limit, we observe spin and charge time-evolution displaying distinct time-scales, an effect that in 1D Hubbard chains is a precursor of the spin-charge separation phenomenon, see for example the recent experiments [117, 405, 406], whereas in 2D it only governs short time scales before the polaron picture and strongly-correlated effects set in [381, 407, 408].

The chapter is structured as follows: in Sec. 5.1, we revisit the gauge-based encoding to locally remove the fermionic matter, or gauge defermentation. Such an approach can be seen as a generalization of the dressed-site formalism developed in Sec. 1.2, as in this case there are no gauge fields. We devote Sec. 5.2 to the implementation of the encoding on a tree-tensor network (TTN) ansatz and show ground state simulation results of the 2D Hubbard model. Finally, in Sec. 5.3, we detail our prescription for digital quantum simulation of the 2D Hubbard model, based on gauge defermentation, and numerically emulate the digital quantum simulation to observe spin-charge separation effects in two-dimensional lattice samples.

5.1 Gauge Defermionization of Lattice Fermion Theories

In this section, we revisit and extend a known technique, based on lattice gauge theories, to eliminate fermionic matter from 2D lattice models [115, 116]. The strategy consists of developing an analytical mapping from an input fermion lattice Hamiltonian (here we consider it to be a pure non-gauge fermion theory) to a lattice gauge Hamiltonian, with a \mathbb{Z}_2 gauge symmetry, equipped with appropriate gauge constraints. Then, by applying the dressed-site formalism developed in Sec. 1.2, the resulting theory can be manipulated so that the fermionic parity at each (dressed) site is protected, thus resulting in a theory where operator algebras at different sites always commute, as in a local spin theory.

Our formulation of the deferfionization technique can be applied to any 2D fermion lattice Hamiltonian, regardless of the lattice system (it works on Honeycomb and Kagome lattices as well as irregular lattices), as long as few general constraints are satisfied: (i) the global parity of fermions is protected; (ii) Hamiltonian terms that flip the local fermion parity must be nearest-neighbor; (iii) the full system must be under open boundary conditions (OBC), i.e. every closed path on the lattice must be topologically shrinkable to a point. These conditions are often satisfied in solid state Hamiltonians and cold atoms systems [409]

Therefore, without any loss of generality, a general fermion Hamiltonian on a two-dimensional lattice Λ with $N = N_x \times N_y$ sites \mathbf{n} reads:

$$\hat{H}_0 = \sum_{\mathbf{n},k} \sum_{\alpha,\beta} \left[\left[h_{\alpha,\beta} \hat{\psi}_{\mathbf{n},\alpha}^\dagger \hat{\psi}_{\mathbf{n}+\boldsymbol{\mu}_k,\beta} + \text{h.c.} \right] + \left[\Delta_{\alpha,\beta} \hat{\psi}_{\mathbf{n},\alpha} \hat{\psi}_{\mathbf{n}+\boldsymbol{\mu}_k,\beta} + \text{h.c.} \right] \right] + V(\{\hat{n}_{\mathbf{n},\alpha}\}), \quad (5.1.1)$$

where the fermion fields satisfy the usual Dirac anti-commutation relations

$$\left\{ \hat{\psi}_{\mathbf{n},\alpha}^\dagger, \hat{\psi}_{\mathbf{n}',\beta} \right\} = i\hbar \delta_{\mathbf{n},\mathbf{n}'} \delta_{\alpha,\beta} \quad \left\{ \hat{\psi}_{\mathbf{n},\alpha}, \hat{\psi}_{\mathbf{n}',\beta} \right\} = 0, \quad (5.1.2)$$

and can exhibit an internal degree of freedom, here labeled by the flavor indices α, β .

The interaction potential V term, which is a function of the fermion densities $\hat{n}_{\mathbf{n},\alpha} = \hat{\psi}_{\mathbf{n},\alpha}^\dagger \hat{\psi}_{\mathbf{n},\alpha}$, can in principle have any range and shape, and even include chemical potentials. For instance, it can also account local terms that do not conserve the spin, like $b_{\alpha,\beta} \hat{\psi}_{\mathbf{n},\alpha}^\dagger \hat{\psi}_{\mathbf{n},\beta}$, or local s-wave superconducting terms as $\Delta \hat{\psi}_{\mathbf{n},\alpha}^\dagger \hat{\psi}_{\mathbf{n},\beta}^\dagger$.

Conversely, the hopping $h_{\alpha,\beta}$ and the double creation/annihilation $\Delta_{\alpha,\beta}$ processes (the latter often seen in superconductors) are the terms that break local fermion parity: their single-site algebras do not commute between distant sites (i.e. they are not *genuinely* local), and this is the source of all the numerical difficulty when simulating lattice fermions.

While in one spatial dimension, the Jordan-Wigner transformation [122] provides an easy solution to this problem, tackling the mapping in higher dimensions requires sophisticated, often cumbersome techniques [62, 157]. In this perspective, converting a fermion algebra into a genuinely local (spin-like) algebra using introducing a lattice gauge field is an elegant strategy, which is also practical from a numerical simulation standpoint, as we discuss later on.

5.1.1 Mapping into a \mathbb{Z}_2 gauge theory

We now perform a set of exact algebraic manipulations to the Hamiltonian of Eq. (5.1.1) until we reach a deferfionized form. The very first step is to promote the total fermion parity operator

at site \mathbf{n} to a gauge transformation (for the matter sites M) that behaves like a parity operator, or an element of the \mathbb{Z}_2 group:

$$G_{\mathbf{n}}^{[M]} = \exp\left(i\pi \sum_{\alpha} \hat{\psi}_{\mathbf{n},\alpha}^{\dagger} \hat{\psi}_{\mathbf{n},\alpha}\right) = G_{\mathbf{n}}^{[M]\dagger} = (G_{\mathbf{n}}^{[M]})^{-1}. \quad (5.1.3)$$

Under $G_{\mathbf{n}}^{[M]}$, operators that preserve total fermion parity, such as densities $\hat{n}_{\mathbf{n},\alpha}$, are left invariant, while operators that flip the total fermion parity, such as $\hat{\psi}_{\mathbf{n},\alpha}^{(\dagger)}$, acquire a sign. Namely:

$$G_{\mathbf{n}}^{[M]} \hat{n}_{\mathbf{n},\alpha} G_{\mathbf{n}}^{[M]} = \hat{n}_{\mathbf{n},\alpha} \quad G_{\mathbf{n}}^{[M]} \hat{\psi}_{\mathbf{n},\alpha} G_{\mathbf{n}}^{[M]} = -\hat{\psi}_{\mathbf{n},\alpha} \quad (5.1.4)$$

At this stage, we promote the gauge transformation into a gauge symmetry. This task is performed by adding an auxiliary quantum lattice field, the gauge field, on the *bonds* $(\mathbf{n}, \boldsymbol{\mu})$ of the lattice. The local Hilbert space for a gauge site should correspond to the regular representation space for the \mathbb{Z}_2 group [160], so it should be a two-level system, or a qubit, equipped with the (genuinely local) algebra of Pauli matrices $\{\hat{\sigma}^x, \hat{\sigma}^y, \hat{\sigma}^z\}$.

Being \mathbb{Z}_2 an Abelian gauge group, the left- $G_{\mathbf{n},\boldsymbol{\mu}}^{[L]}$ and right- $G_{\mathbf{n},\boldsymbol{\mu}}^{[R]}$ groups of transformations of the gauge field must commute and square to the identity. Without loss of generality, we can set them both to the same operator: $G_{\mathbf{n},\boldsymbol{\mu}}^{[L]} = G_{\mathbf{n},\boldsymbol{\mu}}^{[R]} = \hat{\sigma}_{\mathbf{n},\boldsymbol{\mu}}^z$. Thanks to this auxiliary field, we equip the gauge-violating terms of the Hamiltonian with a parallel transporter operator. We replace

$$\hat{\psi}_{\mathbf{n},\alpha}^{\dagger} \hat{\psi}_{\mathbf{n}+\boldsymbol{\mu},\beta} \quad \longrightarrow \quad \hat{\psi}_{\mathbf{n},\alpha}^{\dagger} \hat{U}_{\mathbf{n},\boldsymbol{\mu}} \hat{\psi}_{\mathbf{n}+\boldsymbol{\mu},\beta}, \quad (5.1.5)$$

that transforms covariantly under the gauge field groups:

$$G_{\mathbf{n},\boldsymbol{\mu}}^{[L]} \hat{U}_{\mathbf{n},\boldsymbol{\mu}} G_{\mathbf{n},\boldsymbol{\mu}}^{[L]} = G_{\mathbf{n},\boldsymbol{\mu}}^{[R]} \hat{U}_{\mathbf{n},\boldsymbol{\mu}} G_{\mathbf{n},\boldsymbol{\mu}}^{[R]} = -\hat{U}_{\mathbf{n},\boldsymbol{\mu}} \quad (5.1.6)$$

Again, without loss of generality, we set $\hat{U}_{\mathbf{n},\boldsymbol{\mu}} = \hat{\sigma}_{\mathbf{n},\boldsymbol{\mu}}^x$. Overall, this procedure translates into modifying the fermion parity-flipping terms from Eq. (5.1.1) according to

$$\begin{aligned} h_{\alpha,\beta} \hat{\psi}_{\mathbf{n},\alpha}^{\dagger} \hat{\psi}_{\mathbf{n}+\boldsymbol{\mu},\beta} &\longrightarrow h_{\alpha,\beta} \hat{\psi}_{\mathbf{n},\alpha}^{\dagger} \hat{\sigma}_{\mathbf{n},\boldsymbol{\mu}}^x \hat{\psi}_{\mathbf{n}+\boldsymbol{\mu},\beta} \\ \Delta_{\alpha,\beta} \hat{\psi}_{\mathbf{n},\alpha} \hat{\psi}_{\mathbf{n}+\boldsymbol{\mu},\beta} &\longrightarrow \Delta_{\alpha,\beta} \hat{\psi}_{\mathbf{n},\alpha} \hat{\sigma}_{\mathbf{n},\boldsymbol{\mu}}^x \hat{\psi}_{\mathbf{n}+\boldsymbol{\mu},\beta}. \end{aligned} \quad (5.1.7)$$

With this modification, the Hamiltonian satisfies a gauge symmetry around every site, precisely $G_{\mathbf{n}}^{[\text{total}]} = G_{\mathbf{n}}^{[M]} \prod_{\boldsymbol{\mu}} G_{\mathbf{n},\boldsymbol{\mu}}^{[L/R]}$. Consequently, we have to choose a symmetry sector (for each of these symmetries) to play the role of physical space. As it is common for lattice gauge theories, we consider the quantum states *invariant* under all the $G_{\mathbf{n}}^{[\text{total}]}$, i.e. which satisfy

$$\left[\exp\left(i\pi \sum_{\alpha} \hat{\psi}_{\mathbf{n},\alpha}^{\dagger} \hat{\psi}_{\mathbf{n},\alpha}\right) \prod_{\boldsymbol{\mu}} \hat{\sigma}_{\mathbf{n},\boldsymbol{\mu}}^z \right] |\Psi_{\text{phys}}\rangle = |\Psi_{\text{phys}}\rangle, \quad (5.1.8)$$

in order to be the physical states $|\Psi_{\text{phys}}\rangle$. This equation plays the role of effective Gauss' Law of the resulting gauge theory, and the condition can be satisfied at every site *only* if the total number of fermions in the system is even. To simulate an odd number of fermions, one or more virtual bonds, going out of the system, must be added to keep track of the appropriate parity gauge flux.

5.1.2 Restoring equivalence with Plaquette Operators

It is then possible to check that, under the Gauss' Law of Eq. (5.1.8), the gauge-theory modification in Eq. (5.1.7) does not change the actual dynamics given by the original Hamiltonian as in Eq. (5.1.1), *but only* when the lattice is a non-cyclic graph (such as a 1D chain, or a dendrimer lattice). For each (product state) fermion configuration, the extra degrees of freedom introduced by the gauge fields are completely locked by Gauss' Law; thus all residual degeneracy is removed, and all the matrix elements of \hat{H}_0 are unaltered.

Conversely, when lattice cycles are present, the modification changes the dynamics. In fact, for each elementary closed cycle of sites, or *plaquette* $\square \in \Lambda$, one Gauss' Law operator becomes linearly dependent on others, thus contributing to degeneracy with a 2-fold space. Moreover, when a fermion winds around a closed cycle, all of the gauge fields in its path undergo a $\hat{\sigma}^x$ flip, thus the final state may differ from the original one. If we want to restore the dynamics of the original model, we have to add more physical contents to the plaquette, either in terms of an additional *pure gauge field* Hamiltonian or in terms of *extra symmetries*.

Fortunately, a simple recipe to do either is inspired by Kitaev's Toric Code [401]. The idea is to add a plaquette Hamiltonian term with a $\hat{\sigma}^x$ for each gauge link of the plaquette, that is

$$\hat{H}_p = - \sum_{\square \in \Lambda} \prod_{\langle \mathbf{n}, \mathbf{n}' \rangle \in \square} \hat{\sigma}_{\mathbf{n}, \mathbf{n}'}^x = - \sum_{\square \in \Lambda} \left(\begin{array}{ccc} \ulcorner & \hat{\sigma}^x & \urcorner \\ \hat{\sigma}^x & & \hat{\sigma}^x \\ \llcorner & \hat{\sigma}^x & \lrcorner \end{array} \right). \quad (5.1.9)$$

Notably, each of these plaquette operators commutes with the lattice gauge Hamiltonian and can be equivalently cast as a (gauge) symmetry. Moreover, plaquettes also commute with Gauss' laws, because a vertex and a plaquette always share either zero or two bonds, regardless of the lattice system, and $[\hat{\sigma}_1^x \hat{\sigma}_2^x, \hat{\sigma}_1^z \hat{\sigma}_2^z] = 0$.

We can then map the original lattice fermion Hamiltonian, Eq. (5.1.1), to a dynamically-equivalent, \mathbb{Z}_2 -invariant lattice gauge model, which reads

$$\hat{H}_1 = \sum_{\mathbf{n}, k} \sum_{\alpha, \beta} \left[h_{\alpha, \beta} \hat{\psi}_{\mathbf{n}, \alpha}^\dagger \hat{\sigma}_{\mathbf{n}, \mu}^x \hat{\psi}_{\mathbf{n}+\mu, \beta} + \Delta_{\alpha, \beta} \hat{\psi}_{\mathbf{n}, \alpha} \hat{\sigma}_{\mathbf{n}, \mu}^x \hat{\psi}_{\mathbf{n}+\mu, \beta} \text{h.c.} \right] + V(\{\hat{n}_{\mathbf{n}, \alpha}\}), \quad (5.1.10)$$

with the constraints

$$\left[e^{i\pi \sum_{\alpha} \hat{n}_{\mathbf{n}, \alpha}} \prod_{\mu}^{\text{vertex}} \hat{\sigma}_{\mathbf{n}, \mu}^z \right] |\Psi_{\text{phys}}\rangle = |\Psi_{\text{phys}}\rangle, \quad \left[\prod_{\langle \mathbf{n}, \mathbf{n}' \rangle}^{\text{plaquette}} \hat{\sigma}_{\mathbf{n}, \mathbf{n}'}^x \right] |\Psi_{\text{phys}}\rangle = |\Psi_{\text{phys}}\rangle. \quad (5.1.11)$$

Indeed, the combined constraints in Eq. (5.1.11) completely resolve the 2-fold degeneracy introduced by the plaquette, and each closed path of moving fermions returns to its original state with the correct amplitude and phase. Therefore, the whole mapping holds for the subspace of the Hilbert space satisfying Eq. (5.1.11). Any excitations from the ground state of Eq. (5.1.9) break the encoding validity. A rigorous proof of the equivalence between Eq. (5.1.1) and Eqs. (5.1.10) and (5.1.11) was provided for a number-conserving theory on the square lattice in [115]; the generalization to other cases is fairly straightforward.

Notice that the degeneracy is not fully removed in periodic boundary conditions (PBC), where each winding dimension introduces an additional closed cycle. This case requires the additional constraint of a full $\hat{\sigma}^x$ string along each winding dimension, but we will not treat this case here, because the theory becomes non-local.

5.1.3 Fermionic Rishons

So far, it seems that we have increased the complexity of the fermion lattice theory. In this last step, we will locally manipulate the gauge fields and achieve de Fermionization explicitly, ending with an algebra of genuinely local operators only.

Similarly to the rishon decomposition discussed in Secs. 1.3.3 and 1.4.3, we split each gauge field, living on the $(\mathbf{n}, \boldsymbol{\mu})$ lattice link, in a pair of spinless fermion modes (rishons) $\hat{c}_{\mathbf{n},\boldsymbol{\mu}}^{(\dagger)}$ and $\hat{c}_{\mathbf{n}+\boldsymbol{\mu},-\boldsymbol{\mu}}^{(\dagger)}$, equipped with another symmetry. These new Dirac fermion operators belong to dressed sites \mathbf{n} and $\mathbf{n} + \boldsymbol{\mu}$ respectively and satisfy the usual anti-commutation relations between themselves and with the physical matter fermions

$$\left\{ c_{\mathbf{n},\boldsymbol{\mu}}^\dagger, \hat{c}_{\mathbf{n}',\boldsymbol{\mu}'} \right\} = \delta_{\mathbf{n}\mathbf{n}'} \delta_{\boldsymbol{\mu}\boldsymbol{\mu}'} \quad \left\{ \hat{c}_{\mathbf{n},\boldsymbol{\mu}}, \hat{c}_{\mathbf{n}',\boldsymbol{\mu}'} \right\} = 0 \quad \left\{ \hat{\psi}_{\mathbf{n}}, \hat{c}_{\mathbf{n}',\boldsymbol{\mu}'} \right\} = 0. \quad (5.1.12)$$

The combined 4-dimensional space of the two modes is then reduced back to the 2-dimensional space of a qubit by imposing that the total number of rishon fermions on a bond must be an even number. This constraint can again be cast as a *link symmetry*, requiring that

$$\exp \left[i\pi (\hat{c}_{\mathbf{n},\boldsymbol{\mu}}^\dagger \hat{c}_{\mathbf{n},\boldsymbol{\mu}} + \hat{c}_{\mathbf{n}+\boldsymbol{\mu},-\boldsymbol{\mu}}^\dagger \hat{c}_{\mathbf{n}+\boldsymbol{\mu},-\boldsymbol{\mu}}) \right] |\Psi_{\text{phys}}\rangle = |\Psi_{\text{phys}}\rangle. \quad (5.1.13)$$

We then convert the gauge fields Pauli algebra into an operator algebra acting on the rishon pair:

$$\hat{\sigma}_{\mathbf{n},\boldsymbol{\mu}}^z \rightarrow 1 - 2\hat{c}_{\mathbf{n},\boldsymbol{\mu}}^\dagger \hat{c}_{\mathbf{n},\boldsymbol{\mu}} = 1 - 2\hat{c}_{\mathbf{n}+\boldsymbol{\mu},-\boldsymbol{\mu}}^\dagger \hat{c}_{\mathbf{n}+\boldsymbol{\mu},-\boldsymbol{\mu}} \quad \hat{\sigma}_{\mathbf{n},\boldsymbol{\mu}}^x \rightarrow \hat{I} \hat{\gamma}_{\mathbf{n},\boldsymbol{\mu}} \hat{\gamma}_{\mathbf{n}+\boldsymbol{\mu},-\boldsymbol{\mu}}, \quad (5.1.14)$$

where now $\hat{\gamma}_{\mathbf{n},\boldsymbol{\mu}} = \hat{c}_{\mathbf{n},\boldsymbol{\mu}} + c_{\mathbf{n},\boldsymbol{\mu}}^\dagger = \hat{\gamma}_{\mathbf{n},\boldsymbol{\mu}}^\dagger$ is a Majorana operator on the rishon fermion, which squares to the identity $\hat{\gamma}_{\mathbf{n},\boldsymbol{\mu}}^2 = 1$ but still anti-commutes with other fermions $\{\hat{\gamma}_{\mathbf{n},\boldsymbol{\mu}}, \hat{\gamma}_{\mathbf{n}',\boldsymbol{\mu}'}\} = 2\delta_{\mathbf{n},\mathbf{n}'} \delta_{\boldsymbol{\mu},\boldsymbol{\mu}'}$. These operators defined at Eq. (5.1.14) respect the fermion parity symmetry on the bond, and on the even parity sector, they act exactly as Pauli matrices.

We can then plug this exact manipulation into the gauge theory Hamiltonian, resulting in

$$\hat{H}_2 = \sum_{\mathbf{n},k} \sum_{\alpha,\beta} \left[ih_{\alpha,\beta} \hat{\psi}_{\mathbf{n},\alpha}^\dagger \hat{\gamma}_{\mathbf{n},\boldsymbol{\mu}} \hat{\gamma}_{\mathbf{n}+\boldsymbol{\mu},-\boldsymbol{\mu}} \hat{\psi}_{\mathbf{n}+\boldsymbol{\mu},\beta} + i\Delta_{\alpha,\beta} \hat{\psi}_{\mathbf{n},\alpha} \hat{\gamma}_{\mathbf{n},\boldsymbol{\mu}} \hat{\gamma}_{\mathbf{n}+\boldsymbol{\mu},-\boldsymbol{\mu}} \hat{\psi}_{\mathbf{n}+\boldsymbol{\mu},\beta} + \text{h.c.} \right] + V, \quad (5.1.15)$$

where we have to add the new link parity symmetry to the constraints, thus

$$\left[e^{i\pi \sum_{\alpha} \hat{n}_{\mathbf{n},\alpha}} \prod_{\boldsymbol{\mu}}^{\text{vertex}} e^{i\pi \hat{c}_{\mathbf{n},\boldsymbol{\mu}}^\dagger \hat{c}_{\mathbf{n},\boldsymbol{\mu}}} \right] |\Psi_{\text{phys}}\rangle = |\Psi_{\text{phys}}\rangle \quad (5.1.16a)$$

$$\left[\prod_{\mathbf{n},\boldsymbol{\mu}}^{\text{plaquette}} \hat{I} \hat{\gamma}_{\mathbf{n},\boldsymbol{\mu}} \hat{\gamma}_{\mathbf{n}+\boldsymbol{\mu},-\boldsymbol{\mu}} \right] |\Psi_{\text{phys}}\rangle = |\Psi_{\text{phys}}\rangle \quad (5.1.16b)$$

$$e^{i\pi \hat{c}_{\mathbf{n},\boldsymbol{\mu}}^\dagger \hat{c}_{\mathbf{n},\boldsymbol{\mu}}} e^{i\pi \hat{c}_{\mathbf{n}+\boldsymbol{\mu},-\boldsymbol{\mu}}^\dagger \hat{c}_{\mathbf{n}+\boldsymbol{\mu},-\boldsymbol{\mu}}} |\Psi_{\text{phys}}\rangle = |\Psi_{\text{phys}}\rangle, \quad (5.1.16c)$$

which must hold for every vertex, every plaquette, and every bond respectively.

We have finally reached the final form of our model: now, every term of the Hamiltonian and every vertex, link, or plaquette symmetry *protects total fermion parity* at each dressed site, counting together matter and rishon fermions (for plaquettes, remember that each dressed site contributes with two rishon modes in a closed lattice path). Therefore, it is possible to think of each dressed site as a large spin, and both Hamiltonian and extra symmetries can be written in terms of *genuinely local* operator algebras, which commute on different dressed sites. The theory has been effectively de Fermionized.

5.1.4 The price of deformationization

Deformationization of the lattice model using LGT, i.e. going from Eq. (5.1.1) to Eqs. (5.1.15) and (5.1.16) is an exact mapping. And while it provides the clear benefits of eliminating fermionic operator algebras, it does not come free of costs.

First of all, the transformation increases the local space dimension, only to shrink the local dimension again once the gauge symmetries are installed. If the model has N sites, f flavors and coordination number v , we increase the dimension from 2^{fN} to $2^{(f+v)N}$.

Secondly, we impose a new interaction term in the form of the plaquettes. While for typical 2D lattices plaquettes are rather small, it is still an interaction involving three to six sites depending on the lattice geometry. If the original interaction V was on-site, or nearest-neighbor, the deformationization effectively increased the interaction supports. Moreover, there are no more components in the Hamiltonian that are quadratic in the Fermi operators (except chemical potentials within V). This means that Green's function perturbative approaches, which start from the free Fermi gas propagator of the quadratic theory, are no longer viable.

Finally, introducing an auxiliary field whose pure gauge dynamics is analogous to a Toric Code Hamiltonian has the drawback of increasing the entanglement. Even for product states of fermions, where fermions are locked in a specific integer filling configuration, and the original entanglement is zero (e.g. for a Jordan-Wigner encoding), adding a Toric Code field on top of that raises the entanglement entropy to an exact area-law [410], carrying one e-bit of entanglement per plaquette that is cut by the bi-partition. This observation has substantial implications for TN simulations of said models, as we will discuss in detail later on.

5.2 Hubbard Model, Deformationized for tensor networks

Despite its Hamiltonian's apparent simplicity, the Hubbard model has eluded physicists for decades [411–414]. While exact solutions are available for both one-dimensional [409] and infinite-dimensional cases [415, 416], addressing finite-size systems in higher dimensions at arbitrary temperature has required the development of various computational techniques. Although Monte Carlo methods can handle substantially large systems, they suffer from the well-known sign problem when computing physically significant quantities within specific regimes [39, 187, 376]. Comprehensive reviews detailing and comparing the accomplished computational outcomes for the 2D case can be found in the following references [417, 418].

In this section, we join the effort by performing TN simulations of the Hubbard model at equilibrium at zero temperature. We start reviewing the model and manipulating its deformationized formulation to be ready for a numerical approach. Subsequently, we focus on a 2D *square lattice* geometry, fermionic matter with 2 flavors (e.g. \uparrow and \downarrow), and open boundary conditions. On a rectangle lattice Λ of $N = N_x \times N_y$ sites, the Hubbard Hamiltonian reads:

$$\hat{H}_{\text{Hub}} = -t \sum_{\mathbf{n}, k} \sum_{\alpha=\uparrow, \downarrow} \left[\hat{\psi}_{\mathbf{n}, \alpha}^\dagger \hat{\psi}_{\mathbf{n}+\mu_k, \alpha} + \text{h.c.} \right] + U \sum_{\mathbf{n}} \left(\hat{n}_{\mathbf{n}, \uparrow} - \frac{1}{2} \right) \left(\hat{n}_{\mathbf{n}, \downarrow} - \frac{1}{2} \right), \quad (5.2.1)$$

where, apart from an energy rescaling, its ground state properties only depend on the dimensionless parameter U/t . The Hubbard model is regarded as the simplest theory of strongly correlated electrons, where band electrons interact via a two-body repulsive Coulomb interaction [368]. This model enables the description of a wide range of phenomena including metal-insulator transitions, superconductivity, and magnetism [370]. The Hubbard Hamiltonian in Eq. (5.2.1) belongs

to the Hamiltonian class of Eq. (5.1.1), with flavor-transparent hopping terms ($h_{\alpha,\beta} = -t\delta_{\alpha,\beta}$) and no pair creation processes ($\Delta_{\alpha,\beta} = 0$), so it can be readily deformed.

The form of Eq. (5.2.1) includes the $-\frac{1}{2}$ terms in the interaction component, which are equivalent to setting a specific uniform chemical potential, which explicitly reveals the rich symmetry content of the Hubbard model. In fact, besides the obvious lattice symmetries (translation by 1 site in x and y , $\frac{\pi}{2}$ rotations, vertical and horizontal reflection, and compositions thereof) Hubbard dynamics exhibits two useful *glocal* symmetries, where the transformation is global but comprised of separate single-site non-Abelian operations.

The first symmetry, an SU(2) group, represents rotational invariance in the flavors. Since the hopping is flavor-transparent and the interaction is based on double occupancy, the model has to be flavor-invariant. This symmetry is a Lie group, generated by the operator algebra

$$\hat{S}_{\text{tot}}^a = \sum_{\mathbf{n}} \hat{S}_{\mathbf{n}}^a, \quad \text{where} \quad \hat{S}_{\mathbf{n}}^a = \frac{1}{2} \sum_{\alpha,\beta} \hat{\sigma}_{\alpha,\beta}^a \hat{\psi}_{\mathbf{n},\alpha}^\dagger \hat{\psi}_{\mathbf{n},\beta} \quad (5.2.2)$$

are the single-site flavor (spin) operators previously introduced in Eq. (1.3.5), acting non-trivially only on the singly-occupied sites.

The second symmetry, assembling total fermion number conservation and particle-hole inversion, is an O(2) group, the symmetry group of the circle (rotations of a scalar angle plus one reflection). Despite being a continuous group, it is not Lie, but any element can be written as a rotation $\hat{R}_{\text{tot}}(\theta)$ eventually followed by a reflection \hat{F}_{tot} :

$$\hat{R}_{\text{tot}}(\theta) = \prod_{\mathbf{n}} \hat{R}_{\mathbf{n}}(\theta) = \prod_{\mathbf{n}} e^{i\theta(\hat{n}_{\mathbf{n},\uparrow} + \hat{n}_{\mathbf{n},\downarrow})} \quad \hat{F}_{\text{tot}} = \prod_{\mathbf{n}} \hat{F}_{\mathbf{n}}. \quad (5.2.3)$$

It is indeed possible to write the particle-hole transformation \hat{F} in a way that commutes with the flavor-rotations \vec{S} , thus the two symmetries are independent. By doing so, we get

$$\hat{R}_{\mathbf{n}}(\theta) \hat{\psi}_{\mathbf{n},\alpha} \hat{R}_{\mathbf{n}}^\dagger(\theta) = e^{-i\theta} \hat{\psi}_{\mathbf{n},\alpha} \quad \hat{F}_{\mathbf{n}} \hat{\psi}_{\mathbf{n},\alpha} \hat{F}_{\mathbf{n}}^\dagger = (-1)^{\mathbf{n}} \sum_{\beta} \hat{\sigma}_{\alpha,\beta}^y \hat{\psi}_{\mathbf{n},\beta}^\dagger. \quad (5.2.4)$$

Other symmetries, such as the pseudospin conservation [414, 419], are indeed present, but not practically useful for our numerical simulation purposes.

When deformed the Hubbard model for TN simulation, we find it convenient to enforce the *vertex gauge constraint* as an exact, actual symmetry. By the prescription discussed in Ref. [158], this constraint will allow us to select a reduced canonical basis for the dressed site, made by only and all the vertex-gauge invariant states. Conversely, the *link constraint* and especially the *plaquette constraint* are cumbersome to treat as exact symmetries (their local algebras do not commute) can be equivalently included in the Hamiltonian as penalty terms, increasing the energy of gauge symmetry-violating sectors. In conclusion, we have

$$\hat{H}'_{\text{Hub}} = -t \sum_{\mathbf{n},k} \sum_{\alpha} \left[i \hat{\psi}_{\mathbf{n},\alpha}^\dagger \hat{\gamma}_{\mathbf{n},\mu_k} \hat{\gamma}_{\mathbf{n}+\mu_k,-\mu_k} \hat{\psi}_{\mathbf{n}+\mu_k,\alpha} \right] + U \sum_{\mathbf{n}} \left(\hat{n}_{\mathbf{n},\uparrow} - \frac{1}{2} \right) \left(\hat{n}_{\mathbf{n},\downarrow} - \frac{1}{2} \right), \quad (5.2.5)$$

plus a penalty

$$\hat{H}'_{\text{pen}} = -\alpha_b \sum_{\mathbf{n},k} \left[(-1)^{c_{\mathbf{n},\mu_k}^\dagger c_{\mathbf{n},\mu_k} + c_{\mathbf{n}+\mu_k,-\mu_k}^\dagger c_{\mathbf{n}+\mu_k,-\mu_k}} \hat{c}_{\mathbf{n}+\mu_k,-\mu_k} - 1 \right] - \alpha_p \sum_{\square \in \Lambda} \left[\begin{array}{ccc} \lrcorner & \hat{\gamma}_{+\mu_x} \hat{\gamma}_{-\mu_x} & \llcorner \\ \hat{\gamma}_{-\mu_y} & & \hat{\gamma}_{-\mu_y} \\ \llcorner & \hat{\gamma}_{+\mu_y} & \lrcorner \\ \lrcorner & \hat{\gamma}_{+\mu_x} \hat{\gamma}_{-\mu_x} & \llcorner \end{array} - 1 \right], \quad (5.2.6)$$

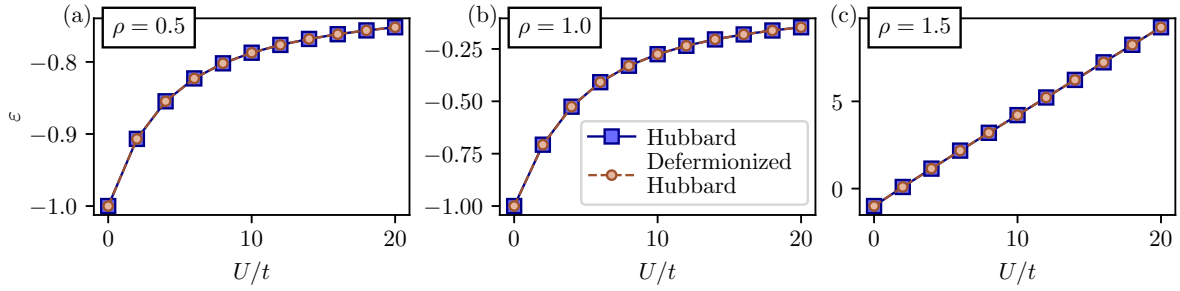


Figure 5.2: Exact Diagonalization comparison on a 2×2 lattice between the ground state energy density ε of the original 2D Hubbard model and its deformed version as a function of U/t , and for three values of the particle density ρ : (a) below half-filling with $\rho = 0.5$, (b) at half-filling with $\rho = 1.0$, (c) above half-filling with $\rho = 1.5$.

with separate penalty couplings $\alpha_p > 0$ and $\alpha_b > 0$ for the plaquette and bond violations respectively. The added -1 constants ensure that the correct gauge symmetry sector provides no energy contribution. Notice that, for the mapping to be perfectly equivalent to the original model, the penalty terms of Eq. (5.2.6) must represent the largest energy-scale contribution of the Hamiltonian. Therefore, the penalties α_p and α_b must be sufficiently larger than t and U .

5.2.1 Dressed-site Hamiltonian

Once the vertex gauge symmetry is successfully installed, we are left with a dressed-site vertex gauge-invariant canonical basis of dimension 32 (4 matter states and four 2-dimensional rishon modes, divided in half by the vertex constraint). Within this canonical basis, the algebra of 1-site operators is genuinely local and can be expressed in terms of the following quadratic operators

$$\hat{Q}_{\mathbf{n},\mu,\alpha} = \hat{\gamma}_{\mathbf{n},\mu} \hat{\psi}_{\mathbf{n},\alpha} \quad \hat{c}_{\mathbf{n},\mu_1,\mu_2} = \hat{\gamma}_{\mathbf{n},\mu_1} \hat{\gamma}_{\mathbf{n},\mu_2} \quad \hat{W}_{\mathbf{n},\mu} = 1 - 2\hat{c}_{\mathbf{n},\mu}^\dagger \hat{c}_{\mathbf{n},\mu}, \quad (5.2.7)$$

each one preserving local fermion parity by design. After this re-formatting, we have a final expression for the deformed Hubbard model, and it reads

$$\hat{H}_{\text{Hub}}'' = -t \sum_{\mathbf{n},k} \sum_{\alpha} \left[i\hat{Q}_{\mathbf{n},\mu_k,\alpha}^\dagger \hat{Q}_{\mathbf{n}+\mu_k,-\mu_k,\alpha} + \text{h.c.} \right] + U \sum_{\mathbf{n}} \left(\hat{n}_{\mathbf{n},\uparrow} - \frac{1}{2} \right) \left(\hat{n}_{\mathbf{n},\downarrow} - \frac{1}{2} \right), \quad (5.2.8)$$

plus a penalty

$$\hat{H}_{\text{pen}}'' = -\alpha_b \sum_{\mathbf{n},k} \left(\hat{W}_{\mathbf{n},\mu_k} \hat{W}_{\mathbf{n}+\mu_k,-\mu_k} - 1 \right) - \alpha_p \sum_{\square \in \Lambda} \begin{pmatrix} \hat{C}_r & \hat{C}_\uparrow \\ \hat{C}_l & \hat{C}_\downarrow \end{pmatrix} - 1, \quad (5.2.9)$$

where \hat{C} are the *corner* operators defined in Eq. (5.2.7) and form the plaquette interaction previously defined in Eq. (5.1.9) in terms of links. Using tensor networks, we simulate the model as it exactly appears in these expressions.

5.2.2 Numerical Results

In this section, we present the numerical results obtained using exact diagonalization (ED) and tree tensor networks (TTN) algorithms [1, 208]. Our numerical computations concern only open boundary conditions (OBC).

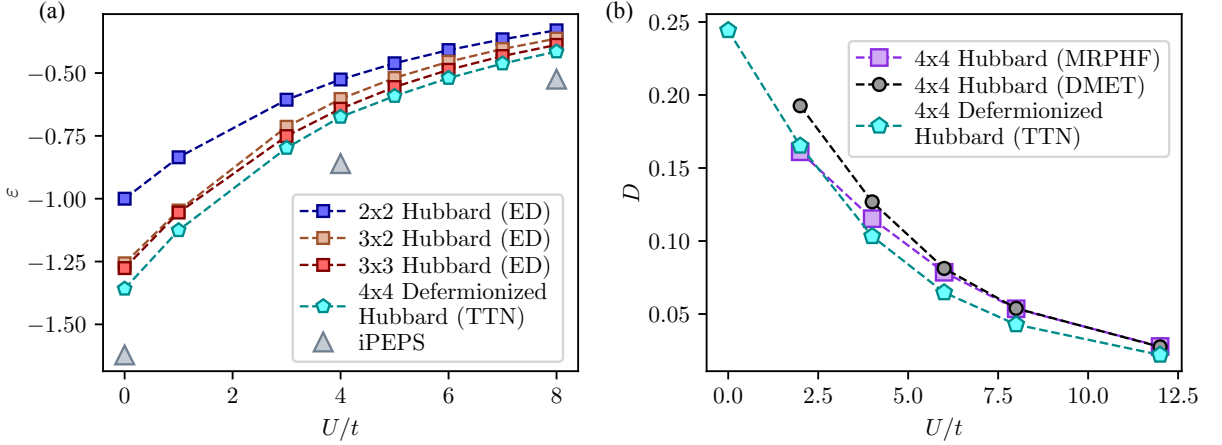


Figure 5.3: (a) Ground state energy density of the 2D Hubbard Hamiltonian at $\rho = 1$ for different lattice sizes. Results concerning 2×2 , 3×2 , and 3×3 lattices are obtained via exact diagonalization (ED) of the original Hubbard Hamiltonian in Eq. (5.2.1). Energies of the 4×4 lattice result from TTN simulations of the deferfionized Hamiltonian in Eqs. (5.2.8)-(5.2.9) with bond dimension $\chi = 350$ and energy penalties $\alpha_p = \alpha_b = 15$. (b) Double occupancy D as a function of U/t is computed with different numerical methods. Data for MRPHF and DMET are taken from [418].

To numerically check the validity of our mapping, we compare the original 2D Hubbard model of Eq. (5.2.1) and its deferfionized version described in Eqs. (5.2.8)-(5.2.9). For both Hamiltonians, we perform ED on a 2×2 lattice.

Since the two Hamiltonians do not fix a specific number of particles on the lattice, we add to them an extra term of the form $\hat{H}_N = \tilde{\mu}(\sum_{\mathbf{n}}(\hat{n}_{\mathbf{n},\uparrow} + \hat{n}_{\mathbf{n},\downarrow}) - N_0)^2$, where $\tilde{\mu}$ plays the role of a large penalty coefficient that increases the energy of all the states with a number of particles differing from N_0 . In this way, by tuning N_0 and setting $\alpha_p = \alpha_b = 20$ and $\tilde{\mu} = 20$, we perform ED at fixed values of the particle density $\rho = N_0/N$, comparing the ground-state energy densities of the two models as a function of the ratio U/t . The chosen values of the penalty coefficients are enough to satisfy both link and plaquette constraints with a precision larger than 10^{-7} .

As displayed in Fig. 5.2 for three values of the particle density, i.e. $\rho \in \{0.5, 1.0, 1.5\}$, the relative distance between the energy densities of the two models (ϵ_H for the original Hubbard model, $\epsilon_{def.H}$ for its deferfionized version) $\Delta\epsilon = |\epsilon_H - \epsilon_{def.H}|/|\epsilon_H| < 10^{-12}$ confirms the exactness of our mapping. As expected, the above half-filling particles are forced to form at least a single-site pair which determines a linear dependence of the energy with U/t .

Aware of the equivalence between the two Hamiltonians, we focus on the deferfionized model for larger lattice sizes by using TTN simulations. Our TTN algorithm for variational ground state search exploits the global $U(1)$ symmetry of the Hubbard model and the Krylov subspace expansion [49]. Thus, the additional term H_N is no longer needed, as the algorithm directly conserves the total number of particles by encoding the $U(1)$ symmetry sector in the TTN.

Given the deferfionized Hubbard Hamiltonian of Eqs. (5.2.8) and (5.2.9), the ground state at a specified bond dimension χ is determined by iteratively optimizing each of the tensors in TTN, gradually reducing the energy expectation value. This procedure is iterated several times to reach the desired convergence. For a detailed and exhaustive description of the algorithms, please see Sec. 2.4 and the technical reviews and textbooks [48, 49]. In our TTN simulations, we use a

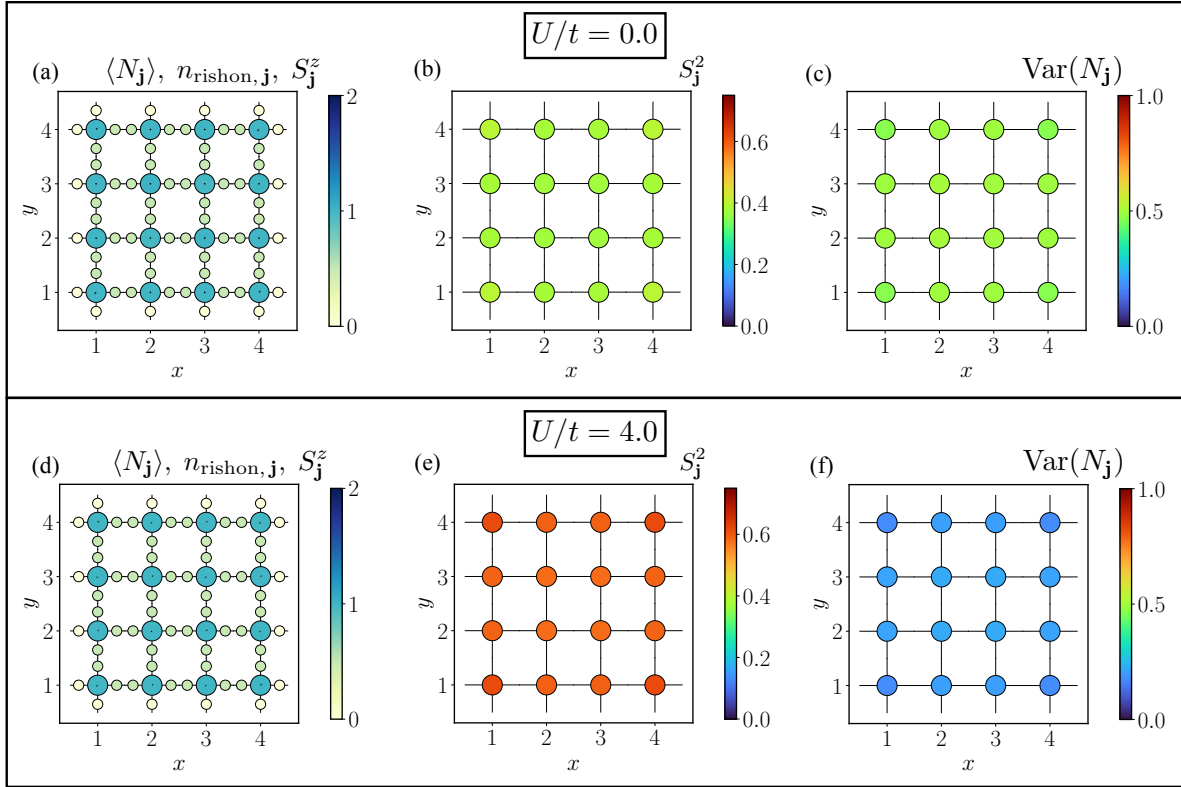


Figure 5.4: Ground state characterization for the deformed Hubbard model with $U/t = 0.0, 4.0$ numerically simulated via TTNs. Computed observables: (a),(d) local configurations of fermionic matter for each lattice site $\langle \hat{n}_{\mathbf{n}} \rangle$, local spin along the z -axis $\hat{S}_{\mathbf{n}}^z$ represented by arrows in the center of the lattice sites (values are close to zero), rishton modes occupation on the links $\hat{n}_{\text{rishton},\mathbf{n}}$; (b),(e) spin modulus squared $\hat{S}_{\mathbf{n}}^2$; (c),(f) variance of the matter occupation number $\text{Var}(\hat{n}_{\mathbf{n}})$.

maximum bond dimension $\chi = 350$, which is sufficient to reach a relative error on the energy density of the order 10^{-6} , ensuring the stability of our findings.

In Fig. 5.3(a), we show the TTN results concerning the deformed Hamiltonian on a 4×4 lattice at half-filling, i.e. $\rho = 1$. We also report the corresponding energy densities obtained via ED for the original Hubbard Hamiltonian at smaller lattice sizes, and the results of the extrapolation of the infinite-size limit obtained by using iPEPS methods [61]. The energies obtained with the TTN simulations for the deformed Hamiltonian are in agreement with the overall scaling shown by the exact energies as a function of U/t and the lattice sizes.

To further test the equivalence between the original Hubbard model and its deformed version, we compute the ground-state pair density $D \equiv \sum_{\mathbf{n}} \langle \hat{n}_{\mathbf{n},\uparrow} \hat{n}_{\mathbf{n},\downarrow} \rangle / N$. In Fig. 5.3(b), we show the results obtained from the TTN simulations of the deformed model on the 4×4 lattice. For the sake of comparison, we report the data of the original Hubbard Hamiltonian, obtained in Ref. [418] by using two independent numerical methods, i.e. the multireference projected Hartree-Fock method (MRPHF) and the Density matrix embedding theory (DMET). A good agreement and consistency of our results with the reference data is visible for all the simulated values of U/t .

TTN simulations allow for an extra characterization of the ground state in terms of local observables, such as the occupation of fermionic matter and its variance

$$\langle \hat{n}_{\mathbf{n}} \rangle = \langle \hat{n}_{\mathbf{n},\uparrow} + \hat{n}_{\mathbf{n},\downarrow} \rangle \quad \text{Var}(\hat{n}_{\mathbf{n}}) = \langle (\hat{n}_{\mathbf{n}})^2 \rangle - \langle \hat{n}_{\mathbf{n}} \rangle^2, \quad (5.2.10)$$

the local spin along the z -axis and its square modulus,

$$\hat{S}_{\mathbf{n}}^z = \frac{1}{2} \langle \hat{n}_{\mathbf{n},\uparrow} - \hat{n}_{\mathbf{n},\downarrow} \rangle \quad \hat{S}_{\mathbf{n}}^2 = \frac{3}{4} \langle (\hat{n}_{\mathbf{n},\uparrow} - \hat{n}_{\mathbf{n},\downarrow})^2 \rangle, \quad (5.2.11)$$

but also the rishon mode occupation on lattice links $\hat{n}_{\text{rishon},\mathbf{n}} = \langle c_{\mathbf{n},\mu}^\dagger \hat{c}_{\mathbf{n},\mu} \rangle$.

In Fig. 5.4, we show the results for $U/t = 0$ and $U/t = 4$. In both cases (see Fig. 5.4(a) and Fig. 5.4(d)), the fermionic occupation number $\hat{n}_{\mathbf{n}} \sim 1$, while the local spin along z , represented by arrows in the center of the lattice sites, is close to zero; correspondingly, all the rishon modes occupations on the links are $\hat{n}_{\text{rishon},\mathbf{n}} \sim 0.5$, as a consequence of the satisfied link and plaquette penalty constraints that encode the fermion parity. By looking at Figs. 5.4(b) and 5.4(e), we observe that the squared spin modulus $\hat{S}_{\mathbf{n}}^2$ increases for all lattice sites by varying U/t from 0.0 to 4.0, whereas the variance of the fermionic occupation number $\text{Var}(\hat{n}_{\mathbf{n}})$ decreases, as shown in Figs. 5.4(c) and 5.4(f).

These configurations agree with the expected ground state of the original Hubbard model, which in the half-filling case, maps to the Heisenberg model [369], and its ground state mimics an antiferromagnetically long-range ordered state.

5.3 Digital quantum simulation

The gauge *deformation* offers a natural encoding of fermionic degrees of freedom to qubits, thus allowing for the digital quantum simulation of fermionic models on quantum computers. Here, we break down the procedure to express the spin- $\frac{1}{2}$ Hubbard deformed model on a square lattice in terms of qubits and Pauli operators on a generic platform, see Sec. 5.3.1, Sec. 5.3.3, and Sec. 5.3.2. This gauge-field-based encoding is genuinely local, \hat{I} est the lattice support of each Hamiltonian term is not increased in the encoding, and thus each Pauli weight W is conserved and does not depend on the system size N . However, locality comes at the cost of including auxiliary qubits representing the deformed modes, i.e. fermionic modes and \mathbb{Z}_2

	Qubit-fermion ratio	Fermion parity weight	Hopping weight	Stabilizers weight
Our	3	1	6	6
[123]	1	1	$O(L)$	-
[124]	1	$O(\log_2 L^2)$	$O(\log_2 L^2)$	-
[125]	1	$O(\log_3(L+1))$	$O(\log_3(L+1))$	-
[115] *	3	1	5-7	5-6
[400]	2	4	2-6	6
[402]	1.25	1-2	2-6	12

Table 5.1: Comparison of different encoding mapping a single species of fermions to qubits for a 2D square lattice of size $L \times L$: Jordan-Wigner [123] Bravyi-Kitaev [124] Optimal fermion-to-qubit mapping [125] Zohar-Cirac [115] Exact bosonization [400] Supercompact fermion-to-qubit mapping [402]. The mapping with * is specifically developed for LGTs, similarly to [403].

gauge fields. There currently exists a few local mappings [124, 125, 157, 400, 420–423] and the relation between them is analyzed in [402]. Fermion-to-qubit mappings need resources that are usually quantified in terms of the number of qubits to simulate one fermion on average (qubit-fermion ratio), the number of qubits to express the parity of a fermionic state (parity weight), the length of the hopping operators expressed as Pauli strings, and, ultimately, the maximum length of Pauli strings for the stabilizers. The resources required by the gauge-field-based encoding are comparable with state-of-the-art methods: values for qubit-fermion ratio, fermion parity weight, hopping weight, and stabilizer weight are (3, 1, 6, 6) respectively. Building on Table 1 of [402], we present a comparison of different fermionic encodings in Tab. 5.1.

Within these prescriptions, we test our construction in out-of-equilibrium scenarios that will be relevant to investigate nontrivial dynamical effects. In particular, the Hubbard model offers the opportunity to explore the dynamics of spin-like and charge-like excitations, which in one dimension manifest as distinct degrees of freedom with independent propagation velocities [370, 424], and have been recently observed in cold gases experiments [381, 406] and digital quantum simulations [117]. In two dimensions, the dynamics of spin and charge degrees of freedom is highly nontrivial [425] as strongly-correlated effects become relevant, still a subject of ongoing theoretical and experimental analysis with quantum simulation platforms [407, 408].

For these reasons, we simulate the digital dynamics of spin and charge excitations over a half-filled ($\rho = 1$) 2×4 system in the antiferromagnetic phase with $U/t = 10$. In Sec. 5.3.4, we lay out the protocols to adiabatically prepare the antiferromagnetic ground state, and then inject the excitations. Finally, in Sec. 5.3.5, we observe the corresponding out-of-equilibrium dynamics for spin and charge excitations. While protocols are designed for a general digital quantum computer, the presented results are obtained from tensor networks CITE to emulate the evolution of the quantum circuit.

5.3.1 Fermion to qubits mapping of the defermionized Hubbard Hamiltonian

We introduce a qubit for each flavor (up u and down d) and one for each rishon (north N , west w , east e , south s). To minimize the Pauli weight of the Hamiltonian terms, a specific ordering for the qubits composing each dressed site is defined:

$$\begin{cases} \{u, d, w, s, e, n\} & \text{if } (-1)^{n_x+n_y} = +1 \text{ (even site)} \\ \{d, u, s, w, n, e\} & \text{if } (-1)^{n_x+n_y} = -1 \text{ (odd site)}. \end{cases} \quad (5.3.1)$$

All the operators in Eq. (5.2.8) and penalties in Eq. (5.2.9) are first mapped to Majorana fermions and then to spin- $\frac{1}{2}$ algebra, while preserving all the commutation relations. We recall that a hopping operator from an odd (O) and an even (E) site for the up species can be written as:

$$\hat{\psi}_{\uparrow E}^\dagger \hat{\gamma}_{eE} \hat{\gamma}_{wO} \hat{\psi}_{\uparrow O} - \hat{\psi}_{\uparrow E} \hat{\gamma}_{eE} \hat{\gamma}_{wO} \hat{\psi}_{\uparrow O}^\dagger = \hat{\gamma}_{eE} \hat{\gamma}_{wO} \left(\hat{\psi}_{\uparrow E}^\dagger \hat{\psi}_{\uparrow O} - \hat{\psi}_{\uparrow E} \hat{\psi}_{\uparrow O}^\dagger \right). \quad (5.3.2)$$

Then, by defining the Majorana degrees of freedom $d_{x_{\uparrow E}, \uparrow O}, d_{y_{\uparrow E}, \uparrow O}$ as:

$$\hat{d}_{x_{\uparrow E}, \uparrow O} = \hat{\psi}_{\uparrow E, \uparrow O} + \hat{\psi}_{\uparrow E, \uparrow O}^\dagger \quad \hat{d}_{y_{\uparrow E}, \uparrow O} = i \left(\hat{\psi}_{\uparrow E, \uparrow O} - \hat{\psi}_{\uparrow E, \uparrow O}^\dagger \right), \quad (5.3.3)$$

we can trivially prove that

$$\hat{d}_{x_{\uparrow E}} \hat{d}_{y_{\uparrow O}} - \hat{d}_{y_{\uparrow E}} \hat{d}_{x_{\uparrow O}} = 2i \left(\hat{\psi}_{\uparrow E}^\dagger \hat{\psi}_{\uparrow O} - \hat{\psi}_{\uparrow E} \hat{\psi}_{\uparrow O}^\dagger \right). \quad (5.3.4)$$

We can thus express the hopping in terms of the Majorana fermions. Following the order defined in Eq. (5.3.1), the operators acting on an even site \mathbf{n} can be written as:

$$\hat{d}_{x_{\mathbf{n}, \uparrow}} = \hat{X} \hat{Z} \hat{Z} \hat{Z} \hat{Z} \hat{Z} \quad \hat{d}_{x_{\mathbf{n}, \downarrow}} = \hat{I} \hat{X} \hat{Z} \hat{Z} \hat{Z} \hat{Z} \quad \hat{d}_{y_{\mathbf{n}, \uparrow}} = \hat{Y} \hat{Z} \hat{Z} \hat{Z} \hat{Z} \hat{Z} \quad \hat{d}_{y_{\mathbf{n}, \downarrow}} = \hat{I} \hat{Y} \hat{Z} \hat{Z} \hat{Z} \hat{Z} \quad (5.3.5)$$

$$\hat{\gamma}_{\mathbf{n}, r} = \hat{I}_u \hat{I}_d \bigotimes_{k=w}^{r-1} \hat{I}_k \otimes \hat{X}_r \bigotimes_{k=r+1}^n \hat{Z}_k, \quad (5.3.6)$$

where $\hat{X}, \hat{Y}, \hat{Z}$ are Pauli matrices, while \hat{I} is the identity operator. In the two equations above we dropped the index of species and rishons for clarity. The string of \hat{Z} operators applies to all the qubits forming a site. The index r runs over the different rishon species of a site, as defined in Eq. (5.3.1). The mapping for an odd sites can be obtained analogously using Eq. (5.3.1), and is equivalent to swapping the first two operators and using the odd-ordered sites.

Now, we compute the explicit form of the Hamiltonian terms, hopping and on-site interaction, in terms of Pauli operators. Following the notation defined in Eq. (5.3.1), the horizontal hopping operator from an odd to an even site for flavor up reads:

	u	d	w	s	e	n	d	u	s	w	n	e
$\hat{d}_{x_{\uparrow E}}$	\hat{X}	\hat{Z}	\hat{Z}	\hat{Z}	\hat{Z}	\hat{Z}	\hat{I}	\hat{I}	\hat{I}	\hat{I}	\hat{I}	\hat{I}
$\hat{\gamma}_{eE}$	\hat{I}	\hat{I}	\hat{I}	\hat{I}	\hat{X}	\hat{Z}	\hat{I}	\hat{I}	\hat{I}	\hat{I}	\hat{I}	\hat{I}
$\hat{\gamma}_{wO}$	\hat{I}	\hat{I}	\hat{I}	\hat{I}	\hat{I}	\hat{I}	\hat{I}	\hat{I}	\hat{I}	\hat{X}	\hat{Z}	\hat{Z}
$\hat{d}_{y_{\uparrow O}}$	\hat{I}	\hat{I}	\hat{I}	\hat{I}	\hat{I}	\hat{I}	\hat{I}	\hat{Y}	\hat{Z}	\hat{Z}	\hat{Z}	\hat{Z}
hopping	\hat{X}	\hat{Z}	\hat{Z}	\hat{Z}	$i\hat{Y}$	\hat{I}	\hat{I}	\hat{Y}	\hat{Z}	$-i\hat{Y}$	\hat{I}	\hat{I}

(5.3.7)

Matrix multiplication goes from bottom to top. By computing also the hermitian conjugate, the hopping term results:

$$\hat{d}_{x_{\uparrow E}} \hat{\gamma}_{eE} \hat{\gamma}_{wO} \hat{d}_{y_{\uparrow O}} - \hat{d}_{y_{\uparrow E}} \hat{\gamma}_{eE} \hat{\gamma}_{wO} \hat{d}_{x_{\uparrow O}} = \left(\hat{X} \hat{Z} \hat{Z} \hat{Z} \hat{Y} \hat{I} \hat{I} \hat{Y} \hat{Z} \hat{Y} \hat{I} \hat{I} - \hat{Y} \hat{Z} \hat{Z} \hat{Z} \hat{Y} \hat{I} \hat{I} \hat{X} \hat{Z} \hat{Y} \hat{I} \hat{I} \right). \quad (5.3.8)$$

Terms for vertical hopping or hoppings involving different species can be derived analogously.

Similarly, we derive the on-site interaction term. The number operator acting on site \mathbf{n} can be written as $\hat{n}_{\mathbf{n}, \alpha} = \frac{1}{2}(1 - \hat{Z}_{\mathbf{n}, \alpha})$, then the on-site interaction reads:

$$\left(\hat{n}_{\mathbf{n}, \uparrow} - \frac{1}{2} \right) \left(\hat{n}_{\mathbf{n}, \downarrow} - \frac{1}{2} \right) = \frac{1}{4} \hat{Z}_{\mathbf{n}, \uparrow} \hat{Z}_{\mathbf{n}, \downarrow}. \quad (5.3.9)$$

Once we obtain the Hamiltonian terms described as Pauli strings, we decompose the relative time propagator in single and two-qubit gates following Ref. [420].

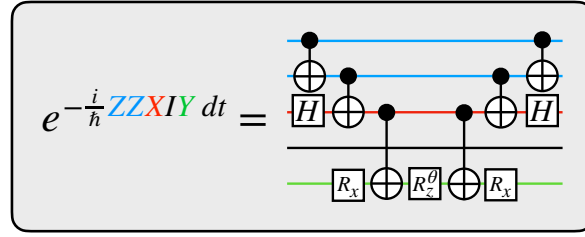


Figure 5.5: Mapping of the time propagator of a generic Pauli string to a quantum circuit using only single and two-qubit gates.

Mapping the time propagator to a quantum circuit

To simulate the dynamics of our system on a quantum computer it is important to map the evolution operator to a quantum circuit using single and two-qubit gates since those are the available operations. First, we Trotterize the evolution treating each Hamiltonian term separately. Then, it has been shown that the propagator $e^{-\frac{i}{\hbar}J\hat{H}_i dt}$ of a $\hat{H}_i = \hat{Z}\hat{Z}\dots\hat{Z}$ interaction with strength J can be compiled by combining a cascade of CNOTs gates and a rotation along the z axis [420]:

$$\hat{R}_z^\theta = \begin{pmatrix} 1 & 0 \\ 0 & e^{i\theta} \end{pmatrix}, \quad \theta = Jdt. \quad (5.3.10)$$

In general, we can treat an arbitrary Pauli string by moving to the Z basis along the CNOTs cascade. Practically, we apply the following single-qubit basis change gate before and after the CNOT, respectively for the \hat{X} and \hat{Y} Pauli matrices:

$$\hat{H} = \frac{1}{\sqrt{2}} \begin{pmatrix} 1 & 1 \\ 1 & -1 \end{pmatrix}, \quad \hat{R}_x\left(-\frac{\pi}{2}\right) = \frac{1}{\sqrt{2}} \begin{pmatrix} 1 & \hat{I} \\ \hat{I} & 1 \end{pmatrix}. \quad (5.3.11)$$

In Fig. 5.5, we report the form of the CNOTs cascade with the basis change, showing an example for a general Pauli string.

5.3.2 Vertex and plaquette constraints

Following the prescription of the gauge fermionization, we have to constrain the state to a specific subspace of the Hilbert space, a condition set by Eqs. (5.1.16a) and (5.1.16b). Each symmetry can be cast into a language that directly translates into a quantum circuit scenario and is equivalent to a stabilizer of a quantum error correcting code; to respect the gauge symmetry, the state is restrained to the $+1$ eigenstate of the stabilizers [426]. The Pauli representation of the stabilizers can be obtained following the mapping presented in Eq. (5.3.5). As expected, all the stabilizers commute with the Hamiltonian.

The vertex stabilizer term reads from Eq. (5.1.16a). As the exponentials are counting the parity of a given species/rishon, these operators correspond to \hat{Z} operators in the qubit language. Thus, the stabilizer acting on each lattice vertex \mathbf{n} results in

$$\hat{S}_{\mathbf{n}} = \bigotimes_{\alpha=u,d} \hat{Z}_\alpha \bigotimes_k \hat{Z}_{\mathbf{n}+\boldsymbol{\mu}_k}, \quad (5.3.12)$$

where $\boldsymbol{\mu}_k$ spans on all rishons connected to the vertex \mathbf{n} .

The plaquette stabilizer reads from Eq. (5.1.16b). As the product always runs on four terms, the imaginary unit i drops. Following the representation of the $\hat{\gamma}$ operators reported in Eq. (5.3.6),

	u	d	w	s	e	n	d	u	s	w	n	e	d	u	s	w	n	e	u	d	w	s	e	n
$\hat{\gamma}_{00e}$	\hat{I}	\hat{I}	\hat{I}	\hat{I}	\hat{X}	\hat{Z}	\hat{I}	\hat{I}	\hat{I}	\hat{I}	\hat{I}	\hat{I}	\hat{I}	\hat{I}	\hat{I}	\hat{I}	\hat{I}	\hat{I}	\hat{I}	\hat{I}	\hat{I}	\hat{I}	\hat{I}	\hat{I}
$\hat{\gamma}_{00n}$	\hat{I}	\hat{I}	\hat{I}	\hat{I}	\hat{I}	\hat{X}	\hat{I}	\hat{I}	\hat{I}	\hat{I}	\hat{I}	\hat{I}	\hat{I}	\hat{I}	\hat{I}	\hat{I}	\hat{I}	\hat{I}	\hat{I}	\hat{I}	\hat{I}	\hat{I}	\hat{I}	\hat{I}
$\hat{\gamma}_{01s}$	\hat{I}	\hat{I}	\hat{I}	\hat{I}	\hat{I}	\hat{I}	\hat{I}	\hat{I}	\hat{X}	\hat{Z}	\hat{Z}	\hat{Z}	\hat{I}	\hat{I}	\hat{I}	\hat{I}	\hat{I}	\hat{I}	\hat{I}	\hat{I}	\hat{I}	\hat{I}	\hat{I}	\hat{I}
$\hat{\gamma}_{01e}$	\hat{I}	\hat{I}	\hat{I}	\hat{I}	\hat{I}	\hat{I}	\hat{I}	\hat{I}	\hat{I}	\hat{I}	\hat{I}	\hat{X}	\hat{I}	\hat{I}	\hat{I}	\hat{I}	\hat{I}	\hat{I}	\hat{I}	\hat{I}	\hat{I}	\hat{I}	\hat{I}	$\mathbb{1}$
$\hat{\gamma}_{10w}$	\hat{I}	\hat{I}	\hat{I}	\hat{I}	\hat{I}	\hat{I}	\hat{I}	\hat{I}	\hat{I}	\hat{I}	\hat{I}	\hat{I}	\hat{I}	\hat{I}	\hat{I}	\hat{X}	\hat{Z}	\hat{Z}	\hat{I}	\hat{I}	\hat{I}	\hat{I}	\hat{I}	\hat{I}
$\hat{\gamma}_{10n}$	\hat{I}	\hat{I}	\hat{I}	\hat{I}	\hat{I}	\hat{I}	\hat{I}	\hat{I}	\hat{I}	\hat{I}	\hat{I}	\hat{I}	\hat{I}	\hat{I}	\hat{I}	\hat{I}	\hat{X}	\hat{Z}	\hat{I}	\hat{I}	\hat{I}	\hat{I}	\hat{I}	\hat{I}
$\hat{\gamma}_{11w}$	\hat{I}	\hat{I}	\hat{I}	\hat{I}	\hat{I}	\hat{I}	\hat{I}	\hat{I}	\hat{I}	\hat{I}	\hat{I}	\hat{I}	\hat{I}	\hat{I}	\hat{I}	\hat{I}	\hat{I}	\hat{I}	\hat{I}	\hat{I}	\hat{X}	\hat{Z}	\hat{Z}	\hat{Z}
$\hat{\gamma}_{11s}$	\hat{I}	\hat{I}	\hat{I}	\hat{I}	\hat{I}	\hat{I}	\hat{I}	\hat{I}	\hat{I}	\hat{I}	\hat{I}	\hat{I}	\hat{I}	\hat{I}	\hat{I}	\hat{I}	\hat{I}	\hat{I}	\hat{I}	\hat{I}	\hat{I}	\hat{X}	\hat{Z}	\hat{Z}
stabilizer	\hat{I}	\hat{I}	\hat{I}	\hat{I}	\hat{X}	$i\hat{Y}$	\hat{I}	\hat{I}	\hat{X}	\hat{Z}	\hat{Z}	$i\hat{Y}$	\hat{I}	\hat{I}	\hat{I}	\hat{X}	$i\hat{Y}$	\hat{I}	\hat{I}	\hat{I}	\hat{X}	$i\hat{Y}$	\hat{I}	\hat{I}

Table 5.2: Explicit definition of the stabilizer for an even plaquette. This calculation does not take into account the link symmetry: thus it is necessary to do that further computation to obtain the final expression of the qubit mapping.

the final form of each plaquette term respects the qubits ordering of the dressed site. Thus, the form of an even plaquette stabilizer is different from an odd one, where a plaquette is said even (odd) if the lower-left corner of the plaquette lies on an even (odd) site. We report the explicit computation for an even plaquette in Tab. 5.2.

Finally, we report the size of the Hilbert space to perform a digital quantum simulation of the deformationized Hubbard model over a $x \times y$ grid, and compare it to the size of the accessible subspace:

$$\dim(\mathcal{H}) = 2^{2xy+x(y-1)+y(x-1)} = 2^{4xy-x-y} \quad (5.3.13a)$$

$$\dim(\mathcal{H}_{\text{eff}}) = 2^{2xy+x(y-1)+y(x-1)-(x-1)(y-1)-xy} = 2^{2xy-1}. \quad (5.3.13b)$$

We notice that constraining the system to the physical subspace quadratically decreases the dimension of the Hilbert space, showing that we are working with a highly redundant space.

5.3.3 Link constraint

The state of the two rishons sharing the same link is also subject to a constraint set by the third line of Eq. (5.1.16c). The only qubits states fulfilling this constraint are $|00\rangle$ and $|11\rangle$. The effective Hilbert space for a pair of rishons is 2-dimensional; for this reason, both rishons can be described with a single qubit, by mapping $|00\rangle \rightarrow |0\rangle$, $|11\rangle \rightarrow |1\rangle$. After this procedure, we need to project all the operators acting on the two rishons on the new subspace. Given an operator $A_{r_1 r_2}$ we can write the new operator living on the two-dimensional space as:

$$A_{\bar{r}} = \text{Tr}_{|01\rangle, |10\rangle} A_{r_1 r_2}, \quad (5.3.14)$$

where we trace out the states violating the constraint. We report the new form of some operators of interest as an example: $\hat{Z}\hat{Z} \rightarrow \hat{I}$, $\hat{X}\hat{X} \rightarrow \hat{X}$. This way, each dressed site shares a rishon with its nearest neighbors, and thus there is no longer a clear separation between the dressed sites. In Fig. 5.6, we report the final form of the stabilizers and the Hamiltonian terms, once the link constraint is applied.

5.3.4 Preparation of spin and charge excitations

Here, we lay out the protocols to adiabatically prepare the antiferromagnetic ground state, and to inject spin- and charge-excitations.

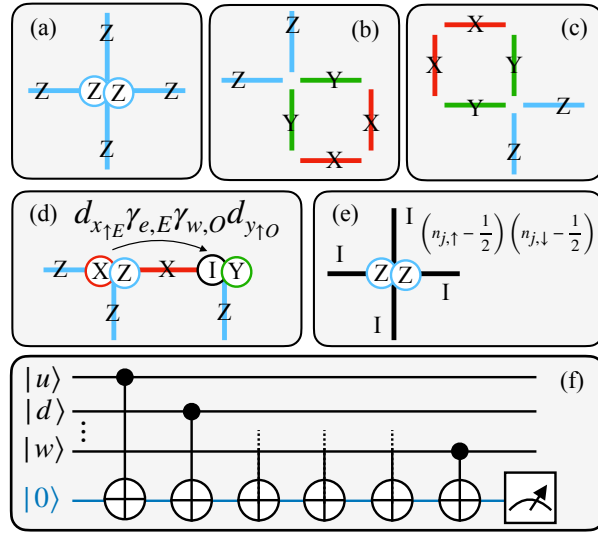


Figure 5.6: Graphical representation of the Hamiltonian terms in the deformed Hubbard model and of the stabilizers for installing the gauge symmetries. These terms result from applying Eq. (5.3.14), where the states of the two rishons satisfying the link constraint are mapped to a single qubit for each link. In (a), we depict the vertex stabilizer, while (b) corresponds to the even plaquette stabilizer, and (c) represents the odd plaquette stabilizer. Figures (d) and (e) illustrate the hopping term and the onsite interaction respectively. As dictated by Eq. (5.3.1), in (d), the u qubit is the first on the even site and the second on the odd site. In (f) we report the quantum circuit used to measure the stabilizer in figure (a) using CNOT gates and a projective measurement on an ancilla qubit (depicted in blue). The qubits $|n\rangle, |e\rangle, |s\rangle$ are not reported in the figure, even if their CNOT gate is present with a dashed line.

Adiabatic ground state preparation

The adiabatic state preparation targets the ground state of the deformed Hubbard model over a 4×2 lattice, at half-filling ($\rho = 1$) with $t = 0.1$ and $U = 1$. The adiabatic evolution starts from the ground state of Eq. (5.2.8) with $t = 0$, here renamed $\hat{H}_0 = \hat{H}_{\text{Hub}}''(t = 0)$; the hopping terms are slowly switched on to reach $\hat{H}_1 = \hat{H}_{\text{Hub}}''$. Then, the time-dependent Hamiltonian reads:

$$\hat{H} = (1 - \beta)\hat{H}_0 + \beta\hat{H}_1, \quad (5.3.15)$$

where $\beta \in [0, 1]$ is the adiabatic parameter that increases linearly for 100 steps; for each β , the system evolves for ten time-steps $d\tau$ to ensure a smooth convergence, for a total of 1000 evolution steps. The real-time evolution is simulated by decomposing the evolution operator via a first-order Trotterization with time step $dt = d\tau = 0.01$.

Since the initial state of \hat{H}_0 is hugely degenerate, we select as initial state for the adiabatic process is the ground state of \hat{H}_0 at half-filling ($\rho = 1$) and respects the spin-flip symmetry. While neglecting the rishons' state, we consider only the state of the matter qubits (u and d) for each dressed site over the 4×2 lattice, where $|10\rangle = |\uparrow\rangle$ and $|01\rangle = |\downarrow\rangle$. It results in

$$\frac{1}{\sqrt{2}} \left(\left| \begin{array}{cccc} \uparrow & \downarrow & \uparrow & \downarrow \\ \downarrow & \uparrow & \downarrow & \uparrow \end{array} \right\rangle + \left| \begin{array}{cccc} \downarrow & \uparrow & \downarrow & \uparrow \\ \uparrow & \downarrow & \uparrow & \downarrow \end{array} \right\rangle \right). \quad (5.3.16)$$

Notice that the state in Eq. (5.3.16) is a GHZ state, thus it can be easily prepared using only Hadamard, NOT, and controlled-NOT gates. Finally, the rishons' state is uniquely determined

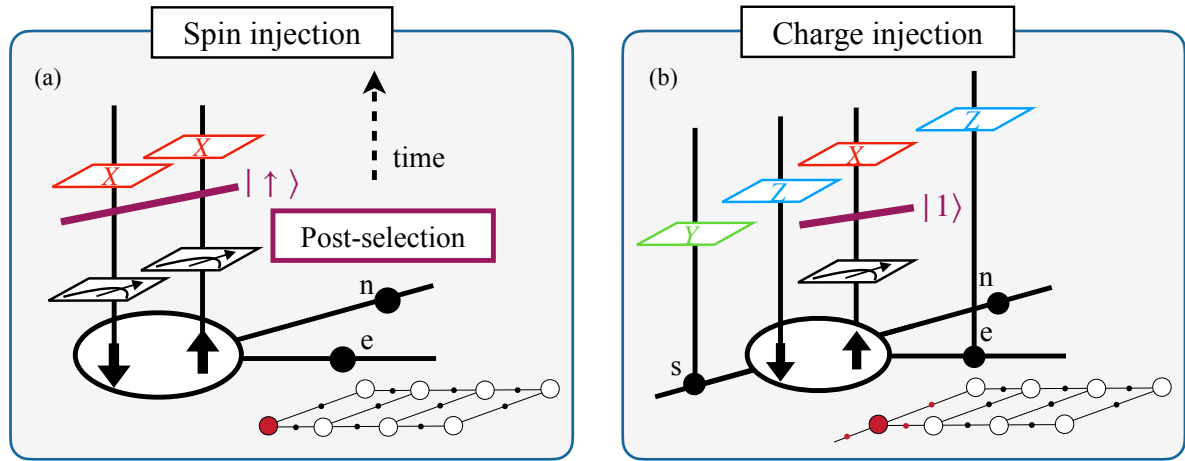


Figure 5.7: Schematic of injecting spin- and charge-excitations on the $(0,0)$ corner. Both figures depict the qubit lattice, highlighting up and down qubits within the matter site. Rishons are represented as black dots and labeled with respect to the corner. In the bottom right of each subfigure, we report the entire lattice, highlighting in red the site and rishons involved in the operation. All applied operations commute with the stabilizers. (a) *Spin excitation*: To inject the spin excitation, we initially measure the qubit states for up and down, post-selecting only the $|01\rangle = |\uparrow\rangle$ state. Then, the $\hat{X}\hat{X}$ operator flips the spin state. (b) *Charge excitation*: Injecting the charge excitation involves measuring the up qubit and post-selecting the state $|1\rangle$. We then apply the Pauli operators as depicted in the figure, equivalent to causing the matter qubit u to jump outside the lattice. To achieve this, an additional rishon (the s rishon in this case) must be added.

once the stabilizers are measured, after which we apply a conditional operation to ensure the state lies in the correct symmetry sector. For a depiction of the stabilizers see Fig. 5.6, while, for an example of the measurement of the stabilizer depicted in Fig. 5.6(a), see Fig. 5.6(f). This measurement is performed through a projective measurement of an ancilla qubit.

At the end of the adiabatic evolution, we checked that local spin projection $\hat{S}_{\mathbf{n}}^z$ and local charge $\hat{n}_{\mathbf{n}}$ are stationary up to oscillations compatible with the cut of the singular values in the TN emulator (10^{-8}). For a discussion about convergence see [3].

While an adiabatic state preparation is performed in this case, we do not think this approach to be scalable on real quantum devices. However, there are multiple possibilities for preparing the initial state with shallower circuits. If a TN state can efficiently represent the target state, we can variationally map the state to a quantum circuit [427]. Another possibility is to implement a Quantum Approximate Optimization Algorithm (QAOA), which can encode the Hamiltonian interactions in the quantum circuit structure [428]. Both approaches have the advantage of being able to tune the fidelity of the algorithm with the depth of the quantum circuit.

Excitations

Spin- and charge-excitations are injected in the ground state of H_1 using local operations and classical communication (LOCC)s: this procedure is, in principle, completely reproducible on state-of-the-art quantum computers. Both protocols preserve the symmetries of the system, namely every constraint previously defined is satisfied. In Fig. 5.7, we provide a graphical representation of the two methods.

Spin excitation Without losing any generality, the spin excitation is created on the site $(0, 0)$. Recalling that qubits u, d represent up and down flavors, we choose a general superposition of the two states; after a projective measurement on both qubits, only the flavor up is post-selected, i.e. the qubits state $|10\rangle = |\uparrow\rangle$. Then, a spin excitation is introduced by flipping the spin state:

$$|\uparrow\rangle \longrightarrow |\downarrow\rangle, \quad |1_u 0_d\rangle \xrightarrow{\hat{X}\hat{X}} |0_u 1_d\rangle. \quad (5.3.17)$$

This operation corresponds to applying the operator $\hat{X}\hat{X}$ on the qubits u, d . Notice that $\hat{X}\hat{X}$ commutes with all the stabilizers, since it shares support only with the vertex stabilizer in $(0, 0)$, and they commute.

Charge excitation In principle, the charge excitation can be created anywhere on the lattice. However, for improved efficiency, we restrict the protocol to the sites along the border and in particular to the site $(0, 0)$. A projective measurement is performed on the u qubit, then post-selecting the state $|1\rangle$. Being left with a single charge on the site, the excitation is obtained by removing that very charge. However, this operation does not commute with the vertex stabilizer in $(0, 0)$, thus breaking that constraint. To preserve Gauss' law we introduce an additional qubit, labeled as an extra rishon of site $(0, 0)$, in this case, s (or w). The excitation is implemented by flipping the state of the qubits u, s :

$$|1_u 0_s\rangle \xrightarrow{\hat{X}\hat{X}} |0_u 1_s\rangle. \quad (5.3.18)$$

This procedure, however, does not commute with the stabilizers, and it would bring the state outside the subspace of the physical states. To avoid this issue, we implement this operation by applying the hopping operator $i\hat{\gamma}_{\mathbf{n},s}\hat{\psi}_{\mathbf{n},\uparrow}$ with $\mathbf{n} = (0, 0)$, which makes the particle in u hop through s outside the lattice. The operator reads $g_{charge} = \hat{X}_u \hat{Z}_d \hat{Z}_w \hat{Y}_s$, and it is equivalent to the bit-flip just discussed. We stress that qubit d is not projected during this protocol.

5.3.5 Propagation of spin and charge excitations

By employing the local encoding, we simulate the dynamics of spin and charge excitations over a half-filled ($\rho = 1$) 2×4 system in the antiferromagnetic phase $U/t = 10$. To this aim, we use quantum matcha TEA [429], an emulator of quantum circuits based on MPS. All the simulations converge with bond dimension $\chi = 1024$ - below the maximum achievable for 27 qubits, where the maximum bond dimension is bound by $\chi_{\max} = 8192$ - and Trotter step $dt = 0.01$. In this regime with $U \gg t$, the Hubbard model dynamics is effectively described by the $t-J$ model [368], where high-energy doublon states are perturbatively removed and lead to an antiferromagnetic spin-exchange coupling $J = 2t^2/U$ of the Heisenberg type. In this regime, we therefore expect to observe slower spin dynamics governed by the J coupling and faster hole dynamics governed by t .

The first column of Fig. 5.8 shows the evolution of the spin excitation. By measuring the local spin along the z direction $\hat{S}_{\mathbf{n}}^z(\tau)$, one can monitor in time the deviations from the initial condition, i.e. the excitation injection:

$$\hat{S}_{\mathbf{n}}^z(\tau) = \frac{1}{2}(\langle \hat{n}_{\mathbf{n},\uparrow} \rangle(\tau) - \langle \hat{n}_{\mathbf{n},\downarrow} \rangle(\tau)). \quad (5.3.19)$$

This assessment requires only the expectation values of local observables, since

$$\langle \hat{n}_{\mathbf{n},\uparrow(\downarrow)} \rangle = \frac{1 - \langle \hat{Z}_{\mathbf{n},u(d)} \rangle}{2}, \quad \text{where} \quad \langle \hat{Z}_{\mathbf{n},u(d)} \rangle \quad (5.3.20)$$

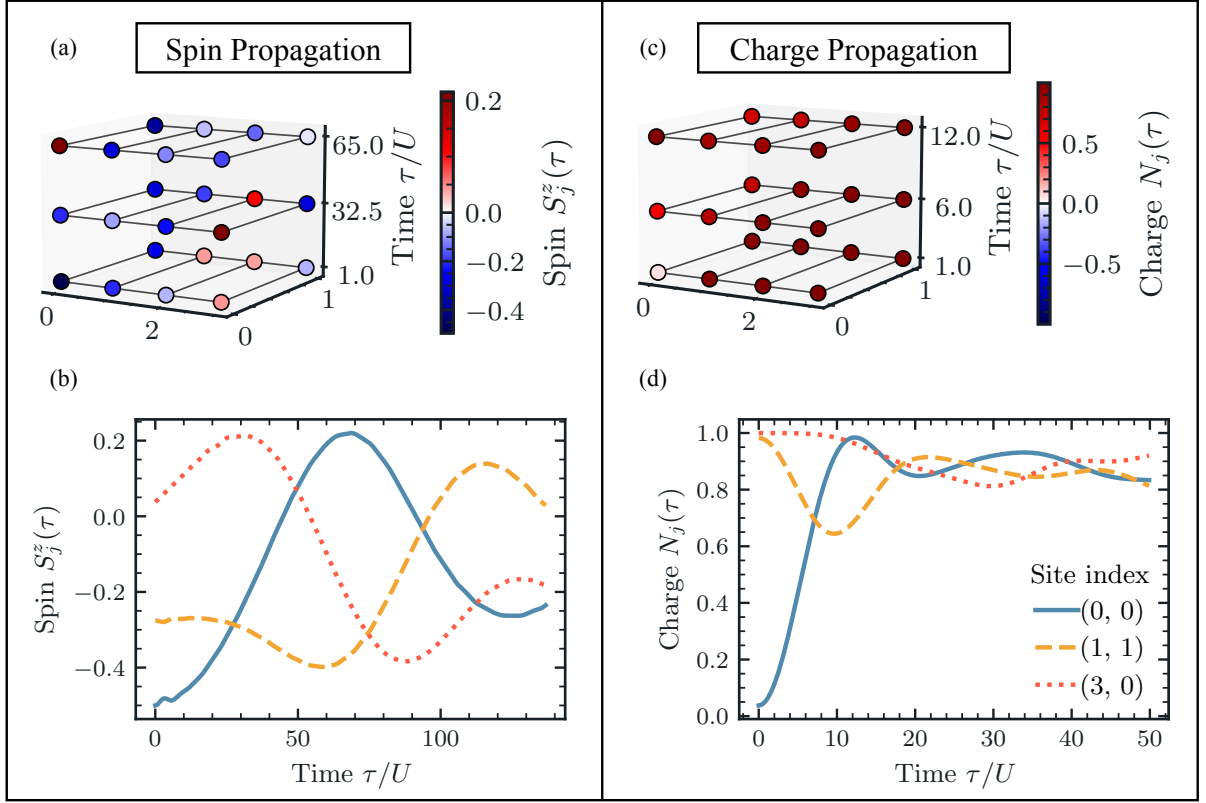


Figure 5.8: Digital quantum simulation of spin-charge dynamics in the $t - J$ model limit: (a) Propagation of the spin S_j^z profile on each site at different times in the evolution $\tau/U = 1, 32.5, 65$. (b) Spin profile for selected sites on the lattice. (c) Propagation of the charge N_j profile on each site at different times in the evolution $\tau/U = 1, 6, 12$. (d) Charge profile for selected sites on the lattice. Notice that different timescales for spin and charge dynamics occur as $t \gg J$.

is the expectation value of the $u(d)$ qubits over the \hat{Z} basis. The second column of Fig. 5.8 shows the evolution of the injected charge excitation. Similarly to the previous case, we measure the local charge $\hat{n}_{\mathbf{n}}(\tau)$:

$$\hat{n}_{\mathbf{n}}(\tau) = \langle \hat{n}_{\mathbf{n},\uparrow} \rangle(\tau) + \langle \hat{n}_{\mathbf{n},\downarrow} \rangle(\tau), \quad (5.3.21)$$

where τ is the time dependence. The numerical findings are in agreement with the $t - J$ model description, namely show much faster hole dynamics ($\tau_h \sim 1/t$) and slower spin dynamics ($\tau_s \sim 1/J$). This is also quantitatively confirmed for the parameters chosen in these simulations by the corresponding monitored observables. Considering the injection site $\mathbf{n} = (0, 0)$, the first peak in the charge sector, $N_j(\tau)$, occurs at $\tau_h \approx 12/U = 1.2/t$, whereas the first peak in the spin sector, $S_j^z(\tau)$, occurs at $\tau_s \approx 65/U = 6.5/t$. The corresponding ratio $\tau_s/\tau_h = 5.4$ is close to the ratio $t/J = U/2t = 5$, as expected. Notice that this analysis only provides evidence of the short timescale propagation of the excitations and is additionally affected by the small system size. While in 1D spin and charge would manifest as independent degrees of freedom also at longer times due to the well-known spin-charge separation phenomenon, this will not be the case in two-dimensional lattices. Spin and charge would indeed display strongly-correlated dynamics at longer times, as a consequence of spinon-holon coupling (see, for example, Refs. [381, 425] and references therein).

5.4 Summary

We have generalized a technique for local fermion encoding to any 2D lattice configurations eliminating the fermionic degrees of freedom by absorbing them into an auxiliary \mathbb{Z}_2 gauge field (gauge de fermionization). We have successfully tested this method against the 2D spin- $\frac{1}{2}$ Hubbard model. The ground state properties have been computed for varying particle densities utilizing both tree-tensor network ansatz and exact diagonalization methods. Here, we have observed the expected transition from the liquid to the anti-ferromagnetically ordered phase, accessing lattice sizes up to 4×4 . Furthermore, gauge de fermionization introduces a fermion-to-qubit mapping with comparable resource requirements to state-of-the-art encodings. We have shown that this mapping offers a scalable pathway for the digital quantum simulation of fermionic theories when the available fault-tolerant quantum computers [430, 431] will be scaled. For the de fermionized 2D Hubbard Hamiltonian, hopping terms and gauge constraints, here included as stabilizers, result in a maximum Pauli weight of 6. We have then demonstrated the feasibility of this approach by simulating the digital out-of-equilibrium dynamics of the de fermionized 2D Hubbard Hamiltonian over a 4×2 lattice in the antiferromagnetic phase. Our protocol entails the adiabatic preparation of the ground state (half-filling, $U/t = 10$), the injection of a charge (spin)-excitation in the system, and the time evolution of the perturbed state. Finally, we have observed a faster propagation for the charge excitation compared to the spin one as expected from the low-energy description based on the $t - J$ model.

Our collected results show numerical evidence that the local encoding is a scalable and feasible pathway toward the digital quantum simulation of fermionic lattice theories. We have highlighted that is indeed feasible to provide physically relevant results with the current technology of digital quantum processing platforms.

Tensor networks also showed positive results, although specifically the tree tensor network ansatz state manifests some limitations to accommodate the area-law of entanglement introduced by the auxiliary, resonant gauge fields. We expect tensor network geometries capable of capturing a wider entanglement distribution, such as ATTN [173] or iPEPS [432], to yield even better results.

Code and Data availability The code to map the fermionic Hamiltonian to a de fermionized one and run the digital quantum simulation is available at [433]. The engine of the simulations are distributed through the quantum tea leaves [275] and quantum matcha tea [429] python packages of *Quantum TEA*.

Chapter 6

Conclusions and Outlook

This thesis presents advances in the numerical and theoretical study of Lattice Gauge Theories (LGTs) by exploiting Tensor Network (TN) simulations. The use of TN methods aims to overcome longstanding challenges in non-perturbative quantum field theory (QFT), particularly those arising in traditional Monte Carlo (MC) simulations, like the sign problem [187]. By leveraging TNs and gauge-invariant formulations, we have made substantial progress in addressing LGTs, especially non-Abelian theories, and outlined pathways for exploring them in higher-dimensional systems and real-time dynamics, which remain some of the most challenging tasks in lattice high-energy physics.

Theoretical advancements The main theoretical contribution of this thesis is the dressed-site formalism, introduced in Sec. 1.2. This formalism enables the encoding of gauge and matter fields into local, bosonic, and gauge-invariant degrees of freedom, thus simplifying the complexities typically encountered when simulating LGTs on both classical and quantum hardware. It has been reviewed for Abelian $U(1)$ LGTs (see Sec. 1.4 and [5, 89, 90]) and successfully extended to the non-Abelian $SU(2)$ Yang-Mills case with dynamical matter (see [2] and Sec. 1.3), allowing us to explore challenging regimes of these models in two spatial dimensions.

The dressed-site formalism facilitated the development of a more general fermion-to-qubit encoding based on gauge defermentation [3], which addresses the issue of fermion statistics in LGTs and other fermionic lattice models, such as those found in condensed matter physics. Among other proposals [115, 123–125, 400, 402], this approach efficiently maps fermionic degrees of freedom onto bosonic ones, making them easier to handle in both classical TN methods and quantum simulations. We applied this encoding to the two-dimensional Fermi-Hubbard model (Chap. 5), demonstrating its effectiveness for both equilibrium and non-equilibrium simulations.

The numerical implementation of the dressed-site scheme and its generalizations is available in the Python library ED-LGT [6], designed for simulating LGT Hamiltonians in arbitrary spatial dimensions. It offers scalable precision for gauge field truncation, making it a versatile tool for pre-processing complex theories in future simulations on various platforms, including classical and quantum hardware.

Numerical results Within this theoretical scheme, we have provided the first TN simulations of the $SU(2)$ Yang-Mills LGT in two spatial dimensions [2], successfully exploring zero and finite baryon number densities. Our results revealed new insights into the ground-state properties of these systems with a rich phase-diagram, including the emergence of a baryon liquid phase in the

proximity of the continuum limit location. We extended the study to non-equilibrium dynamics, where we uncovered Quantum Many-Body Scars (QMBS) in non-Abelian LGTs [4]. These exotic states, which weakly violate the Eigenstate Thermalization Hypothesis (ETH) [302], offer a novel way to study weak violations of ergodic dynamics occurring in LGTs. Our findings indicate that the connection between QMBS and gauge invariance persists even in the more complex non-Abelian cases, hinting at possible deeper links between gauge theory and non-thermal states of matter.

Methodological Innovations Aside from the theoretical and numerical achievements, a key aspect of this thesis lies in the methodological improvements made to TN algorithms for high-dimensional LGTs. The first advancement was the development of an optimal encoding for quantum correlations and distances within the TN structure by leveraging space-filling curves, such as the Hilbert ordering (see Sec. 2.3.2). This mapping significantly enhanced the precision and efficiency of TN simulations for large-scale high-dimensional quantum many-body (QMB) systems, such as the 2D Ising model near its critical point [1].

In parallel, we outlined a broader roadmap aimed at enabling large-scale TN simulations of LGT, incorporating innovative strategies for high-performance and parallelized computing [5] (see Sec. 2.6). These improvements are designed to manage the computational demands of simulating complex gauge groups with high gauge-field truncations and large bond dimensions.

Outlook

While the accomplishments reported here demonstrate the effectiveness of TN methods for LGTs, they also highlight the remaining challenges in tackling cutting-edge research problems, such as reaching the continuum limit or high-dimensional QCD simulations on large-scale lattices. In focusing on algorithmic improvements and numerical strategies, we have presented a roadmap to make TN algorithms competitive in contemporary research problems in high-energy physics and strongly correlated fermionic systems.

Despite the progress made, several challenges and open questions remain, particularly regarding the finite truncation of gauge fields and the scalability of simulations to larger lattice sizes. Although we have addressed these issues with innovative truncation techniques, further improvements are necessary to fully capture the gauge dynamics, especially in high-dimensional systems. Additionally, while TN methods have proven successful in simulating intermediate system sizes, expanding these methods to larger scales comparable to MC state-of-the-art will require advancements in both algorithms and computational infrastructure. To these extents, the results and methods developed in this thesis open up several exciting avenues for future research, some of them representing ongoing projects.

Improved truncation schemes for gauge fields One of the key challenges in simulating LGTs is the finite representation of continuous gauge fields, which motivated several truncation strategies, such as Quantum Link Models (QLM) [96–100], finite subgroups [82, 86, 112], digitization of gauge fields [113], and fusion-algebra deformation [114]. As shown in Sec. 1.4.5, extending the dressed-site formalism to include larger gauge-representations in the gauge-invariant Hilbert space would bring the model closer to the continuum limit, particularly in the weak coupling regime [5]. However, approaching this region of the couplings would require a large computational effort in terms of resources (due to the increase of the local Hilbert space) and entanglement scaling (see Fig. 1.3), as the continuum limit corresponds to a quantum critical point of the underlying lattice theory [12, 184]. Developing new truncation schemes that preserve gauge invariance and simultaneously reduce computational costs is crucial for accurately

simulating systems at finer lattice spacings. Along this direction, there are ongoing efforts on a new algorithm for an optimal and scalable reduction of large dressed-site local Hilbert spaces that could significantly reduce these foundational bottlenecks.

Scaling to large lattice sizes While our TN simulations have provided valuable insights into SU(2) Yang-Mills LGTs, accessing larger lattice sizes is necessary to investigate long-range correlations and magnetic effects. Advanced TN geometries, such as the augmented Tree Tensor Network (aTTN) [173] or Infinite Projected Entangled Pair States (iPEPS) [47, 432], could significantly enhance the capability of TN methods to handle the large entanglement inherent in high-dimensional systems. Furthermore, running these simulations on pre-exascale high-performance computing (HPC) platforms [70, 262, 263, 266, 271] would enable larger-scale studies of LGTs. Along this direction, we could profit from the numerical optimization schemes developed in [5] and detailed in Sec. 2.6.

Applications to quantum chromodynamics (QCD) A natural extension of the work presented here is the application of TN methods to full lattice QCD, which involves the SU(3) gauge group. Progress in simulating SU(2) systems provides a foundation for tackling the more complex SU(3) theory, with the long-term goal of addressing open questions such as confinement [26, 434], and the QCD phase diagram at finite density [13]. Despite the inherent complexity of the model, recent strategies have been proposed to attack QCD via quantum hardware [99, 175] and TN methods, the latter being already successful in one spatial dimension [93, 155].

Real-Time Dynamics and Quantum Simulation The ability of TN methods to access real-time dynamics in LGTs is particularly promising for simulating out-of-equilibrium phenomena such as scattering processes [435]. These methods, combined with the dressed-site formalism, provide a framework for studying the non-equilibrium behavior of gauge fields and dynamical matter. Furthermore, our results serve as benchmarks for experimental quantum simulations [143], which are rapidly evolving with platforms such as ultra-cold atoms and trapped-ion systems. Extending our formalism to quantum hardware will enable experimental observation of LGT dynamics.

Quantum Many-Body Scarring and Exotic Dynamics in Gauge Theories The discovery of QMBS in non-Abelian LGTs [4] opens a new field of exploration in both fundamental physics and quantum computing. Future research could explore the role of gauge symmetry in protecting scarred states and investigate whether such scarring persists in more complex models like lattice QCD. Additionally, driving protocols could be developed to enhance scarring behavior in non-Abelian systems, offering new insights into the relationship between gauge theories and non-ergodic quantum phases. Our dressed-site scheme reveals further suitable for exploring different gauge invariant sectors and eventual background charges, allowing for numerical studies of other exotic dynamical behaviors such as Disorder Free Localization [436] in non-Abelian LGTs, which is currently under study.

Defermionization and Quantum Simulation of Fermionic Theories The fermion-to-qubit mapping developed in this thesis [3] offers a scalable approach to simulating fermionic theories on quantum hardware. As fault-tolerant quantum processors become available, this mapping could be applied to more complex fermionic models, such as the Hubbard model in higher dimensions or lattice gauge theories with dynamical fermions. These quantum simulations would provide valuable insights into strongly correlated fermionic systems, which are currently difficult to study using classical methods.

In conclusion, the advancements made in this thesis not only contribute to the theoretical and numerical understanding of LGTs, but also pave the way for future developments in quantum simulations and numerical techniques. By extending TN methods and gauge invariant encodings, we are well-positioned to address some of the most pressing challenges in high-energy and condensed matter physics, providing a foundation for future breakthroughs in understanding the fundamental interactions that govern the behavior of quantum systems.

Bibliography

- [1] Giovanni Cataldi, Ashkan Abedi, Giuseppe Magnifico, Simone Notarnicola, Nicola Dalla Pozza, Vittorio Giovannetti, and Simone Montangero. “Hilbert Curve vs Hilbert Space: Exploiting Fractal 2D Covering to Increase Tensor Network Efficiency”. *Quantum*, Sept. 2021. DOI: [10.22331/q-2021-09-29-556](https://doi.org/10.22331/q-2021-09-29-556).
- [2] Giovanni Cataldi, Giuseppe Magnifico, Pietro Silvi, and Simone Montangero. “Simulating (2+1)D SU(2) Yang-Mills Lattice Gauge Theory at Finite Density with Tensor Networks”. *Physical Review Research*, July 2024. DOI: [10.1103/PhysRevResearch.6.033057](https://doi.org/10.1103/PhysRevResearch.6.033057).
- [3] Giovanni Cataldi*, Marco Ballarin*, Giuseppe Magnifico, Daniel Jaschke, Marco Di Liberto, Ilaria Siloi, Simone Montangero, and Pietro Silvi. “Digital Quantum Simulation of Lattice Fermion Theories with Local Encoding”. *Quantum*, Sept. 2024. DOI: [10.22331/q-2024-09-04-1460](https://doi.org/10.22331/q-2024-09-04-1460).
- [4] Giovanni Cataldi*, Giuseppe Calajò*, Marco Rigobello, Darvin Wanisch, Giuseppe Magnifico, Pietro Silvi, Simone Montangero, and Jad C. Halimeh. *Quantum Many-Body Scarring in a Non-Abelian Lattice Gauge Theory*. May 2024. DOI: [10.48550/arXiv.2405.13112](https://doi.org/10.48550/arXiv.2405.13112).
- [5] Giuseppe Magnifico, Giovanni Cataldi, Marco Rigobello, Peter Majcen, Daniel Jaschke, Pietro Silvi, and Simone Montangero. *Tensor Networks for Lattice Gauge Theories beyond One Dimension: A Roadmap*. July 2024. DOI: [10.48550/arXiv.2407.03058](https://doi.org/10.48550/arXiv.2407.03058).
- [6] Giovanni Cataldi. *Ed-Lgt. Exact Diagonalization Code for Lattice Gauge Theories and Quantum Many Body Hamiltonians*. May 2024. DOI: [10.5281/ZENODO.11145318](https://doi.org/10.5281/ZENODO.11145318).
- [7] Mary K. Gaillard, Paul D. Grannis, and Frank J. Sciulli. “The Standard Model of Particle Physics”. *Reviews of Modern Physics*, Mar. 1999. DOI: [10.1103/RevModPhys.71.S96](https://doi.org/10.1103/RevModPhys.71.S96).
- [8] John B. Kogut. “An Introduction to Lattice Gauge Theory and Spin Systems”. *Reviews of Modern Physics*, Oct. 1979. DOI: [10.1103/RevModPhys.51.659](https://doi.org/10.1103/RevModPhys.51.659).
- [9] Heinz J. Rothe. *Lattice Gauge Theories: An Introduction (Fourth Edition)*. World Scientific Publishing Company, 2012. ISBN: 978-981-4365-87-1 978-981-4365-85-7.
- [10] John B. Kogut. “The Lattice Gauge Theory Approach to Quantum Chromodynamics”. *Reviews of Modern Physics*, July 1983. DOI: [10.1103/RevModPhys.55.775](https://doi.org/10.1103/RevModPhys.55.775).
- [11] Rajan Gupta. “Introduction to Lattice QCD”. *Introduction to Lattice QCD*, July 1998.
- [12] M. Pilar Hernández. “1 Lattice Field Theory Fundamentals”. In: *Modern Perspectives in Lattice QCD: Quantum Field Theory and High Performance Computing: Lecture Notes of the Les Houches Summer School: Volume 93, August 2009*. Ed. by Laurent Lellouch, Rainer Sommer, Benjamin Svetitsky, Anastassios Vladikas, and Leticia F. Cugliandolo. Oxford University Press, Aug. 2011, p. 0. ISBN: 978-0-19-969160-9. DOI: [10.1093/acprof:oso/9780199691609.003.0001](https://doi.org/10.1093/acprof:oso/9780199691609.003.0001).
- [13] Keitaro Nagata. “Finite-Density Lattice QCD and Sign Problem: Current Status and Open Problems”. *Progress in Particle and Nuclear Physics*, Nov. 2022. DOI: [10.1016/j.pnpnp.2022.103991](https://doi.org/10.1016/j.pnpnp.2022.103991).
- [14] Kenneth G. Wilson. “Confinement of Quarks”. *Physical Review D*, Oct. 1974. DOI: [10.1103/PhysRevD.10.2445](https://doi.org/10.1103/PhysRevD.10.2445).
- [15] Minati Biswal, Mridupawan Deka, Sanatan Digal, and P. S. Saumia. “Confinement - Deconfinement Transition in an $SSU(2)S$ Higgs Theory”. *Physical Review D*, July 2017. DOI: [10.1103/PhysRevD.96.014503](https://doi.org/10.1103/PhysRevD.96.014503).
- [16] V. G. Bornyakov, V. V. Braguta, E. M. Ilgenfritz, A. Yu. Kotov, I. E. Kudrov, A. V. Molochkov, A. A. Nikolaev, and R. N. Rogalyov. “Confinement-Deconfinement Transition in Dense SU(2) QCD”. *EPJ Web Conf.*, 2018. DOI: [10.1051/epjconf/201817507009](https://doi.org/10.1051/epjconf/201817507009).

- [17] M. Engelhardt, K. Langfeld, H. Reinhardt, and O. Tennert. “Deconfinement in SU(2) Yang-Mills Theory as a Center Vortex Percolation Transition”. *Physical Review D*, Feb. 2000. DOI: [10.1103/PhysRevD.61.054504](https://doi.org/10.1103/PhysRevD.61.054504).
- [18] J. Ambjørn, P. Olesen, and C. Peterson. “Stochastic Confinement and Dimensional Reduction (I). Four-Dimensional SU(2) Lattice Gauge Theory”. *Nuclear Physics B*, Sept. 1984. DOI: [10.1016/0550-3213\(84\)90475-9](https://doi.org/10.1016/0550-3213(84)90475-9).
- [19] J. Ambjørn, P. Olesen, and C. Peterson. “Stochastic Confinement and Dimensional Reduction (II). Three-Dimensional SU(2) Lattice Gauge Theory”. *Nuclear Physics B*, Nov. 1984. DOI: [10.1016/0550-3213\(84\)90242-6](https://doi.org/10.1016/0550-3213(84)90242-6).
- [20] Mario Mitter, Jan M. Pawłowski, and Nils Strodthoff. “Chiral Symmetry Breaking in Continuum QCD”. *Physical Review D*, Mar. 2015. DOI: [10.1103/PhysRevD.91.054035](https://doi.org/10.1103/PhysRevD.91.054035).
- [21] Steven Gottlieb, W. Liu, D. Toussaint, R. L. Renken, and R. L. Sugar. “Chiral-Symmetry Breaking in Lattice QCD with Two and Four Fermion Flavors”. *Physical Review D*, June 1987. DOI: [10.1103/PhysRevD.35.3972](https://doi.org/10.1103/PhysRevD.35.3972).
- [22] Mark Alford, Krishna Rajagopal, and Frank Wilczek. “Color-Flavor Locking and Chiral Symmetry Breaking in High Density QCD”. *Nuclear Physics B*, Jan. 1999. DOI: [10.1016/S0550-3213\(98\)00668-3](https://doi.org/10.1016/S0550-3213(98)00668-3).
- [23] J. Kogut, M. Stone, H. W. Wyld, J. Shigemitsu, S. H. Shenker, and D. K. Sinclair. “Scales of Chiral Symmetry Breaking in Quantum Chromodynamics”. *Physical Review Letters*, Apr. 1982. DOI: [10.1103/PhysRevLett.48.1140](https://doi.org/10.1103/PhysRevLett.48.1140).
- [24] Michael Creutz. “Monte Carlo Study of Quantized SU(2) Gauge Theory”. *Physical Review D*, Apr. 1980. DOI: [10.1103/PhysRevD.21.2308](https://doi.org/10.1103/PhysRevD.21.2308).
- [25] Michael Creutz and K. J. M. Moriarty. “Numerical Studies of Wilson Loops in SU(3) Gauge Theory in Four Dimensions”. *Physical Review D*, Oct. 1982. DOI: [10.1103/PhysRevD.26.2166](https://doi.org/10.1103/PhysRevD.26.2166).
- [26] J. Kogut, J. Polonyi, H. W. Wyld, J. Shigemitsu, and D. K. Sinclair. “Further Evidence for the First-Order Nature of the Pure Gauge SU(3) Deconfinement Transition”. *Nuclear Physics B*, Jan. 1985. DOI: [10.1016/0550-3213\(85\)90264-0](https://doi.org/10.1016/0550-3213(85)90264-0).
- [27] Michael Creutz, Laurence Jacobs, and Claudio Rebbi. “Monte Carlo Study of Abelian Lattice Gauge Theories”. *Physical Review D*, Oct. 1979. DOI: [10.1103/PhysRevD.20.1915](https://doi.org/10.1103/PhysRevD.20.1915).
- [28] B. Berg and J. Stehr. “SU(2) Lattice Gauge Theory and Monte Carlo Calculations”. *Zeitschrift für Physik C Particles and Fields*, Dec. 1981. DOI: [10.1007/BF01548769](https://doi.org/10.1007/BF01548769).
- [29] Michael Creutz, Laurence Jacobs, and Claudio Rebbi. “Monte Carlo Computations in Lattice Gauge Theories”. *Physics Reports*, Apr. 1983. DOI: [10.1016/0370-1573\(83\)90016-9](https://doi.org/10.1016/0370-1573(83)90016-9).
- [30] M. Creutz. *Lattice Gauge Theory and Monte Carlo Methods*. Tech. rep. BNL-42086. Brookhaven National Lab. (BNL), Upton, NY (United States), Nov. 1988. DOI: [10.2172/6530895](https://doi.org/10.2172/6530895).
- [31] Michael Creutz. “Lattice Gauge Theories and Monte Carlo Algorithms”. *Nuclear Physics B - Proceedings Supplements*, July 1989. DOI: [10.1016/0920-5632\(89\)90061-3](https://doi.org/10.1016/0920-5632(89)90061-3).
- [32] T. D. Kieu and C. J. Griffin. “Monte Carlo Simulations with Indefinite and Complex-Valued Measures”. *Phys. Rev. E*, May 1994. DOI: [10.1103/PhysRevE.49.3855](https://doi.org/10.1103/PhysRevE.49.3855).
- [33] Elham Ghobadpour, Max Kolb, Mohammad Reza Ejtehadi, and Ralf Everaers. “Monte Carlo Simulation of a Lattice Model for the Dynamics of Randomly Branching Double-Folded Ring Polymers”. *Physical Review E*, July 2021. DOI: [10.1103/PhysRevE.104.014501](https://doi.org/10.1103/PhysRevE.104.014501).
- [34] H. J. M. van Bommel, D. F. B. ten Haaf, W. van Saarloos, J. M. J. van Leeuwen, and G. An. “Fixed-Node Quantum Monte Carlo Method for Lattice Fermions”. *Phys. Rev. Lett.*, Apr. 1994. DOI: [10.1103/PhysRevLett.72.2442](https://doi.org/10.1103/PhysRevLett.72.2442).
- [35] Xiao Yan Xu, Yang Qi, Long Zhang, Fakher F. Assaad, Cenke Xu, and Zi Yang Meng. “Monte Carlo Study of Lattice Compact Quantum Electrodynamics with Fermionic Matter: The Parent State of Quantum Phases”. *Physical Review X*, May 2019. DOI: [10.1103/PhysRevX.9.021022](https://doi.org/10.1103/PhysRevX.9.021022).
- [36] Mushtaq Loan, Michael Brunner, Clare Sloggett, and Chris Hamer. “Path Integral Monte Carlo Approach to the U(1) Lattice Gauge Theory in 2+1 Dimensions”. *Physical Review D*, Aug. 2003. DOI: [10.1103/PhysRevD.68.034504](https://doi.org/10.1103/PhysRevD.68.034504).
- [37] J.E. Lynn, I. Tews, S. Gandolfi, and A. Lovato. “Quantum Monte Carlo Methods in Nuclear Physics: Recent Advances”. *Annual Review of Nuclear and Particle Science*, Oct. 2019. DOI: [10.1146/annurev-nucl-101918-023600](https://doi.org/10.1146/annurev-nucl-101918-023600).

- [38] Matthias Troyer and Uwe-Jens Wiese. “Computational Complexity and Fundamental Limitations to Fermionic Quantum Monte Carlo Simulations”. *Physical Review Letters*, May 2005. DOI: [10.1103/PhysRevLett.94.170201](https://doi.org/10.1103/PhysRevLett.94.170201).
- [39] Zi-Xiang Li, Yi-Fan Jiang, and Hong Yao. “Solving the Fermion Sign Problem in Quantum Monte Carlo Simulations by Majorana Representation”. *Phys. Rev. B*, June 2015. DOI: [10.1103/PhysRevB.91.241117](https://doi.org/10.1103/PhysRevB.91.241117).
- [40] Esteban A. Martinez, Christine A. Muschik, Philipp Schindler, Daniel Nigg, Alexander Erhard, Markus Heyl, Philipp Hauke, Marcello Dalmonte, Thomas Monz, Peter Zoller, and Rainer Blatt. “Real-Time Dynamics of Lattice Gauge Theories with a Few-Qubit Quantum Computer”. *Nature*, June 2016. DOI: [10.1038/nature18318](https://doi.org/10.1038/nature18318).
- [41] Christian Schweizer, Fabian Grusdt, Moritz Berngruber, Luca Barbiero, Eugene Demler, Nathan Goldman, Immanuel Bloch, and Monika Aidelsburger. “Floquet Approach to \mathbb{Z}_2 Lattice Gauge Theories with Ultracold Atoms in Optical Lattices”. *Nature Physics*, Nov. 2019. DOI: [10.1038/s41567-019-0649-7](https://doi.org/10.1038/s41567-019-0649-7).
- [42] Bing Yang, Hui Sun, Robert Ott, Han-Yi Wang, Torsten V. Zache, Jad C. Halimeh, Zhen-Sheng Yuan, Philipp Hauke, and Jian-Wei Pan. “Observation of Gauge Invariance in a 71-Site Bose–Hubbard Quantum Simulator”. *Nature*, Nov. 2020. DOI: [10.1038/s41586-020-2910-8](https://doi.org/10.1038/s41586-020-2910-8).
- [43] Zhao-Yu Zhou, Guo-Xian Su, Jad C. Halimeh, Robert Ott, Hui Sun, Philipp Hauke, Bing Yang, Zhen-Sheng Yuan, Jürgen Berges, and Jian-Wei Pan. “Thermalization Dynamics of a Gauge Theory on a Quantum Simulator”. *Science*, July 2022. DOI: [10.1126/science.abl6277](https://doi.org/10.1126/science.abl6277).
- [44] Nhung H. Nguyen, Minh C. Tran, Yingyue Zhu, Alaina M. Green, C. Huerta Alderete, Zohreh Davoudi, and Norbert M. Linke. “Digital Quantum Simulation of the Schwinger Model and Symmetry Protection with Trapped Ions”. *PRX Quantum*, May 2022. DOI: [10.1103/PRXQuantum.3.020324](https://doi.org/10.1103/PRXQuantum.3.020324).
- [45] Julius Mildenerberger, Wojciech Mruczkiewicz, Jad C. Halimeh, Zhang Jiang, and Philipp Hauke. *Probing Confinement in a \mathbb{Z}_2 Lattice Gauge Theory on a Quantum Computer*. Aug. 2022. DOI: [10.48550/arXiv.2203.08905](https://doi.org/10.48550/arXiv.2203.08905).
- [46] F. Verstraete, V. Murg, and J.I. Cirac. “Matrix Product States, Projected Entangled Pair States, and Variational Renormalization Group Methods for Quantum Spin Systems”. *Advances in Physics*, Mar. 2008. DOI: [10.1080/14789940801912366](https://doi.org/10.1080/14789940801912366).
- [47] Román Orús. “Tensor Networks for Complex Quantum Systems”. *Nature Reviews Physics*, Sept. 2019. DOI: [10.1038/s42254-019-0086-7](https://doi.org/10.1038/s42254-019-0086-7).
- [48] Simone Montangero. *Introduction to Tensor Network Methods: Numerical Simulations of Low-Dimensional Many-Body Quantum Systems*. Cham: Springer International Publishing, 2018. ISBN: 978-3-030-01408-7 978-3-030-01409-4. DOI: [10.1007/978-3-030-01409-4](https://doi.org/10.1007/978-3-030-01409-4).
- [49] Pietro Silvi, Ferdinand Tschirsich, Matthias Gerster, Johannes Jünemann, Daniel Jaschke, Matteo Rizzi, and Simone Montangero. “The Tensor Networks Anthology: Simulation Techniques for Many-Body Quantum Lattice Systems”. *SciPost Physics Lecture Notes*, Mar. 2019. DOI: [10.21468/SciPostPhysLectNotes.8](https://doi.org/10.21468/SciPostPhysLectNotes.8).
- [50] J. Eisert, M. Cramer, and M. B. Plenio. “Colloquium: Area Laws for the Entanglement Entropy”. *Reviews of Modern Physics*, Feb. 2010. DOI: [10.1103/RevModPhys.82.277](https://doi.org/10.1103/RevModPhys.82.277).
- [51] M. Fannes, B. Nachtergaele, and R. F. Werner. “Finitely Correlated States on Quantum Spin Chains”. *Communications in Mathematical Physics*, Mar. 1992. DOI: [10.1007/BF02099178](https://doi.org/10.1007/BF02099178).
- [52] A. Klümper, A. Schadschneider, and J. Zittartz. “Matrix Product Ground States for One-Dimensional Spin-1 Quantum Antiferromagnets”. *Europhysics Letters*, Nov. 1993. DOI: [10.1209/0295-5075/24/4/010](https://doi.org/10.1209/0295-5075/24/4/010).
- [53] Garnet Kin-Lic Chan, Anna Keselman, Naoki Nakatani, Zhendong Li, and Steven R. White. *Matrix Product Operators, Matrix Product States, and Ab Initio Density Matrix Renormalization Group Algorithms*. June 2016. DOI: [10.48550/arXiv.1605.02611](https://doi.org/10.48550/arXiv.1605.02611).
- [54] Sebastian Paeckel, Thomas Köhler, Andreas Swoboda, Salvatore R. Manmana, Ulrich Schollwöck, and Claudius Hubig. “Time-Evolution Methods for Matrix-Product States”. *Annals of Physics*, Dec. 2019. DOI: [10.1016/j.aop.2019.167998](https://doi.org/10.1016/j.aop.2019.167998).
- [55] Ulrich Schollwöck. “The Density-Matrix Renormalization Group in the Age of Matrix Product States”. *Annals of Physics*, Jan. 2011. DOI: [10.1016/j.aop.2010.09.012](https://doi.org/10.1016/j.aop.2010.09.012).

- [56] F. Verstraete, M. M. Wolf, D. Perez-Garcia, and J. I. Cirac. “Criticality, the Area Law, and the Computational Power of Projected Entangled Pair States”. *Physical Review Letters*, June 2006. DOI: [10.1103/PhysRevLett.96.220601](https://doi.org/10.1103/PhysRevLett.96.220601).
- [57] F. Verstraete and J. I. Cirac. *Renormalization Algorithms for Quantum-Many Body Systems in Two and Higher Dimensions*. July 2004. DOI: [10.48550/arXiv.cond-mat/0407066](https://doi.org/10.48550/arXiv.cond-mat/0407066).
- [58] Norbert Schuch, Michael M. Wolf, Frank Verstraete, and J. Ignacio Cirac. “Computational Complexity of Projected Entangled Pair States”. *Physical Review Letters*, Apr. 2007. DOI: [10.1103/PhysRevLett.98.140506](https://doi.org/10.1103/PhysRevLett.98.140506).
- [59] Juan Ignacio Cirac, José Garre-Rubio, and David Pérez-García. “Mathematical Open Problems in Projected Entangled Pair States”. *Revista Matemática Complutense*, Sept. 2019. DOI: [10.1007/s13163-019-00318-x](https://doi.org/10.1007/s13163-019-00318-x).
- [60] J. Ignacio Cirac, David Pérez-García, Norbert Schuch, and Frank Verstraete. “Matrix Product States and Projected Entangled Pair States: Concepts, Symmetries, Theorems”. *Reviews of Modern Physics*, Dec. 2021. DOI: [10.1103/RevModPhys.93.045003](https://doi.org/10.1103/RevModPhys.93.045003).
- [61] Philippe Corboz. “Improved Energy Extrapolation with Infinite Projected Entangled-Pair States Applied to the Two-Dimensional Hubbard Model”. *Phys. Rev. B*, Jan. 2016. DOI: [10.1103/PhysRevB.93.045116](https://doi.org/10.1103/PhysRevB.93.045116).
- [62] Philippe Corboz, Román Orús, Bela Bauer, and Guifré Vidal. “Simulation of Strongly Correlated Fermions in Two Spatial Dimensions with Fermionic Projected Entangled-Pair States”. *Physical Review B*, Apr. 2010. DOI: [10.1103/PhysRevB.81.165104](https://doi.org/10.1103/PhysRevB.81.165104).
- [63] Christina V. Kraus, Norbert Schuch, Frank Verstraete, and J. Ignacio Cirac. “Fermionic Projected Entangled Pair States”. *Physical Review A*, May 2010. DOI: [10.1103/PhysRevA.81.052338](https://doi.org/10.1103/PhysRevA.81.052338).
- [64] Michael Lubasch, J. Ignacio Cirac, and Mari-Carmen Bañuls. “Algorithms for Finite Projected Entangled Pair States”. *Physical Review B*, Aug. 2014. DOI: [10.1103/PhysRevB.90.064425](https://doi.org/10.1103/PhysRevB.90.064425).
- [65] Michael Lubasch, J. Ignacio Cirac, and Mari-Carmen Bañuls. “Unifying Projected Entangled Pair State Contractions”. *New Journal of Physics*, Mar. 2014. DOI: [10.1088/1367-2630/16/3/033014](https://doi.org/10.1088/1367-2630/16/3/033014).
- [66] Román Orús. “A Practical Introduction to Tensor Networks: Matrix Product States and Projected Entangled Pair States”. *Annals of Physics*, Oct. 2014. DOI: [10.1016/j.aop.2014.06.013](https://doi.org/10.1016/j.aop.2014.06.013).
- [67] Laurens Vanderstraeten, Lander Burgelman, Boris Ponsioen, Maarten Van Damme, Bram Vanhecke, Philippe Corboz, Jutho Haegeman, and Frank Verstraete. “Variational Methods for Contracting Projected Entangled-Pair States”. *Physical Review B*, May 2022. DOI: [10.1103/PhysRevB.105.195140](https://doi.org/10.1103/PhysRevB.105.195140).
- [68] Erez Zohar, Thorsten B. Wahl, Michele Burrello, and J. Ignacio Cirac. “Projected Entangled Pair States with Non-Abelian Gauge Symmetries: An SU(2) Study”. *Annals of Physics*, Nov. 2016. DOI: [10.1016/j.aop.2016.08.008](https://doi.org/10.1016/j.aop.2016.08.008).
- [69] Y.-Y. Shi, L.-M. Duan, and G. Vidal. “Classical Simulation of Quantum Many-Body Systems with a Tree Tensor Network”. *Physical Review A*, Aug. 2006. DOI: [10.1103/PhysRevA.74.022320](https://doi.org/10.1103/PhysRevA.74.022320).
- [70] M. Gerster, P. Silvi, M. Rizzi, R. Fazio, T. Calarco, and S. Montangero. “Unconstrained Tree Tensor Network: An Adaptive Gauge Picture for Enhanced Performance”. *Physical Review B*, Sept. 2014. DOI: [10.1103/PhysRevB.90.125154](https://doi.org/10.1103/PhysRevB.90.125154).
- [71] P. Silvi, V. Giovannetti, S. Montangero, M. Rizzi, J. I. Cirac, and R. Fazio. “Homogeneous Binary Trees as Ground States of Quantum Critical Hamiltonians”. *Physical Review A*, June 2010. DOI: [10.1103/PhysRevA.81.062335](https://doi.org/10.1103/PhysRevA.81.062335).
- [72] Xiangjian Qian and Mingpu Qin. “From Tree Tensor Network to Multiscale Entanglement Renormalization Ansatz”. *Physical Review B*, May 2022. DOI: [10.1103/PhysRevB.105.205102](https://doi.org/10.1103/PhysRevB.105.205102).
- [73] G. Vidal. “Entanglement Renormalization”. *Physical Review Letters*, Nov. 2007. DOI: [10.1103/PhysRevLett.99.220405](https://doi.org/10.1103/PhysRevLett.99.220405).
- [74] G. Evenbly and G. Vidal. “Entanglement Renormalization in Two Spatial Dimensions”. *Physical Review Letters*, May 2009. DOI: [10.1103/PhysRevLett.102.180406](https://doi.org/10.1103/PhysRevLett.102.180406).
- [75] M.C. Bañuls, K. Cichy, J.I. Cirac, and K. Jansen. “The Mass Spectrum of the Schwinger Model with Matrix Product States”. *Journal of High Energy Physics*, Nov. 2013. DOI: [10.1007/JHEP11\(2013\)158](https://doi.org/10.1007/JHEP11(2013)158).

- [76] E. Rico, T. Pichler, M. Dalmonte, P. Zoller, and S. Montangero. “Tensor Networks for Lattice Gauge Theories and Atomic Quantum Simulation”. *Physical Review Letters*, May 2014. DOI: [10.1103/PhysRevLett.112.201601](https://doi.org/10.1103/PhysRevLett.112.201601).
- [77] Stefan Kühn, J. Ignacio Cirac, and Mari-Carmen Bañuls. “Quantum Simulation of the Schwinger Model: A Study of Feasibility”. *Physical Review A*, Oct. 2014. DOI: [10.1103/PhysRevA.90.042305](https://doi.org/10.1103/PhysRevA.90.042305).
- [78] M. C. Bañuls, K. Cichy, J. I. Cirac, K. Jansen, and H. Saito. “Thermal Evolution of the Schwinger Model with Matrix Product Operators”. *Physical Review D*, Aug. 2015. DOI: [10.1103/PhysRevD.92.034519](https://doi.org/10.1103/PhysRevD.92.034519).
- [79] Boye Buyens, Frank Verstraete, and Karel Van Acoleyen. “Hamiltonian Simulation of the Schwinger Model at Finite Temperature”. *Physical Review D*, Oct. 2016. DOI: [10.1103/PhysRevD.94.085018](https://doi.org/10.1103/PhysRevD.94.085018).
- [80] Boye Buyens, Jutho Haegeman, Florian Hebenstreit, Frank Verstraete, and Karel Van Acoleyen. “Real-Time Simulation of the Schwinger Effect with Matrix Product States”. *Physical Review D*, Dec. 2017. DOI: [10.1103/PhysRevD.96.114501](https://doi.org/10.1103/PhysRevD.96.114501).
- [81] Boye Buyens, Simone Montangero, Jutho Haegeman, Frank Verstraete, and Karel Van Acoleyen. “Finite-Representation Approximation of Lattice Gauge Theories at the Continuum Limit with Tensor Networks”. *Physical Review D*, May 2017. DOI: [10.1103/PhysRevD.95.094509](https://doi.org/10.1103/PhysRevD.95.094509).
- [82] Elisa Ercolessi, Paolo Facchi, Giuseppe Magnifico, Saverio Pascazio, and Francesco V. Pepe. “Phase Transitions in \mathbb{Z}_n Gauge Models: Towards Quantum Simulations of the Schwinger-Weyl QED”. *Physical Review D*, Oct. 2018. DOI: [10.1103/PhysRevD.98.074503](https://doi.org/10.1103/PhysRevD.98.074503).
- [83] G. Magnifico, D. Vodola, E. Ercolessi, S. P. Kumar, M. Müller, and A. Bermudez. “ \mathbb{Z}_N Gauge Theories Coupled to Topological Fermions: QED $_2$ with a Quantum Mechanical θ Angle”. *Physical Review B*, Sept. 2019. DOI: [10.1103/PhysRevB.100.115152](https://doi.org/10.1103/PhysRevB.100.115152).
- [84] G. Magnifico, D. Vodola, E. Ercolessi, S. P. Kumar, M. Müller, and A. Bermudez. “Symmetry-Protected Topological Phases in Lattice Gauge Theories: Topological QED $_2$ ”. *Physical Review D*, Jan. 2019. DOI: [10.1103/PhysRevD.99.014503](https://doi.org/10.1103/PhysRevD.99.014503).
- [85] Lena Funcke, Karl Jansen, and Stefan Kühn. “Topological Vacuum Structure of the Schwinger Model with Matrix Product States”. *Physical Review D*, Mar. 2020. DOI: [10.1103/PhysRevD.101.054507](https://doi.org/10.1103/PhysRevD.101.054507).
- [86] Giuseppe Magnifico, Marcello Dalmonte, Paolo Facchi, Saverio Pascazio, Francesco V. Pepe, and Elisa Ercolessi. “Real Time Dynamics and Confinement in the \mathbb{Z}_n Schwinger-Weyl Lattice Model for 1+1 QED”. *Quantum*, June 2020. DOI: [10.22331/q-2020-06-15-281](https://doi.org/10.22331/q-2020-06-15-281).
- [87] Marco Rigobello, Simone Notarnicola, Giuseppe Magnifico, and Simone Montangero. “Entanglement Generation in $(1+1)\mathrm{D}$ QED Scattering Processes”. *Physical Review D*, Dec. 2021. DOI: [10.1103/PhysRevD.104.114501](https://doi.org/10.1103/PhysRevD.104.114501).
- [88] Mari Carmen Banuls, Michal P. Heller, Karl Jansen, Johannes Knaute, and Viktor Svensson. *A Quantum Information Perspective on Meson Melting*. June 2022. DOI: [10.48550/arXiv.2206.10528](https://doi.org/10.48550/arXiv.2206.10528).
- [89] Timo Felser, Pietro Silvi, Mario Collura, and Simone Montangero. “Two-Dimensional Quantum-Link Lattice Quantum Electrodynamics at Finite Density”. *Physical Review X*, Nov. 2020. DOI: [10.1103/PhysRevX.10.041040](https://doi.org/10.1103/PhysRevX.10.041040).
- [90] Giuseppe Magnifico, Timo Felser, Pietro Silvi, and Simone Montangero. “Lattice Quantum Electrodynamics in (3+1)-Dimensions at Finite Density with Tensor Networks”. *Nature Communications*, June 2021. DOI: [10.1038/s41467-021-23646-3](https://doi.org/10.1038/s41467-021-23646-3).
- [91] Patrick Emonts, Ariel Kelman, Umberto Borla, Sergej Moroz, Snir Gazit, and Erez Zohar. “Finding the Ground State of a Lattice Gauge Theory with Fermionic Tensor Networks: A $2+1\mathrm{D}$ \mathbb{Z}_2 Demonstration”. *Physical Review D*, Jan. 2023. DOI: [10.1103/PhysRevD.107.014505](https://doi.org/10.1103/PhysRevD.107.014505).
- [92] Pietro Silvi, Enrique Rico, Marcello Dalmonte, Ferdinand Tschirsich, and Simone Montangero. “Finite-Density Phase Diagram of a $(1+1)\mathrm{D}$ Non-Abelian Lattice Gauge Theory with Tensor Networks”. *Quantum*, Apr. 2017. DOI: [10.22331/q-2017-04-25-9](https://doi.org/10.22331/q-2017-04-25-9).

- [93] Pietro Silvi, Yannick Sauer, Ferdinand Tschirsich, and Simone Montangero. “Tensor Network Simulation of an SU(3) Lattice Gauge Theory in 1D”. *Physical Review D*, Oct. 2019. DOI: [10.1103/PhysRevD.100.074512](https://doi.org/10.1103/PhysRevD.100.074512).
- [94] Saurabh Vasant Kadam, Indrakshi Raychowdhury, and Jesse Stryker. “Loop-String-Hadron Formulation of an SU(3) Gauge Theory with Dynamical Quarks”. In: *Proceedings of The 39th International Symposium on Lattice Field Theory — PoS(LATTICE2022)*. Vol. 430. SISSA Medialab, Apr. 2023, p. 373. DOI: [10.22323/1.430.0373](https://doi.org/10.22323/1.430.0373).
- [95] Julian Bender and Erez Zohar. “Gauge Redundancy-Free Formulation of Compact QED with Dynamical Matter for Quantum and Classical Computations”. *Physical Review D*, Dec. 2020. DOI: [10.1103/PhysRevD.102.114517](https://doi.org/10.1103/PhysRevD.102.114517).
- [96] D. Horn. “Finite Matrix Models with Continuous Local Gauge Invariance”. *Physics Letters B*, Mar. 1981. DOI: [10.1016/0370-2693\(81\)90763-2](https://doi.org/10.1016/0370-2693(81)90763-2).
- [97] Peter Orland and Daniel Rohrlich. “Lattice Gauge Magnets: Local Isospin from Spin”. *Nuclear Physics B*, July 1990. DOI: [10.1016/0550-3213\(90\)90646-U](https://doi.org/10.1016/0550-3213(90)90646-U).
- [98] S Chandrasekharan and U. J Wiese. “Quantum Link Models: A Discrete Approach to Gauge Theories”. *Nuclear Physics B*, May 1997. DOI: [10.1016/S0550-3213\(97\)80041-7](https://doi.org/10.1016/S0550-3213(97)80041-7).
- [99] R. Brower, S. Chandrasekharan, and U.-J. Wiese. “QCD as a Quantum Link Model”. *Physical Review D*, Sept. 1999. DOI: [10.1103/PhysRevD.60.094502](https://doi.org/10.1103/PhysRevD.60.094502).
- [100] L. Tagliacozzo, A. Celi, and M. Lewenstein. “Tensor Networks for Lattice Gauge Theories with Continuous Groups”. *Physical Review X*, Nov. 2014. DOI: [10.1103/PhysRevX.4.041024](https://doi.org/10.1103/PhysRevX.4.041024).
- [101] Tim Byrnes and Yoshihisa Yamamoto. “Simulating Lattice Gauge Theories on a Quantum Computer”. *Physical Review A*, Feb. 2006. DOI: [10.1103/PhysRevA.73.022328](https://doi.org/10.1103/PhysRevA.73.022328).
- [102] Simon V. Mathis, Guglielmo Mazzola, and Ivano Tavernelli. “Toward Scalable Simulations of Lattice Gauge Theories on Quantum Computers”. *Physical Review D*, Nov. 2020. DOI: [10.1103/PhysRevD.102.094501](https://doi.org/10.1103/PhysRevD.102.094501).
- [103] Zohreh Davoudi, Mohammad Hafezi, Christopher Monroe, Guido Pagano, Alireza Seif, and Andrew Shaw. “Towards Analog Quantum Simulations of Lattice Gauge Theories with Trapped Ions”. *Physical Review Research*, Apr. 2020. DOI: [10.1103/PhysRevResearch.2.023015](https://doi.org/10.1103/PhysRevResearch.2.023015).
- [104] Giulia Mazzola, Simon V. Mathis, Guglielmo Mazzola, and Ivano Tavernelli. “Gauge-Invariant Quantum Circuits for SU(1) and Yang-Mills Lattice Gauge Theories”. *Physical Review Research*, Dec. 2021. DOI: [10.1103/PhysRevResearch.3.043209](https://doi.org/10.1103/PhysRevResearch.3.043209).
- [105] Angus Kan, Lena Funcke, Stefan Kühn, Luca Dellantonio, Jinglei Zhang, Jan F. Haase, Christine A. Muschik, and Karl Jansen. “Investigating a $(3+1)\text{-D}$ Topological θ -Term in the Hamiltonian Formulation of Lattice Gauge Theories for Quantum and Classical Simulations”. *Physical Review D*, Aug. 2021. DOI: [10.1103/PhysRevD.104.034504](https://doi.org/10.1103/PhysRevD.104.034504).
- [106] Erez Zohar. “Quantum Simulation of Lattice Gauge Theories in More than One Space Dimension—Requirements, Challenges and Methods”. *Philosophical Transactions of the Royal Society A: Mathematical, Physical and Engineering Sciences*, Dec. 2021. DOI: [10.1098/rsta.2021.0069](https://doi.org/10.1098/rsta.2021.0069).
- [107] A. Mariani, S. Pradhan, and E. Ercolessi. “Hamiltonians and Gauge-Invariant Hilbert Space for Lattice Yang-Mills-like Theories with Finite Gauge Group”. *Physical Review D*, June 2023. DOI: [10.1103/PhysRevD.107.114513](https://doi.org/10.1103/PhysRevD.107.114513).
- [108] Domenico Pomarico, Leonardo Cosmai, Paolo Facchi, Cosmo Lupo, Saverio Pascazio, and Francesco V. Pepe. “Dynamical Quantum Phase Transitions of the Schwinger Model: Real-Time Dynamics on IBM Quantum”. *Entropy*, Apr. 2023. DOI: [10.3390/e25040608](https://doi.org/10.3390/e25040608).
- [109] Christian W. Bauer, Zohreh Davoudi, Natalie Klco, and Martin J. Savage. “Quantum Simulation of Fundamental Particles and Forces”. *Nature Reviews Physics*, July 2023. DOI: [10.1038/s42254-023-00599-8](https://doi.org/10.1038/s42254-023-00599-8).
- [110] Christian W. Bauer, Zohreh Davoudi, A. Baha Balantekin, Tanmoy Bhattacharya, Marcela Carena, Wibe A. de Jong, Patrick Draper, Aida El-Khadra, Nate Gemelke, Masanori Hanada, Dmitri Kharzeev, Henry Lamm, Ying-Ying Li, Junyu Liu, Mikhail Lukin, Yannick Meurice, Christopher Monroe, Benjamin Nachman, Guido Pagano, John Preskill, Enrico Rinaldi, Alessandro Roggero, David I. Santiago, Martin J. Savage, Irfan Siddiqi, George Siopsis, David Van Zanten, Nathan Wiebe, Yukari Yamauchi, Kübra Yeter-Aydeniz, and

- Silvia Zorzetti. “Quantum Simulation for High-Energy Physics”. *PRX Quantum*, May 2023. DOI: [10.1103/PRXQuantum.4.027001](https://doi.org/10.1103/PRXQuantum.4.027001).
- [111] Pierpaolo Fontana, Joao C. Pinto Barros, and Andrea Trombettoni. “Quantum Simulator of Link Models Using Spinor Dipolar Ultracold Atoms”. *Physical Review A*, Apr. 2023. DOI: [10.1103/PhysRevA.107.043312](https://doi.org/10.1103/PhysRevA.107.043312).
- [112] Jan F. Haase, Luca Dellantonio, Alessio Celi, Danny Paulson, Angus Kan, Karl Jansen, and Christine A. Muschik. “A Resource Efficient Approach for Quantum and Classical Simulations of Gauge Theories in Particle Physics”. *Quantum*, Feb. 2021. DOI: [10.22331/q-2021-02-04-393](https://doi.org/10.22331/q-2021-02-04-393).
- [113] Daniel C. Hackett, Kiel Howe, Ciaran Hughes, William Jay, Ethan T. Neil, and James N. Simone. “Digitizing Gauge Fields: Lattice Monte Carlo Results for Future Quantum Computers”. *Physical Review A*, June 2019. DOI: [10.1103/PhysRevA.99.062341](https://doi.org/10.1103/PhysRevA.99.062341).
- [114] Torsten V. Zache, Daniel González-Cuadra, and Peter Zoller. *Quantum and Classical Spin Network Algorithms for q -Deformed Kogut-Susskind Gauge Theories*. May 2023. DOI: [10.48550/arXiv.2304.02527](https://doi.org/10.48550/arXiv.2304.02527).
- [115] Erez Zohar and J. Ignacio Cirac. “Eliminating Fermionic Matter Fields in Lattice Gauge Theories”. *Physical Review B*, Aug. 2018. DOI: [10.1103/PhysRevB.98.075119](https://doi.org/10.1103/PhysRevB.98.075119).
- [116] Erez Zohar and J. Ignacio Cirac. “Removing Staggered Fermionic Matter in U(N) and SU(N) Lattice Gauge Theories”. *Physical Review D*, June 2019. DOI: [10.1103/PhysRevD.99.114511](https://doi.org/10.1103/PhysRevD.99.114511).
- [117] Frank Arute, Kunal Arya, Ryan Babbush, Dave Bacon, Joseph C. Bardin, Rami Barends, Andreas Bengtsson, Sergio Boixo, Michael Broughton, Bob B. Buckley, David A. Buell, Brian Burkett, Nicholas Bushnell, Yu Chen, Zijun Chen, Yu-An Chen, Ben Chiaro, Roberto Collins, Stephen J. Cotton, William Courtney, Sean Demura, Alan Derk, Andrew Dunsworth, Daniel Eppens, Thomas Eickl, Catherine Erickson, Edward Farhi, Austin Fowler, Brooks Foxen, Craig Gidney, Marissa Giustina, Rob Graff, Jonathan A. Gross, Steve Habegger, Matthew P. Harrigan, Alan Ho, Sabrina Hong, Trent Huang, William Huggins, Lev B. Ioffe, Sergei V. Isakov, Evan Jeffrey, Zhang Jiang, Cody Jones, Dvir Kafri, Kostyantyn Kechedzhi, Julian Kelly, Seon Kim, Paul V. Klimov, Alexander N. Korotkov, Fedor Kostritsa, David Landhuis, Pavel Laptev, Mike Lindmark, Erik Lucero, Michael Marthaler, Orion Martin, John M. Martinis, Anika Marusczyk, Sam McArdle, Jarrod R. McClean, Trevor McCourt, Matt McEwen, Anthony Megrant, Carlos Mejuto-Zaera, Xiao Mi, Masoud Mohseni, Wojciech Mroczkiewicz, Josh Mutus, Ofer Naaman, Matthew Neeley, Charles Neill, Hartmut Neven, Michael Newman, Murphy Yuezhen Niu, Thomas E. O’Brien, Eric Ostby, Bálint Pató, Andre Petukhov, Harald Putterman, Chris Quintana, Jan-Michael Reiner, Pedram Roushan, Nicholas C. Rubin, Daniel Sank, Kevin J. Satzinger, Vadim Smelyanskiy, Doug Strain, Kevin J. Sung, Peter Schmitteckert, Marco Szalay, Norm M. Tubman, Amit Vainsencher, Theodore White, Nicolas Vogt, Z. Jamie Yao, Ping Yeh, Adam Zalcman, and Sebastian Zanker. *Observation of Separated Dynamics of Charge and Spin in the Fermi-Hubbard Model*. Oct. 2020. DOI: [10.48550/arXiv.2010.07965](https://doi.org/10.48550/arXiv.2010.07965).
- [118] R. Barends, L. Lamata, J. Kelly, L. García-Álvarez, A. G. Fowler, A. Megrant, E. Jeffrey, T. C. White, D. Sank, J. Y. Mutus, B. Campbell, Yu Chen, Z. Chen, B. Chiaro, A. Dunsworth, I.-C. Hoi, C. Neill, P. J. J. O’Malley, C. Quintana, P. Roushan, A. Vainsencher, J. Wenner, E. Solano, and John M. Martinis. “Digital Quantum Simulation of Fermionic Models with a Superconducting Circuit”. *Nature Communications*, July 2015. DOI: [10.1038/ncomms8654](https://doi.org/10.1038/ncomms8654).
- [119] Y. Salathé, M. Mondal, M. Oppliger, J. Heinsoo, P. Kurpiers, A. Potočnik, A. Mezzacapo, U. Las Heras, L. Lamata, E. Solano, S. Filipp, and A. Wallraff. “Digital Quantum Simulation of Spin Models with Circuit Quantum Electrodynamics”. *Physical Review X*, June 2015. DOI: [10.1103/PhysRevX.5.021027](https://doi.org/10.1103/PhysRevX.5.021027).
- [120] P. J. J. O’Malley, R. Babbush, I. D. Kivlichan, J. Romero, J. R. McClean, R. Barends, J. Kelly, P. Roushan, A. Tranter, N. Ding, B. Campbell, Y. Chen, Z. Chen, B. Chiaro, A. Dunsworth, A. G. Fowler, E. Jeffrey, E. Lucero, A. Megrant, J. Y. Mutus, M. Neeley, C. Neill, C. Quintana, D. Sank, A. Vainsencher, J. Wenner, T. C. White, P. V. Coveney, P. J. Love, H. Neven, A. Aspuru-Guzik, and J. M. Martinis. “Scalable Quantum Simulation of Molecular Energies”. *Physical Review X*, July 2016. DOI: [10.1103/PhysRevX.6.031007](https://doi.org/10.1103/PhysRevX.6.031007).
- [121] Stasja Stanisic, Jan Lukas Bosse, Filippo Maria Gambetta, Raul A. Santos, Wojciech Mroczkiewicz, Thomas E. O’Brien, Eric Ostby, and Ashley Montanaro. “Observing

- Ground-State Properties of the Fermi-Hubbard Model Using a Scalable Algorithm on a Quantum Computer”. *Nature Communications*, Oct. 2022. DOI: [10.1038/s41467-022-33335-4](https://doi.org/10.1038/s41467-022-33335-4).
- [122] P. Jordan and E. Wigner. “Über das Paulische Äquivalenzverbot”. *Zeitschrift für Physik*, Sept. 1928. DOI: [10.1007/BF01331938](https://doi.org/10.1007/BF01331938).
- [123] Michael A. Nielsen, Mark R. Dowling, Mile Gu, and Andrew C. Doherty. “Quantum Computation as Geometry”. *Science*, Feb. 2006. DOI: [10.1126/science.1121541](https://doi.org/10.1126/science.1121541).
- [124] Sergey B. Bravyi and Alexei Yu. Kitaev. “Fermionic Quantum Computation”. *Annals of Physics*, May 2002. DOI: [10.1006/aphy.2002.6254](https://doi.org/10.1006/aphy.2002.6254).
- [125] Zhang Jiang, Jarrod McClean, Ryan Babbush, and Hartmut Neven. “Majorana Loop Stabilizer Codes for Error Mitigation in Fermionic Quantum Simulations”. *Physical Review Applied*, Dec. 2019. DOI: [10.1103/PhysRevApplied.12.064041](https://doi.org/10.1103/PhysRevApplied.12.064041).
- [126] Erez Zohar, J. Ignacio Cirac, and Benni Reznik. “Cold-Atom Quantum Simulator for SU(2) Yang-Mills Lattice Gauge Theory”. *Physical Review Letters*, Mar. 2013. DOI: [10.1103/PhysRevLett.110.125304](https://doi.org/10.1103/PhysRevLett.110.125304).
- [127] D. Banerjee, M. Bögli, M. Dalmonte, E. Rico, P. Stebler, U.-J. Wiese, and P. Zoller. “Atomic Quantum Simulation of $\mathbf{U}(N)$ and $\mathrm{SU}(N)$ Non-Abelian Lattice Gauge Theories”. *Physical Review Letters*, Mar. 2013. DOI: [10.1103/PhysRevLett.110.125303](https://doi.org/10.1103/PhysRevLett.110.125303).
- [128] U.-J. Wiese. “Ultracold Quantum Gases and Lattice Systems: Quantum Simulation of Lattice Gauge Theories”. *Annalen der Physik*, Nov. 2013. DOI: [10.1002/andp.201300104](https://doi.org/10.1002/andp.201300104).
- [129] L. Tagliacozzo, A. Celi, P. Orland, M. W. Mitchell, and M. Lewenstein. “Simulations of Non-Abelian Gauge Theories with Optical Lattices”. *Nature Communications*, Dec. 2013. DOI: [10.1038/ncomms3615](https://doi.org/10.1038/ncomms3615).
- [130] Erez Zohar, J. Ignacio Cirac, and Benni Reznik. “Quantum Simulations of Lattice Gauge Theories Using Ultracold Atoms in Optical Lattices”. *Reports on Progress in Physics*, Dec. 2015. DOI: [10.1088/0034-4885/79/1/014401](https://doi.org/10.1088/0034-4885/79/1/014401).
- [131] A. Mezzacapo, E. Rico, C. Sabín, I. L. Egusquiza, L. Lamata, and E. Solano. “Non-Abelian SU(2) Lattice Gauge Theories in Superconducting Circuits”. *Physical Review Letters*, Dec. 2015. DOI: [10.1103/PhysRevLett.115.240502](https://doi.org/10.1103/PhysRevLett.115.240502).
- [132] Mari Carmen Bañuls and Krzysztof Cichy. “Review on Novel Methods for Lattice Gauge Theories”. *Reports on Progress in Physics*, Jan. 2020. DOI: [10.1088/1361-6633/ab6311](https://doi.org/10.1088/1361-6633/ab6311).
- [133] Mari Carmen Bañuls, Rainer Blatt, Jacopo Catani, Alessio Celi, Juan Ignacio Cirac, Marcello Dalmonte, Leonardo Fallani, Karl Jansen, Maciej Lewenstein, Simone Montangero, Christine A. Muschik, Benni Reznik, Enrique Rico, Luca Tagliacozzo, Karel Van Acoleyen, Frank Verstraete, Uwe-Jens Wiese, Matthew Wingate, Jakub Zakrzewski, and Peter Zoller. “Simulating Lattice Gauge Theories within Quantum Technologies”. *The European Physical Journal D*, Aug. 2020. DOI: [10.1140/epjd/e2020-100571-8](https://doi.org/10.1140/epjd/e2020-100571-8).
- [134] Yasar Y. Atas, Jinglei Zhang, Randy Lewis, Amin Jahanpour, Jan F. Haase, and Christine A. Muschik. “SU(2) Hadrons on a Quantum Computer via a Variational Approach”. *Nature Communications*, Nov. 2021. DOI: [10.1038/s41467-021-26825-4](https://doi.org/10.1038/s41467-021-26825-4).
- [135] Natalie Klco, Alessandro Roggero, and Martin J. Savage. “Standard Model Physics and the Digital Quantum Revolution: Thoughts about the Interface”. *Reports on Progress in Physics*, May 2022. DOI: [10.1088/1361-6633/ac58a4](https://doi.org/10.1088/1361-6633/ac58a4).
- [136] Yannick Meurice, James C. Osborn, Ryo Sakai, Judah Unmuth-Yockey, Simon Catterall, and Rolando D. Somma. *Tensor Networks for High Energy Physics: Contribution to Snowmass 2021*. Mar. 2022. DOI: [10.48550/arXiv.2203.04902](https://doi.org/10.48550/arXiv.2203.04902).
- [137] Yasar Y. Atas, Jan F. Haase, Jinglei Zhang, Victor Wei, Sieglinde M.-L. Pfaendler, Randy Lewis, and Christine A. Muschik. *Simulating One-Dimensional Quantum Chromodynamics on a Quantum Computer: Real-Time Evolutions of Tetra- and Pentaquarks*. Feb. 2023. DOI: [10.48550/arXiv.2207.03473](https://doi.org/10.48550/arXiv.2207.03473).
- [138] Zohreh Davoudi, Alexander F. Shaw, and Jesse R. Stryker. *General Quantum Algorithms for Hamiltonian Simulation with Applications to a Non-Abelian Lattice Gauge Theory*. Jan. 2023. DOI: [10.48550/arXiv.2212.14030](https://doi.org/10.48550/arXiv.2212.14030).
- [139] Torsten V. Zache, Daniel González-Cuadra, and Peter Zoller. “Fermion-Qudit Quantum Processors for Simulating Lattice Gauge Theories with Matter”. *Quantum*, Oct. 2023. DOI: [10.22331/q-2023-10-16-1140](https://doi.org/10.22331/q-2023-10-16-1140).

- [140] Yiqing Zhou, E. Miles Stoudenmire, and Xavier Waintal. “What Limits the Simulation of Quantum Computers?” *Physical Review X*, Nov. 2020. DOI: [10.1103/PhysRevX.10.041038](https://doi.org/10.1103/PhysRevX.10.041038).
- [141] Thomas Ayrat, Thibaud Louvet, Yiqing Zhou, Cyprien Lambert, E. Miles Stoudenmire, and Xavier Waintal. “Density-Matrix Renormalization Group Algorithm for Simulating Quantum Circuits with a Finite Fidelity”. *PRX Quantum*, Apr. 2023. DOI: [10.1103/PRXQuantum.4.020304](https://doi.org/10.1103/PRXQuantum.4.020304).
- [142] Zohreh Davoudi, Ethan T. Neil, Christian W. Bauer, Tanmoy Bhattacharya, Thomas Blum, Peter Boyle, Richard C. Brower, Simon Catterall, Norman H. Christ, Vincenzo Cirigliano, Gilberto Colangelo, Carleton DeTar, William Detmold, Robert G. Edwards, Aida X. El-Khadra, Steven Gottlieb, Rajan Gupta, Daniel C. Hackett, Anna Hasenfratz, Taku Izubuchi, William I. Jay, Luchang Jin, Christopher Kelly, Andreas S. Kronfeld, Christoph Lehner, Huey-Wen Lin, Meifeng Lin, Andrew T. Lytle, Stefan Meinel, Yannick Meurice, Swagato Mukherjee, Amy Nicholson, Sasa Prelovsek, Martin J. Savage, Phiala E. Shanahan, Ruth S. Van De Water, Michael L. Wagman, and Oliver Witzel. *Report of the Snowmass 2021 Topical Group on Lattice Gauge Theory*. Sept. 2022. DOI: [10.48550/arXiv.2209.10758](https://doi.org/10.48550/arXiv.2209.10758).
- [143] Giuseppe Calajó, Giuseppe Magnifico, Claire Edmunds, Martin Ringbauer, Simone Montangero, and Pietro Silvi. “Digital Quantum Simulation of a (1+1)D SU(2) Lattice Gauge Theory with Ion Qudits”. *PRX Quantum*, Oct. 2024. DOI: [10.1103/PRXQuantum.5.040309](https://doi.org/10.1103/PRXQuantum.5.040309).
- [144] John Kogut and Leonard Susskind. “Hamiltonian Formulation of Wilson’s Lattice Gauge Theories”. *Physical Review D*, Jan. 1975. DOI: [10.1103/PhysRevD.11.395](https://doi.org/10.1103/PhysRevD.11.395).
- [145] Michael Creutz. *Quantum Fields on the Computer*. World Scientific, 1992. ISBN: 978-981-02-0940-7.
- [146] Giuseppe Clemente, Arianna Crippa, and Karl Jansen. “Strategies for the Determination of the Running Coupling of (2+1)-Dimensional QED with Quantum Computing”. *Physical Review D*, Dec. 2022. DOI: [10.1103/PhysRevD.106.114511](https://doi.org/10.1103/PhysRevD.106.114511).
- [147] Arianna Crippa, Simone Romiti, Lena Funcke, Karl Jansen, Stefan Kühn, Paolo Stornati, and Carsten Urbach. *Towards Determining the (2+1)-Dimensional Quantum Electrodynamics Running Coupling with Monte Carlo and Quantum Computing Methods*. June 2024. DOI: [10.48550/arXiv.2404.17545](https://doi.org/10.48550/arXiv.2404.17545).
- [148] Leonard Susskind. “Lattice Fermions”. *Physical Review D*, Nov. 1977. DOI: [10.1103/PhysRevD.16.3031](https://doi.org/10.1103/PhysRevD.16.3031).
- [149] H. B. Nielsen and M. Ninomiya. “Absence of Neutrinos on a Lattice: (I). Proof by Homotopy Theory”. *Nuclear Physics B*, July 1981. DOI: [10.1016/0550-3213\(81\)90361-8](https://doi.org/10.1016/0550-3213(81)90361-8).
- [150] H. B. Nielsen and M. Ninomiya. “Absence of Neutrinos on a Lattice: (II). Intuitive Topological Proof”. *Nuclear Physics B*, Dec. 1981. DOI: [10.1016/0550-3213\(81\)90524-1](https://doi.org/10.1016/0550-3213(81)90524-1).
- [151] A. Bermudez, L. Mazza, M. Rizzi, N. Goldman, M. Lewenstein, and M. A. Martin-Delgado. “Wilson Fermions and Axion Electrodynamics in Optical Lattices”. *Physical Review Letters*, Nov. 2010. DOI: [10.1103/PhysRevLett.105.190404](https://doi.org/10.1103/PhysRevLett.105.190404).
- [152] Leonardo Mazza, Alejandro Bermudez, Nathan Goldman, Matteo Rizzi, Miguel Angel Martin-Delgado, and Maciej Lewenstein. “An Optical-Lattice-Based Quantum Simulator for Relativistic Field Theories and Topological Insulators”. *New Journal of Physics*, Jan. 2012. DOI: [10.1088/1367-2630/14/1/015007](https://doi.org/10.1088/1367-2630/14/1/015007).
- [153] Yoshihito Kuno, Ikuo Ichinose, and Yoshiro Takahashi. “Generalized Lattice Wilson–Dirac Fermions in (1 + 1) Dimensions for Atomic Quantum Simulation and Topological Phases”. *Scientific Reports*, July 2018. DOI: [10.1038/s41598-018-29143-w](https://doi.org/10.1038/s41598-018-29143-w).
- [154] T. V. Zache, F. Hebenstreit, F. Jendrzejewski, M. K. Oberthaler, J. Berges, and P. Hauke. “Quantum Simulation of Lattice Gauge Theories Using Wilson Fermions”. *Quantum Science and Technology*, June 2018. DOI: [10.1088/2058-9565/aac33b](https://doi.org/10.1088/2058-9565/aac33b).
- [155] Marco Rigobello, Giuseppe Magnifico, Pietro Silvi, and Simone Montangero. *Hadrons in (1+1)D Hamiltonian Hardcore Lattice QCD*. Sept. 2023. DOI: [10.48550/arXiv.2308.04488](https://doi.org/10.48550/arXiv.2308.04488).
- [156] Richard Brauer and Hermann Weyl. “Spinors in n Dimensions”. *American Journal of Mathematics*, 1935. DOI: [10.2307/2371218](https://doi.org/10.2307/2371218).
- [157] F. Verstraete and J. I. Cirac. “Mapping Local Hamiltonians of Fermions to Local Hamiltonians of Spins”. *Journal of Statistical Mechanics: Theory and Experiment*, Sept. 2005. DOI: [10.1088/1742-5468/2005/09/P09012](https://doi.org/10.1088/1742-5468/2005/09/P09012).

- [158] Pietro Silvi, Enrique Rico, Tommaso Calarco, and Simone Montangero. “Lattice Gauge Tensor Networks”. *New Journal of Physics*, Oct. 2014. DOI: [10.1088/1367-2630/16/10/103015](https://doi.org/10.1088/1367-2630/16/10/103015).
- [159] Indrakshi Raychowdhury and Jesse R. Stryker. “Loop, String, and Hadron Dynamics in SU(2) Hamiltonian Lattice Gauge Theories”. *Physical Review D*, June 2020. DOI: [10.1103/PhysRevD.101.114502](https://doi.org/10.1103/PhysRevD.101.114502).
- [160] Erez Zohar and Michele Burrello. “Formulation of Lattice Gauge Theories for Quantum Simulations”. *Physical Review D*, Mar. 2015. DOI: [10.1103/PhysRevD.91.054506](https://doi.org/10.1103/PhysRevD.91.054506).
- [161] P. Sala, T. Shi, S. Kühn, M. C. Bañuls, E. Demler, and J. I. Cirac. “Variational Study of U(1) and SU(2) Lattice Gauge Theories with Gaussian States in $1+1$ Dimensions”. *Physical Review D*, Aug. 2018. DOI: [10.1103/PhysRevD.98.034505](https://doi.org/10.1103/PhysRevD.98.034505).
- [162] Franco Strocchi. “Non-Perturbative Foundations of Quantum Field Theory”. In: *An Introduction to Non-Perturbative Foundations of Quantum Field Theory*. Ed. by Franco Strocchi. Oxford University Press, Feb. 2013, p. 0. ISBN: 978-0-19-967157-1. DOI: [10.1093/acprof:oso/9780199671571.003.0003](https://doi.org/10.1093/acprof:oso/9780199671571.003.0003).
- [163] G. Burgio, R. De Pietri, H. A. Morales-Técotl, L. F. Urrutia, and J. D. Vergara. “The Basis of the Physical Hilbert Space of Lattice Gauge Theories”. *Nuclear Physics B*, Feb. 2000. DOI: [10.1016/S0550-3213\(99\)00533-7](https://doi.org/10.1016/S0550-3213(99)00533-7).
- [164] Xiaojun Yao. *SU(2) Non-Abelian Gauge Theory on a Plaquette Chain Obeys Eigenstate Thermalization Hypothesis*. June 2023. DOI: [10.48550/arXiv.2303.14264](https://doi.org/10.48550/arXiv.2303.14264).
- [165] Berndt Müller and Xiaojun Yao. *Simple Hamiltonian for Quantum Simulation of Strongly Coupled 2+1D SU(2) Lattice Gauge Theory on a Honeycomb Lattice*. June 2023. DOI: [10.48550/arXiv.2307.00045](https://doi.org/10.48550/arXiv.2307.00045).
- [166] Martin Ringbauer, Michael Meth, Lukas Postler, Roman Stricker, Rainer Blatt, Philipp Schindler, and Thomas Monz. “A Universal Qudit Quantum Processor with Trapped Ions”. *Nature Physics*, Sept. 2022. DOI: [10.1038/s41567-022-01658-0](https://doi.org/10.1038/s41567-022-01658-0).
- [167] Danny Paulson, Luca Dellantonio, Jan F. Haase, Alessio Celi, Angus Kan, Andrew Jena, Christian Kokail, Rick van Bijnen, Karl Jansen, Peter Zoller, and Christine A. Muschik. “Simulating 2D Effects in Lattice Gauge Theories on a Quantum Computer”. *PRX Quantum*, Aug. 2021. DOI: [10.1103/PRXQuantum.2.030334](https://doi.org/10.1103/PRXQuantum.2.030334).
- [168] C. Senko, P. Richerme, J. Smith, A. Lee, I. Cohen, A. Retzker, and C. Monroe. “Realization of a Quantum Integer-Spin Chain with Controllable Interactions”. *Physical Review X*, June 2015. DOI: [10.1103/PhysRevX.5.021026](https://doi.org/10.1103/PhysRevX.5.021026).
- [169] Yoshihito Kuno, Kenichi Kasamatsu, Yoshiro Takahashi, Ikuo Ichinose, and Tetsuo Matsui. “Real-Time Dynamics and Proposal for Feasible Experiments of Lattice Gauge–Higgs Model Simulated by Cold Atoms”. *New Journal of Physics*, June 2015. DOI: [10.1088/1367-2630/17/6/063005](https://doi.org/10.1088/1367-2630/17/6/063005).
- [170] Yoshihito Kuno, Shinya Sakane, Kenichi Kasamatsu, Ikuo Ichinose, and Tetsuo Matsui. “Atomic Quantum Simulation of a Three-Dimensional U(1) Gauge-Higgs Model”. *Physical Review A*, Dec. 2016. DOI: [10.1103/PhysRevA.94.063641](https://doi.org/10.1103/PhysRevA.94.063641).
- [171] Jin Zhang, J. Unmuth-Yockey, J. Zeiher, A. Bazavov, S.-W. Tsai, and Y. Meurice. “Quantum Simulation of the Universal Features of the Polyakov Loop”. *Physical Review Letters*, Nov. 2018. DOI: [10.1103/PhysRevLett.121.223201](https://doi.org/10.1103/PhysRevLett.121.223201).
- [172] Simone Notarnicola, Mario Collura, and Simone Montangero. “Real-Time-Dynamics Quantum Simulation of $(1+1)$ -Dimensional Lattice QED with Rydberg Atoms”. *Physical Review Research*, Mar. 2020. DOI: [10.1103/PhysRevResearch.2.013288](https://doi.org/10.1103/PhysRevResearch.2.013288).
- [173] Timo Felser, Simone Notarnicola, and Simone Montangero. “Efficient Tensor Network Ansatz for High-Dimensional Quantum Many-Body Problems”. *Physical Review Letters*, Apr. 2021. DOI: [10.1103/PhysRevLett.126.170603](https://doi.org/10.1103/PhysRevLett.126.170603).
- [174] Johannes Hauschild and Frank Pollmann. “Efficient Numerical Simulations with Tensor Networks: Tensor Network Python (TeNPy)”. *SciPost Physics Lecture Notes*, Oct. 2018. DOI: [10.21468/SciPostPhysLectNotes.5](https://doi.org/10.21468/SciPostPhysLectNotes.5).
- [175] Anthony Ciavarella, Natalie Klco, and Martin J. Savage. “Trailhead for Quantum Simulation of SU(3) Yang-Mills Lattice Gauge Theory in the Local Multiplet Basis”. *Physical Review D*, May 2021. DOI: [10.1103/PhysRevD.103.094501](https://doi.org/10.1103/PhysRevD.103.094501).

- [176] Zohreh Davoudi, Indrakshi Raychowdhury, and Andrew Shaw. “Search for Efficient Formulations for Hamiltonian Simulation of Non-Abelian Lattice Gauge Theories”. *Physical Review D*, Oct. 2021. DOI: [10.1103/PhysRevD.104.074505](https://doi.org/10.1103/PhysRevD.104.074505).
- [177] Yu Tong, Victor V. Albert, Jarrod R. McClean, John Preskill, and Yuan Su. “Provably Accurate Simulation of Gauge Theories and Bosonic Systems”. *Quantum*, Sept. 2022. DOI: [10.22331/q-2022-09-22-816](https://doi.org/10.22331/q-2022-09-22-816).
- [178] Roberto Fiore, Pietro Giudice, Domenico Giuliano, Donatella Marmottini, Alessandro Papa, and Pasquale Sodano. “QED₃ on a Space-Time Lattice: A Comparison between Compact and Noncompact Formulation”. In: *Proceedings of XXIIIrd International Symposium on Lattice Field Theory — PoS(LAT2005)*. Vol. 20. SISSA Medialab, Dec. 2005, p. 243. DOI: [10.22323/1.020.0243](https://doi.org/10.22323/1.020.0243).
- [179] Ohad Raviv, Yigal Shamir, and Benjamin Svetitsky. “Nonperturbative Beta Function in Three-Dimensional Electrodynamics”. *Physical Review D*, July 2014. DOI: [10.1103/PhysRevD.90.014512](https://doi.org/10.1103/PhysRevD.90.014512).
- [180] Benjamin Svetitsky, Ohad Raviv, and Yigal Shamir. “Beta Function of Three-Dimensional QED”. In: *Proceedings of The 32nd International Symposium on Lattice Field Theory — PoS(LATTICE2014)*. Vol. 214. SISSA Medialab, May 2015, p. 051. DOI: [10.22323/1.214.0051](https://doi.org/10.22323/1.214.0051).
- [181] Lena Funcke, Christiane Franziska Groß, Karl Jansen, Stefan Kühn, Simone Romiti, and Carsten Urbach. “Hamiltonian Limit of Lattice QED in 2+1 Dimensions”. In: *Proceedings of The 39th International Symposium on Lattice Field Theory — PoS(LATTICE2022)*. Vol. 430. SISSA Medialab, Apr. 2023, p. 292. DOI: [10.22323/1.430.0292](https://doi.org/10.22323/1.430.0292).
- [182] Costas Strouthos and John B. Kogut. *The Phases of Non-Compact QED(3)*. Apr. 2008. DOI: [10.48550/arXiv.0804.0300](https://doi.org/10.48550/arXiv.0804.0300).
- [183] Julian Bender. “Quantum and Classical Methods for Lattice Gauge Theories in Higher Dimensions”. PhD thesis. Technische Universität München, 2023.
- [184] J. Eisert. *Entanglement and Tensor Network States*. Sept. 2013. DOI: [10.48550/arXiv.1308.3318](https://doi.org/10.48550/arXiv.1308.3318).
- [185] Christopher Kang, Micheline B. Soley, Eleanor Crane, S. M. Girvin, and Nathan Wiebe. *Leveraging Hamiltonian Simulation Techniques to Compile Operations on Bosonic Devices*. Mar. 2023. DOI: [10.48550/arXiv.2303.15542](https://doi.org/10.48550/arXiv.2303.15542).
- [186] J. Grotendorst, A. Muramatsu, and D. Marx. *Quantum Simulations of Complex Many-Body Systems: From Theory to Algorithms, Lecture Notes; Winter School, 25 February - 1 March 2002, Rolduc Conference Centre, Kerkrade, The Netherlands*. Tech. rep. PreJuSER-24560. John von Neumann Institute for Computing, 2002.
- [187] E. Y. Loh, J. E. Gubernatis, R. T. Scalettar, S. R. White, D. J. Scalapino, and R. L. Sugar. “Sign Problem in the Numerical Simulation of Many-Electron Systems”. *Physical Review B*, May 1990. DOI: [10.1103/PhysRevB.41.9301](https://doi.org/10.1103/PhysRevB.41.9301).
- [188] Anders W. Sandvik. “Computational Studies of Quantum Spin Systems”. *AIP Conference Proceedings*, Nov. 2010. DOI: [10.1063/1.3518900](https://doi.org/10.1063/1.3518900).
- [189] Sukhwinder Singh, Robert N. C. Pfeifer, and Guifré Vidal. “Tensor Network Decompositions in the Presence of a Global Symmetry”. *Physical Review A*, Nov. 2010. DOI: [10.1103/PhysRevA.82.050301](https://doi.org/10.1103/PhysRevA.82.050301).
- [190] Sukhwinder Singh, Robert N. C. Pfeifer, and Guifre Vidal. “Tensor Network States and Algorithms in the Presence of a Global U(1) Symmetry”. *Physical Review B*, Mar. 2011. DOI: [10.1103/PhysRevB.83.115125](https://doi.org/10.1103/PhysRevB.83.115125).
- [191] Martin B. Plenio and S. Virmani. *An Introduction to Entanglement Measures*. June 2006. DOI: [10.48550/arXiv.quant-ph/0504163](https://doi.org/10.48550/arXiv.quant-ph/0504163).
- [192] Luigi Amico, Rosario Fazio, Andreas Osterloh, and Vlatko Vedral. “Entanglement in Many-Body Systems”. *Reviews of Modern Physics*, May 2008. DOI: [10.1103/RevModPhys.80.517](https://doi.org/10.1103/RevModPhys.80.517).
- [193] Pasquale Calabrese and John Cardy. “Entanglement Entropy and Quantum Field Theory”. *Journal of Statistical Mechanics: Theory and Experiment*, June 2004. DOI: [10.1088/1742-5468/2004/06/P06002](https://doi.org/10.1088/1742-5468/2004/06/P06002).
- [194] M. B. Hastings. “An Area Law for One-Dimensional Quantum Systems”. *Journal of Statistical Mechanics: Theory and Experiment*, Aug. 2007. DOI: [10.1088/1742-5468/2007/08/P08024](https://doi.org/10.1088/1742-5468/2007/08/P08024).
- [195] Tomotaka Kuwahara and Keiji Saito. “Area Law of Noncritical Ground States in 1D Long-Range Interacting Systems”. *Nature Communications*, Sept. 2020. DOI: [10.1038/s41467-020-18055-x](https://doi.org/10.1038/s41467-020-18055-x).

- [196] Jaeyoon Cho. “Realistic Area-Law Bound on Entanglement from Exponentially Decaying Correlations”. *Physical Review X*, July 2018. DOI: [10.1103/PhysRevX.8.031009](https://doi.org/10.1103/PhysRevX.8.031009).
- [197] Michael M. Wolf, Frank Verstraete, Matthew B. Hastings, and J. Ignacio Cirac. “Area Laws in Quantum Systems: Mutual Information and Correlations”. *Physical Review Letters*, Feb. 2008. DOI: [10.1103/PhysRevLett.100.070502](https://doi.org/10.1103/PhysRevLett.100.070502).
- [198] Lluís Masanes. “Area Law for the Entropy of Low-Energy States”. *Physical Review A*, Nov. 2009. DOI: [10.1103/PhysRevA.80.052104](https://doi.org/10.1103/PhysRevA.80.052104).
- [199] Eman Hamza, Spyridon Michalakis, Bruno Nachtergaele, and Robert Sims. “Approximating the Ground State of Gapped Quantum Spin Systems”. *Journal of Mathematical Physics*, Sept. 2009. DOI: [10.1063/1.3206662](https://doi.org/10.1063/1.3206662).
- [200] Michael J. Kastoryano, Angelo Lucia, and David Perez-Garcia. “Locality at the Boundary Implies Gap in the Bulk for 2D PEPS”. *Communications in Mathematical Physics*, Mar. 2019. DOI: [10.1007/s00220-019-03404-9](https://doi.org/10.1007/s00220-019-03404-9).
- [201] C. Brockett, F. Dorfner, L. Vidmar, F. Heidrich-Meisner, and E. Jeckelmann. “Matrix-Product-State Method with a Dynamical Local Basis Optimization for Bosonic Systems out of Equilibrium”. *Physical Review B*, Dec. 2015. DOI: [10.1103/PhysRevB.92.241106](https://doi.org/10.1103/PhysRevB.92.241106).
- [202] M. Kliesch, D. Gross, and J. Eisert. “Matrix-Product Operators and States: NP-Hardness and Undecidability”. *Physical Review Letters*, Oct. 2014. DOI: [10.1103/PhysRevLett.113.160503](https://doi.org/10.1103/PhysRevLett.113.160503).
- [203] Steven R. White. “Density Matrix Formulation for Quantum Renormalization Groups”. *Physical Review Letters*, Nov. 1992. DOI: [10.1103/PhysRevLett.69.2863](https://doi.org/10.1103/PhysRevLett.69.2863).
- [204] Steven R. White. “Density-Matrix Algorithms for Quantum Renormalization Groups”. *Physical Review B*, Oct. 1993. DOI: [10.1103/PhysRevB.48.10345](https://doi.org/10.1103/PhysRevB.48.10345).
- [205] Laurens Vanderstraeten, Jutho Haegeman, Philippe Corboz, and Frank Verstraete. “Gradient Methods for Variational Optimization of Projected Entangled-Pair States”. *Physical Review B*, Oct. 2016. DOI: [10.1103/PhysRevB.94.155123](https://doi.org/10.1103/PhysRevB.94.155123).
- [206] Maurits S. J. Tepaske and David J. Luitz. “Three-Dimensional Isometric Tensor Networks”. *Physical Review Research*, June 2021. DOI: [10.1103/PhysRevResearch.3.023236](https://doi.org/10.1103/PhysRevResearch.3.023236).
- [207] Lukasz Cincio, Jacek Dziarmaga, and Marek M. Rams. “Multiscale Entanglement Renormalization Ansatz in Two Dimensions: Quantum Ising Model”. *Physical Review Letters*, June 2008. DOI: [10.1103/PhysRevLett.100.240603](https://doi.org/10.1103/PhysRevLett.100.240603).
- [208] Giovanni Ferrari, Giuseppe Magnifico, and Simone Montangero. “Adaptive-Weighted Tree Tensor Networks for Disordered Quantum Many-Body Systems”. *Physical Review B*, June 2022. DOI: [10.1103/PhysRevB.105.214201](https://doi.org/10.1103/PhysRevB.105.214201).
- [209] Guifré Vidal. “Efficient Classical Simulation of Slightly Entangled Quantum Computations”. *Physical Review Letters*, Oct. 2003. DOI: [10.1103/PhysRevLett.91.147902](https://doi.org/10.1103/PhysRevLett.91.147902).
- [210] Guifré Vidal. “Efficient Simulation of One-Dimensional Quantum Many-Body Systems”. *Physical Review Letters*, July 2004. DOI: [10.1103/PhysRevLett.93.040502](https://doi.org/10.1103/PhysRevLett.93.040502).
- [211] D. Perez-Garcia, F. Verstraete, M. M. Wolf, and J. I. Cirac. *Matrix Product State Representations*. May 2007. DOI: [10.48550/arXiv.quant-ph/0608197](https://doi.org/10.48550/arXiv.quant-ph/0608197).
- [212] A. Klumper, A. Schadschneider, and J. Zittartz. “Equivalence and Solution of Anisotropic Spin-1 Models and Generalized t-J Fermion Models in One Dimension”. *Journal of Physics A: Mathematical and General*, Aug. 1991. DOI: [10.1088/0305-4470/24/16/012](https://doi.org/10.1088/0305-4470/24/16/012).
- [213] Andreas Gleis, Jheng-Wei Li, and Jan von Delft. “Controlled Bond Expansion for DMRG Ground State Search at Single-Site Costs”. *Physical Review Letters*, June 2023. DOI: [10.1103/PhysRevLett.130.246402](https://doi.org/10.1103/PhysRevLett.130.246402).
- [214] Andrew J. Ferris. “Area Law and Real-Space Renormalization”. *Physical Review B*, Mar. 2013. DOI: [10.1103/PhysRevB.87.125139](https://doi.org/10.1103/PhysRevB.87.125139).
- [215] Ho N. Phien, Johann A. Bengua, Hoang D. Tuan, Philippe Corboz, and Román Orús. “Infinite Projected Entangled Pair States Algorithm Improved: Fast Full Update and Gauge Fixing”. *Physical Review B*, July 2015. DOI: [10.1103/PhysRevB.92.035142](https://doi.org/10.1103/PhysRevB.92.035142).
- [216] M. T. Fishman, L. Vanderstraeten, V. Zauner-Stauber, J. Haegeman, and F. Verstraete. “Faster Methods for Contracting Infinite Two-Dimensional Tensor Networks”. *Physical Review B*, Dec. 2018. DOI: [10.1103/PhysRevB.98.235148](https://doi.org/10.1103/PhysRevB.98.235148).
- [217] Z. Y. Xie, H. J. Liao, R. Z. Huang, H. D. Xie, J. Chen, Z. Y. Liu, and T. Xiang. “Optimized Contraction Scheme for Tensor-Network States”. *Physical Review B*, July 2017. DOI: [10.1103/PhysRevB.96.045128](https://doi.org/10.1103/PhysRevB.96.045128).

- [218] Philippe Corboz, Piotr Czarnik, Geert Kapteijns, and Luca Tagliacozzo. “Finite Correlation Length Scaling with Infinite Projected Entangled-Pair States”. *Physical Review X*, July 2018. DOI: [10.1103/PhysRevX.8.031031](https://doi.org/10.1103/PhysRevX.8.031031).
- [219] A. Kshetrimayum, M. Rizzi, J. Eisert, and R. Orús. “Tensor Network Annealing Algorithm for Two-Dimensional Thermal States”. *Physical Review Letters*, Feb. 2019. DOI: [10.1103/PhysRevLett.122.070502](https://doi.org/10.1103/PhysRevLett.122.070502).
- [220] Mazen Ali. *On the Ordering of Sites in the Density Matrix Renormalization Group Using Quantum Mutual Information*. Mar. 2021. DOI: [10.48550/arXiv.2103.01111](https://doi.org/10.48550/arXiv.2103.01111).
- [221] Greta Ghelli, Giuseppe Magnifico, Cristian Degli Esposti Boschi, and Elisa Ercolessi. “Topological Phases in Two-Legged Heisenberg Ladders with Alternating Interactions”. *Physical Review B*, Feb. 2020. DOI: [10.1103/PhysRevB.101.085124](https://doi.org/10.1103/PhysRevB.101.085124).
- [222] A. Kantian, M. Dolfi, M. Troyer, and T. Giamarchi. “Understanding Repulsively Mediated Superconductivity of Correlated Electrons via Massively Parallel Density Matrix Renormalization Group”. *Physical Review B*, Aug. 2019. DOI: [10.1103/PhysRevB.100.075138](https://doi.org/10.1103/PhysRevB.100.075138).
- [223] Tao Xiang, Jizhong Lou, and Zhaobin Su. “Two-Dimensional Algorithm of the Density-Matrix Renormalization Group”. *Physical Review B*, Aug. 2001. DOI: [10.1103/PhysRevB.64.104414](https://doi.org/10.1103/PhysRevB.64.104414).
- [224] Ferdinand Tschirsich, Simone Montangero, and Marcello Dalmonte. “Phase Diagram and Conformal String Excitations of Square Ice Using Gauge Invariant Matrix Product States”. *SciPost Physics*, Mar. 2019. DOI: [10.21468/SciPostPhys.6.3.028](https://doi.org/10.21468/SciPostPhys.6.3.028).
- [225] Susumu Yamada, Toshiyuki Imamura, and Masahiko Machida. “Parallelization Design on Multi-Core Platforms in Density Matrix Renormalization Group toward 2-D Quantum Strongly-Correlated Systems”. In: *Proceedings of 2011 International Conference for High Performance Computing, Networking, Storage and Analysis*. SC '11. New York, NY, USA: Association for Computing Machinery, Nov. 2011, pp. 1–10. ISBN: 978-1-4503-0771-0. DOI: [10.1145/2063384.2063467](https://doi.org/10.1145/2063384.2063467).
- [226] H. V. Jagadish. “Linear Clustering of Objects with Multiple Attributes”. *SIGMOD Rec.*, May 1990. DOI: [10.1145/93605.98742](https://doi.org/10.1145/93605.98742).
- [227] David M. Abel David J. Mark. “A Comparative Analysis of Some Two-Dimensional Orderings”. *International Journal of Geographical Information Systems*, 1990. DOI: [10.1080/02693799008941526](https://doi.org/10.1080/02693799008941526).
- [228] B. Moon, H. V. Jagadish, C. Faloutsos, and J. H. Saltz. “Analysis of the Clustering Properties of the Hilbert Space-Filling Curve”. *IEEE Transactions on Knowledge and Data Engineering*, 2001. DOI: [10.1109/69.908985](https://doi.org/10.1109/69.908985).
- [229] Tilmann Gneiting, Hana Ševčíková, and Donald B. Percival. “Estimators of Fractal Dimension: Assessing the Roughness of Time Series and Spatial Data”. *Statistical Science*, May 2012. DOI: [10.1214/11-STS370](https://doi.org/10.1214/11-STS370).
- [230] David Hilbert. “Ueber Die Stetige Abbildung Einer Line Auf Ein Flächenstück”. *Mathematische Annalen*, Sept. 1891. DOI: [10.1007/BF01199431](https://doi.org/10.1007/BF01199431).
- [231] Daniel Lemire and Owen Kaser. “Reordering Columns for Smaller Indexes”. *Information Sciences*, 2011. DOI: [10.1016/j.ins.2011.02.002](https://doi.org/10.1016/j.ins.2011.02.002).
- [232] Simon Anders. “Visualization of Genomic Data with the Hilbert Curve”. *Bioinformatics*, Mar. 2009. DOI: [10.1093/bioinformatics/btp152](https://doi.org/10.1093/bioinformatics/btp152).
- [233] Sei Suzuki, Jun-ichi Inoue, and Bikas K. Chakrabarti. *Quantum Ising Phases and Transitions in Transverse Ising Models*. Vol. 862. Lecture Notes in Physics. Berlin, Heidelberg: Springer, 2013. ISBN: 978-3-642-33038-4 978-3-642-33039-1. DOI: [10.1007/978-3-642-33039-1](https://doi.org/10.1007/978-3-642-33039-1).
- [234] Zvi Friedman. “Ising Model with a Transverse Field in Two Dimensions: Phase Diagram and Critical Properties from a Real-Space Renormalization Group”. *Physical Review B*, Feb. 1978. DOI: [10.1103/PhysRevB.17.1429](https://doi.org/10.1103/PhysRevB.17.1429).
- [235] Sheng-Hao Li and Guo-Ping Lei. “Quantum Phase Transition in a Two-Dimensional Quantum Ising Model: Tensor Network States and Ground-State Fidelity”. *Journal of Physics: Conference Series*, Sept. 2018. DOI: [10.1088/1742-6596/1087/5/052011](https://doi.org/10.1088/1742-6596/1087/5/052011).
- [236] J. A. Mydosh. “Spin Glasses: Redux: An Updated Experimental/Materials Survey”. *Reports on Progress in Physics*, Apr. 2015. DOI: [10.1088/0034-4885/78/5/052501](https://doi.org/10.1088/0034-4885/78/5/052501).
- [237] Yudong Cao, Jonathan Romero, Jonathan P. Olson, Matthias Degroote, Peter D. Johnson, Mária Kieferová, Ian D. Kivlichan, Tim Menke, Borja Peropadre, Nicolas P. D. Sawaya,

- Sukin Sim, Libor Veis, and Alán Aspuru-Guzik. “Quantum Chemistry in the Age of Quantum Computing”. *Chemical Reviews*, Oct. 2019. DOI: [10.1021/acs.chemrev.8b00803](https://doi.org/10.1021/acs.chemrev.8b00803).
- [238] Richard B. Lehoucq, Danny C. Sorensen, and Chao Yang. *ARPACK Users’ Guide: Solution of Large-Scale Eigenvalue Problems with Implicitly Restarted Arnoldi Methods*. SIAM, Jan. 1998. ISBN: 978-0-89871-407-4.
- [239] Daniel Jaschke and Lincoln D. Carr. “Open Source Matrix Product States: Exact Diagonalization and Other Entanglement-Accurate Methods Revisited in Quantum Systems”. *Journal of Physics A: Mathematical and Theoretical*, Oct. 2018. DOI: [10.1088/1751-8121/aae4d1](https://doi.org/10.1088/1751-8121/aae4d1).
- [240] Norbert Schuch, Michael M. Wolf, Frank Verstraete, and J. Ignacio Cirac. “Entropy Scaling and Simulability by Matrix Product States”. *Physical Review Letters*, Jan. 2008. DOI: [10.1103/PhysRevLett.100.030504](https://doi.org/10.1103/PhysRevLett.100.030504).
- [241] Christopher David White, Michael Zaletel, Roger S. K. Mong, and Gil Refael. “Quantum Dynamics of Thermalizing Systems”. *Physical Review B*, Jan. 2018. DOI: [10.1103/PhysRevB.97.035127](https://doi.org/10.1103/PhysRevB.97.035127).
- [242] J. Surace, M. Piani, and L. Tagliacozzo. “Simulating the Out-of-Equilibrium Dynamics of Local Observables by Trading Entanglement for Mixture”. *Physical Review B*, June 2019. DOI: [10.1103/PhysRevB.99.235115](https://doi.org/10.1103/PhysRevB.99.235115).
- [243] Jutho Haegeman, J. Ignacio Cirac, Tobias J. Osborne, Iztok Pižorn, Henri Verschelde, and Frank Verstraete. “Time-Dependent Variational Principle for Quantum Lattices”. *Physical Review Letters*, Aug. 2011. DOI: [10.1103/PhysRevLett.107.070601](https://doi.org/10.1103/PhysRevLett.107.070601).
- [244] Daniel Bauernfeind and Markus Aichhorn. “Time Dependent Variational Principle for Tree Tensor Networks”. *SciPost Physics*, Feb. 2020. DOI: [10.21468/SciPostPhys.8.2.024](https://doi.org/10.21468/SciPostPhys.8.2.024).
- [245] L. Kohn, P. Silvi, M. Gerster, M. Keck, R. Fazio, G. E. Santoro, and S. Montangero. “Superfluid-to-Mott Transition in a Bose-Hubbard Ring: Persistent Currents and Defect Formation”. *Physical Review A*, Feb. 2020. DOI: [10.1103/PhysRevA.101.023617](https://doi.org/10.1103/PhysRevA.101.023617).
- [246] R L Workman, V D Burkert, V Crede, E Klempt, U Thoma, L Tiator, K Agashe, G Aielli, B C Allanach, C Amsler, M Antonelli, E C Aschenauer, D M Asner, H Baer, Sw Banerjee, R M Barnett, L Baudis, C W Bauer, J J Beatty, V I Belousov, J Beringer, A Bettini, O Biebel, K M Black, E Blucher, R Bonventre, V V Bryzgalov, O Buchmuller, M A Bychkov, R N Cahn, M Carena, A Ceccucci, A Cerri, R Sekhar Chivukula, G Cowan, K Cranmer, O Cremonesi, G D’Ambrosio, T Damour, D de Florian, A de Gouvêa, T DeGrand, P de Jong, S Demers, B A Dobrescu, M D’Onofrio, M Doser, H K Dreiner, P Eerola, U Egede, S Eidelman, A X El-Khadra, J Ellis, S C Eno, J Erler, V V Ezhela, W Fetscher, B D Fields, A Freitas, H Gallagher, Y Gershtein, T Gherghetta, M C Gonzalez-Garcia, M Goodman, C Grab, A V Gritsan, C Grojean, D E Groom, M Grünewald, A Gurtu, T Gutsche, H E Haber, Matthieu Hamel, C Hanhart, S Hashimoto, Y Hayato, A Hebecker, S Heinemeyer, J J Hernández-Rey, K Hikasa, J Hisano, A Höcker, J Holder, L Hsu, J Huston, T Hyodo, Al Ianni, M Kado, M Karliner, U F Katz, M Kenzie, V A Khoze, S R Klein, F Krauss, M Kreps, P Križan, B Krusche, Y Kwon, O Lahav, J Laiho, et al. “Review of Particle Physics”. *Progress of Theoretical and Experimental Physics*, Aug. 2022. DOI: [10.1093/ptep/ptac097](https://doi.org/10.1093/ptep/ptac097).
- [247] Ariel Kelman, Umberto Borla, Itay Gomelski, Jonathan Elyovich, Gertian Roose, Patrick Emonts, and Erez Zohar. *Gauged Gaussian PEPS – A High Dimensional Tensor Network Formulation for Lattice Gauge Theories*. Apr. 2024. DOI: [10.48550/arXiv.2404.13123](https://doi.org/10.48550/arXiv.2404.13123).
- [248] T Holstein. “Studies of Polaron Motion: Part I. The Molecular-Crystal Model”. *Annals of Physics*, Nov. 1959. DOI: [10.1016/0003-4916\(59\)90002-8](https://doi.org/10.1016/0003-4916(59)90002-8).
- [249] Immanuel Bloch. “Ultracold Quantum Gases in Optical Lattices”. *Nature Physics*, Oct. 2005. DOI: [10.1038/nphys138](https://doi.org/10.1038/nphys138).
- [250] F. Schlawin, D. M. Kennes, and M. A. Sentef. “Cavity Quantum Materials”. *Applied Physics Reviews*, Feb. 2022. DOI: [10.1063/5.0083825](https://doi.org/10.1063/5.0083825).
- [251] Jan Stolpp, Thomas Köhler, Salvatore R. Manmana, Eric Jeckelmann, Fabian Heidrich-Meisner, and Sebastian Paeckel. “Comparative Study of State-of-the-Art Matrix-Product-State Methods for Lattice Models with Large Local Hilbert Spaces without $U(1)$ Symmetry”. *Computer Physics Communications*, Dec. 2021. DOI: [10.1016/j.cpc.2021.108106](https://doi.org/10.1016/j.cpc.2021.108106).
- [252] Eric Jeckelmann and Steven R. White. “Density-Matrix Renormalization-Group Study of the Polaron Problem in the Holstein Model”. *Physical Review B*, Mar. 1998. DOI: [10.1103/PhysRevB.57.6376](https://doi.org/10.1103/PhysRevB.57.6376).

- [253] Cheng Guo, Andreas Weichselbaum, Jan von Delft, and Matthias Vojta. “Critical and Strong-Coupling Phases in One- and Two-Bath Spin-Boson Models”. *Physical Review Letters*, Apr. 2012. DOI: [10.1103/PhysRevLett.108.160401](https://doi.org/10.1103/PhysRevLett.108.160401).
- [254] Jan Stolpp, Jacek Herbrych, Florian Dorfner, Elbio Dagotto, and Fabian Heidrich-Meisner. “Charge-Density-Wave Melting in the One-Dimensional Holstein Model”. *Physical Review B*, Jan. 2020. DOI: [10.1103/PhysRevB.101.035134](https://doi.org/10.1103/PhysRevB.101.035134).
- [255] Chunli Zhang, Eric Jeckelmann, and Steven R. White. “Density Matrix Approach to Local Hilbert Space Reduction”. *Physical Review Letters*, Mar. 1998. DOI: [10.1103/PhysRevLett.80.2661](https://doi.org/10.1103/PhysRevLett.80.2661).
- [256] Florian A. Y. N. Schröder and Alex W. Chin. “Simulating Open Quantum Dynamics with Time-Dependent Variational Matrix Product States: Towards Microscopic Correlation of Environment Dynamics and Reduced System Evolution”. *Physical Review B*, Feb. 2016. DOI: [10.1103/PhysRevB.93.075105](https://doi.org/10.1103/PhysRevB.93.075105).
- [257] Manu Mathur and Atul Rathor. “Exact Duality and Local Dynamics in SU(N) Lattice Gauge Theory”. *Physical Review D*, Apr. 2023. DOI: [10.1103/PhysRevD.107.074504](https://doi.org/10.1103/PhysRevD.107.074504).
- [258] Jan Kessler, Francesco Calcavecchia, and Thomas D. Kühne. “Artificial Neural Networks as Trial Wave Functions for Quantum Monte Carlo”. *Advanced Theory and Simulations*, 2021. DOI: [10.1002/adts.202000269](https://doi.org/10.1002/adts.202000269).
- [259] Florian A. Y. N. Schröder, David H. P. Turban, Andrew J. Musser, Nicholas D. M. Hine, and Alex W. Chin. “Tensor Network Simulation of Multi-Environmental Open Quantum Dynamics via Machine Learning and Entanglement Renormalisation”. *Nature Communications*, Mar. 2019. DOI: [10.1038/s41467-019-09039-7](https://doi.org/10.1038/s41467-019-09039-7).
- [260] W. E. Arnoldi. “The Principle of Minimized Iterations in the Solution of the Matrix Eigenvalue Problem”. *Quarterly of Applied Mathematics*, 1951. DOI: [10.1090/qam/42792](https://doi.org/10.1090/qam/42792).
- [261] L. Dagum and R. Menon. “OpenMP: An Industry Standard API for Shared-Memory Programming”. *IEEE Computational Science and Engineering*, Jan. 1998. DOI: [10.1109/99.660313](https://doi.org/10.1109/99.660313).
- [262] Yang Shi, U. N. Niranjan, Animashree Anandkumar, and Cris Cecka. “Tensor Contractions with Extended BLAS Kernels on CPU and GPU”. In: *2016 IEEE 23rd International Conference on High Performance Computing (HiPC)*. Dec. 2016, pp. 193–202. DOI: [10.1109/HiPC.2016.031](https://doi.org/10.1109/HiPC.2016.031).
- [263] A. Abdelfattah, M. Baboulin, V. Dobrev, J. Dongarra, C. Earl, J. Falcou, A. Haidar, I. Karlin, Tz. Kolev, I. Masliah, and S. Tomov. “High-Performance Tensor Contractions for GPUs”. *Procedia Computer Science*, Jan. 2016. DOI: [10.1016/j.procs.2016.05.302](https://doi.org/10.1016/j.procs.2016.05.302).
- [264] Trevor Vincent, Lee J. O’Riordan, Mikhail Andrenkov, Jack Brown, Nathan Killoran, Haoyu Qi, and Ish Dhand. “Jet: Fast Quantum Circuit Simulations with Parallel Task-Based Tensor-Network Contraction”. *Quantum*, May 2022. DOI: [10.22331/q-2022-05-09-709](https://doi.org/10.22331/q-2022-05-09-709).
- [265] Feng Pan and Pan Zhang. “Simulation of Quantum Circuits Using the Big-Batch Tensor Network Method”. *Physical Review Letters*, Jan. 2022. DOI: [10.1103/PhysRevLett.128.030501](https://doi.org/10.1103/PhysRevLett.128.030501).
- [266] Norman P. Jouppi, Cliff Young, Nishant Patil, David Patterson, Gaurav Agrawal, Raminder Bajwa, Sarah Bates, Suresh Bhatia, Nan Boden, Al Borchers, Rick Boyle, Pierre-luc Cantin, Clifford Chao, Chris Clark, Jeremy Coriell, Mike Daley, Matt Dau, Jeffrey Dean, Ben Gelb, Tara Vazir Ghaemmghami, Rajendra Gottipati, William Gulland, Robert Hagmann, C. Richard Ho, Doug Hogberg, John Hu, Robert Hundt, Dan Hurt, Julian Ibarz, Aaron Jaffey, Alek Jaworski, Alexander Kaplan, Harshit Khaitan, Andy Koch, Naveen Kumar, Steve Lacy, James Laudon, James Law, Diemthu Le, Chris Leary, Zhuyuan Liu, Kyle Lucke, Alan Lundin, Gordon MacKean, Adriana Maggiore, Maire Mahony, Kieran Miller, Rahul Nagarajan, Ravi Narayanaswami, Ray Ni, Kathy Nix, Thomas Norrie, Mark Omernick, Narayana Penukonda, Andy Phelps, Jonathan Ross, Matt Ross, Amir Salek, Emad Samadiani, Chris Severn, Gregory Sizikov, Matthew Snelham, Jed Souter, Dan Steinberg, Andy Swing, Mercedes Tan, Gregory Thorson, Bo Tian, Horia Toma, Erick Tuttle, Vijay Vasudevan, Richard Walter, Walter Wang, Eric Wilcox, and Doe Hyun Yoon. *In-Datacenter Performance Analysis of a Tensor Processing Unit*. Apr. 2017. DOI: [10.48550/arXiv.1704.04760](https://doi.org/10.48550/arXiv.1704.04760).
- [267] Markus Hauru, Alan Morningstar, Jackson Beall, Martin Ganahl, Adam Lewis, and Guifre Vidal. *Simulation of Quantum Physics with Tensor Processing Units: Brute-Force Computation of Ground States and Time Evolution*. Nov. 2021. DOI: [10.48550/arXiv.2111.10466](https://doi.org/10.48550/arXiv.2111.10466).

- [268] Alan Morningstar, Markus Hauru, Jackson Beall, Martin Ganahl, Adam G.M. Lewis, Vedika Khemani, and Guifre Vidal. “Simulation of Quantum Many-Body Dynamics with Tensor Processing Units: Floquet Prethermalization”. *PRX Quantum*, May 2022. DOI: [10.1103/PRXQuantum.3.020331](https://doi.org/10.1103/PRXQuantum.3.020331).
- [269] Martin Ganahl, Jackson Beall, Markus Hauru, Adam G.M. Lewis, Tomasz Wojno, Jae Hyeon Yoo, Yijian Zou, and Guifre Vidal. “Density Matrix Renormalization Group with Tensor Processing Units”. *PRX Quantum*, Feb. 2023. DOI: [10.1103/PRXQuantum.4.010317](https://doi.org/10.1103/PRXQuantum.4.010317).
- [270] L. S. Blackford, J. Choi, A. Cleary, E. D’Azevedo, J. Demmel, I. Dhillon, J. Dongarra, S. Hammarling, G. Henry, A. Petitet, K. Stanley, D. Walker, and R. C. Whaley. *ScaLAPACK Users’ Guide*. Software, Environments, and Tools. Society for Industrial and Applied Mathematics, Jan. 1997. ISBN: 978-0-89871-400-5. DOI: [10.1137/1.9780898719642](https://doi.org/10.1137/1.9780898719642).
- [271] Yuechao Lu, Fumihiko Ino, and Yasuyuki Matsushita. *High-Performance Out-of-Core Block Randomized Singular Value Decomposition on GPU*. June 2017. DOI: [10.48550/arXiv.1706.07191](https://doi.org/10.48550/arXiv.1706.07191).
- [272] Edgar Gabriel, Graham E. Fagg, George Bosilca, Thara Angskun, Jack J. Dongarra, Jeffrey M. Squyres, Vishal Sahay, Prabhanjan Kambadur, Brian Barrett, Andrew Lumsdaine, Ralph H. Castain, David J. Daniel, Richard L. Graham, and Timothy S. Woodall. “Open MPI: Goals, Concept, and Design of a Next Generation MPI Implementation”. In: *Recent Advances in Parallel Virtual Machine and Message Passing Interface*. Ed. by Dieter Kranzlmüller, Péter Kacsuk, and Jack Dongarra. Berlin, Heidelberg: Springer, 2004, pp. 97–104. ISBN: 978-3-540-30218-6. DOI: [10.1007/978-3-540-30218-6_19](https://doi.org/10.1007/978-3-540-30218-6_19).
- [273] E. M. Stoudenmire and Steven R. White. “Real-Space Parallel Density Matrix Renormalization Group”. *Physical Review B*, Apr. 2013. DOI: [10.1103/PhysRevB.87.155137](https://doi.org/10.1103/PhysRevB.87.155137).
- [274] Paul Secular, Nikita Gourianov, Michael Lubasch, Sergey Dolgov, Stephen R. Clark, and Dieter Jaksch. “Parallel Time-Dependent Variational Principle Algorithm for Matrix Product States”. *Physical Review B*, June 2020. DOI: [10.1103/PhysRevB.101.235123](https://doi.org/10.1103/PhysRevB.101.235123).
- [275] Davide Bacilieri, Marco Ballarin, Giovanni Cataldi, Aurora Costantini, Daniel Jaschke, Giuseppe Magnifico, Simone Montangero, Simone Notarnicola, Alice Pagano, Luka Pavesic, Davide Rattacaso, Marco Rigobello, Nora Reinić, Simone Scarlatella, Pietro Silvi, and Darwin Wanisch. *Quantum TEA: Qtealeaves*. Zenodo. Aug. 2024. DOI: [10.5281/zenodo.13383350](https://doi.org/10.5281/zenodo.13383350).
- [276] F. Verstraete, J. J. García-Ripoll, and J. I. Cirac. “Matrix Product Density Operators: Simulation of Finite-Temperature and Dissipative Systems”. *Physical Review Letters*, Nov. 2004. DOI: [10.1103/PhysRevLett.93.207204](https://doi.org/10.1103/PhysRevLett.93.207204).
- [277] Michael Zwolak and Guifré Vidal. “Mixed-State Dynamics in One-Dimensional Quantum Lattice Systems: A Time-Dependent Superoperator Renormalization Algorithm”. *Physical Review Letters*, Nov. 2004. DOI: [10.1103/PhysRevLett.93.207205](https://doi.org/10.1103/PhysRevLett.93.207205).
- [278] A. H. Werner, D. Jaschke, P. Silvi, M. Kliesch, T. Calarco, J. Eisert, and S. Montangero. “Positive Tensor Network Approach for Simulating Open Quantum Many-Body Systems”. *Physical Review Letters*, June 2016. DOI: [10.1103/PhysRevLett.116.237201](https://doi.org/10.1103/PhysRevLett.116.237201).
- [279] L. Arceci, P. Silvi, and S. Montangero. “Entanglement of Formation of Mixed Many-Body Quantum States via Tree Tensor Operators”. *Physical Review Letters*, Jan. 2022. DOI: [10.1103/PhysRevLett.128.040501](https://doi.org/10.1103/PhysRevLett.128.040501).
- [280] C. J. Hamer and A. C. Irving. “SU(2) Lattice Gauge Theory in (2+1)D”. *Zeitschrift für Physik C Particles and Fields*, June 1985. DOI: [10.1007/BF01556621](https://doi.org/10.1007/BF01556621).
- [281] Joel Giedt. “Anomalous Dimensions on the Lattice”. *International Journal of Modern Physics A*, Apr. 2016. DOI: [10.1142/S0217751X16300118](https://doi.org/10.1142/S0217751X16300118).
- [282] Alexei Kitaev. “Anyons in an Exactly Solved Model and Beyond”. *Annals of Physics*, Jan. 2006. DOI: [10.1016/j.aop.2005.10.005](https://doi.org/10.1016/j.aop.2005.10.005).
- [283] J. M. Drouffe and J. B. Zuber. “Roughening Transition in Lattice Gauge Theories in Arbitrary Dimension: (II). The Groups Z₃, U(1), SU(2), SU(3)”. *Nuclear Physics B*, Mar. 1981. DOI: [10.1016/0550-3213\(81\)90419-3](https://doi.org/10.1016/0550-3213(81)90419-3).
- [284] Gernot Münster and Peter Weisz. “On the Roughening Transition in Non-Abelian Lattice Gauge Theories”. *Nuclear Physics B*, Mar. 1981. DOI: [10.1016/0550-3213\(81\)90424-7](https://doi.org/10.1016/0550-3213(81)90424-7).
- [285] Hiroaki Arisue and Toshiaki Fujiwara. “New Cluster Expansion Method in Lattice Gauge Theory*”). *Progress of Theoretical Physics*, Dec. 1984. DOI: [10.1143/PTP.72.1176](https://doi.org/10.1143/PTP.72.1176).

- [286] Benjamin Svetitsky and Laurence G. Yaffe. “Critical Behavior at Finite-Temperature Confinement Transitions”. *Nuclear Physics B*, Dec. 1982. DOI: [10.1016/0550-3213\(82\)90172-9](https://doi.org/10.1016/0550-3213(82)90172-9).
- [287] L. Tagliacozzo and G. Vidal. “Entanglement Renormalization and Gauge Symmetry”. *Physical Review B*, Mar. 2011. DOI: [10.1103/PhysRevB.83.115127](https://doi.org/10.1103/PhysRevB.83.115127).
- [288] Y. R. Wang. “Ground State of the Two-Dimensional Antiferromagnetic Heisenberg Model Studied Using an Extended Wigner-Jordon Transformation”. *Physical Review B*, Feb. 1991. DOI: [10.1103/PhysRevB.43.3786](https://doi.org/10.1103/PhysRevB.43.3786).
- [289] U. J. Wiese and H. P. Ying. “A Determination of the Low Energy Parameters of the 2-d Heisenberg Antiferromagnet”. *Zeitschrift für Physik B Condensed Matter*, June 1994. DOI: [10.1007/BF01316955](https://doi.org/10.1007/BF01316955).
- [290] J. Ambjørn, P. Olesen, and C. Peterson. “Observation of a String in Three-Dimensional SU(2) Lattice Gauge Theory”. *Physics Letters B*, Aug. 1984. DOI: [10.1016/0370-2693\(84\)91352-2](https://doi.org/10.1016/0370-2693(84)91352-2).
- [291] J. Ambjørn, P. Olesen, and C. Peterson. “Three-Dimensional Lattice Gauge Theory and Strings”. *Nuclear Physics B*, Sept. 1984. DOI: [10.1016/0550-3213\(84\)90193-7](https://doi.org/10.1016/0550-3213(84)90193-7).
- [292] David B. Kaplan and Jesse R. Stryker. “Gauss’s Law, Duality, and the Hamiltonian Formulation of U(1) Lattice Gauge Theory”. *Physical Review D*, Nov. 2020. DOI: [10.1103/PhysRevD.102.094515](https://doi.org/10.1103/PhysRevD.102.094515).
- [293] Anthony N. Ciavarella. *Quantum Simulation of Lattice QCD with Improved Hamiltonians*. Nov. 2023. DOI: [10.48550/arXiv.2307.05593](https://doi.org/10.48550/arXiv.2307.05593).
- [294] Joe Kiskis. “Numerical Study of Flux Patterns in Non-Abelian Lattice Gauge Theory”. *Physical Review D*, Nov. 1983. DOI: [10.1103/PhysRevD.28.2637](https://doi.org/10.1103/PhysRevD.28.2637).
- [295] Joe Kiskis and Kevin Sparks. “Illustrated Study of Flux Patterns in SU(2) Lattice Gauge Theory”. *Physical Review D*, Sept. 1984. DOI: [10.1103/PhysRevD.30.1326](https://doi.org/10.1103/PhysRevD.30.1326).
- [296] Ari Hietanen and Aleksi Kurkela. “Plaquette Expectation Value and Lattice Free Energy of Three-Dimensional SU(Nc) Gauge Theory”. *Journal of High Energy Physics*, Nov. 2006. DOI: [10.1088/1126-6708/2006/11/060](https://doi.org/10.1088/1126-6708/2006/11/060).
- [297] Alberto Di Meglio, Karl Jansen, Ivano Tavernelli, Constantia Alexandrou, Srinivasan Arunachalam, Christian W. Bauer, Kerstin Borras, Stefano Carrazza, Arianna Crippa, Vincent Croft, Roland de Putter, Andrea Delgado, Vedran Dunjko, Daniel J. Egger, Elias Fernandez-Combarro, Elina Fuchs, Lena Funcke, Daniel Gonzalez-Cuadra, Michele Grossi, Jad C. Halimeh, Zoe Holmes, Stefan Kuhn, Denis Lacroix, Randy Lewis, Donatella Lucchesi, Miriam Lucio Martinez, Federico Meloni, Antonio Mezzacapo, Simone Montangero, Lento Nagano, Voica Radescu, Enrique Rico Ortega, Alessandro Roggero, Julian Schuhmacher, Joao Seixas, Pietro Silvi, Panagiotis Spentzouris, Francesco Tacchino, Kristan Temme, Koji Terashi, Jordi Tura, Cenk Tuysuz, Sofia Vallecorsa, Uwe-Jens Wiese, Shinjae Yoo, and Jinglei Zhang. *Quantum Computing for High-Energy Physics: State of the Art and Challenges. Summary of the QC4HEP Working Group*. July 2023.
- [298] Pengfei Zhang, Hang Dong, Yu Gao, Liangtian Zhao, Jie Hao, Jean-Yves Desaulles, Qiujiang Guo, Jiachen Chen, Jinfeng Deng, Bobo Liu, Wenhui Ren, Yunyan Yao, Xu Zhang, Shibo Xu, Ke Wang, Feitong Jin, Xuhao Zhu, Bing Zhang, Hekang Li, Chao Song, Zhen Wang, Fangli Liu, Zlatko Papić, Lei Ying, H. Wang, and Ying-Cheng Lai. “Many-Body Hilbert Space Scarring on a Superconducting Processor”. *Nature Physics*, Jan. 2023. DOI: [10.1038/s41567-022-01784-9](https://doi.org/10.1038/s41567-022-01784-9).
- [299] Guo-Xian Su, Hui Sun, Ana Hudomal, Jean-Yves Desaulles, Zhao-Yu Zhou, Bing Yang, Jad C. Halimeh, Zhen-Sheng Yuan, Zlatko Papić, and Jian-Wei Pan. “Observation of Many-Body Scarring in a Bose-Hubbard Quantum Simulator”. *Physical Review Research*, Apr. 2023. DOI: [10.1103/PhysRevResearch.5.023010](https://doi.org/10.1103/PhysRevResearch.5.023010).
- [300] Peter Reimann. “Foundation of Statistical Mechanics under Experimentally Realistic Conditions”. *Physical Review Letters*, Nov. 2008. DOI: [10.1103/PhysRevLett.101.190403](https://doi.org/10.1103/PhysRevLett.101.190403).
- [301] Israel Reichenhalt, Anat Klempner, Yariv Kafri, and Daniel Podolsky. “Thermalization in Open Quantum Systems”. *Physical Review B*, Apr. 2018. DOI: [10.1103/PhysRevB.97.134301](https://doi.org/10.1103/PhysRevB.97.134301).
- [302] Joshua M. Deutsch. “Eigenstate Thermalization Hypothesis”. *Reports on Progress in Physics*, July 2018. DOI: [10.1088/1361-6633/aac9f1](https://doi.org/10.1088/1361-6633/aac9f1).
- [303] J. M. Deutsch. “Quantum Statistical Mechanics in a Closed System”. *Physical Review A*, Feb. 1991. DOI: [10.1103/PhysRevA.43.2046](https://doi.org/10.1103/PhysRevA.43.2046).
- [304] Mark Srednicki. “Chaos and Quantum Thermalization”. *Physical Review E*, Aug. 1994. DOI: [10.1103/PhysRevE.50.888](https://doi.org/10.1103/PhysRevE.50.888).

- [305] Luca D’Alessio, Yariv Kafri, Anatoli Polkovnikov, and Marcos Rigol. “From Quantum Chaos and Eigenstate Thermalization to Statistical Mechanics and Thermodynamics”. *Advances in Physics*, May 2016. DOI: [10.1080/00018732.2016.1198134](https://doi.org/10.1080/00018732.2016.1198134).
- [306] Marcos Rigol, Vanja Dunjko, and Maxim Olshanii. “Thermalization and Its Mechanism for Generic Isolated Quantum Systems”. *Nature*, Apr. 2008. DOI: [10.1038/nature06838](https://doi.org/10.1038/nature06838).
- [307] L. Vidmar, J. P. Ronzheimer, M. Schreiber, S. Braun, S. S. Hodgman, S. Langer, F. Heidrich-Meisner, I. Bloch, and U. Schneider. “Dynamical Quasicondensation of Hard-Core Bosons at Finite Momenta”. *Physical Review Letters*, Oct. 2015. DOI: [10.1103/PhysRevLett.115.175301](https://doi.org/10.1103/PhysRevLett.115.175301).
- [308] Giulio Biroli, Corinna Kollath, and Andreas M. Läuchli. “Effect of Rare Fluctuations on the Thermalization of Isolated Quantum Systems”. *Physical Review Letters*, Dec. 2010. DOI: [10.1103/PhysRevLett.105.250401](https://doi.org/10.1103/PhysRevLett.105.250401).
- [309] W. Beugeling, R. Moessner, and Masudul Haque. “Finite-Size Scaling of Eigenstate Thermalization”. *Physical Review E*, Apr. 2014. DOI: [10.1103/PhysRevE.89.042112](https://doi.org/10.1103/PhysRevE.89.042112).
- [310] Wouter Beugeling, Roderich Moessner, and Masudul Haque. “Off-Diagonal Matrix Elements of Local Operators in Many-Body Quantum Systems”. *Physical Review E*, Jan. 2015. DOI: [10.1103/PhysRevE.91.012144](https://doi.org/10.1103/PhysRevE.91.012144).
- [311] Marcos Rigol. “Breakdown of Thermalization in Finite One-Dimensional Systems”. *Physical Review Letters*, Sept. 2009. DOI: [10.1103/PhysRevLett.103.100403](https://doi.org/10.1103/PhysRevLett.103.100403).
- [312] Lea F. Santos and Marcos Rigol. “Localization and the Effects of Symmetries in the Thermalization Properties of One-Dimensional Quantum Systems”. *Physical Review E*, Sept. 2010. DOI: [10.1103/PhysRevE.82.031130](https://doi.org/10.1103/PhysRevE.82.031130).
- [313] Ehsan Khatami, Guido Pupillo, Mark Srednicki, and Marcos Rigol. “Fluctuation-Dissipation Theorem in an Isolated System of Quantum Dipolar Bosons after a Quench”. *Physical Review Letters*, July 2013. DOI: [10.1103/PhysRevLett.111.050403](https://doi.org/10.1103/PhysRevLett.111.050403).
- [314] R. Steinigeweg, A. Khodja, H. Niemeyer, C. Gogolin, and J. Gemmer. “Pushing the Limits of the Eigenstate Thermalization Hypothesis towards Mesoscopic Quantum Systems”. *Physical Review Letters*, Apr. 2014. DOI: [10.1103/PhysRevLett.112.130403](https://doi.org/10.1103/PhysRevLett.112.130403).
- [315] Marcos Rigol. “Quantum Quenches and Thermalization in One-Dimensional Fermionic Systems”. *Physical Review A*, Nov. 2009. DOI: [10.1103/PhysRevA.80.053607](https://doi.org/10.1103/PhysRevA.80.053607).
- [316] Ehsan Khatami, Marcos Rigol, Armando Relaño, and Antonio M. García-García. “Quantum Quenches in Disordered Systems: Approach to Thermal Equilibrium without a Typical Relaxation Time”. *Physical Review E*, May 2012. DOI: [10.1103/PhysRevE.85.050102](https://doi.org/10.1103/PhysRevE.85.050102).
- [317] S. Genway, A. F. Ho, and D. K. K. Lee. “Thermalization of Local Observables in Small Hubbard Lattices”. *Physical Review A*, Aug. 2012. DOI: [10.1103/PhysRevA.86.023609](https://doi.org/10.1103/PhysRevA.86.023609).
- [318] Clemens Neuenhahn and Florian Marquardt. “Thermalization of Interacting Fermions and Delocalization in Fock Space”. *Physical Review E*, June 2012. DOI: [10.1103/PhysRevE.85.060101](https://doi.org/10.1103/PhysRevE.85.060101).
- [319] C. J. Turner, A. A. Michailidis, D. A. Abanin, M. Serbyn, and Z. Papić. “Weak Ergodicity Breaking from Quantum Many-Body Scars”. *Nature Physics*, July 2018. DOI: [10.1038/s41567-018-0137-5](https://doi.org/10.1038/s41567-018-0137-5).
- [320] Sanjay Moudgalya, Stephan Rachel, B. Andrei Bernevig, and Nicolas Regnault. “Exact Excited States of Nonintegrable Models”. *Physical Review B*, Dec. 2018. DOI: [10.1103/PhysRevB.98.235155](https://doi.org/10.1103/PhysRevB.98.235155).
- [321] Michael Schecter and Thomas Iadecola. “Weak Ergodicity Breaking and Quantum Many-Body Scars in Spin-1 XY Magnets”. *Physical Review Letters*, Oct. 2019. DOI: [10.1103/PhysRevLett.123.147201](https://doi.org/10.1103/PhysRevLett.123.147201).
- [322] Cheng-Ju Lin and Olexei I. Motrunich. “Exact Quantum Many-Body Scar States in the Rydberg-Blockaded Atom Chain”. *Physical Review Letters*, Apr. 2019. DOI: [10.1103/PhysRevLett.122.173401](https://doi.org/10.1103/PhysRevLett.122.173401).
- [323] Hannes Bernien, Sylvain Schwartz, Alexander Keesling, Harry Levine, Ahmed Omran, Hannes Pichler, Soonwon Choi, Alexander S. Zibrov, Manuel Endres, Markus Greiner, Vladan Vuletić, and Mikhail D. Lukin. “Probing Many-Body Dynamics on a 51-Atom Quantum Simulator”. *Nature*, Nov. 2017. DOI: [10.1038/nature24622](https://doi.org/10.1038/nature24622).

- [324] Hongzheng Zhao, Joseph Vovrosh, Florian Mintert, and Johannes Knolle. “Quantum Many-Body Scars in Optical Lattices”. *Physical Review Letters*, Apr. 2020. DOI: [10.1103/PhysRevLett.124.160604](https://doi.org/10.1103/PhysRevLett.124.160604).
- [325] Paul Niklas Jepsen, Yoo Kyung ‘Eunice’ Lee, Hanzhen Lin, Ivana Dimitrova, Yair Margalit, Wen Wei Ho, and Wolfgang Ketterle. “Long-Lived Phantom Helix States in Heisenberg Quantum Magnets”. *Nature Physics*, Aug. 2022. DOI: [10.1038/s41567-022-01651-7](https://doi.org/10.1038/s41567-022-01651-7).
- [326] Maksym Serbyn, Dmitry A. Abanin, and Zlatko Papić. “Quantum Many-Body Scars and Weak Breaking of Ergodicity”. *Nature Physics*, June 2021. DOI: [10.1038/s41567-021-01230-2](https://doi.org/10.1038/s41567-021-01230-2).
- [327] Sanjay Moudgalya, B. Andrei Bernevig, and Nicolas Regnault. “Quantum Many-Body Scars and Hilbert Space Fragmentation: A Review of Exact Results”. *Reports on Progress in Physics*, July 2022. DOI: [10.1088/1361-6633/ac73a0](https://doi.org/10.1088/1361-6633/ac73a0).
- [328] Anushya Chandran, Thomas Iadecola, Vedika Khemani, and Roderich Moessner. “Quantum Many-Body Scars: A Quasiparticle Perspective”. *Annual Review of Condensed Matter Physics*, Mar. 2023. DOI: [10.1146/annurev-conmatphys-031620-101617](https://doi.org/10.1146/annurev-conmatphys-031620-101617).
- [329] D. Bluvstein, A. Omran, H. Levine, A. Keesling, G. Semeghini, S. Ebadi, T. T. Wang, A. A. Michailidis, N. Maskara, W. W. Ho, S. Choi, M. Serbyn, M. Greiner, V. Vuletić, and M. D. Lukin. “Controlling Quantum Many-Body Dynamics in Driven Rydberg Atom Arrays”. *Science*, Mar. 2021. DOI: [10.1126/science.abg2530](https://doi.org/10.1126/science.abg2530).
- [330] Dolev Bluvstein, Harry Levine, Giulia Semeghini, Tout T. Wang, Sepehr Ebadi, Marcin Kalinowski, Alexander Keesling, Nishad Maskara, Hannes Pichler, Markus Greiner, Vladan Vuletić, and Mikhail D. Lukin. “A Quantum Processor Based on Coherent Transport of Entangled Atom Arrays”. *Nature*, Apr. 2022. DOI: [10.1038/s41586-022-04592-6](https://doi.org/10.1038/s41586-022-04592-6).
- [331] Wei-Yong Zhang, Ying Liu, Yanting Cheng, Ming-Gen He, Han-Yi Wang, Tian-Yi Wang, Zi-Hang Zhu, Guo-Xian Su, Zhao-Yu Zhou, Yong-Guang Zheng, Hui Sun, Bing Yang, Philipp Hauke, Wei Zheng, Jad C. Halimeh, Zhen-Sheng Yuan, and Jian-Wei Pan. *Observation of Microscopic Confinement Dynamics by a Tunable Topological θ -Angle*. June 2023. DOI: [10.48550/arXiv.2306.11794](https://doi.org/10.48550/arXiv.2306.11794).
- [332] Hang Dong, Jean-Yves Desaulles, Yu Gao, Ning Wang, Zexian Guo, Jiachen Chen, Yiren Zou, Feitong Jin, Xuhao Zhu, Pengfei Zhang, Hekang Li, Zhen Wang, Qiujiang Guo, Junxiang Zhang, Lei Ying, and Zlatko Papić. “Disorder-Tunable Entanglement at Infinite Temperature”. *Science Advances*, Dec. 2023. DOI: [10.1126/sciadv.adj3822](https://doi.org/10.1126/sciadv.adj3822).
- [333] Federica M. Surace, Paolo P. Mazza, Giuliano Giudici, Alessio Leroose, Andrea Gambassi, and Marcello Dalmonte. “Lattice Gauge Theories and String Dynamics in Rydberg Atom Quantum Simulators”. *Physical Review X*, May 2020. DOI: [10.1103/PhysRevX.10.021041](https://doi.org/10.1103/PhysRevX.10.021041).
- [334] Jad C. Halimeh, Monika Aidelsburger, Fabian Grusdt, Philipp Hauke, and Bing Yang. *Cold-Atom Quantum Simulators of Gauge Theories*. Oct. 2023. DOI: [10.48550/arXiv.2310.12201](https://doi.org/10.48550/arXiv.2310.12201).
- [335] Jean-Yves Desaulles, Ana Hudomal, Debasish Banerjee, Arnab Sen, Zlatko Papić, and Jad C. Halimeh. “Prominent Quantum Many-Body Scars in a Truncated Schwinger Model”. *Physical Review B*, May 2023. DOI: [10.1103/PhysRevB.107.205112](https://doi.org/10.1103/PhysRevB.107.205112).
- [336] Jean-Yves Desaulles, Debasish Banerjee, Ana Hudomal, Zlatko Papić, Arnab Sen, and Jad C. Halimeh. “Weak Ergodicity Breaking in the Schwinger Model”. *Physical Review B*, May 2023. DOI: [10.1103/PhysRevB.107.L201105](https://doi.org/10.1103/PhysRevB.107.L201105).
- [337] Thomas Iadecola and Michael Schechter. “Quantum Many-Body Scar States with Emergent Kinetic Constraints and Finite-Entanglement Revivals”. *Physical Review B*, Jan. 2020. DOI: [10.1103/PhysRevB.101.024306](https://doi.org/10.1103/PhysRevB.101.024306).
- [338] Adith Sai Aramthottil, Utso Bhattacharya, Daniel González-Cuadra, Maciej Lewenstein, Luca Barbiero, and Jakub Zakrzewski. “Scar States in Deconfined \mathbb{Z}_2 Lattice Gauge Theories”. *Physical Review B*, July 2022. DOI: [10.1103/PhysRevB.106.L041101](https://doi.org/10.1103/PhysRevB.106.L041101).
- [339] Jean-Yves Desaulles, Thomas Iadecola, and Jad C. Halimeh. *Mass-Assisted Local Deconfinement in a Confined \mathbb{Z}_2 Lattice Gauge Theory*. Apr. 2024. DOI: [10.48550/arXiv.2404.11645](https://doi.org/10.48550/arXiv.2404.11645).
- [340] Debasish Banerjee and Arnab Sen. “Quantum Scars from Zero Modes in an Abelian Lattice Gauge Theory on Ladders”. *Physical Review Letters*, June 2021. DOI: [10.1103/PhysRevLett.126.220601](https://doi.org/10.1103/PhysRevLett.126.220601).

- [341] Saptarshi Biswas, Debasish Banerjee, and Arnab Sen. “Scars from Protected Zero Modes and beyond in $U(1)$ Quantum Link and Quantum Dimer Models”. *SciPost Physics*, May 2022. DOI: [10.21468/SciPostPhys.12.5.148](https://doi.org/10.21468/SciPostPhys.12.5.148).
- [342] Indrajit Sau, Paolo Stornati, Debasish Banerjee, and Arnab Sen. “Sublattice Scars and beyond in Two-Dimensional $U(1)$ Quantum Link Lattice Gauge Theories”. *Physical Review D*, Feb. 2024. DOI: [10.1103/PhysRevD.109.034519](https://doi.org/10.1103/PhysRevD.109.034519).
- [343] Jesse Osborne, Ian P. McCulloch, and Jad C. Halimeh. *Quantum Many-Body Scarring in $SU(2)$ Gauge Theories with Dynamical Matter*. Mar. 2024. DOI: [10.48550/arXiv.2403.08858](https://doi.org/10.48550/arXiv.2403.08858).
- [344] Thea Budde, Marina Krstić Marinković, and Joao C. Pinto Barros. *Quantum Many-Body Scars for Arbitrary Integer Spin in $SU(2)$ Abelian Gauge Theories*. Mar. 2024. DOI: [10.48550/arXiv.2403.08892](https://doi.org/10.48550/arXiv.2403.08892).
- [345] Lukas Ebner, Andreas Schäfer, Clemens Seidl, Berndt Müller, and Xiaojun Yao. *Entanglement Entropy of $SU(2)$ Lattice Gauge Theory on Plaquette Chains*. May 2024. DOI: [10.48550/arXiv.2401.15184](https://doi.org/10.48550/arXiv.2401.15184).
- [346] Yakov G. Sinai. “Dynamical Systems with Elastic Reflections”. *Russian Mathematical Surveys*, Apr. 1970. DOI: [10.1070/RM1970v025n02ABEH003794](https://doi.org/10.1070/RM1970v025n02ABEH003794).
- [347] L. A. Bunimovich. “On the Ergodic Properties of Nowhere Dispersing Billiards”. *Communications in Mathematical Physics*, Oct. 1979. DOI: [10.1007/BF01197884](https://doi.org/10.1007/BF01197884).
- [348] J. Maldacena and L. Susskind. “Cool Horizons for Entangled Black Holes”. *Fortschritte der Physik*, 2013. DOI: [10.1002/prop.201300020](https://doi.org/10.1002/prop.201300020).
- [349] Donald Marolf and Joseph Polchinski. “Gauge-Gravity Duality and the Black Hole Interior”. *Physical Review Letters*, Oct. 2013. DOI: [10.1103/PhysRevLett.111.171301](https://doi.org/10.1103/PhysRevLett.111.171301).
- [350] Rahul Nandkishore and David A. Huse. “Many-Body Localization and Thermalization in Quantum Statistical Mechanics”. *Annual Review of Condensed Matter Physics*, Mar. 2015. DOI: [10.1146/annurev-conmatphys-031214-014726](https://doi.org/10.1146/annurev-conmatphys-031214-014726).
- [351] Johannes Zeiher, Jae-yoon Choi, Antonio Rubio-Abadal, Thomas Pohl, Rick van Bijnen, Immanuel Bloch, and Christian Gross. “Coherent Many-Body Spin Dynamics in a Long-Range Interacting Ising Chain”. *Physical Review X*, Dec. 2017. DOI: [10.1103/PhysRevX.7.041063](https://doi.org/10.1103/PhysRevX.7.041063).
- [352] Daniel Barredo, Vincent Lienhard, Sylvain de Léséleuc, Thierry Lahaye, and Antoine Browaeys. “Synthetic Three-Dimensional Atomic Structures Assembled Atom by Atom”. *Nature*, Sept. 2018. DOI: [10.1038/s41586-018-0450-2](https://doi.org/10.1038/s41586-018-0450-2).
- [353] Paul Fendley, K. Sengupta, and Subir Sachdev. “Competing Density-Wave Orders in a One-Dimensional Hard-Boson Model”. *Physical Review B*, Feb. 2004. DOI: [10.1103/PhysRevB.69.075106](https://doi.org/10.1103/PhysRevB.69.075106).
- [354] Ana Hudomal, Jean-Yves Desaulles, Bhaskar Mukherjee, Guo-Xian Su, Jad C. Halimeh, and Zlatko Papić. “Driving Quantum Many-Body Scars in the PXP Model”. *Physical Review B*, Sept. 2022. DOI: [10.1103/PhysRevB.106.104302](https://doi.org/10.1103/PhysRevB.106.104302).
- [355] Esteban A. Calzetta and Bei-Lok B. Hu. *Nonequilibrium Quantum Field Theory*. Cambridge University Press, 2009. ISBN: 978-1-00-929003-6 978-1-00-928998-6 978-1-00-929002-9. DOI: [10.1017/9781009290036](https://doi.org/10.1017/9781009290036).
- [356] Gunnar S. Bali, Hartmut Neff, Thomas Düssel, Thomas Lippert, Klaus Schilling, and SESAM Collaboration. “Observation of String Breaking in QCD”. *Physical Review D*, June 2005. DOI: [10.1103/PhysRevD.71.114513](https://doi.org/10.1103/PhysRevD.71.114513).
- [357] F. Hebenstreit, J. Berges, and D. Gelfand. “Real-Time Dynamics of String Breaking”. *Physical Review Letters*, Nov. 2013. DOI: [10.1103/PhysRevLett.111.201601](https://doi.org/10.1103/PhysRevLett.111.201601).
- [358] M. Dalmonte and S. Montangero. “Lattice Gauge Theory Simulations in the Quantum Information Era”. *Contemporary Physics*, July 2016. DOI: [10.1080/00107514.2016.1151199](https://doi.org/10.1080/00107514.2016.1151199).
- [359] Yuri Alexeev, Dave Bacon, Kenneth R. Brown, Robert Calderbank, Lincoln D. Carr, Frederic T. Chong, Brian DeMarco, Dirk Englund, Edward Farhi, Bill Fefferman, Alexey V. Gorshkov, Andrew Houck, Jungsang Kim, Shelby Kimmel, Michael Lange, Seth Lloyd, Mikhail D. Lukin, Dmitri Maslov, Peter Maunz, Christopher Monroe, John Preskill, Martin Roetteler, Martin J. Savage, and Jeff Thompson. “Quantum Computer Systems for Scientific Discovery”. *PRX Quantum*, Feb. 2021. DOI: [10.1103/PRXQuantum.2.017001](https://doi.org/10.1103/PRXQuantum.2.017001).
- [360] Monika Aidelsburger, Luca Barbiero, Alejandro Bermudez, Titas Chanda, Alexandre Dauphin, Daniel González-Cuadra, Przemysław R. Grzybowski, Simon Hands, Fred Jendrzejewski, Johannes Jünemann, Gediminas Juzeliūnas, Valentin Kasper, Angelo Piga, Shi-Ju Ran,

- Matteo Rizzi, Germán Sierra, Luca Tagliacozzo, Emanuele Tirrito, Torsten V. Zache, Jakub Zakrzewski, Erez Zohar, and Maciej Lewenstein. “Cold Atoms Meet Lattice Gauge Theory”. *Philosophical Transactions of the Royal Society A: Mathematical, Physical and Engineering Sciences*, Dec. 2021. DOI: [10.1098/rsta.2021.0064](https://doi.org/10.1098/rsta.2021.0064).
- [361] Yanting Cheng and Hui Zhai. *Emergent Gauge Theory in Rydberg Atom Arrays*. Jan. 2024. DOI: [10.48550/arXiv.2401.07708](https://doi.org/10.48550/arXiv.2401.07708).
- [362] Matthew Fishman, Steven White, and Edwin Miles Stoudenmire. “The ITensor Software Library for Tensor Network Calculations”. *SciPost Physics Codebases*, Aug. 2022. DOI: [10.21468/SciPostPhysCodeb.4](https://doi.org/10.21468/SciPostPhysCodeb.4).
- [363] Matthew Fishman, Steven White, and Edwin Miles Stoudenmire. “Codebase Release 0.3 for ITensor”. *SciPost Physics Codebases*, Aug. 2022. DOI: [10.21468/SciPostPhysCodeb.4-r0.3](https://doi.org/10.21468/SciPostPhysCodeb.4-r0.3).
- [364] Jad C. Halimeh, Luca Barbiero, Philipp Hauke, Fabian Grusdt, and Annabelle Bohrdt. “Robust Quantum Many-Body Scars in Lattice Gauge Theories”. *Quantum*, May 2023. DOI: [10.22331/q-2023-05-15-1004](https://doi.org/10.22331/q-2023-05-15-1004).
- [365] Aiden Daniel, Andrew Hallam, Jean-Yves Desaulles, Ana Hudomal, Guo-Xian Su, Jad C. Halimeh, and Zlatko Papić. “Bridging Quantum Criticality via Many-Body Scarring”. *Physical Review B*, June 2023. DOI: [10.1103/PhysRevB.107.235108](https://doi.org/10.1103/PhysRevB.107.235108).
- [366] Maarten Van Damme, Torsten V. Zache, Debasish Banerjee, Philipp Hauke, and Jad C. Halimeh. “Dynamical Quantum Phase Transitions in Spin- $U(1)$ Quantum Link Models”. *Physical Review B*, Dec. 2022. DOI: [10.1103/PhysRevB.106.245110](https://doi.org/10.1103/PhysRevB.106.245110).
- [367] Maarten Van Damme, Jean-Yves Desaulles, Zlatko Papić, and Jad C. Halimeh. “Anatomy of Dynamical Quantum Phase Transitions”. *Physical Review Research*, Aug. 2023. DOI: [10.1103/PhysRevResearch.5.033090](https://doi.org/10.1103/PhysRevResearch.5.033090).
- [368] Eduardo Fradkin. *Field Theories of Condensed Matter Physics*. 2nd ed. Cambridge: Cambridge University Press, 2013. ISBN: 978-0-521-76444-5. DOI: [10.1017/CB09781139015509](https://doi.org/10.1017/CB09781139015509).
- [369] Assa Auerbach. *Interacting Electrons and Quantum Magnetism*. Ed. by Joseph L. Birman, Jeffrey W. Lynn, Mark P. Silverman, H. Eugene Stanley, and Mikhail Voloshin. Graduate Texts in Contemporary Physics. New York, NY: Springer, 1994. ISBN: 978-1-4612-6928-1 978-1-4612-0869-3. DOI: [10.1007/978-1-4612-0869-3](https://doi.org/10.1007/978-1-4612-0869-3).
- [370] Thierry Giamarchi. *Quantum Physics in One Dimension*. Oxford University Press, Dec. 2003. ISBN: 978-0-19-171190-9. DOI: [10.1093/acprof:oso/9780198525004.001.0001](https://doi.org/10.1093/acprof:oso/9780198525004.001.0001).
- [371] Patrick A. Lee, Naoto Nagaosa, and Xiao-Gang Wen. “Doping a Mott Insulator: Physics of High-Temperature Superconductivity”. *Reviews of Modern Physics*, Jan. 2006. DOI: [10.1103/RevModPhys.78.17](https://doi.org/10.1103/RevModPhys.78.17).
- [372] Thomas Hartke, Botond Oreg, Carter Turnbaugh, Ningyuan Jia, and Martin Zwierlein. “Direct Observation of Nonlocal Fermion Pairing in an Attractive Fermi-Hubbard Gas”. *Science*, July 2023. DOI: [10.1126/science.ade4245](https://doi.org/10.1126/science.ade4245).
- [373] Bertran Halperin and Jainendra K. Jain. *Fractional Quantum Hall Effects: New Developments*. World Scientific, 2020.
- [374] Kévin Hémerly, Khaldoon Ghanem, Eleanor Crane, Sara L. Campbell, Joan M. Dreiling, Caroline Figgatt, Cameron Foltz, John P. Gaebler, Jacob Johansen, Michael Mills, Steven A. Moses, Juan M. Pino, Anthony Ransford, Mary Rowe, Peter Siegfried, Russell P. Stutz, Henrik Dreyer, Alexander Schuckert, and Ramil Nigmatullin. *Measuring the Loschmidt Amplitude for Finite-Energy Properties of the Fermi-Hubbard Model on an Ion-Trap Quantum Computer*. Sept. 2023. DOI: [10.48550/arXiv.2309.10552](https://doi.org/10.48550/arXiv.2309.10552).
- [375] Christian Hofrichter, Luis Riegger, Francesco Scazza, Moritz Höfer, Diogo Rio Fernandes, Immanuel Bloch, and Simon Fölling. “Direct Probing of the Mott Crossover in the $SU(N)$ Fermi-Hubbard Model”. *Physical Review X*, June 2016. DOI: [10.1103/PhysRevX.6.021030](https://doi.org/10.1103/PhysRevX.6.021030).
- [376] Christof Gattringer and Kurt Langfeld. “Approaches to the Sign Problem in Lattice Field Theory”. *International Journal of Modern Physics A*, Aug. 2016. DOI: [10.1142/S0217751X16430077](https://doi.org/10.1142/S0217751X16430077).
- [377] Ehud Altman, Kenneth R. Brown, Giuseppe Carleo, Lincoln D. Carr, Eugene Demler, Cheng Chin, Brian DeMarco, Sophia E. Economou, Mark A. Eriksson, Kai-Mei C. Fu, Markus Greiner, Kaden R.A. Hazzard, Randall G. Hulet, Alicia J. Kollár, Benjamin L. Lev, Mikhail D. Lukin, Ruichao Ma, Xiao Mi, Shashank Misra, Christopher Monroe, Kater Murch, Zaira Nazario, Kang-Kuen Ni, Andrew C. Potter, Pedram Roushan, Mark Saffman,

- Monika Schleier-Smith, Irfan Siddiqi, Raymond Simmonds, Meenakshi Singh, I.B. Spielman, Kristan Temme, David S. Weiss, Jelena Vučković, Vladan Vuletić, Jun Ye, and Martin Zwierlein. “Quantum Simulators: Architectures and Opportunities”. *PRX Quantum*, Feb. 2021. DOI: [10.1103/PRXQuantum.2.017003](https://doi.org/10.1103/PRXQuantum.2.017003).
- [378] Tilman Esslinger. “Fermi-Hubbard Physics with Atoms in an Optical Lattice”. *Annual Review of Condensed Matter Physics*, Aug. 2010. DOI: [10.1146/annurev-conmatphys-070909-104059](https://doi.org/10.1146/annurev-conmatphys-070909-104059).
- [379] Immanuel Bloch, Jean Dalibard, and Sylvain Nascimbène. “Quantum Simulations with Ultracold Quantum Gases”. *Nature Physics*, Apr. 2012. DOI: [10.1038/nphys2259](https://doi.org/10.1038/nphys2259).
- [380] Leticia Tarruell and Laurent Sanchez-Palencia. “Quantum simulation of the Hubbard model with ultracold fermions in optical lattices”. *Comptes Rendus. Physique*, 2018. DOI: [10.1016/j.crhy.2018.10.013](https://doi.org/10.1016/j.crhy.2018.10.013).
- [381] Annabelle Bohrdt, Lukas Homeier, Christian Reinmoser, Eugene Demler, and Fabian Grusdt. “Exploration of Doped Quantum Magnets with Ultracold Atoms”. *Annals of Physics*, Dec. 2021. DOI: [10.1016/j.aop.2021.168651](https://doi.org/10.1016/j.aop.2021.168651).
- [382] Lawrence W. Cheuk, Matthew A. Nichols, Melih Okan, Thomas Gersdorf, Vinay V. Ramasesh, Waseem S. Bakr, Thomas Lompe, and Martin W. Zwierlein. “Quantum-Gas Microscope for Fermionic Atoms”. *Physical Review Letters*, May 2015. DOI: [10.1103/PhysRevLett.114.193001](https://doi.org/10.1103/PhysRevLett.114.193001).
- [383] Pedro M. Duarte, Russell A. Hart, Tsung-Lin Yang, Xinxing Liu, Thereza Paiva, Ehsan Khatami, Richard T. Scalettar, Nandini Trivedi, and Randall G. Hulet. “Compressibility of a Fermionic Mott Insulator of Ultracold Atoms”. *Physical Review Letters*, Feb. 2015. DOI: [10.1103/PhysRevLett.114.070403](https://doi.org/10.1103/PhysRevLett.114.070403).
- [384] G. J. A. Edge, R. Anderson, D. Jervis, D. C. McKay, R. Day, S. Trotzky, and J. H. Thywissen. “Imaging and Addressing of Individual Fermionic Atoms in an Optical Lattice”. *Physical Review A*, Dec. 2015. DOI: [10.1103/PhysRevA.92.063406](https://doi.org/10.1103/PhysRevA.92.063406).
- [385] Daniel Greif, Thomas Uehlinger, Gregor Jotzu, Leticia Tarruell, and Tilman Esslinger. “Short-Range Quantum Magnetism of Ultracold Fermions in an Optical Lattice”. *Science*, June 2013. DOI: [10.1126/science.1236362](https://doi.org/10.1126/science.1236362).
- [386] Elmar Haller, James Hudson, Andrew Kelly, Dylan A. Cotta, Bruno Peaudecerf, Graham D. Bruce, and Stefan Kuhr. “Single-Atom Imaging of Fermions in a Quantum-Gas Microscope”. *Nature Physics*, Sept. 2015. DOI: [10.1038/nphys3403](https://doi.org/10.1038/nphys3403).
- [387] Russell A. Hart, Pedro M. Duarte, Tsung-Lin Yang, Xinxing Liu, Thereza Paiva, Ehsan Khatami, Richard T. Scalettar, Nandini Trivedi, David A. Huse, and Randall G. Hulet. “Observation of Antiferromagnetic Correlations in the Hubbard Model with Ultracold Atoms”. *Nature*, Mar. 2015. DOI: [10.1038/nature14223](https://doi.org/10.1038/nature14223).
- [388] W. Hofstetter, J. I. Cirac, P. Zoller, E. Demler, and M. D. Lukin. “High-Temperature Superfluidity of Fermionic Atoms in Optical Lattices”. *Physical Review Letters*, Nov. 2002. DOI: [10.1103/PhysRevLett.89.220407](https://doi.org/10.1103/PhysRevLett.89.220407).
- [389] Robert Jördens, Niels Strohmaier, Kenneth Günter, Henning Moritz, and Tilman Esslinger. “A Mott Insulator of Fermionic Atoms in an Optical Lattice”. *Nature*, Sept. 2008. DOI: [10.1038/nature07244](https://doi.org/10.1038/nature07244).
- [390] Michael Messer, Rémi Desbuquois, Thomas Uehlinger, Gregor Jotzu, Sebastian Huber, Daniel Greif, and Tilman Esslinger. “Exploring Competing Density Order in the Ionic Hubbard Model with Ultracold Fermions”. *Physical Review Letters*, Sept. 2015. DOI: [10.1103/PhysRevLett.115.115303](https://doi.org/10.1103/PhysRevLett.115.115303).
- [391] S. Murmann, F. Deuretzbacher, G. Zürn, J. Bjerlin, S. M. Reimann, L. Santos, T. Lompe, and S. Jochim. “Antiferromagnetic Heisenberg Spin Chain of a Few Cold Atoms in a One-Dimensional Trap”. *Physical Review Letters*, Nov. 2015. DOI: [10.1103/PhysRevLett.115.215301](https://doi.org/10.1103/PhysRevLett.115.215301).
- [392] Ahmed Omran, Martin Boll, Timon A. Hilker, Katharina Kleinlein, Guillaume Salomon, Immanuel Bloch, and Christian Gross. “Microscopic Observation of Pauli Blocking in Degenerate Fermionic Lattice Gases”. *Physical Review Letters*, Dec. 2015. DOI: [10.1103/PhysRevLett.115.263001](https://doi.org/10.1103/PhysRevLett.115.263001).
- [393] Maxwell F. Parsons, Florian Huber, Anton Mazurenko, Christie S. Chiu, Widagdo Setiawan, Katherine Wooley-Brown, Sebastian Blatt, and Markus Greiner. “Site-Resolved Imaging of Fermionic Li^6 in an Optical Lattice”. *Physical Review Letters*, May 2015. DOI: [10.1103/PhysRevLett.114.213002](https://doi.org/10.1103/PhysRevLett.114.213002).

- [394] U. Schneider, L. Hackermüller, S. Will, Th. Best, I. Bloch, T. A. Costi, R. W. Helmes, D. Rasch, and A. Rosch. “Metallic and Insulating Phases of Repulsively Interacting Fermions in a 3D Optical Lattice”. *Science*, Dec. 2008. DOI: [10.1126/science.1165449](https://doi.org/10.1126/science.1165449).
- [395] Shintaro Taie, Rekishu Yamazaki, Seiji Sugawa, and Yoshiro Takahashi. “An SU(6) Mott Insulator of an Atomic Fermi Gas Realized by Large-Spin Pomeranchuk Cooling”. *Nature Physics*, Nov. 2012. DOI: [10.1038/nphys2430](https://doi.org/10.1038/nphys2430).
- [396] Thomas Uehlinger, Gregor Jotzu, Michael Messer, Daniel Greif, Walter Hofstetter, Ulf Bissbort, and Tilman Esslinger. “Artificial Graphene with Tunable Interactions”. *Physical Review Letters*, Oct. 2013. DOI: [10.1103/PhysRevLett.111.185307](https://doi.org/10.1103/PhysRevLett.111.185307).
- [397] D. González-Cuadra, D. Bluvstein, M. Kalinowski, R. Kaubruegger, N. Maskara, P. Naldesi, T. V. Zache, A. M. Kaufman, M. D. Lukin, H. Pichler, B. Vermersch, Jun Ye, and P. Zoller. “Fermionic Quantum Processing with Programmable Neutral Atom Arrays”. *Proceedings of the National Academy of Sciences*, Aug. 2023. DOI: [10.1073/pnas.2304294120](https://doi.org/10.1073/pnas.2304294120).
- [398] Eduardo Fradkin, Mark Srednicki, and Leonard Susskind. “Fermion Representation for the \mathbb{Z}_2 Lattice Gauge Theory in 2+1 Dimensions”. *Physical Review D*, May 1980. DOI: [10.1103/PhysRevD.21.2885](https://doi.org/10.1103/PhysRevD.21.2885).
- [399] Mark Srednicki. “Hidden Fermions in $\mathbb{Z}(2)$ Theories”. *Physical Review D*, May 1980. DOI: [10.1103/PhysRevD.21.2878](https://doi.org/10.1103/PhysRevD.21.2878).
- [400] Yu-An Chen, Anton Kapustin, and Đorđe Radičević. “Exact Bosonization in Two Spatial Dimensions and a New Class of Lattice Gauge Theories”. *Annals of Physics*, June 2018. DOI: [10.1016/j.aop.2018.03.024](https://doi.org/10.1016/j.aop.2018.03.024).
- [401] A. Yu. Kitaev. “Fault-Tolerant Quantum Computation by Anyons”. *Annals of Physics*, Jan. 2003. DOI: [10.1016/S0003-4916\(02\)00018-0](https://doi.org/10.1016/S0003-4916(02)00018-0).
- [402] Yu-An Chen and Yijia Xu. “Equivalence between Fermion-to-Qubit Mappings in Two Spatial Dimensions”. *PRX Quantum*, Mar. 2023. DOI: [10.1103/PRXQuantum.4.010326](https://doi.org/10.1103/PRXQuantum.4.010326).
- [403] Guy Pardo, Tomer Greenberg, Aryeh Fortinsky, Nadav Katz, and Erez Zohar. “Resource-Efficient Quantum Simulation of Lattice Gauge Theories in Arbitrary Dimensions: Solving for Gauss’s Law and Fermion Elimination”. *Physical Review Research*, May 2023. DOI: [10.1103/PhysRevResearch.5.023077](https://doi.org/10.1103/PhysRevResearch.5.023077).
- [404] Reinis Irmejs, Mari-Carmen Bañuls, and J. Ignacio Cirac. “Quantum Simulation of \mathbb{Z}_2 Lattice Gauge Theory with Minimal Resources”. *Physical Review D*, Oct. 2023. DOI: [10.1103/PhysRevD.108.074503](https://doi.org/10.1103/PhysRevD.108.074503).
- [405] Timon A. Hilker, Guillaume Salomon, Fabian Grusdt, Ahmed Omran, Martin Boll, Eugene Demler, Immanuel Bloch, and Christian Gross. “Revealing Hidden Antiferromagnetic Correlations in Doped Hubbard Chains via String Correlators”. *Science*, Aug. 2017. DOI: [10.1126/science.aam8990](https://doi.org/10.1126/science.aam8990).
- [406] Jayadev Vijayan, Pimonpan Sompert, Guillaume Salomon, Joannis Koepsell, Sarah Hirthe, Annabelle Bohrdt, Fabian Grusdt, Immanuel Bloch, and Christian Gross. “Time-Resolved Observation of Spin-Charge Deconfinement in Fermionic Hubbard Chains”. *Science*, Jan. 2020. DOI: [10.1126/science.aay2354](https://doi.org/10.1126/science.aay2354).
- [407] Geoffrey Ji, Muqing Xu, Lev Haldar Kendrick, Christie S. Chiu, Justus C. Brüggengjürgen, Daniel Greif, Annabelle Bohrdt, Fabian Grusdt, Eugene Demler, Martin Lebrat, and Markus Greiner. “Coupling a Mobile Hole to an Antiferromagnetic Spin Background: Transient Dynamics of a Magnetic Polaron”. *Physical Review X*, Apr. 2021. DOI: [10.1103/PhysRevX.11.021022](https://doi.org/10.1103/PhysRevX.11.021022).
- [408] Joannis Koepsell, Dominik Bourgund, Pimonpan Sompert, Sarah Hirthe, Annabelle Bohrdt, Yao Wang, Fabian Grusdt, Eugene Demler, Guillaume Salomon, Christian Gross, and Immanuel Bloch. “Microscopic Evolution of Doped Mott Insulators from Polaronic Metal to Fermi Liquid”. *Science*, Oct. 2021. DOI: [10.1126/science.abe7165](https://doi.org/10.1126/science.abe7165).
- [409] Elliott H. Lieb and F. Y. Wu. “Absence of Mott Transition in an Exact Solution of the Short-Range, One-Band Model in One Dimension”. *Physical Review Letters*, June 1968. DOI: [10.1103/PhysRevLett.20.1445](https://doi.org/10.1103/PhysRevLett.20.1445).
- [410] Alexei Kitaev and Chris Laumann. *Topological Phases and Quantum Computation*. Apr. 2009. DOI: [10.48550/arXiv.0904.2771](https://doi.org/10.48550/arXiv.0904.2771).
- [411] J. Hubbard. “Electron Correlations in Narrow Energy Bands”. *Proceedings of the Royal Society of London. Series A, Mathematical and Physical Sciences*, 1963.

- [412] J. Hubbard and Brian Hilton Flowers. “Electron Correlations in Narrow Energy Bands II. The Degenerate Band Case”. *Proceedings of the Royal Society of London. Series A. Mathematical and Physical Sciences*, Jan. 1964. DOI: [10.1098/rspa.1964.0019](https://doi.org/10.1098/rspa.1964.0019).
- [413] J. Hubbard and Brian Hilton Flowers. “Electron Correlations in Narrow Energy Bands III. An Improved Solution”. *Proceedings of the Royal Society of London. Series A. Mathematical and Physical Sciences*, Sept. 1964. DOI: [10.1098/rspa.1964.0190](https://doi.org/10.1098/rspa.1964.0190).
- [414] Daniel P. Arovas, Erez Berg, Steven A. Kivelson, and Srinivas Raghu. “The Hubbard Model”. *Annual Review of Condensed Matter Physics*, Mar. 2022. DOI: [10.1146/annurev-conmatphys-031620-102024](https://doi.org/10.1146/annurev-conmatphys-031620-102024).
- [415] Walter Metzner and Dieter Vollhardt. “Correlated Lattice Fermions in $d = \infty$ Dimensions”. *Physical Review Letters*, Jan. 1989. DOI: [10.1103/PhysRevLett.62.324](https://doi.org/10.1103/PhysRevLett.62.324).
- [416] E. Müller-Hartmann. “Correlated Fermions on a Lattice in High Dimensions”. *Zeitschrift für Physik B Condensed Matter*, Dec. 1989. DOI: [10.1007/BF01311397](https://doi.org/10.1007/BF01311397).
- [417] Mingpu Qin, Thomas Schäfer, Sabine Andergassen, Philippe Corboz, and Emanuel Gull. “The Hubbard Model: A Computational Perspective”. *Annual Review of Condensed Matter Physics*, Mar. 2022. DOI: [10.1146/annurev-conmatphys-090921-033948](https://doi.org/10.1146/annurev-conmatphys-090921-033948).
- [418] J. P. F. LeBlanc, Andrey E. Antipov, Federico Becca, Ireneusz W. Bulik, Garnet Kin-Lic Chan, Chia-Min Chung, Youjin Deng, Michel Ferrero, Thomas M. Henderson, Carlos A. Jiménez-Hoyos, E. Kozik, Xuan-Wen Liu, Andrew J. Millis, N. V. Prokof'ev, Mingpu Qin, Gustavo E. Scuseria, Hao Shi, B. V. Svistunov, Luca F. Tocchio, I. S. Tupitsyn, Steven R. White, Shiwei Zhang, Bo-Xiao Zheng, Zhenyue Zhu, and Emanuel Gull. “Solutions of the Two-Dimensional Hubbard Model: Benchmarks and Results from a Wide Range of Numerical Algorithms”. *Phys. Rev. X*, Dec. 2015. DOI: [10.1103/PhysRevX.5.041041](https://doi.org/10.1103/PhysRevX.5.041041).
- [419] Elliott H. Lieb. “Two Theorems on the Hubbard Model”. *Physical Review Letters*, Mar. 1989. DOI: [10.1103/PhysRevLett.62.1201](https://doi.org/10.1103/PhysRevLett.62.1201).
- [420] James D. Whitfield, Vojtěch Havlíček, and Matthias Troyer. “Local Spin Operators for Fermion Simulations”. *Physical Review A*, Sept. 2016. DOI: [10.1103/PhysRevA.94.030301](https://doi.org/10.1103/PhysRevA.94.030301).
- [421] Mark Steudtner and Stephanie Wehner. “Quantum Codes for Quantum Simulation of Fermions on a Square Lattice of Qubits”. *Physical Review A*, Feb. 2019. DOI: [10.1103/PhysRevA.99.022308](https://doi.org/10.1103/PhysRevA.99.022308).
- [422] Kanav Setia, Sergey Bravyi, Antonio Mezzacapo, and James D. Whitfield. “Superfast Encodings for Fermionic Quantum Simulation”. *Physical Review Research*, Oct. 2019. DOI: [10.1103/PhysRevResearch.1.033033](https://doi.org/10.1103/PhysRevResearch.1.033033).
- [423] Charles Derby, Joel Klassen, Johannes Bausch, and Toby Cubitt. “Compact Fermion to Qubit Mappings”. *Physical Review B*, July 2021. DOI: [10.1103/PhysRevB.104.035118](https://doi.org/10.1103/PhysRevB.104.035118).
- [424] C. Kollath, U. Schollwöck, and W. Zwerger. “Spin-Charge Separation in Cold Fermi Gases: A Real Time Analysis”. *Physical Review Letters*, Oct. 2005. DOI: [10.1103/PhysRevLett.95.176401](https://doi.org/10.1103/PhysRevLett.95.176401).
- [425] F. Grusdt, M. Kánasz-Nagy, A. Bohrdt, C. S. Chiu, G. Ji, M. Greiner, D. Greif, and E. Demler. “Parton Theory of Magnetic Polarons: Mesonic Resonances and Signatures in Dynamics”. *Physical Review X*, Mar. 2018. DOI: [10.1103/PhysRevX.8.011046](https://doi.org/10.1103/PhysRevX.8.011046).
- [426] Daniel Gottesman. *Stabilizer Codes and Quantum Error Correction*. May 1997. DOI: [10.48550/arXiv.quant-ph/9705052](https://doi.org/10.48550/arXiv.quant-ph/9705052).
- [427] Manuel S. Rudolph, Jing Chen, Jacob Miller, Atithi Acharya, and Alejandro Perdomo-Ortiz. “Decomposition of Matrix Product States into Shallow Quantum Circuits”. *Quantum Science and Technology*, Nov. 2023. DOI: [10.1088/2058-9565/ad04e6](https://doi.org/10.1088/2058-9565/ad04e6).
- [428] Matteo M. Wauters, Glen B. Mbeng, and Giuseppe E. Santoro. “Polynomial Scaling of the Quantum Approximate Optimization Algorithm for Ground-State Preparation of the Fully Connected $S=1/2$ -Spin Ferromagnet in a Transverse Field”. *Physical Review A*, Dec. 2020. DOI: [10.1103/PhysRevA.102.062404](https://doi.org/10.1103/PhysRevA.102.062404).
- [429] Marco Ballarin, Daniel Jaschke, and Simone Montangero. *Quantum TEA: Qmatchatea*. Zenodo. June 2024. DOI: [10.5281/zenodo.11619266](https://doi.org/10.5281/zenodo.11619266).
- [430] Dolev Bluvstein, Simon J. Evered, Alexandra A. Geim, Sophie H. Li, Hengyun Zhou, Tom Manovitz, Sepehr Ebadi, Madelyn Cain, Marcin Kalinowski, Dominik Hangleiter, J. Pablo Bonilla Ataides, Nishad Maskara, Iris Cong, Xun Gao, Pedro Sales Rodriguez, Thomas Karolyshyn, Giulia Semeghini, Michael J. Gullans, Markus Greiner, Vladan Vuletić, and

- Mikhail D. Lukin. “Logical Quantum Processor Based on Reconfigurable Atom Arrays”. *Nature*, Feb. 2024. DOI: [10.1038/s41586-023-06927-3](https://doi.org/10.1038/s41586-023-06927-3).
- [431] M. P. da Silva, C. Ryan-Anderson, J. M. Bello-Rivas, A. Chernoguzov, J. M. Dreiling, C. Foltz, F. Frachon, J. P. Gaebler, T. M. Gatterman, L. Grans-Samuelsson, D. Hayes, N. Hewitt, J. Johansen, D. Lucchetti, M. Mills, S. A. Moses, B. Neyenhuis, A. Paz, J. Pino, P. Siegfried, J. Strabley, A. Sundaram, D. Tom, S. J. Wernli, M. Zanner, R. P. Stutz, and K. M. Svore. *Demonstration of Logical Qubits and Repeated Error Correction with Better-than-Physical Error Rates*. Apr. 2024. DOI: [10.48550/arXiv.2404.02280](https://doi.org/10.48550/arXiv.2404.02280).
- [432] J. Jordan, R. Orús, G. Vidal, F. Verstraete, and J. I. Cirac. “Classical Simulation of Infinite-Size Quantum Lattice Systems in Two Spatial Dimensions”. *Physical Review Letters*, Dec. 2008. DOI: [10.1103/PhysRevLett.101.250602](https://doi.org/10.1103/PhysRevLett.101.250602).
- [433] Marco Ballarín, Giovanni Cataldi, Giuseppe Magnifico, Daniel Jaschke, Marco Di Liberto, Ilaria Siloi, Simone Montangero, and Pietro Silvi. *Simulation Scripts for "Digital Quantum Simulation of Lattice Fermion Theories with Local Encoding"*. Zenodo. June 2024. DOI: [10.5281/zenodo.11619804](https://doi.org/10.5281/zenodo.11619804).
- [434] J. Greensite and S. Olejnik. *The QCD Vacuum Wave Functional and Confinement in Coulomb Gauge*. Oct. 2010. DOI: [10.48550/arXiv.1010.4995](https://doi.org/10.48550/arXiv.1010.4995).
- [435] Marco Rigobello. “Scattering Processes via Tensor Network Simulations”. MA thesis. University of Padua, June 2020.
- [436] Marlon Brenes, Marcello Dalmonte, Markus Heyl, and Antonello Scardicchio. “Many-Body Localization Dynamics from Gauge Invariance”. *Physical Review Letters*, Jan. 2018. DOI: [10.1103/PhysRevLett.120.030601](https://doi.org/10.1103/PhysRevLett.120.030601).